IRRATIONAL TWIN INTERFACES IN SHAPE MEMORY ALLOYS AND RELEVANCE TO FUNCTIONAL FATIGUE

BY

AHMED SAMEER KHAN MOHAMMED

DISSERTATION

Submitted in partial fulfillment of the requirements
for the degree of Doctor of Philosophy in Mechanical Engineering
in the Graduate College of the
University of Illinois Urbana-Champaign, 2022

Urbana, Illinois

Doctoral Committee:

Professor Huseyin Sehitoglu, Chair and Director of Research
Associate Professor Jessica Krogstad
Associate Professor Elif Ertekin
Professor Petros Sofronis

ABSTRACT

Shape Memory Alloys (SMAs) are functional materials characterized by their ability to undergo large magnitudes of reversible mechanical deformation through a microstructural mechanism known as the martensitic phase transformation. This capacity makes SMAs attractive for several actuating applications spanning biomedical, aerospace, and automotive domains. However, such reversibility is not perfect and a finite magnitude of residual deformation remains trapped in the material upon unload. Over several cycles of deformation, this residual deformation accumulates and leads to failure by a phenomenon termed as functional fatigue. Functional fatigue occurs by the emission and accumulation of slip dislocations at the intersection of two critical interfaces in the phase transformation – the martensitic twin boundary and the "habit plane". Both these interfaces are uniquely complicated by their tendency to exhibit irrational Miller-index identities that is atypical in crystalline materials. Such irrationality has precluded any understanding of the atomistic and topological structure of these interfaces, ultimately precluding an understanding of the source of fatigue. This research addresses this void from a modeling standpoint through anisotropic continuum mechanics, atomistic simulations, and thermodynamics.

This research begins by establishing the atomistic and topological structure of the Type II twin interface in NiTi, one of the most commercially successful SMAs. A Terrace-Disconnection (T-D) topology for the interface is proposed, deriving the necessity for a periodically spaced array of disconnections to relieve coherence strains on rational terraces. The atomic-structure of the rational terrace is determined through Molecular Statics (MS) simulations, establishing the existence of non-trivial lattice-offsets and the role of lattice-motif shuffles in the mechanism of twin migration, both of which are unique to the non-single-lattice structure of the martensitic phase in NiTi. The motion of twinning disconnections on the rational terraces was simulated within a

MS framework. Following an early notional hypothesis on slip-emission proposed in the early 1980s, the interaction of the twinning disconnection with a migration barrier was simulated where the barrier mimics the role of the transformation front of the SMA. It was observed that a dislocation reaction occurs leading to the emission of a dislocation on the twin boundary, explaining the formation of residual slip dislocations.

The structure of the type II twin interface continued to remain a matter of debate in the field with two contrasting propositions offered for its structure, one being the aforementioned T-D topology while the other was a Tilt-Wall (T-W) topology. Through a concerted modeling approach involving both MS simulations and continuum Eshelby-Stroh mechanics, this study establishes the energetic favorability of the T-D topology. It is theoretically shown that such a T-D topology attributes a capacity for the interface to evolve under microstructural strain explaining conflicting experimental observations in literature for the first time. Furthermore, it is shown that even type I and compound twins that are otherwise known to exhibit rational Miller-index identities can evolve under the influence of strain to exhibit irrational topologies in general. In this regard, an irrational T-D topology is proposed to be a norm rather than the exception for twin interfaces in SMAs. The influence of such strain-sensitive interface evolution on functional fatigue is discussed. A general framework to analyze irrational type II twin interfaces in other SMAs is then developed, applied to martensitic crystal structures of the $B19$-orthorhombic form in TiPd, TiPt and AuCd. It is shown that the irrational T-D topology is in effect a compromise achieved by the material to satisfy minimal continuum strain-energy and atomistic potential energy.

Having resolved the irrational twin interface, the structure of the "habit plane" or the phase-transformation front was addressed next. An open problem to address was how the twin-variants in the martensitic phase are oriented with respect to the austenite and how the twin interface

intersects the transformation front as that is the location of accumulating residual slip-dislocations. The study target of FeMnNiAl was chosen for its simpler cubic crystalline forms in the austenitic and martensitic phases. Experimental results for the first time observed multiple non-unique orientation relationships between the austenitic and martensitic phases, observing the Pitsch, Krudjumov-Sachs and Nishiyama-Wasserman orientation-relations independently. These observations were explained based on an energy-minimization theory bridging a gap between the predictions of the continuum theory with the crystallography of the transformation. The atomic-structure of the habit-plane is proposed as a coherent zone hosting large strain-gradients of transformation merging the martensitic twinned/faulted structure with the parent austenitic phase.

The final contribution of this research is to provide a thermodynamic explanation of why slip-emission occurs in martensitic transformations at all. Prior work in the field attributed the necessity of residual slip to accommodate strain-mismatch at the habit-plane. However, these considerations were neither supported by an underlying understanding of interface structure nor by a complete consideration of the Gibbs' free energy. This research proposes the spontaneity of slip-emission during reverse transformation by showing that it is the favored path of reversal for the material upon unload based on Gibbs' free energy considerations. This path is preferred due to an addition of thermodynamic driving force afforded by the increasing transformation-strain of the martensitic inclusion, hypothesized and revealed for the first time. In conclusion, this study addresses multiple voids in revealing the cause of functional fatigue with the ultimate goal of providing tailorable design parameters to engineer superior fatigue-resistant SMAs.

ACKNOWLEDGMENTS

This dissertation would not have seen the light of day if not for the support from several people along the journey. I want to first thank and acknowledge the support from my advisor, Prof. Huseyin Sehitoglu. His unfailing dedication to scientific contribution and to the professional growth of graduate students in his group has inspired and motivated me beyond measure. From introducing the research problem to discussing it over the years, many a time with a humility to work with me as a peer researcher, his encouraging support and steadfast guidance has helped me successfully navigate the ups and downs of the PhD journey (which included a global pandemic!). I am grateful to Richard Rateick for his support during my PhD, for his infectious passion and enthusiasm for scientific discovery and selfless long-term vision for research projects generating value on both academic and commercial fronts. I am grateful to the Air Force Office of Scientific Research (under award number FA9550-18-1-0198, with Dr. Ali Sayir as Program Director) and Honeywell for financial support of my graduate study.

I want to thank my colleagues from the High Temperature Materials Laboratory, Dr. Piyas Chowdhury, Dr. Avinesh Ojha, Dr. Yan Wu, Dr. Sertan Alkan, Dr. Wael Abuzaid, Sidharth Ravi, Orcun Celebi and Gorkem Gengor for their friendship, support, and several enlightening conversations during my time in the lab. I am grateful to the research scientists at the Materials Research Laboratory, Dr. Kathy Walsh, Dr. Jessica Spear, Dr. CQ Chen, Dr. Honghui Zhou, Dr Jade Wang, Dr. Wacek Swiech, Dr. Julio Soares, the director of research facilities Dr. Mauro Sardela, and research scientist Dr. Dianwen Zhang from the Beckman institute, for their time and patience to train me on several experimental techniques and for their prompt support throughout.

Finally, I am grateful to my parents, Mr. Khaleelullah Khan Mohammed and Mrs. Ghousia Jabeen Abdul Aziz and my brother, Mr. Ahmed Zaheer Khan Mohammed, for being patient with me and for always being there.

To my family

TABLE OF CONTENTS

CHAPTER 1: INTRODUCTION

This chapter presents a brief introduction to Shape Memory Alloys and to the problem of functional fatigue. Microstructural evidence of transformation-induced slip is quoted from literature motivating the importance of understanding the two critical interfaces in the transformation, namely the internal twin boundary of martensite and the phase-transformation front (or habit plane). An early hypothesis of slip-emission from literature is discussed as it sets the starting point for the proposed research of this study. And finally the organization of this thesis is presented.

1.1. Shape Memory Alloys and the problem of Functional Fatigue

Shape Memory Alloys (SMAs) are crystalline materials that exhibit intriguing responses to thermo-mechanical stimuli, capable of exhibiting a "memory" of their starting configuration in what is known as the Shape-Memory-Effect (SME) and also of "Superelastic" (SE) recoverable deformation under the influence of mechanical load [1]. Some well-known examples of such SMAs are NiTi, CuZnAl, FeMnNiAl etc. External stimuli are further not limited to temperature or strain and can further include external magnetic field, for instance in Magnetic SMAs such as NiMnGa [2]. These materials are ideal macro-scale actuators in that they can sustain considerable mechanical load while undergoing large strains. And for this reason, they are widely employed in multiple applications in the biomedical, aerospace, and automotive domains [3].

An illustration of both SME and SE behaviors is illustrated in figure 1. In the SME effect illustrated in figure 1 (a), the material can undergo an inelastic history of mechanical deformation that imparts a permanent set to the material at B compared to where it started from, at A. And if the material is then heated, it recovers the permanent set and reaches a high-temperature state of C. Upon cooling, the starting configuration of A is recovered. Thus, the material seemingly

exhibits a memory of the configuration A it began from and offers a pathway to cycle back-and-forth between this configuration and a deformed state B. The SE effect is illustrated in figure 1 (b), where the material can cycle back-and-forth between an undeformed state A_0 and deformed state B_0 under the influence of mechanical load. And in completion, SMAs can also undergo thermally-induced reversible response as shown in figure 1(c).

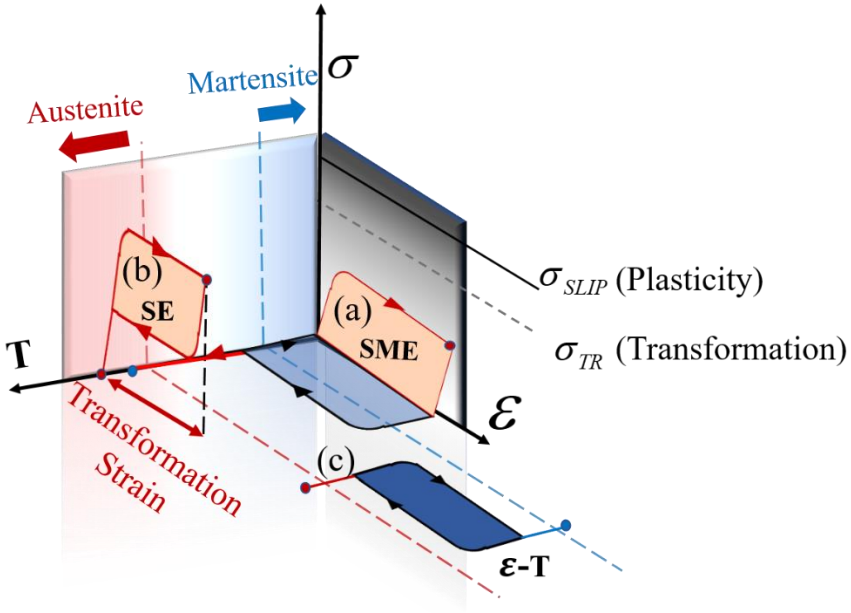

Figure 1: Schematic illustration of strain-response of Shape Memory Alloys (SMAs) under stimuli of external stress and temperature; along the temperature axis, the two phases austenite and martensite are indicated with the former stable at high temperatures while the latter is stable at low temperatures (a) the Shape Memory Effect (SME) is illustrated where an applied plastic deformation can be recovered by subsequent heating, giving the impression of "memory" of the original shape/configuration possessed by the material (b) Superelastic (SE) mechanical response is illustrated where a large recoverable transformation-strain is exhibited by the SMA under the influence of external stress only; the required stress to induce transformation σ_{TR} is generally much lower than that required for austenitic slip σ_{SLIP} (c) Strain-temperature ($\varepsilon - T$) response at constant external stress exhibiting recoverable strain-response under thermal cycling

In all these mechanisms, it is apparent that there is an inbuilt microstructural mechanism that allows the SMA to deform in a predictable and reversible manner. And this mechanism is a phase-transformation that occurs between two equilibrium phases of the SMA. One phase is termed the "Austenite" phase, characterized by a highly-symmetric crystalline structure (often

based on a cubic lattice) and is stable at high temperatures. The second phase is the “Martensite” phase, characterized by a low-symmetry crystalline structure (exhibiting monoclinic, orthorhombic and other complex non-cubic lattices) and is stable at low temperatures. This study focuses on the SE phenomenon henceforth. In the SE response, the material starts from the austenite phase and transforms to the martensitic phase under the influence of mechanical load and then transforms back to the parent austenite phase upon removal of the load. This transformation is diffusionless in nature and thus occurs in a time-independent manner along with increasing mechanical strain [1]. A similar pathway between the two phases is charted in the SME effect as well. The key idea is that SMA materials possess a mechanism that offers reversibility unlike conventional metallic materials and thus hold the promise of offering unprecedented fatigue life.

However, there exists a challenge in that SMA behavior is not perfectly reversible. Every cycle of deformation leaves a certain amount of residual strain in the material and this strain accumulates over cycles. This phenomenon is illustrated in figure 2, where real experimental data from FeNiCoAlTi is shown [4]. Under SE cycling, there is a progressive accumulation of residual strain until at some point, the material no longer exhibits any transformation and only loads-unloads in an elastic manner. This phenomenon is referred to as “Functional Fatigue” since the functional strain attributed by the phase-transformation is gradually diminished and lost over cycles. Such functionality loss directly impacts and limits useful application life of SMA products, such as biomedical stents. An open problem in the field is to determine material parameters that directly quantify the propensity of functional fatigue in SMAs, thereby allowing an approach for tailored design of fatigue-resistant SMAs.

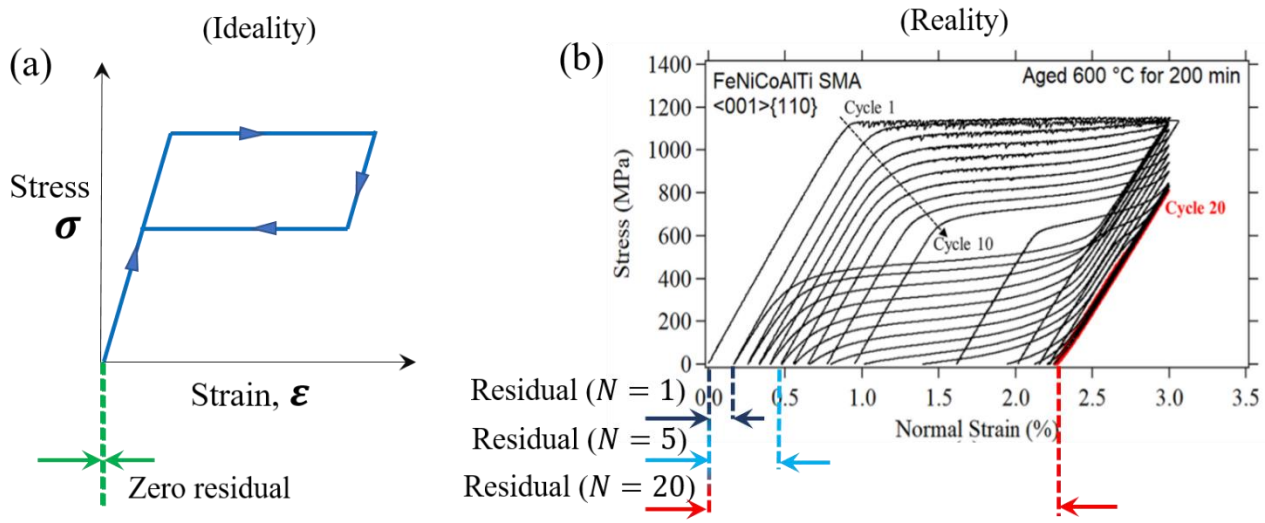

Figure 2: Functional fatigue under Superelastic (SE) cycling (a) Ideal SE behavior exhibiting a fully recoverable response and zero accumulation of residual strain (b) Real SE behavior of an FeNiCoAlTi SMA exhibiting accumulating residual strain (and thus degrading recoverability) over multiple cycles of deformation N (adapted from [4])

1.2. Critical interfaces associated with transformation-induced slip

Several microstructural studies have clarified the cause of functional fatigue as an accumulating density of slip-dislocations in the austenite phase. This observation is perplexing because the external stress required for slip in the austenitic phase is far higher than the stress for transformation. In the case of NiTi for example, the slip stress can be as high as 1000 MPa, well above the transformation stress that is of the order of few 100 MPa [5]. Thus, it comes as a surprise that dislocation-activity is observed at stress-levels of transformation far under that required for dislocation-slip. And further, it is interestingly ironic that a material (SMA) that offered a phase-transforming alternative for deformation (instead of dislocation-mediated plasticity as seen in metals) is still unable to avoid dislocation-activity and associated fatigue behavior.

Figure 3 illustrates multiple TEM images of SMA microstructures illustrating the presence of both the parent austenite phase, the transformed martensite phase, and the accumulating

dislocations in the austenite phase. These dislocations and their slip-systems exhibit multiple interesting characteristics:

a. Dislocation-activity is strongly concentrated at the phase-transformation front
b. The slip-system of the dislocation exhibits a distinctive order in that dislocation-activity is seen in parallel slip-systems separated in a periodic manner and emanating from the martensite into the austenite phase
c. Of all candidate slip systems in the parent austenite phase, there is generally a preferred slip-system that is seemingly "selected" by the transformation [6-10].

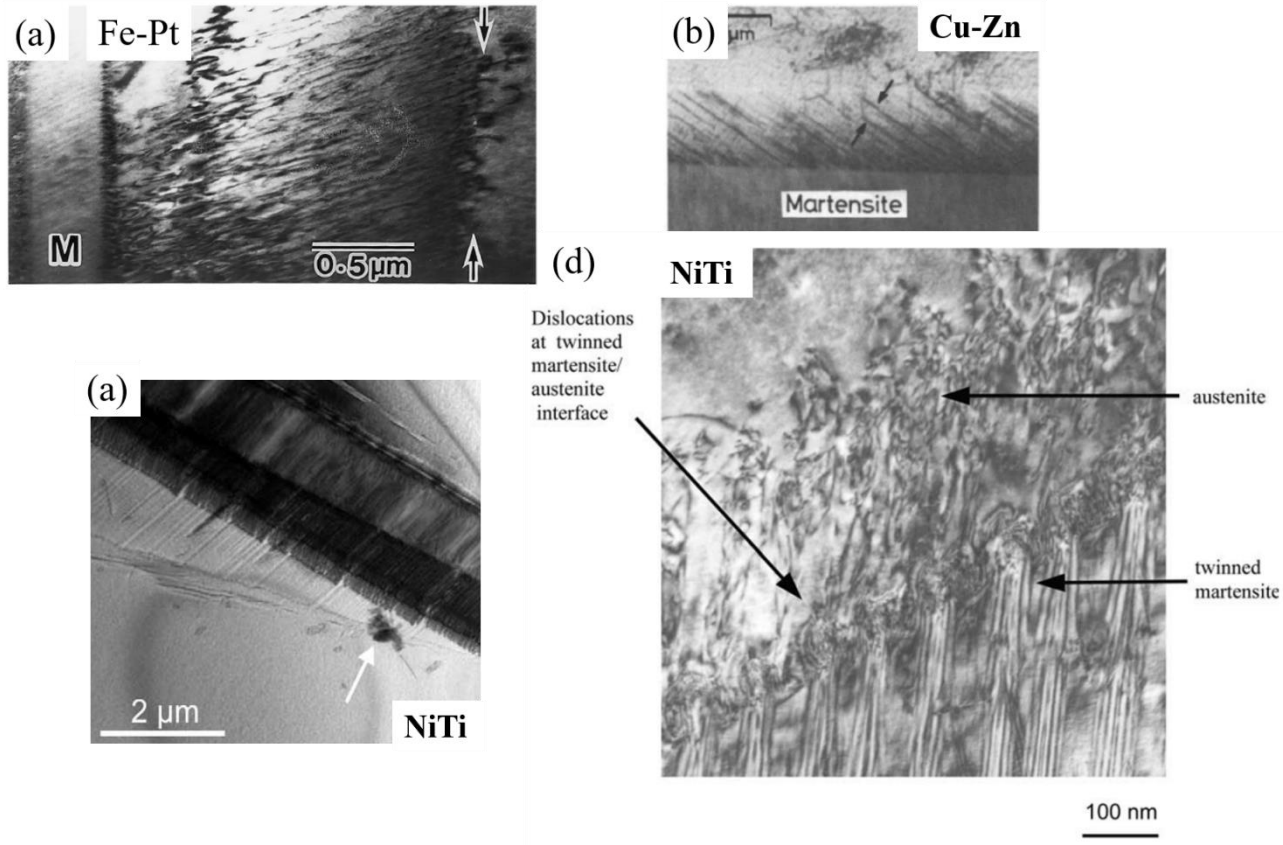

Figure 3: Microstrucutral evidence of transformation-induced slip in multiple SMAs: (a) Fe-Pt [10] (b) Cu-Zn [9] (c, d) NiTi [7, 11]; note that the slip-system emanates from the austenite-martenstie transformation front and exhibits a preferential alignment, known to be consistent with the internal twinning system of the transformed martensite

In addition to such evidence, a mature understanding of the internal microstructure of martensite had been developed simultaneously. It was well-known at the time that the martensitic phase does not generally form as a single-crystal variant but forms in either a twinned configuration (with two twin variants), or in a stacking-faulted configuration (with periodically spaced stacking faults). Each of these configurations nucleates and grows within the austenitic phase as a "Habit-Plane-Variant (HPV)" exhibiting a nearly-planar transformation front. And furthermore, the martensite can also form in morphologies consisted by multiple HPVs if not as a single HPV. With such an understanding developed almost in parallel, it became apparent that the accumulating dislocation slip-system was linked to the internal microstructure of martensite. It is now well-established that the slip-dislocations form on slip-systems aligned with the internal twinning system of the martensitic phase [6-9, 12].

However, multiple open questions remained. To begin with, the causal explanation justifying the necessity for dislocation-slip associated with the phase-transformation is still unclear. The major reason behind this void is the lack of clarity in understanding of the interfaces involved in the process, namely the internal twin interface in martensite and the phase-transformation front. And the primary challenge that has precluded the development of such understanding is the complicated crystallography of the martensitic phase and the tendency for these interfaces to exhibit "irrational" Miller-index identities. This goal of this study is to address both these aspects and bolster the understanding of these interfaces to explain transformation-induced dislocation-slip in SMAs.

1.3. A hypothesis for slip-emission: Kajiwara-Kikuchi mechanism

Possibly the most puzzling aspects of functional fatigue is the occurrence of plastic slip accumulation at stress levels far lower than the plastic flow stresses of the individual phases [13]. In fact, even stress-free thermal cycling of SMAs exhibit increasing dislocation density [7, 8]. A continuum micromechanical approach to the problem may state that the higher local stress state at the interface, necessary to accommodate lattice and constitutive mismatch, can drive plastic slip. However, without a dislocation source, the stress levels must approach those of the ideal shear slip strength of the phases and this is unlikely. This is supported by the high unstable stacking fault energy barrier in the Generalized Stacking Fault Energy (GSFE) curves of the austenitic phase, particularly in those slip systems which have been shown to prevail under fatigue loading [14]. And careful experimental studies had identified that these slip dislocations are prominently observed after reverse transformation from the martensitic phase, appearing in regions priorly swept through by the habit-plane of the transformation. And if these dislocations were always present on the transformation front to accommodate the mismatch strain between the phases, then there would be no abrupt changes in the density of dislocations along the habit-plane as is observed from experiments, and shown in figure 3 [12].

These arguments led to the belief that there is indeed a dislocation mechanism that is active at nominal stress levels (at the transformation stress) and is closely tied to the internal twinning within martensite. To the best of the author's knowledge, only one proposition of candidate dislocation reaction exists in literature and it involves the interaction of twinning disconnections on the internal martensitic TB with the habit plane [9]. A schematic of the mechanism is shown in figure 4, adapted from the original proposition in ref. [9].

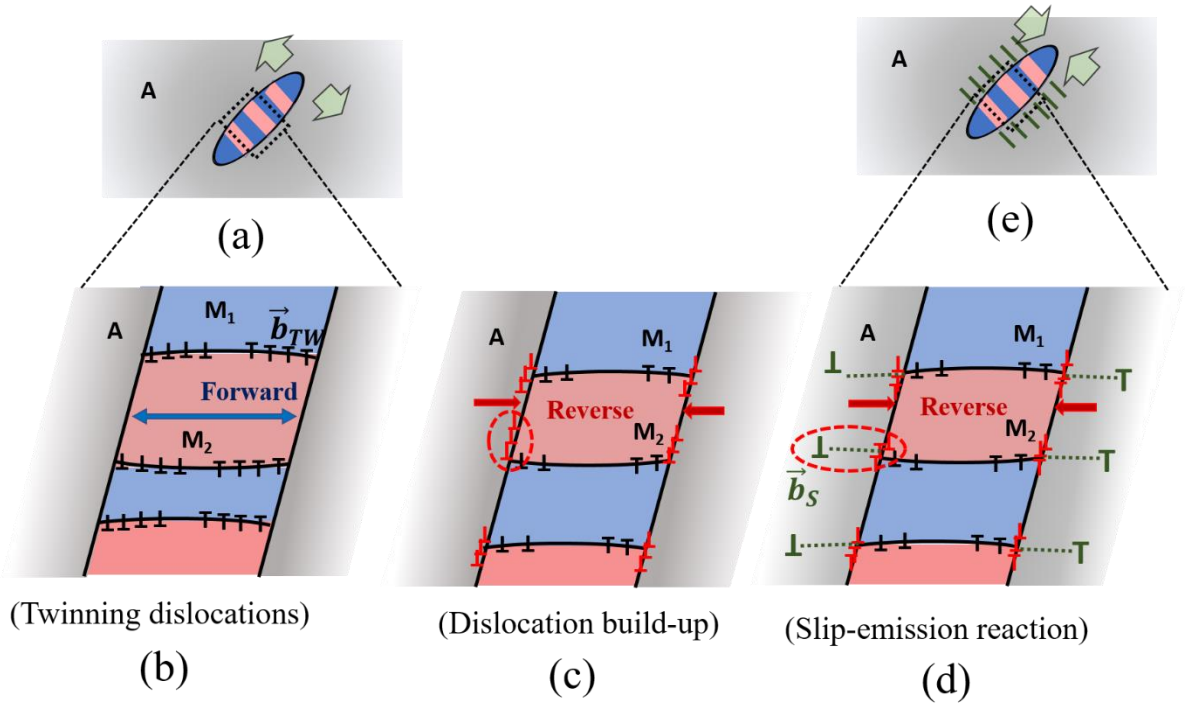

Figure 4: K-K slip-emission mechanism for transformation-induced slip (a) Internally-twinned martensitic inclusion in an austenite matrix (b) Migration of internal twin boundaries within martensite mediated by twinning dislocations with Burgers vectors $\vec{b}_{TW}$, during the forward transformation (growth of martensite) (c) Build-up of arrested twin-dislocations on the austenite-martensite transformation front during the reverse transformation (shrinking martensite) (d) Slip-emission dislocation reaction on the transformation front resulting in slip-dislocations in the austenite phase (with Burgers vector $\vec{b}_S$) (e) Emitted slip-lines are aligned with the internal twinning plane as evidenced experimentally

In brief, the mechanism proposed was that the slip-dislocations are formed by a dislocation reaction occurring on the habit-plane triggered by a build-up of twinning disconnections during the reverse-transformation. It was proposed that during the forward transformation, the habit-plane sweeps through the austenitic phase growing the martensite (figure 4(a)), and additionally there is an evolving microstructure within the martensite. The internal twinned microstructure of martensite is evolving due to migration of the internal twin boundary brought about by twinning disconnections or twin-partials (figure 4(b)). During the reverse-transformation, the habit-plane sweeps back in the reverse-direction (figure 4(c)), and in this process, the twin-partial mobility is limited since the reverse-transformation stress level is lower than that of the forward

transformation (figure 2(a)). In such a scenario, the twin-partials cannot revert and can neither slip through to the austenite phase because the slip-resistance of the phase is much higher. Therefore there occurs a build-up of twin-partials on the habit-plane (figure 4(c)). And at a certain critical build-up, a dislocation reaction ensues leading to emission of the observed slip dislocations in the austenite phase (figure 4(d, e)). The Kajiwara-Kikuchi (K-K) mechanism was an important step towards the understanding of slip-emission and functional fatigue in SMAs. The focus of this thesis is to develop this understanding further and establish the cause of emitted-slip more thoroughly using modern atomistic-simulation techniques and through thermodynamic arguments.

1.4. Thesis organization

This thesis begins from an understanding of the internal twin boundary structure of martensite, simulating the role of twin-partial motion on slip-emission, addressing the relative crystallographic orientation of the austenite-martensite phases and ending with a thermodynamic argument explaining why slip-emission is the most spontaneous response of an SMA during the reverse transformation. The thesis is organized as follows.

Chapter 2 addresses the twin boundary interface within the transformed martensite in Shape Memory Alloys. The most commercially successful alloy of Nickel-Titanium is chosen as the study target and the structure of its internal "Type II" twin boundary is clarified. The major challenge in understanding this twin boundary is that it exhibits irrational Miller indices. This irrationality is rooted in the non-cubic monoclinic unit cell and the complex non-single-lattice structure of the $B19'$ martensitic phase. It is shown that the twin boundary structure is unlike conventional understanding in well-studied cubic crystalline systems (such as Face-Centered-Cubic and Body-Centered-Cubic materials) in that the atomic-structure cannot be constructed apriori. It is revealed that a non-trivial lattice-offset relating the two twin variants needs to be

determined from Molecular Statics (MS) simulations to arrive at the most energetically favorable equilibrium twin boundary structure. Atomic-scale shear-shuffle mechanisms for migration of the twin interface are established along with simulated energetics within the MS framework. The shuffles are shown to switch the lattice-sites and motif-sites of the monoclinic unit cell. The twin interface is shown to exhibit a mismatch strain on a rational terrace plane that is relieved by an array of periodically spaced twinning disconnections attributing a stepped topology to the twin interface. This stepped nature ultimately explains the irrational identity of the interface.

Chapter 3 describes the atomistic simulation of twin-boundary migration of the twin-boundary and proposes an emissary dislocation-reaction when the migration is arrested as initially hypothesized by the K-K mechanism (refer section 1.3 above). Following inputs from priorly clarified equilibrium twin boundary structure and shear-shuffle twinning mechanisms, a disconnection-dipole system was simulated. Introduction of the dipole necessitated a fully-anisotropic calculation of the disconnection strain-fields and their enforcement on atoms in a manner that violates the Cauchy-Born assumption. This was shown for the first time, again in stark contrast with state-of-the-art understanding derived from higher-symmetry cubic-crystalline materials. The disconnection was explicitly shown to migrate under a quasi-static shear-strain mediated by lattice-motif shuffles. The presence of a barrier to disconnection motion on twin interfaces, mimicking the presence of the habit plane, was hypothesized to cause slip-emission. A dislocation-reaction was observed to ensue, validating the emission of dislocations from the twin-interface leading to slip in the austenite phase.

Chapter 4 focuses on addressing the ongoing debate surrounding the structure of the Type II twin boundary where the Terrace-Disconnection (T-D) topology proposed by this study conflicted with a Tilt-Wall (T-W) topology proposed in literature around the same time. Both

topologies exhibited contrasting features in the atomic-structure, dislocation arrangement and mechanism of twin migration. This research proposed a resolution to this debate by illustrating a direct comparison between the two topological models for the twin interface. Through a combination of atomistic simulations and a fully-anisotropic continuum Eshelby-Stroh formalism, it was established for the first time that a comparison of topologies must consider both the atomistic potential energy and the continuum strain-energy of the interface. It is shown that the atomistic potential energy dominates continuum strain-energy the comparison and favors the T-D topology over T-W. Furthermore a novel Evolving-Interface (EI) theory was developed to prove how the T-D topology can evolve under the influence of external microstructural strain. The proposed theory resolved for the first-time conflicting experimental observations in literature that were thus far considered to be conflicting. The theory further rationalized Kajiwara's proposition that twin-disconnection arrangement within the martensite can evolve under strain. A hypothesis based on the law of conservation of Burgers vector is proposed for slip-emission.

Chapter 5 focuses focused on extending this study to other Type II twin interfaces in Shape Memory Alloys (SMAs), namely TiPd, TiPt, and AuCd. The martensites in these SMAs are orthorhombic in structure, differing from the monoclinic martensitic phase of NiTi. Nonetheless, the structure of the Type II twin follows the T-D topology as proposed by us. By extension to other systems, we demonstrate how the interface's salient features arise from fundamental structural properties of the martensite phase. The lattice distortion and motif arrangement within the unit cell are shown to dictate interface coherence strains, lattice offsets and a shuffle-reliant detwinning mechanism all of which seamlessly fit a T-D topological model to ultimately explain the irrational Miller indices. The choice of terrace for the topology is shown to be the nearest crystallographic plane to the effective irrational plane (predicted from classical theory [15]) in the reciprocal space

of the crystal structure. The classical twinning shear is shown to be partitioned between the coherence strain on rational terraces and the twinning shear on the rational-terrace carried by the twinning disconnection. The Burgers vector of the twinning disconnection is established using from the terrace-shear and calculations from Topological Modeling theory. The lattice offsets between the matrix and twin (priorly established for NiTi) for these SMAs is determined from Density Functional Theory (DFT) calculations. The lattice offset dictates the shear-shuffle mechanism of twinning. Thus, a thorough clarification of Type II twin boundaries in SMAs is forwarded, on both atomistic and topological fronts.

Chapter 6 focuses on the relative lattice orientation between the austenitic and martensitic phases. The study target is chosen to be the newer FeMnNiAl alloy, primarily owing to the convenience offered by the cubic crystalline structures of its austenite and martensite phases. Knowledge of the relative lattice-orientations is necessary to know how the internal twin boundary within martensite is oriented with respect to slip-systems in the austenitic phase. The Orientation Relationships (OR) between the two-phases was thus far implicitly assumed to be a property of the material. Recent experimental research on FeMnNiAl, revealed that its phases exhibit 3 distinct ORs, namely the Kurdjumov-Sachs, Nishiyama-Wasserman and Pitsch relationships. A theoretical treatment, based on the energy-minimization theory of martensite [16], is undertaken to predict and explain these ORs. It is shown that the observed OR depends on the internal morphology of martensite, which can either be twinned or stacking-faulted. A novel framework for the case of stacking-faulted martensite is developed in this study. It is shown that there is a non-trivial rotational misalignment between the austenite and martensite phases of the order of few degrees.

Chapter 7 summarizes the contributions of this study and proposes future extensions. And in conclusion, a thermomechanical framework for SE behavior of SMAs is developed, motivated

from early work in refs. [11, 17, 18], to establish why slip-emission can occur spontaneously during the reverse-transformation based on Gibbs' free energy considerations. It is shown that in the reverse-transformation, there is a propensity for the transformation strain of the martensitic inclusion to increase by emitting dislocations. When this propensity overcomes the cost of slip-emission related to the core-energy of slip-dislocations in the austenitic phase, slip occurs.

CHAPTER 2: THE TYPE II TWIN BOUNDARY IN NICKEL-TITANIUM

2.1. Introduction

Twinning plays a central role in dictating mechanical response of crystalline materials, be it as a governing microstructural constituent [19-22], a mode of inelastic deformation (deformation twinning) [23, 24] or as an accommodative mode in diffusionless martensitic phase transformations (transformation twinning) [25-27]. The proposed study is most pertinent to the latter role where twinning provides a mode of Lattice Invariant Deformation (LID). This allows an energetically feasible accommodation of high distortions in transforming the parent austenite phase to the martensite phase. The impetus for this narrowed focus derives from the importance of such phase transformations in Shape Memory Alloys (SMAs) which are technologically important functional materials applied in biomedical (stents, orthodontics), automotive (valves) and aerospace fields [3]. Thermo-mechanical behavior of SMAs is significantly influenced by the mechanism of formation and migration (detwinning) of these transformation twin interfaces [28-31]. In the following study, equiatomic NiTi is chosen as the model shape memory material owing to its commercial success [32, 33]. A major twinning mode in martensitic transformations in NiTi is termed the $\langle 011 \rangle$ type II twinning mode [33-38]. The orientation relationship between the variants is found to be a 180-degree rotation about $\langle 011 \rangle$. It is implied (here and henceforth) that the indices are referenced to the martensite crystallographic axes. After being identified experimentally [39], these twins were characterized through the classical theory of deformation twinning [40].

2.1.1. Classical theory of deformation twinning

The classical theory serves as a foundation for understanding twinning crystallography, and provides a rigorous mathematical approach to translate experimentally determined orientation

relationships (deduced typically from diffraction methods) to fundamental crystallographic twinning parameters (atomic planes and directions). Under the key presumption that a deformation twin is formed by a homogeneous shear of the parent lattice to twinned positions, required atomic movements (shear and shuffle) can be derived. Even now, this theory is an authoritative guide to understand atomic structure around the TB [41-43]. There are five basic twinning elements needed to describe twinning crystallography. The twinning elements comprise the invariant twinning plane K_1, twinning direction η_1, the second undistorted conjugate plane K_2, the conjugate twinning direction η_2 and the magnitude of the twinning shear S. These elements are derived starting from a known orientation relationship between the twin variants. On the basis of these orientation relationships, the theory establishes three twinning modes [40]:

(a) Type I: The twin variant lattices are related by a reflection. This reflection can either be in K_1 or in the plane normal to η_1. The elements $(K_1,\ \eta_2)$ are rational while the others are irrational

(b) Type II: The twin variant lattices are related by a 180 degree rotation. The rotation can either be about η_1 or about the normal to K_1. The elements $(K_2,\ \eta_1)$ are rational while the others are irrational

(c) Compound: The twin variants follow both Type I and Type II relationships and all twinning elements are rational

The twinning mode of interest in this study falls under the Type II orientation relationship, hence its designation. The twinning elements are tabulated in Table 1. The plane K_1 is the invariant plane under twinning deformation, whose indices are found to be irrational.

Table 1: Twinning elements for Type II twins in NiTi, determined using the classical theory of deformation twinning (directions and planes referenced to crystallographic axes of one of the twin variants) [39]

K_1	$\left(0.7205\ 1\ \bar{1}\right)$
η_1	$\left[011\right]$
K_2	(011)
η_2	$\left[1\ 0.636\ \overline{0.636}\right]$
S	0.280

Given that the predicted twinning plane is irrational, some 10° away from $(11\bar{1})$, it is non-crystallographic in nature. The classical theory by itself cannot sufficiently explain the complete atomic structure of such an interface. Furthermore, it cannot (a) characterize the mechanism of physical growth/propagation of the twin, (b) clarify possible involvement of twinning partials in the mechanism or (c) shed light on energy-based factors that determine nucleation/propagation of the twinning modes. Addressing such aspects is neither the purpose nor within scope of these theories and they are intended primarily for a rigorous characterization of admissible twinning modes in any crystalline material. For a more detailed discussion, the reader is referred to comprehensive reviews [23, 24].

2.1.2. Importance of a physical understanding of twin interface structure

An understanding from a classical standpoint has long sufficed the Phenomenological Theory of Martensite Crystallography (PTMC) in explaining the crystallography of the transformation [44, 45]. It has also extended to the constitutive modelling of shape memory alloys [46, 47]. On the flipside, a physical understanding of the irrationality of the twin interface garnered relatively limited attention. There are several reasons why such an understanding is crucial. For

one, knowledge of the interface structure allows conception of nucleation and growth mechanisms for the twin on an atomic scale [48]. These mechanisms can extend to *ab initio* predictions of critical twin nucleation and propagation stresses [49, 50], thereby determining the ease of activation of different twinning modes under mechanical or even thermal loads. These predictive models reveal dependencies on key physical parameters of the material, such as the stacking fault energy [24]. Such parameters can possibly be tailored by materials processing methods to engineer superior thermo-mechanical behaviors [51]. Secondly, the TB structure may hold the key to understanding functional fatigue in SMAs [4, 52, 53]. This is particularly significant for NiTi whose applications typically involve fatigue conditions [54]. A consistent agreement has been shown between fatigue-activated slip systems in the austenite phase and the internal twinning system of the martensite phase [6, 7]. An understanding of the structure is an important precursor to model possible dislocation mechanisms that can explain such fatigue-activated slip. Such a dislocation mechanism has been hypothesized in [9, 12]. On a similar note, a structural understanding of the type II twin interface is vital for the magnetomechanical behavior of NiMnGa [55] (specifically to model TB mobility during the phenomenon of Magnetically Induced Reorientation or MIR [56]) which is often considered the most attractive ferromagnetic SMA [27]. The significance of such understanding cannot be overstated as type II twin interfaces find presence in other SMAs such as CuAlNi [57-59], CuZnAl [60] and AuCd [61].

2.1.3. Interpretation of Type II twin plane irrationality: HRTEM studies

In addition to limited endeavors in this direction, there is added complexity due to controversial propositions in understanding the structure. There are dominantly two schools of thought, both of which approach the structure by observation under High-Resolution Transmission Electron Microscopy (HRTEM). An absence of consensus in the interpretation of available

HRTEM images has led to a dichotomy in the understanding of the type II twin interface. While one group of researchers propose a ledged/terraced geometry with the nearest low-index rational plane $\{111\}$ constituting each terrace [38, 62-65], another group of researchers claim the interface to be randomly curved possessing no such features [34, 35, 66-68] (further extending it for type II interfaces in TiPd and NiMnGa systems, apart from NiTi). In addition, a disagreement in the irrational indices of the effective twinning plane has also been claimed [38], further adding to the perplexity in understanding the interface structure. There could be several reasons for these discrepancies. For example, slight deviations around the $[011]$ zone axis of observation can involve effects of projectional geometry and hinder resolvability of the terraces [62]. Thus, HRTEM studies on such type II twins is a challenge and poses open problems for research.

2.1.4. Interpretation of Type II twin plane irrationality: Topological Models (TM)

Another approach was spurred by the advent of topological modelling [69] renewing interest in the physical understanding of such irrationally-indexed interfaces [70, 71]. This method relies on characterization of admissible defects on crystalline interfaces on the basis of mathematically abstracted crystallographic symmetry operations [72]. It formalizes classical theorizations of interfaces with varying degrees of coherence [73]. The classical understanding of a disconnection, prevalent particularly in context of heterogeneous twin growth mechanisms [74, 75], was also formalized within the Topological Model (TM) [69]. Geometrically, the disconnection is a step-like feature separating parallel coherent terraces that are not on the same plane. These coherent terraces are crystallographic planes with rational indices. The dislocation and step character at the interface was combined within the umbrella term of a “transformation dislocation” for hetero-phase interfaces and “twinning dislocation” for the homo-phase twin interface [76, 77]. The “transformation dislocation” in particular served as a useful entity in

modelling interfaces of diffusionless phase transformations. One of the successes of TM was in explaining the structure of habit-planes in martensitic transformations [78-80], consistently reproducing its irrational indices so far predicted only using the PTMC [81]. Consequently, this approach was applied to the type II interface very recently by the same authors who pioneered the field [82, 83]. However, in applying the model to the Type II interface, the authors cite difficulties in theorizing disconnections for an irrational interface. Instead, their approach hypothesizes close-spaced transformation dislocations on the conjugate plane $K_2 = (011)$. To the merit of this approach, the twinning elements are well-reproduced. Yet, it is acknowledged that the final microstructure of the type II interface is still unknown. Further, there is a challenge in reconciling this model with the experimentally deduced $\{111\}$-terrace model [62, 64].

Similarly, contrasting propositions have also been put forth for the mechanism by which the TB migrates. One of the proponents of the stepped geometry [64] proposed a coordinated homogeneous shear of one variant allowing a progression of the coherent terraces normal to the interface. As one of the first propositions tied with a physical interface model, this mechanism is analogous to the earliest propositions of "homogeneous" twin growth mechanism involving coordinated shear of atoms along the twinning direction η_1. However, it is now well-accepted that such mechanisms are energetically unfavorable as compared to dislocation-mediated "heterogeneous" mechanisms [24, 84, 85]. This is affirmed by experimental measurements of the detwinning stress in NiTi $B19'$ martensite [50, 86] found to be under 100 MPa. If the mechanism was homogeneous, a detwinning stress of the same order as the martensitic shear moduli ~ 50 GPa [87] would be expected. Although the TM provides for such dislocations and outlines a heterogeneous growth mechanism for the twin, it is suggested that the disconnections cannot

advance the same way as for the rational type I twin. Also, it is acknowledged that an understanding of the complete micro-mechanism of twin migration is still absent [83].

Although the aforementioned approaches seem to be at odds with each other, each offers propositions that are significant breakthroughs supporting the ensuing study. The tussle between the approaches may be resolved at two fronts. First, the elaborate atomic structural details of the HRTEM model should be reconciled within the TM framework. Secondly, the growth mechanism from the TM can be interpreted on a fundamental atomic scale for the HRTEM interface model to explain the mechanism of detwinning in a consistent manner. The proposed study attempts to reach this exact consensus, providing a bridge via atomic-scale simulations.

2.1.5. Overview of current approach

Atomistic simulation tools such as Molecular Dynamics (MD) [88] and Density Functional Theory (DFT) [89] have offered a probe for atomic structures at scales beyond reach of experimental techniques. They have already been employed in context of Type II interfaces [37, 90], in different capacities. For the current study, these tools present a favorable environment to directly explore the nature of the type II interface on an atomic level. The methodology of this study is briefly presented here. The focus is to show the key role played by atomistic simulations. Following the propositions of the $\{111\}$-terrace model, the conditions for crystallographic coherence are explored on the terrace plane. It is shown that a certain lattice offset parameter must be determined to complete the atomic model of the terrace provided in [64]. It immediately becomes apparent that an evaluation of atomistic potential energy at various offsets is required to determine the parameter value that minimizes the energy. This evaluation would have otherwise been inaccessible in the absence of such tools. Further, if a step/disconnection is to be accommodated on the TB, there is a need to check for degeneracy in the interface energy of

consecutive terrace planes separated by a step. This can be evaluated through a simulation of an atomistic twinning energy signature called the Generalized Planar Fault Energy (GPFE) [91], particularly its twin migration segment. The disconnection step height is not a topological property (in the sense, it cannot be derived solely from topological arguments) and serves as a key input parameter for the TM [69]. Furthermore, this calculation establishes the mechanism of detwinning that must be operative for migration of the TB, and also provides a magnitude for the twinning partial. The twin partial and step height are combined within a TM framework to eventually complete the type II interface model, causally explaining the irrational indices of the twinning plane. In summary, the proposed study attempts a concerted exploration of the structure of the $\langle 011 \rangle$ type II twin interface in $B19'$ NiTi through a combination of atomistic and topological modelling.

2.2. Modelling Methodology and Results

In this section, the atomistic and topological modelling approaches are presented in concurrence with their results. This purpose is to present sequential stages of a coordinated approach where the results of one step provide vital information for the methodology of the next. This is done to avoid any break in following the logical flow of the arguments. The atomistic simulations are performed in LAMMPS [88] with a governing empirical interatomic potential, solely working with energy minimization routines within a Molecular Statics (MS) framework. This tool was chosen over DFT [89] with the foresight that the resulting atomic model sets the foundation to simulate candidate dislocation-mechanisms on the TB explaining fatigue-activated slip [9, 12] (refer section 2.1.2). Such a simulation requires a fairly large atomic system and will incur an impractically high computational cost with DFT. Moreover, the following study does not require high accuracy in reproducing accurate potential energies of atomic interaction. Instead it

only requires the interatomic potential to be capable enough to quantify, in a relative sense, the peaks and valleys of the potential energy landscape for different atomic configurations. It will be shown that this is sufficient to adequately clarify structural and mechanistic aspects relevant in this study. It is fortunate that the commercial importance of NiTi has sparked development of many state-of-the-art interatomic potentials proven to show good physical fidelity in different applications [92-94]. The interatomic potential [94] was chosen for this study.

2.2.1. Twin Boundary Crystallography

The lattice spacing and monoclinic angle in the $B19'$ unit cell are chosen following [94], consistent with the interatomic potential. The unit cell has 4 atoms, which for equiatomic NiTi are two Ti and two Ni atoms. A commonly adopted crystal description [33, 95] is chosen where one of the Ti atoms is positioned at the lattice point $(0,0,0)$ of the unit cell. This Ti atom is termed a lattice Ti, while the other Ti atom of the monoclinic cell is termed as a motif Ti. This is shown in figure 5(i). This labelling of lattice and motif atomic sites will serve a vital role in understanding atomic shuffles subsequently. These shuffles will prove important in the description of the detwinning mechanism and hence it is necessary to pay attention to the coloring schema and the labelling. Note that no distinction is made between the Ni atoms. Their behavior (in terms of relative shuffle movements) is adequately typified by the behavior of the Ti atoms and hence a further distinction would be an unnecessary complexity. The orientation relationship between the martensitic variants on either side of the TB have long been known [39]. The twinning plane, and the corresponding crystallographic system for both variants are explained in figure 5(ii). Here and henceforth, the variant on the top will be labeled variant A and the bottom is variant B. Under the Type II twinning relationship, the crystallographic planes $(\bar{1}\bar{1}1)_A$ and $(11\bar{1})_B$ are parallel (and hence so are their normals).

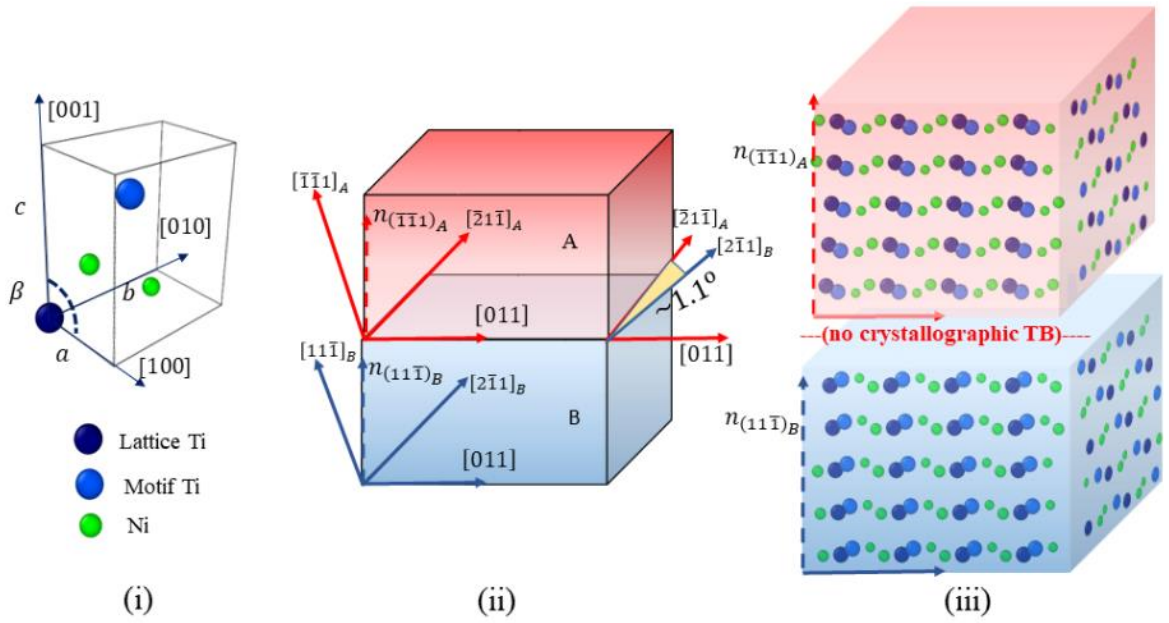

Figure 5: (i) Designation of atomic sites in $B19'$ (ii) Crystallography of the TB (iii) Projected views of twin variants on two orthogonal planes, illustrating absence of a crystallographic twin plane (refer 2.2.3); note that this figure shows a notional positioning of the two variant blocks constructed independently (details of constructing this structure are elaborated in 2.2.4) and should not be mistaken for the final twin atomic structure; complete specification of the final twin structure requires a calculation of lattice offset between the variants, as explained in section 2.2.5

2.2.2. Interface Shear Strain mismatch on the $\{111\}$ coherent terraces

This section shows the calculation of the interface shear strain mismatch between the planes $(\bar{1}\bar{1}1)_A$ and $(11\bar{1})_B$ in variants A and B respectively. First, the lattice vectors of the monoclinic unit cell are represented in an orthonormal basis $\{\hat{e}_1, \hat{e}_2, \hat{e}_3\}$. The basis is chosen such that $\hat{e}_1 \parallel [100]$, $\hat{e}_2 \parallel [010]$ and $\hat{e}_3 = \hat{e}_1 \times \hat{e}_2$. The lattice parameters are chosen consistent with the interatomic potential [94], $a = 2.699$ $\overset{0}{\text{A}}$, $b = 4.386$ $\overset{0}{\text{A}}$, $c = 4.606$ $\overset{0}{\text{A}}$, $\beta = 93.41^{\circ}$. In the orthonormal basis, the components of the lattice vectors are:

$$[100]=\begin{pmatrix}2.699\\0\\0\end{pmatrix};\ [010]=\begin{pmatrix}0\\4.386\\0\end{pmatrix};\ [001]=\begin{pmatrix}-0.274\\0\\4.598\end{pmatrix} \tag{2.1}$$

Then we have,

$$[011]=\begin{pmatrix}-0.274\\4.386\\4.598\end{pmatrix};\ [\bar{2}1\bar{1}]=\begin{pmatrix}-5.124\\4.386\\-4.598\end{pmatrix};\ [2\bar{1}1]=\begin{pmatrix}5.124\\-4.386\\4.598\end{pmatrix} \tag{2.2}$$

Taking dot products, we can compute the angle between $[011]$ and $[\bar{2}1\bar{1}]$ as 90.55^{o}. The angle between $[011]$ and $[2\bar{1}1]$ is 89.45^{o}. Now following the crystallography specified in section 2.2.1, if the variant planes $(\bar{1}\bar{1}1)_A$ and $(11\bar{1})_B$ are overlapped, the scenario represented in figure 6 results.

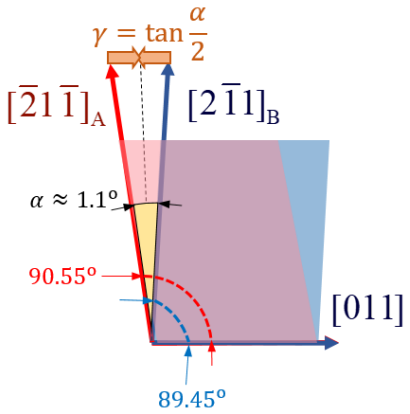

Figure 6: Illustration of the angular mismatch when the variant planes $(\bar{1}\bar{1}1)_A$ (red) and $(11\bar{1})_B$ (blue) are overlapped

The angular mismatch $\alpha \approx 1.1^{o}$ is specified. An equal and opposite shear strain must be applied to both variants, calculated as $\gamma = \tan\frac{\alpha}{2}$. The net interface shear strain mismatch is $2\gamma \approx 1.92\%$

The following details are important to note:

a. Within each variant, no pair of the given crystallographic directions (those indicated in figure 5(ii)) are orthogonal. For instance, in variant A, no pair of directions in the set $\left\{[011], [\bar{2}1\bar{1}]_A, [\bar{1}\bar{1}1]_A\right\}$ are orthogonal to each other

b. Comparing the planes $(\bar{1}\bar{1}1)_A$ and $(11\bar{1})_B$ in variants A and B respectively, if the $[011]$ directions of both are aligned, the directions $[\bar{2}1\bar{1}]_A$ and $[2\bar{1}1]_B$ do not align (figure 5(ii)). They form an acute angle, which for the chosen set of lattice constants, can be calculated as $\approx 1.12^o$ (refer section 2.2.2). It must be mentioned that this result will change if either *ab initio* [96] or experimental lattice parameters [97] are utilized. Nevertheless, this angle is always non-zero. We choose to follow the lattice parameters of [94] for consistency with the interatomic potential.

c. The periodic spacing of the lattice points in each of these directions is the same for both the variants

In summary, there is an in-plane shear mismatch of $\approx$ 1.92% at the twinning plane but no normal strain mismatch. This implies that there can be no atomic registry across the plane unless there is an interface shear strain applied to both the variants. Equal and opposite shear strains are applied to both variants since both are of the same phase (the TB is a homo-phase interface) and obey certain symmetry. It must be mentioned that for a general hetero-phase interface, the strain partitioning need not be equal [98]. The strain is applied following the Cauchy-Born assumption. The strain magnitude comes out to be $\approx$0.96%, a high value well beyond practically measured engineering elastic strains.

2.2.3. Non-crystallographic Twin Boundary

The crystal structures of twin variants A and B of $B19'$ NiTi martensite are visualized, given in figure 7. No crystallographic TB is admissible between the variants because no atomic plane adhering to the arrangement in both variants is possible. Now consider only the lattice sites (only lattice Ti) in each variant. With only the lattice points, a crystallographic TB is possible. This is because the lattice sites of both variants coincide on this plane (figure 8). An atomistic computation of lattice offset (section 2.2.5) is unrequited here. The relative offset (of section 2.2.5) is zero and the lattice points of both variants coincide. The purpose of this exercise is to show that the absence of a crystallographic TB arises fundamentally from the presence of motif atoms within the unit cell of martensite (figure 5(i)). This attributes a unique crystallographic arrangement within each variant which cannot be matched to form an atomic plane for the TB.

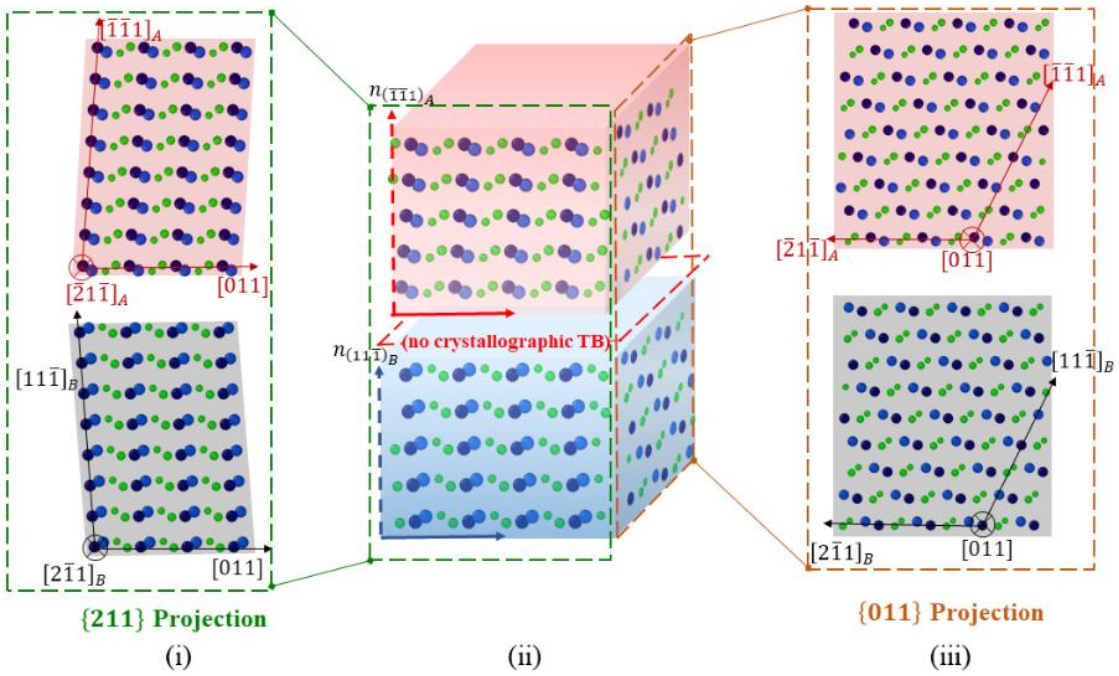

Figure 7: (i) $\{211\}$ projection of twin variant crystal structures (ii) Combined variant projections in a three-dimensional form, indicating inadmissibility of a crystallographic TB (iii) $\{011\}$ projection of twin variant crystal structures

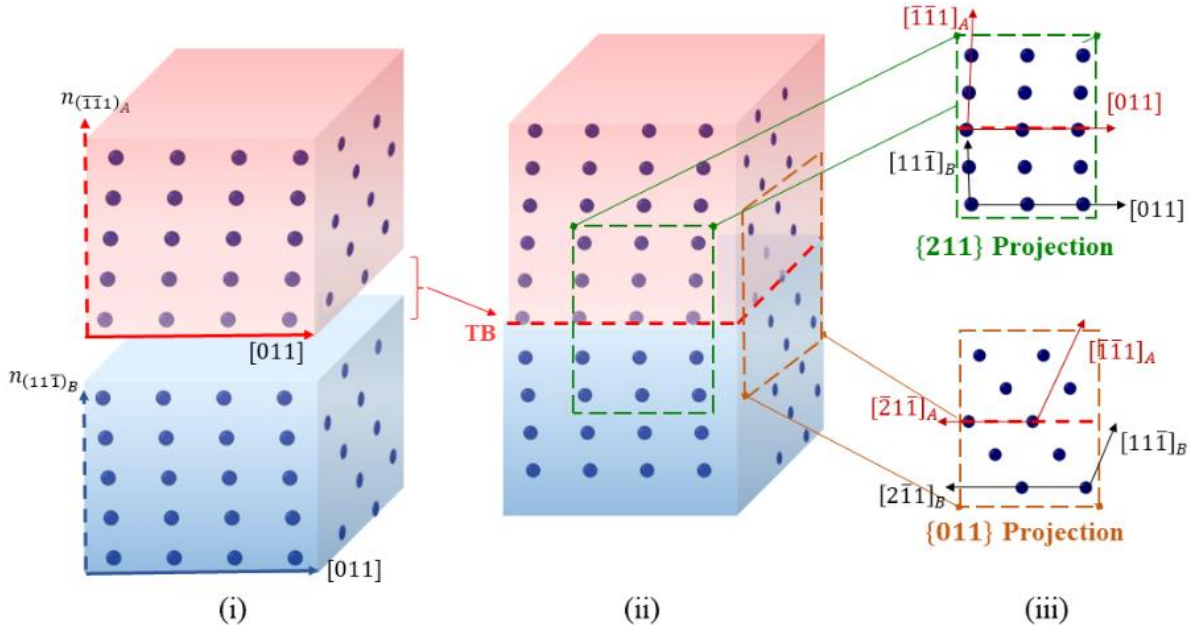

Figure 8: (i) Combined variant projections in a three-dimensional form, considering only lattice sites and ignoring motif atoms (ii) The lattice sites of both variants coincide on a crystallographic TB (iii) $\{211\}$ and $\{011\}$ projection of twin variant lattices, indicating a crystallographic TB

2.2.4. Crystallographic construction of the $\{111\}$ terraces of the Type II twin boundary

This section provides a detailed account of how the atomic structure on the $\{111\}$ rational terrace can be constructed within the framework of LAMMPS. We start with the dimensions and axes of the simulation cell defined in a global orthonormal system $\{\hat{i}, \hat{j}, \hat{k}\}$. The *x*-axis aligns with $\hat{i}$, y-axis with $\hat{j}$ and z-axis with $\hat{k}$. LAMMPS allows a definition of a simulation box in space, where the span along each axis is given by a start and end coordinate. Thus the limits on each axis are given by the pairs $(x_{\min}, x_{\max})$, $(y_{\min}, y_{\max})$ and $(z_{\min}, z_{\max})$. Additionally, the simulation box can be defined as a parallelepiped, suited for a general triclinic structure. Setting the origin of the parallelepiped at $(x_{\min}, y_{\min}, z_{\min})$, the edge vectors are defined in the global basis by the coordinate sets: $\vec{L}_1 = (x_{\max} - x_{\min}, 0, 0)$, $\vec{L}_2 = (xy, y_{\max} - y_{\min}, 0)$ and

$\vec{L}_3 = (xz, yz, z_{\max} - z_{\min})$. This is similar to the definitions in [99]. Next, a crystal is defined in space. This is done by indicating the unit cell lattice vectors and the basis atoms in the unit cell. The unit cell lattice vectors must be defined in the global basis depending on how the lattice is to be oriented in space. Given the lattice and the motif atoms, a crystal is generated in space. Then LAMMPS cuts-off all atoms outside the boundaries of the defined simulation box and only retains the atoms that fall within it. We illustrate this with the example of constructing a single variant, variant A, in an appropriate simulation box.

Following the crystallography of section 2.2.1, we define a parallelepiped such that $\vec{L}_1 \| [011]$, $\vec{L}_2 \| \left[\bar{2}1\bar{1}\right]_A$ and $\vec{L}_3 \| \left[\bar{1}\bar{1}1\right]$. Selecting the edges to be crystallographic directions is crucial to allow enforcement of periodic boundary conditions along them. Also the edge lengths must be an integral multiple of the periodic spacing along these directions. Otherwise, "critical-edge" effects can arise, as noted in [99]. We choose the edge lengths to be 10 periodic spacings in each of these directions. This means that $\vec{L}_1 = 10[011]$, $\vec{L}_2 = 10\left[\bar{2}1\bar{1}\right]$ and $\vec{L}_3 = 10\left[\bar{1}\bar{1}1\right]$. Also, we choose $x_{\min} = 0; y_{\min} = 0; z_{\min} = 0$. To determine the coordinates of the edge vectors we must determine their lengths and also the angles between them. Let the angles between $\vec{L}_1$ and $\vec{L}_2$ be defined as γ, the angle between $\vec{L}_2$ and $\vec{L}_3$ be α and that between $\vec{L}_1$ and $\vec{L}_3$ be β. The lengths and angles of these vectors can be computed by expressing coordinates of these crystallographic directions in a common orthonormal basis. We use the $\{\hat{e}_1, \hat{e}_2, \hat{e}_3\}$ basis defined in 2.2.2, and follow that procedure to get the coordinates of $\vec{L}_i$'s. In other words, the coordinates in equation (2.2) will be used. The lengths can be computed by taking norms and the angles by taking dot products. The following parameters are determined.

$$L_1 = 63.602\ \overset{0}{\text{A}}; L_2 = 81.629\ \overset{0}{\text{A}}; L_3 = 71.015\ \overset{0}{\text{A}} \qquad (2.3)$$
$$\alpha = 116.044^{\text{o}}; \beta = 86.508^{\text{o}}; \gamma = 90.551^{\text{o}}$$

They can be recast into the relevant coordinates to specify the simulation box. Let $[011]$ be chosen to be aligned to the *x*-axis of the simulation box and the *x-y* plane as the $(\bar{1}\bar{1}1)$ terrace. This means the *x-y* plane contains the direction $[\bar{2}1\bar{1}]$. Then in the global basis, the coordinates of the edge vectors will be $\vec{L}_1 = (L_x, 0, 0)$, $\vec{L}_2 = (xy, L_y, 0)$ and $\vec{L}_3 = (xz, yz, L_z)$. The following equations can be derived based on trigonometric relations.

$$L_x = L_1 = 63.602\ \overset{0}{\text{A}}$$
$$xy = L_2 \cos\gamma = -0.785\ \overset{0}{\text{A}}$$
$$xz = L_3 \cos\beta = 4.273\ \overset{0}{\text{A}}$$
$$L_y = \left(L_2^2 - xy^2\right)^{1/2} = 81.625\,\overset{0}{\text{A}} \qquad (2.4)$$
$$yz = \frac{\left(L_2 L_3 \cos\alpha - xy.xz\right)}{L_y} = -30.763\,\overset{0}{\text{A}}$$
$$L_z = \left(L_3^2 - xz^2 - yz^2\right)^{1/2} = 62.904\,\overset{0}{\text{A}}$$

These parameters allow definition of the simulation box (refer Figure 9 (i)-(iii)). Next, the crystal must be defined in a specific orientation. The orientation of the crystallographic vectors $\{[100],[010],[001]\}$ must be specified in the global basis $\{\hat{i}, \hat{j}, \hat{k}\}$. For this purpose, the set of vector equations $\vec{L}_1 = 10[011]$, $\vec{L}_2 = 10[\bar{2}1\bar{1}]$ and $\vec{L}_3 = 10[\bar{1}\bar{1}1]$ can be recast in a matrix form:

$$10\begin{pmatrix} 0 & 1 & 1 \\ -2 & 1 & -1 \\ -1 & -1 & 1 \end{pmatrix}\begin{pmatrix} [100] \\ [010] \\ [001] \end{pmatrix} = \begin{pmatrix} L_x & 0 & 0 \\ xy & L_y & 0 \\ xz & yz & L_z \end{pmatrix}\begin{pmatrix} \hat{i} \\ \hat{j} \\ \hat{k} \end{pmatrix} \qquad (2.5)$$

Then, the crystallographic unit cell vectors can be expressed in the global basis as:

$$\begin{aligned}[100] &= -0.116\hat{i} - 1.695\hat{j} - 2.097\hat{k} \\ [010] &= 3.025\hat{i} + 2.386\hat{j} - 2.097\hat{k} \\ [001] &= 3.336\hat{i} - 2.386\hat{j} - 2.097\hat{k}\end{aligned} \tag{2.6}$$

It can be verified that $|100| = a = 2.699\overset{0}{\text{A}}$, $|010| = b = 4.386\overset{0}{\text{A}}$, $|001| = c = 4.606\overset{0}{\text{A}}$. In this form, the lattice corresponds to unstrained variant A configuration. However, section 2.2.1 and 2.2.2 establishes the need for coherence strains in both variants. The shear deformation to be applied, as indicated in figure 6, can be represented by the deformation gradient:

$$\mathbf{F} = \begin{pmatrix} 1 & \gamma & 0 \\ 0 & 1 & 0 \\ 0 & 0 & 1 \end{pmatrix} \tag{2.7}$$

The deformation gradient is referenced to the global basis. Here, $\gamma = 0.96\%$, which is identical to $-xy/L_y$. This deformation gradient is applied to the entire simulation box. This is done by operating the deformation gradient on the current edge vectors to generate edge vectors for the strained box. Hence, the new edge vectors are:

$$\mathbf{F}\begin{pmatrix} L_x \\ 0 \\ 0 \end{pmatrix} = \begin{pmatrix} L_x \\ 0 \\ 0 \end{pmatrix};\ \mathbf{F}\begin{pmatrix} xy \\ L_y \\ 0 \end{pmatrix} = \begin{pmatrix} 0 \\ L_y \\ 0 \end{pmatrix};\ \mathbf{F}\begin{pmatrix} xz \\ yz \\ L_z \end{pmatrix} = \begin{pmatrix} xz - \dfrac{yz}{L_y}.xy \\ yz \\ L_z \end{pmatrix} \tag{2.8}$$

After straining, the edge vector $[011]$ (parallel to the *x*-axis) remains unchanged, but the direction $[\bar{2}1\bar{1}]$ is now parallel to the *y*-axis. To get the crystallographic unit cell vectors corresponding to the strained variant A, we reapply (2.5), except with the modified edge vectors. Hence, we have the matrix of vector equations as

$$10\begin{pmatrix} 0 & 1 & 1 \\ -2 & 1 & -1 \\ -1 & -1 & 1 \end{pmatrix}\begin{pmatrix} [100] \\ [010] \\ [001] \end{pmatrix} = \begin{pmatrix} L_x & 0 & 0 \\ 0 & L_y & 0 \\ xz - \frac{yz}{L_y}.xy & yz & L_z \end{pmatrix}\begin{pmatrix} \hat{i} \\ \hat{j} \\ \hat{k} \end{pmatrix} \tag{2.9}$$

, resulting in:

$$\begin{aligned} [100] &= -0.132\hat{i} - 1.695\hat{j} - 2.097\hat{k} \\ [010] &= 3.047\hat{i} + 2.386\hat{j} - 2.097\hat{k} \\ [001] &= 3.313\hat{i} - 2.386\hat{j} - 2.097\hat{k} \end{aligned} \tag{2.10}$$

Essentially, the coherence strain translates to applying a certain strain at the unit cell level. The lattice can now be generated. Starting from a reference point, the rest of the lattice points are generated from it using the lattice vectors defined in equations (2.10). This reference is specified as the "origin", O. The origin essentially represents coordinates of one lattice point in space, in the global basis. Changing the origin by a magnitude smaller than the lattice spacing (in any direction) allows the lattice to physically translate in space. Hence it is alternatively viewed as a specification of lattice shift. If the translation magnitudes in each direction equal lattice spacings of those directions (or their multiples), the lattice remains invariant. Once the lattice is defined in space, the motif arrangement is repeated at each lattice point to complete the crystal definition. Hence, the motif arrangement corresponding to $B19'$ martensite (taken from [94], illustrated in figure 5(i)) is chosen. The atoms that fall within the boundaries of the simulation box are retained while those that are outside are ignored. The definition and straining of the simulation box is schematically shown in figure 9. The construction of the atomic structure in variant A is illustrated in figure 10. Only the projections on the $(\bar{2}1\bar{1})$ plane is shown for simplicity of presentation.

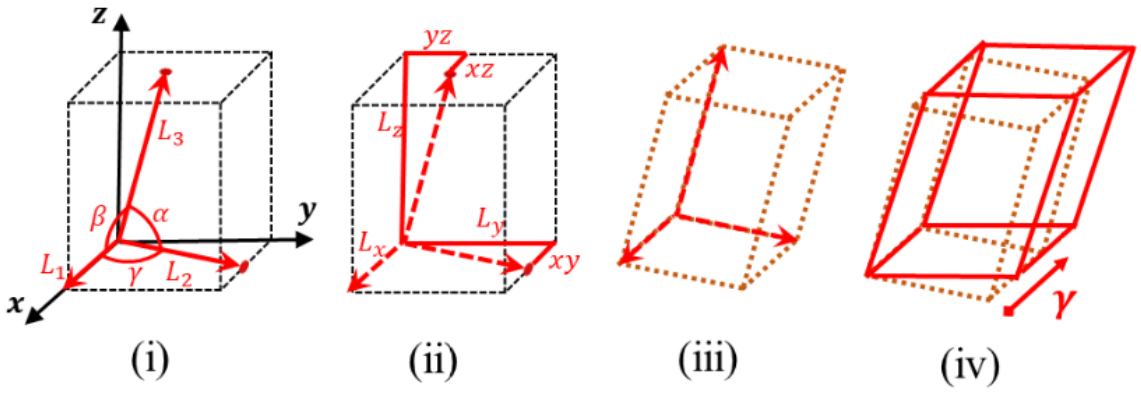

Figure 9: Schematic construction of simulation box (i) The edge vectors and angles between them are indicated in the global basis (ii) Components of the edge vectors projected on the global basis are shown (iii) Schematic of strain-free simulation box (iv) In-plane shear applied on the *xy* plane to strain the simulation box

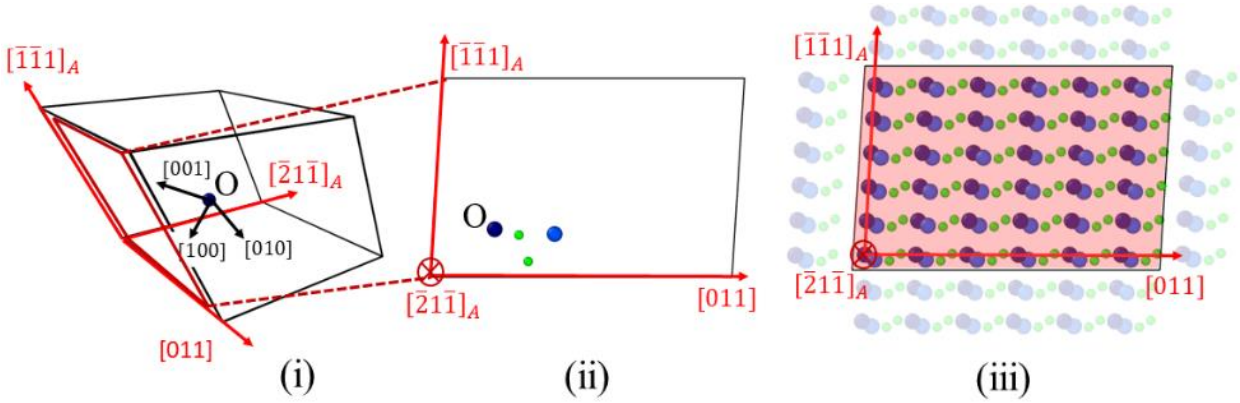

Figure 10: Construction of variant A structure in the simulation box; (i) Simulation box with edge vectors aligned with crystallographic directions; a reference lattice Ti site (marked as O) is shown, marked with the oriented unit cell vectors (ii) The $\{211\}$ projection is shown with the same lattice Ti site and accompanying motif atoms (iii) Variant A is constructed by repeating the motif arrangement at each point of the oriented lattice; the atoms inside the simulation box are retained while the ones outside are ignored (by LAMMPS).

Repeating this for variant B, we construct the structure in figure 11 (i). In both structures (figure 10 (iii) and figure 11), since the edge vectors are crystallographic directions, periodic boundary conditions can be enforced across the parallelepiped faces. This allows a simulation of the bulk material within Molecular Statics (MS). To check the stability of the structure (in variant A or B), the simulation box was relaxed within periodic boundary conditions, until the energy

converged within a fractional change of 1.0×10^{-8}. Both structures were stable, as was expected from the work in [94].

However, if the $\{111\}$ terrace of the Type II twin boundary is to be simulated, then both variants must be constructed within the same simulation box. Then the choice of a suitable edge vector $\vec{L}_3$ is not straightforward. In this model, the choice was made to use $\vec{L}_3 \parallel \mathrm{n}_{\{111\}}$, where $\mathrm{n}_{\{111\}}$ is used to represent $\mathrm{n}_{(\bar{1}\bar{1}1)_\mathrm{A}} = \mathrm{n}_{(11\bar{1})_\mathrm{B}}$. Since this vector is not crystallographic, periodic boundary conditions cannot be enforced. Instead, shrink-wrapped boundary conditions are enforced with a constrained/frozen layer in the top and bottom. All the atoms in this layer are frozen in place and constrained from moving in any direction, during the simulation. This layer is chosen to have a thickness higher than the cut-off of the interatomic potential ($r_c = 5.2$ $\overset{0}{\mathrm{A}}$). Based on this constraint, the frozen layer is chosen to contain three $\{111\}$ planes (with interplanar spacing $d = 2.097$ $\overset{0}{\mathrm{A}}$) at both extremities of the *z*-edge. This constrains the boundary from relaxing as a free-surface and provides a stable structure (representative of the bulk material) for relaxing the atoms within the simulation box. This structure is relaxed with lateral periodic boundary conditions (along *x* and *y*), and shrink-wrapped condition along *z* (as specified before). Both variant structures were found to be stable, and are shown in figure 11 (ii) and 11 (iii). Again, only the $\{211\}$ projections are shown for clarity of presentation. Results from simulation of a smaller simulation box are shown for illustration purposes. The box sizes used for simulations, for instance in section 2.2.5, are larger.

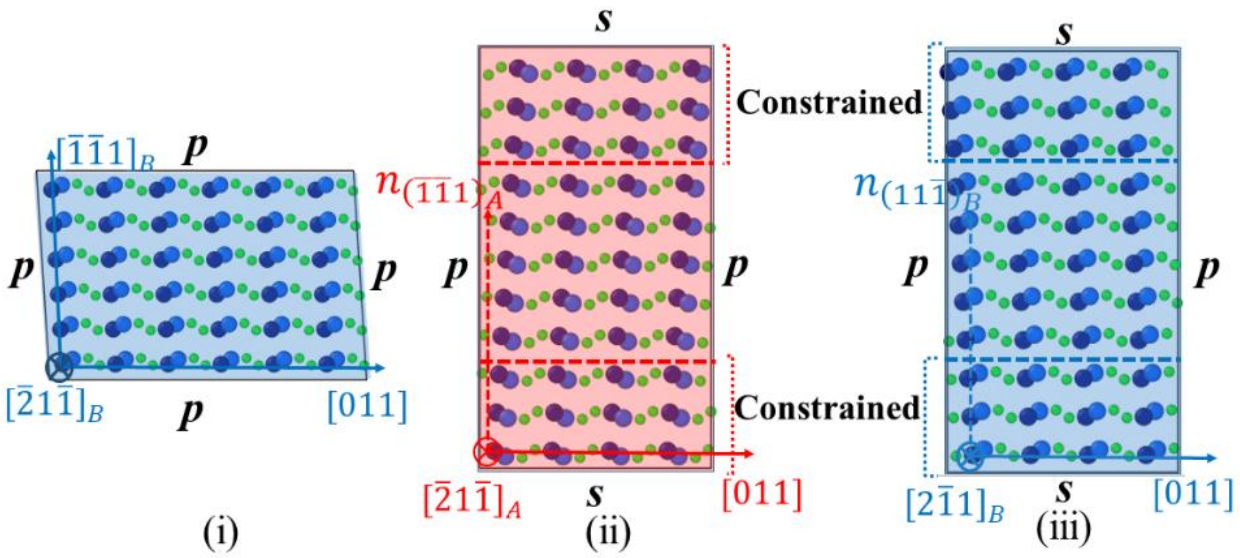

Figure 11: (i) Variant B constructed in a simulation with edge vectors along respective crystallographic directions (ii) Variant A structure with the edge vector $\vec{L}_3$ along the normal to the $(\bar{1}\bar{1}1)_A$ plane; periodic boundary conditions (*p*) can be enforced along the lateral directions $[011]$ and $[\bar{2}1\bar{1}]_A$; shrink-wrapped boundary condition (*s*) are enforced with a constrained layer in the normal direction (iii) Variant B structure constructed in the same way as (ii)

Two blocks of variant A and B were constructed in this manner and analyzed for section 2.2.1 and 2.2.3. They were positioned on top of each other to show that the atomic arrangements in their respective $\{111\}$ planes are incompatible. This was done to establish the absence of a crystallographic TB between the variants.

To construct the twinned structure (the $\{111\}$ terrace structure) within the simulation box, the following procedure is adopted (refer figure 12). The simulation box is partitioned into two regions. The strained structure of variant B is filled in the bottom region. We establish in section 2.2.3 that the twin boundary cannot be an atomic plane and can only exist as a virtual boundary separating the variants. Hence, the origin of variant B is chosen such that the first atomic plane nearest to the partition clears it with sufficient tolerance. Now variant A is constructed in the top

region. The distance between the origins defines the offsets. The definition and calculation of lattice offsets is elaborated in section 2.2.5.

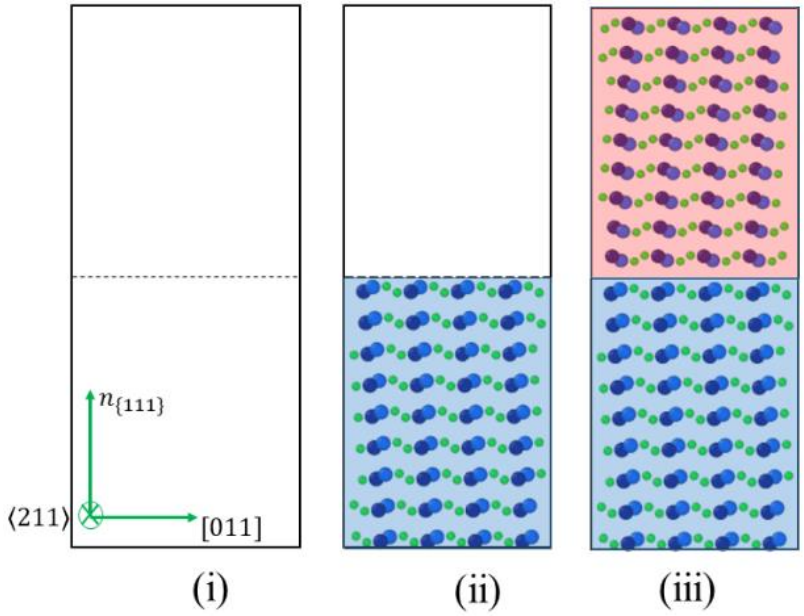

Figure 12: (i) Simulation box is defined with two regions (ii) Variant B is defined such that the atomic planes clear the partition with sufficient tolerance (iii) Variant A is constructed in the top region (accurate definition of the structure requires the calculation of lattice offsets, elaborated in section 2.2)

2.2.5. Relative Positioning of twin variants across the boundary: Lattice offset parameter

Most metallic structures possess high enough symmetry that the twinning modes exhibited are mostly of compound type [39]. In fact, *only* compound twinning is possible in the cubic lattice [100]. In such cases, the first four twinning elements of Table 1 are rational [40] and the TB separating the variants is a crystallographic plane hosting atomic sites of the crystal. This is because that plane adheres to the atomic configuration of both the twin variants. However, from the crystallography of the {111} planes in both variants (figure 5 (iii)), it becomes clear that there is no crystallographic plane of atoms that can match both arrangements. The reader is referred to section 2.2.4 for a detailed account of how the TB structure can be constructed within the framework of LAMMPS. Two-dimensional projections of the complicated three-dimensional

structure on the $\{211\}$ and $\{011\}$ planes are shown in figure 5 (iii) to illustrate the absence of such a crystallographic plane. A more detailed illustration is given in section 2.2.3. Visually, this is easy to see because of the unique arrangement of motif atoms around the lattice sites, in each variant. Hence, the TB here refers to a virtual plane separating the twin variants. While this may seem to be a detail of no importance, it immediately poses the question: What is the relative positioning of variants across the TB? This is equivalent to a formalism within the TM [71] wherein an offset vector $\vec{p}$ is defined between the variant lattices on a coincident plane. Two atomic planes are defined here to illustrate the offset coordinates. The crystallographic plane in variant A immediate to the TB is labelled $\mathbb{P}_{\mathbb{A}}$ and an additional plane $\mathbb{P}_{\mathbb{B}}$ of variant B is presumed to extend beyond the TB into variant A. The plane $\mathbb{P}_{\mathbb{B}}$ only serves as a virtual construct to define the offsets and does not exist as a real plane in the twinned configuration. The offsets are defined by examining coincidence between the two planes. Select origins O_{A} and O_{B} on two arbitrarily chosen lattice sites on $\mathbb{P}_{\mathbb{A}}$ and $\mathbb{P}_{\mathbb{B}}$ respectively. The relative position of O_{A} with respect to O_{B} defines the offset vector, having coordinates (x_0, y_0, z_0). This is illustrated in figure 13. When all three components are zero, the lattice sites of plane $\mathbb{P}_{\mathbb{A}}$ and $\mathbb{P}_{\mathbb{B}}$ coincide. Of course, the offsets (x_0, y_0, z_0) exhibit periodicity corresponding to the periodic spacing along $([011], \langle 211 \rangle, \langle 111 \rangle)$ respectively and hence we narrow focus to values within the constraints $\left(0 \le {x_0}/{|[011]|} < 1,\ 0 \le {y_0}/{|\langle 211 \rangle|} < 1,\ 0 \le {z_0}/{|\langle 111 \rangle|} < 1\right)$. The offsets will henceforth be represented by the normalized counterparts $\left(\bar{x}_0 = {x_0}/{|[011]|},\ \bar{y}_0 = {y_0}/{|\langle 211 \rangle|},\ \bar{z}_0 = {z_0}/{|\langle 111 \rangle|}\right)$.

At any offset value, the structural relationship between the two, as established by diffraction techniques (like electron diffraction in the TEM), wouldn't be any different. Hence, the foundational TEM studies that established the orientation relationship [39] could not have clarified this detail. This issue of lattice offset is not particularly an alien concept in the context of crystalline interfaces. Offsets feature in the geometry of the "isosceles" twin boundaries [24, 101] and other hetero-phase boundaries [102] as well. In fact, atomistic simulations employing static relaxation techniques were utilized to determine the structure of the "isosceles" TB in BCC structures [24].

The TEM-inspired atomic model proposed by [64] provides key insights to partially solve the problem. From their high-resolution imaging of the TB, they show that both variants appear identical when viewed along $[011]$. This fixes the offsets in the $\langle 211 \rangle - \langle 111 \rangle$ plane. The offset normal to the TB takes a unique value $\bar{z}_0 = 0.048$, while there are two possibilities for $\bar{y}_0 = 0.128,\ 0.628$ (i.e. for both $\bar{y}_0$, the variants appear identical when viewed along $[011]$). The relative position along $[011]$ is not directly apparent from the atomic model. An atomistic calculation similar to that performed for isosceles twins in BCC crystals [101] is carried out here. We perform an iterative energy minimization to determine the offset $\bar{x}_0$ through molecular statics, and this is performed for each value of $\bar{y}_0$. By initiating the statics relaxation from various atomic configurations distinguishable by $\bar{x}_0$ offset, the offset value corresponding to the least energy is identified. After enforcing the coherence strain, the axes of the simulation box align as follows: $x \parallel [011],\ \mathrm{y} \parallel [\bar{2}1\,\bar{1}]_{\mathrm{A}},\ \mathrm{z} \parallel \mathrm{n}_{\{111\}}$. The lateral axes, *x* and *y* are crystallographic, implying that periodic conditions can be setup to represent the bulk material, while the boundary parallel to the TB is shrink-wrapped. For the box size, a span of 10 periodic spacings along $[011]$ (one periodic

spacing $\sim 6.36\,\text{Å}$) and $\langle 211 \rangle$ (one periodic spacing $\sim 8.29\,\text{Å}$) is chosen, and 30 $\{111\}$ planes chosen along z direction (spacing between consecutive planes $\sim 2.097\,\text{Å}$). Assuming that the structure far from the twin interface remains unaffected in this iterative relaxation procedure, a $6\,\text{Å}$ boundary is constrained or "frozen" on the top and bottom. The relative positions of atoms in these layers are constrained to remain unaffected by the forces enforced by the energy minimization routine. The thickness was chosen to be higher than the cutoff distance of the interatomic potential ($r_c = 5.2\,\text{Å}$). The conjugate gradient relaxation scheme in LAMMPS is employed where convergence is said to be achieved when the fractional energy change over successive iterations is less than 1.0×10^{-8}. During the relaxation, the dimensions of the simulation box is allowed to vary using the box/relax option, thus allowing a dilatational relaxation to the TB aiding it in achieving the lowest energy configuration for each offset. The parametric variation of the offset is achieved by changing an "origin" parameter (a provision in LAMMPS when defining lattices) within the code. The result are the values of the offset parameters $(\bar{x}_0, \bar{y}_0, \bar{z}_0) = (0.522, 0.628, 0.048)$ or $(0.022, 0.128, 0.048)$. Both these offsets are crystallographically equivalent in that they correspond to the same resulting TB structure. This completes the atomic model of the coherent twin segments proposed by [64], for the Type II TB in $B19'$ NiTi martensite. The plot in figure 13 (iii) presents the relative energies with reference to the lowest energy configuration. The absolute value of this minimum energy reflects the twin boundary energy (more generally it is the grain boundary energy, estimated from atomistics following [103]) for the $\{111\}$ terrace plane. An alternate choice of the terrace plane, such as $\{344\}$, yields a higher twin boundary energy. Moreover, it does not relax as well as the $\{111\}$

interface, producing significant local distortions around the twin boundary. This justifies the choice of terrace plane as $\{111\}$.

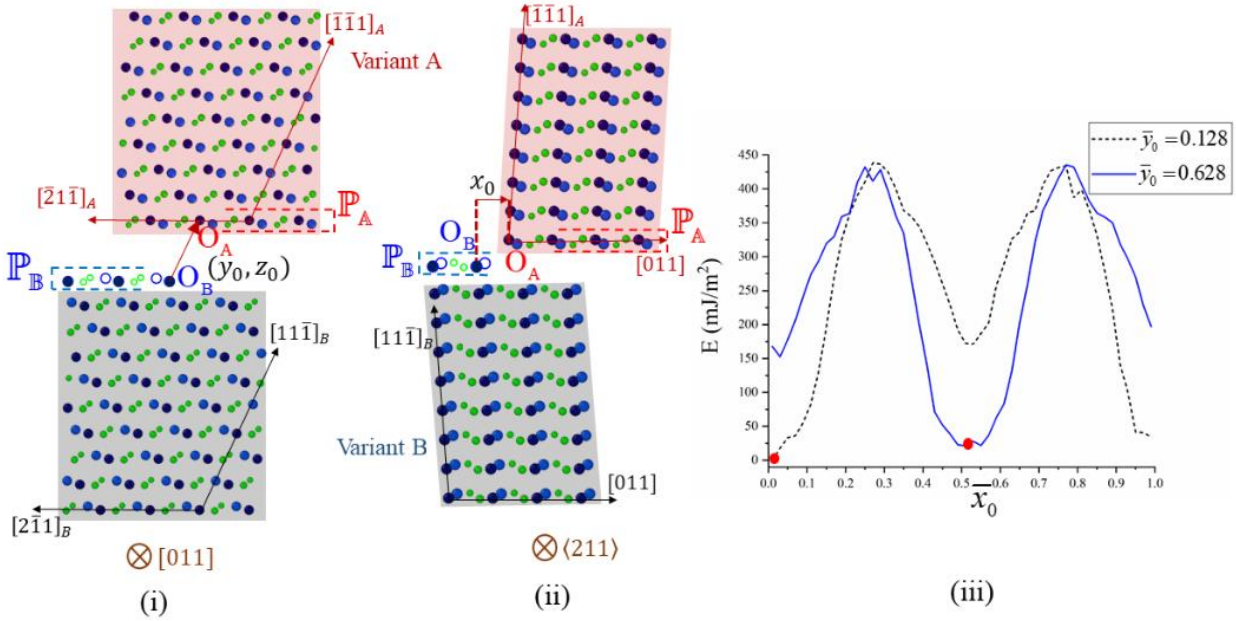

Figure 13: Completion of TB geometry through a MS simulation to determine offsets (x_0, y_0, z_0 represent translational offsets of variant A with respect to variant B) (i) Illustrating (y_0, z_0) offsets on the (011) plane between the lattice origins O_A, O_B, on respective reference planes $\mathbb{P}_A$,$\mathbb{P}_B$ (ii) Illustrating x_0 offset on the $\{211\}$ plane (iii) MS simulation results indicating offset magnitudes corresponding to minimum energy

2.2.6. Atomic Shuffles transforming one twin variant to another

Now that the crystallography of the TB has been established, the atomic motions necessary for detwinning are determined. For this purpose, two twinned configurations T1 and T2 are compared that differ by the existence of one additional detwinned layer plane in T2. It must be pointed that the setup of both these configurations is now conceivable only after due completion of previous offset calculation. The crystallographic arrangement in $(11\bar{1})_B$ plane of variant B in T1 is compared against the corresponding detwinned $(\bar{1}\bar{1}1)_A$ plane in variant A of T2 (figure 14).

Sub-regions of the corresponding planes are overlapped to aid the visualization of the atomic movements. The following observations are made:

a. The entirety of atomic movements has a negligible average translational component and dominantly comprises shuffling movements around the TB. These are the shuffles that must be realized for migrating the TB.
b. The lattice Ti site (L) of variant B must move to the motif site (M) in variant A of T2. Similarly, the motif Ti of variant B (T1) are to move to the lattice Ti sites in variant B (figure 14 (iii)). These movements are along $[011]$ only.
c. As for the Ni atoms, an equal and opposite movement along $\langle 211 \rangle$ and $n_{\{111\}}$ is required

This analysis was done in expectation of the GPFE calculation elaborated in the next section. Knowledge of these atomic movements is necessary to simulate the detwinning within the MS framework under the right constraints.

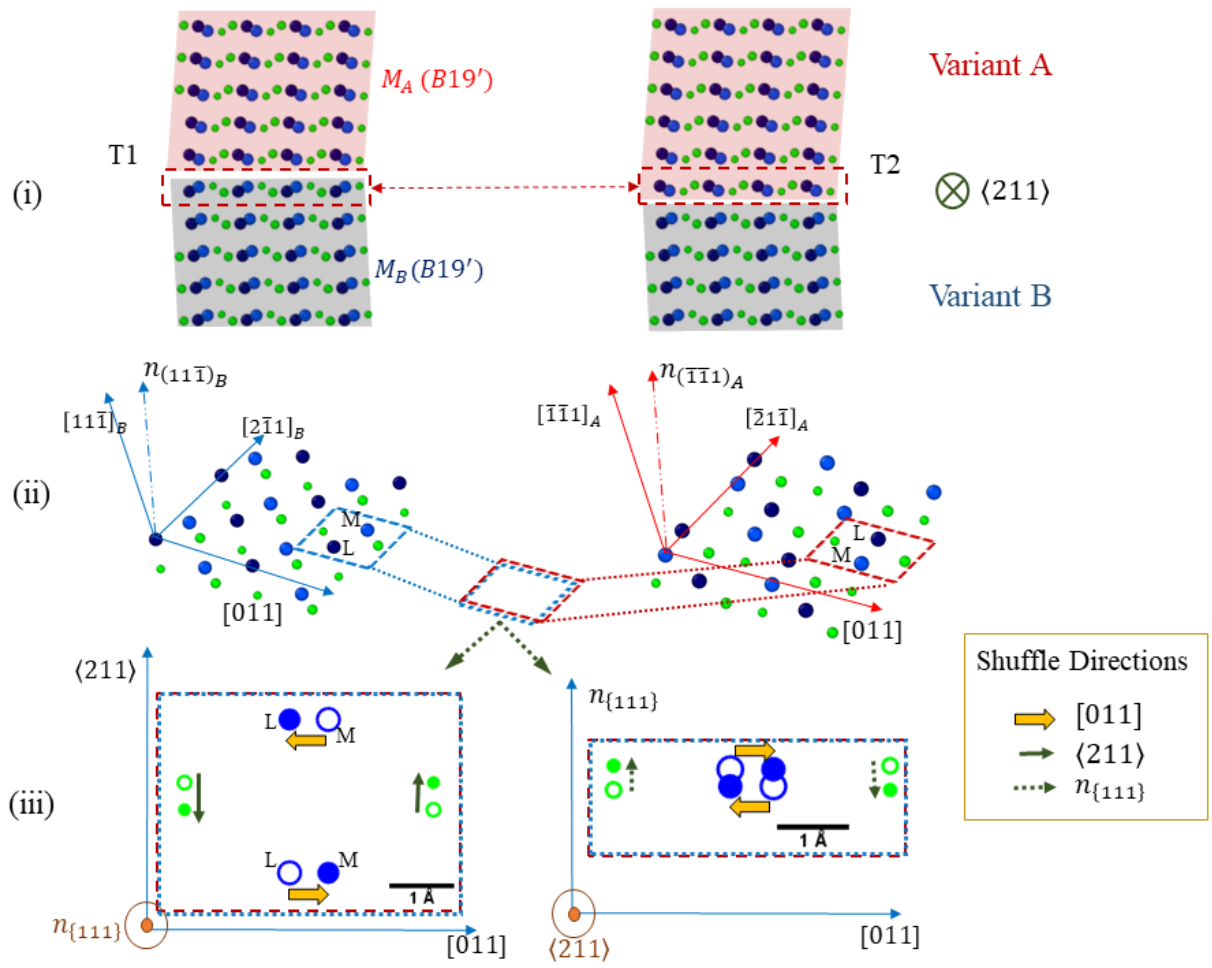

Figure 14: (i) Atomic arrangement of twin as viewed along $\langle 211 \rangle$, highlighting the crystallographic plane which detwins from a variant B configuration in T1 to a variant A configuration in T2 (ii) Comparison of atomic arrangement on the plane undergoing detwinning (iii) Overlapped atomic positions indicating necessary atomic shuffles for detwinning (filled circles correspond to atom positions in variant A while open circles correspond to variant B; L: Lattice Ti, M: Motif Ti), achieving the conversion of the crystallographic plane in variant B to a plane in variant A

2.2.7. Twin Migration segment of the GPFE curve

Following the previous section's analysis, if the detwinning dominantly requires shuffles at the TB, then it can be asked what role is played by the twinning shear S(Table 1)? How does an applied shear on the TB connect with the shuffles required to migrate the same? An atomistic simulation of the GPFE curve is ideal to elaborate this shear-shuffle interplay, and will be calculated in this section. It would be unreasonable to expect the exact energy landscape because the MS framework

is not truly ab-initio. It relies on an empirical interatomic potential that was not fit to any energy signature corresponding to twinning. An *ab initio* calculation of the GPFE landscape is given in [37]. In particular, we will focus on the twin migration segment of the GPFE curve and ignore the nucleation segment. The reader is referred to [91] for details on the procedure to obtain the GPFE curve, and also to 2.2.8 where certain specifics in the applicability of the procedure to this low-symmetry phase is discussed. In short, the standard procedure attempts to incrementally introduce a rigid translational disregistry between the two variants at the TB and tracks the energy cost for the same. This is typically done by rigidly displacing one variant (mobile half of the system) on top of the other (fixed half of the system) until the TB has migrated to the next plane. The translational disregistry plays the role of the twinning shear and following [37], it is known to be along $[011]$. This causes a TB migration into variant B, causing one layer plane of variant B to detwin into variant A.

Following these guidelines, a MS simulation is setup. The twin configuration T1 (section 2.2.6) is setup with periodic lateral conditions and shrink-wrapped conditions on the top and bottom. The constrained layers with thickness higher than the potential cut-off are set at the top and bottom, following section 2.2.5. The mobile half of the system is defined as variant A along with an additional atomic plane of variant B which is about to detwin. The remaining portion of the system is the fixed half. In the mobile half of the system, the lattice Ti sites are constrained to follow incremental rigid displacements along $[011]$, while in the other half they are constrained to stay fixed (figure 15). With the lattice Ti constrained, the motif Ti atoms and the Ni atoms are allowed to relax about their positions without any constraint in any direction. An additional out-of-plane shuffle is also allowed for the lattice Ti atoms. Explaining the rationale behind this procedure requires a digression that is not directly pertinent to the main study and is hence deferred

to section 2.2.8. At every increment of rigid displacement, an energy minimization is carried out with the conjugate gradient method in LAMMPS, until energy converges to within a fractional change of 1.0×10^{-8}. The volume of the simulation box is maintained constant throughout. The results are presented in figure 15. A steep drop is obtained at the onset of the lattice-motif Ti shuffle. Different points of the obtained GPFE curve are corresponded with snapshots of the intermediate structural states at that position. Although only the Ti shuffles have been illustrated in the figure, the Ni shuffles also happen simultaneously.

We focus on two takeaways for the final modelling step. Note that the potential energy after detwinning (configuration T2, at 4) nearly recovers to the initial value (configuration T1, at 1). This reflects the periodicity of the twin migration segment in the GPFE curve and this periodicity corresponds to the magnitude of the twinning partial [91, 104]. The "partial" nature is associated with the property of the dislocation in migrating the generalized planar fault that is the twin boundary (TB). The magnitude is only slightly lower than that proposed in [37] i.e. $b \approx 1/9\ [011]$, and was used as a scaling factor for the displacement axis in the plot in figure 15. The TB has migrated by one plane and the TB energy is degenerate before and after migration. Both aspects are relevant to the TM derived in the following section, and a discussion on the shear-shuffle interplay is deferred to the discussions section.

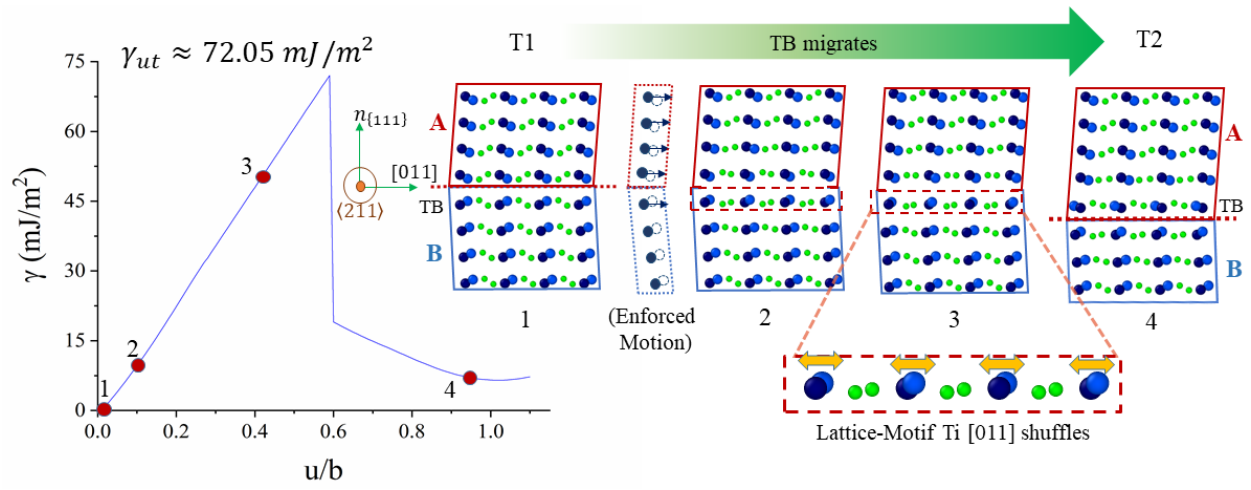

Figure 15: GPFE curve from Molecular Statics: The enforced rigid motion on the lattice Ti sites $(u \parallel [011])$ is schematically indicated, and snapshots of atomic positions at different stages is presented

2.2.8. GPFE: Key differences from higher-symmetry crystallographic structures

Although the procedure to calculate the GSFE/GPFE is fairly standard [91] and finds ubiquitous presence in understanding twinning energy barriers [48-50] it shall be briefly repeated here. This repetition is necessary to elaborate the intricacies that separate twinning in high-symmetry BCC/FCC systems from the low-symmetry phase dealt with here. In these cubic phases, the twinning mode is *only* of the compound type [100]. To extract the twin migration part of the GPFE, we need to setup a TB with two variant blocks in a relaxed state. Then, keeping one part of the configuration fixed rigidly, the remaining part is rigidly translated over it and the energy is extracted at each incremented position. In other words, a translational disregistry is introduced and the associated energy cost obtained per unit area. In the example shown in figure 16 (i), the translated part consists of the top twin variant along with the crystallographic TB. Atomic shuffles normal to the twinning plane are allowed while those along the direction of translation are ignored. As the translation occurs, the top part crosses the unstable twinning energy and then forms an

additional twinned plane, with the crystallographic TB having moved down by one plane. The example is based on twinning in a high-symmetry cubic phase, FCC Cu on the $\{111\}$ plane [105]. Now, attempt the same procedure with the $B19'$ TB setup. The initial twin configuration T1 is shown in figure 16(ii). The rigidly translated part includes the top variant M_A. The net displacement that must be achieved at the top boundary with respect to the bottom fixed boundary should equal the twinning partial magnitude. The initial and final states are already known from the previous analysis of crystallography (section 2.2.6), and the objective is to get to configuration T2 from T1. A reliable estimate of the twinning partial is available from [37] and is *approximately* $\frac{1}{9}[011]$. If a translation of this magnitude is enforced without allowing any shuffles parallel to the direction of translation, then the resulting structure would not resemble that of T2. Hence, there is a need to allow shuffles parallel to the direction of shear/translation. This is implemented in the procedure outlined in section 2.2.7, where the rigid displacements are only applied to specific atomic sites (lattice Ti only) while the remaining (motif Ti and Ni atoms) are allowed to shuffle.

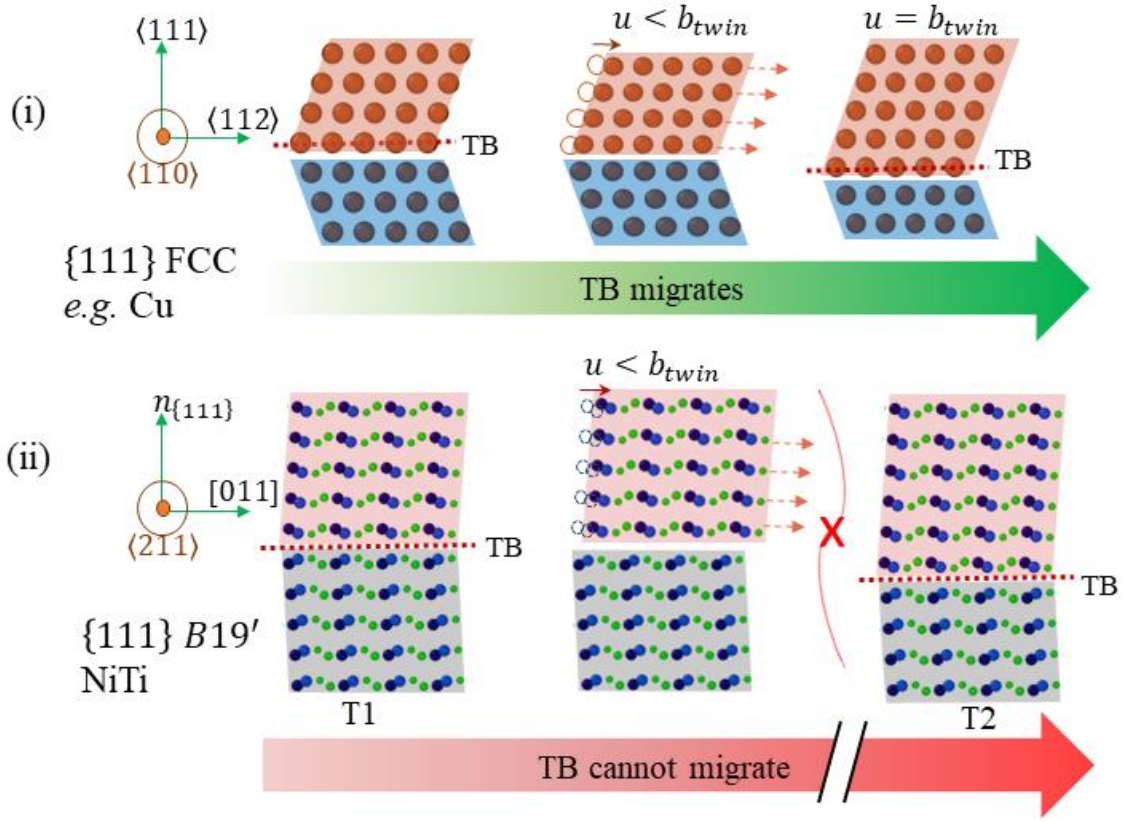

Figure 16: A comparative illustration of the validity of enforced rigid displacements to calculate the GPFE twin migration segment in (i) higher symmetry FCC system versus (ii) lower symmetry $B19'$ (TB: Twin Boundary), illustrating the inability of a translation sans shuffle in migrating the TB in $B19'$ martensite

2.2.9. Disconnected Geometry of $\langle 011 \rangle$ Type II twin boundary: Topological Modelling (TM)

The ensuing section attempts to causally explain the observed disconnected geometry of the TB observed in [38]. In sections 2.2.1 and 2.2.2 it was established that there is an interface shear strain needed to have perfect atomic registry across the TB. To minimize the elastic strain energy cost associated with the TB, long-range strains must be minimized by an array of dislocations at the interface rendering it semi-coherent [73]. Further, the twin interface also accommodates disconnections [38, 62], which from TM are responsible for the diffusionless migration of the twin interface [85]. Such a dislocation-disconnection combination is directly embodied in the twinning partial calculated in the previous section. The presence of a twinning

dislocation on the interface separates two coherent $\{111\}$ terrace planes by a step/disconnection [24, 74, 76]. Given the degeneracy in energy for the TB residing on successive planes (section 2.2.7), the disconnection can step between consecutive $\{111\}$ terraces separated by one interplanar spacing i.e. $d_{\{111\}} \sim 2.097\,\mathring{\mathrm{A}}$. Then the twinning partial is a "perfect" interface dislocation, following terminology of [76]. This step height in combination with the magnitude $|b| \approx \frac{1}{9}\,|[011]|$ are key parameters for the TM. The iterative approach described in [79] is utilized. For the first iteration, the twinning plane indices are assumed as $n_0 = \left(11\bar{1}\right)_B$, and the axes are chosen with the x axis aligned along the common $[011]$ direction, y along $\langle 211 \rangle$ and the z axis pointing into variant A, aligned with $n_{(11\bar{1})_B}$ (refer figure 17). The linear density of interfacial defects (dislocations), **B**, is given by Frank-Bilby equation, expressed here in the tensorial form:

$$\mathbf{B} = -\mathbf{E}_c.\mathbf{v} = -(\mathbf{D}_A^{-1} - \mathbf{D}_B^{-1}).\mathbf{v} \tag{2.11}$$

Where $\mathbf{E}_c$ is the interface coherence strain and $\mathbf{v}$ is a unit probe vector along which the linear density is sought, and $\mathbf{D}_{A\,(\text{or}\,B)}^{-1}$ is the deformation gradient tensor that maps the strained state in the twin configuration to the un-deformed crystallography of the individual variant A (or B). The magnitude of the coherence shear strain in each variant is given by $\gamma = 0.96\%$. The individual deformation gradients are given by:

$$\mathbf{D}_A^{-1} = \begin{pmatrix} 1 & -\gamma & 0 \\ 0 & 1 & 0 \\ 0 & 0 & 1 \end{pmatrix};\ \mathbf{D}_B^{-1} = \begin{pmatrix} 1 & \gamma & 0 \\ 0 & 1 & 0 \\ 0 & 0 & 1 \end{pmatrix} \tag{2.12}$$

Substituting in (2.11), and using the probe vector along the y-axis $[0\ 1\ 0]^T$ (which is aligned with $\langle 211 \rangle$), the dislocation density is given by:

$$\frac{\mathbf{b}}{d} = \mathbf{B} = 0.0192 \tag{2.13}$$

The twinning partials are of screw nature with their dislocation lines and Burgers vector aligned along $[011]$, having magnitude $b = 1/9\ [011] \approx [0.7067\ 0\ 0]^T$ Å. Substituting in (2.13), we solve for the disconnection spacing, which in the first iteration is $d_0 = 36.80$ Å. For this spacing, the effective normal to the twinning plane is rotated by the transformation

$$Q = \begin{pmatrix} 1 & 0 & 0 \\ 0 & \cos\theta & -\sin\theta \\ 0 & \sin\theta & \cos\theta \end{pmatrix} \tag{2.14}$$

where, given the inter-planar spacing of $(11\bar{1})_B$ planes as $h_{(11\bar{1})} \approx 2.097$ Å, we get $\theta_0 = \tan^{-1}(h_{(11\bar{1})} / d_0)$. Thus, an inclination is introduced into the effective twinning plane which changes it slightly from $(11\bar{1})_B$. The calculation is repeated in a rotated set of axes $x' - y' - z'$ (figure 17), where $x' \| [011]$ and z' is along the normal to the new effective plane. Applying this rotation to the homogeneous coherence strain and repeating the calculation iteratively, a self-consistent twinning plane is determined. To show the convergence, results of 3 iterations are given in Table 2. The resulting twinning plane agrees with the HRTEM observation of [38], being closer to $(8\ 9\ \bar{9})_B$ than the classical/PTMC indices of $(0.7205\ 1\ \bar{1})_B$.

Table 2: Iterative topological model calculation of effective twinning plane for Type II system

Iteration	Spacing of partials $(\overset{0}{A})$	Inclination (deg)	Effective Twinning plane
1	36.798	3.261	$(11\bar{1})_B$
2	36.858	3.261	$(0.8619\ 1.0229\ \overline{1.0269})_B$
3	36.858	3.261	$(0.8621\ 1.0229\ \overline{1.0269})_B$

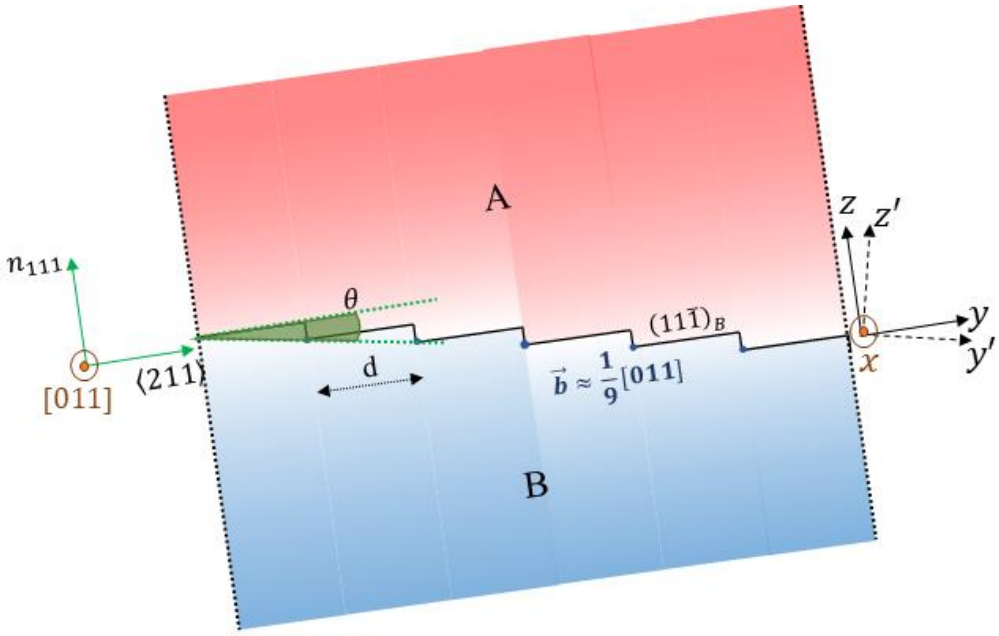

Figure 17: Schematic for topological model parameters

2.3. Discussions

2.3.1. Coherence strains for crystallographic registry

The requirement of coherence strain for atomic registry is solely due to the non-orthogonality of the crystallographic axes (figure 5 (ii)), and does not involve any further atomic-feature as such. And as shown in section 2.2.9, these coherence strains are counteracted away from the interface

by the presence of an array of twinning dislocations at the interface. After multiple iterations, there is still a residual elastic strain energy corresponding to the TB. This elastic energy corresponds to a small magnitude of residual strain far away from the interface (it can't be perfectly nullified by the interface dislocations). It also includes the self-energies and interaction energies of the interface dislocations. And this is independent of the intrinsic stable twin stacking fault energy γ_{tsf} that typically governs the thermodynamics of nucleation of a given twinning mode [106].

As mentioned earlier, the root cause of the coherence strain is the non-orthogonality of the axes which can be traced down to the monoclinic distortion in the unit cell of $B19'$. This extends to a more fundamental question on the crystal structure of low-symmetry phases, particularly those of martensitic phases in SMAs: If the axes of the unit cell are further away from orthogonality, what implications does it have on the occurrence and the structure of such Type II twinning modes? From the present analysis, a first guess would be that the elastic strain energy cost would be higher. This is because closer spaced dislocations (and hence higher repulsive interaction) would be required to alleviate higher coherence strains. And the shorter spans of crystallographic terrace planes implies the effective TB has irrational indices further removed away from the rational indices of the coherent terraces. Note that the classical theory [40] does not account for the presence of such strains. The lattice vectors of the unstrained variants (which only prevail furthest from the interface) are used as an input and hence it becomes obvious that there can be no rational twinning plane K_1 in the absence of coherence strains. Note that the rationality of the shear direction $\eta_1 = [011]$ remains unaffected because this direction is out of the plane which hosts the inclination angle θ (refer figure 17). Hence, the direction of twinning shear $\eta_1 = [011]$ established

on the coherent $\{111\}$ terrace planes directly translates to the effective irrational twinning plane as well.

2.3.2. Absence of crystallographic TB and Lattice Offsets

The unique arrangement of motif atoms in the unit cell of $B19'$ are primarily responsible for the absence of a crystallographic TB. Further supporting arguments are provided in 2.2.3. It is shown there that if these motif atoms are ignored and the twin is constructed using lattice points alone, a crystallographic TB does exist hosting coincident lattice sites of both variants. As a direct consequence of the motif atoms, the twin configuration has a relative offset between the lattices. It is remarkable to note that this offset positions the variants in such a manner that a shuffle among the Ti (lattice-motif shuffle) and Ni atoms is sufficient to migrate the TB by one crystallographic plane (refer figure 14). Hence, to draw a fundamental connotation, although the motif units of the $B19'$ unit cell complicate the twin configuration geometry and necessitate the calculation of an offset, they attribute the unique capability of shuffling into twinned positions with relatively low energy barriers [37].

2.3.3. Shear-Shuffle interplay

A few comments on the GPFE calculation are prudent here. The unstable twinning energy γ_{ut} is $72\ \mathrm{mJ/m^2}$, which is significantly higher than the accepted value [37]. Also, while the shuffling movements amongst Ni atoms are achieved, there are minor deviations in their final positions within the detwinned plane. This is in comparison to the T2 configuration setup in the previous section. Thirdly, the GPFE twin migration segment looks highly unsymmetric (figure 15), exhibiting a steep energy drop at the onset of the lattice-motif shuffles (again, does not agree with [37]). Nevertheless, these discrepancies must be borne as a limitation of the interatomic

potential, which is state-of-the-art. Moreover, the motive of this calculation is significantly different than that of [37], and primarily aims at thoroughly characterizing the detwinning mechanism. For these purposes the MS simulation and the interatomic potential are sufficiently useful.

Note that the lattice-motif Ti distinction (section 2.2.1) was crucial in the GPFE simulation. Selectively applying the rigid displacements to lattice sites allows us to infer a gradation in the degree of shuffle from near the interface to away from the interface. Treat the rigid displacements enforced on lattice sites equivalent to an applied shear. Further away from the interface, the motif units follow the lattice Ti and contribute to the magnitude of the twinning shear $\boldsymbol{S}$. As we move closer to the TB, there is a higher propensity for the motif atoms to shuffle. At the TB, the entirety of atomic movements are shuffles with negligible average displacement of atoms. This is very different from the compound twinning modes in higher-symmetry cubic systems where the shear plays a more dominant role than shuffle (refer section 2.2.8).

2.3.4. Topological Model (TM) complete with atomistic twin migration mechanism

Possibly the key ingredient in applying the TM was the interface coherence strain. It causally explains the need to have a periodic array of interface dislocations which eventually explains the irrational effective twin plane. The GPFE calculation was necessary to establish a degeneracy in interface energy between consecutive $\{111\}$ terrace planes. This is the additional input required by the TM to stipulate the disconnection step height [69]. In addition, it was necessary to establish the shuffles required for detwinning or TB migration.

The advantage of approaching the problem from an atomistic standpoint can now be realized where, along with the topological model the mechanism of twin migration can be fully clarified. It allows the partitioning of shears and shuffles in detwinning to the disconnection and

dislocation components [85], respectively, of the interface twinning dislocation. The motion of the disconnection is accompanied by a progression of the shuffles (elaborated in sections 2.2.6 and 2.2.7). The twinning dislocation magnitude is not as pertinent to the interface structure and has a more macroscopic implication in counteracting the interface coherence strains from extending long-range. Further, it acts as a carrier of the twinning shear as it moves along with the disconnection.

A complete picture of the interface structure is provided in figure 18. The atomic structure around the disconnection is also shown where the Twin Boundary Disconnection, TB (D), demarcates the two variants on the same crystallographic plane. Only the Ti atoms are shown for clarity of presentation. The difference in the relative positions of Lattice (L) and motif (M) Ti's are illustrated in both variants A and B. Suffice it to say that the Ni atoms also exhibit similar distinctions. It must be mentioned here that the structure here only highlights the crystallography and has not been relaxed within MS. If it was, there would be a more gradual change in structure across the TB (D). This is an unnecessary complication for this study and is excluded. Figure 19 highlights the lattice-motif Ti shuffles accompanying migration of the TB (D), that advances the TB. There are lattice-motif exchanges along $[011]$ as indicated. These shuffles are consistent with the analysis in section 2.2.6 and from the GPFE calculation (section 2.2.7). Although not shown, the Ni atoms also exhibit shuffles following section 2.2.7. As the dislocation component progresses to migrate the terraces by one crystallographic plane, the net twinning shear is $s = b/h$ [24] equaling ≈ 0.34, where the twin dislocation magnitude is $b = \frac{1}{9}|011| = 0.7067$ $\overset{0}{\text{A}}$ and the step height is $h = d_{\{111\}} = 2.097$ $\overset{0}{\text{A}}$. If, instead of the interatomic potential's lattice parameters, more

accurate experimental [97] or *ab initio* lattice parameters [96] are utilized, the value improves to $s = 0.31$, close to the phenomenologically determined twinning shear (Table 1).

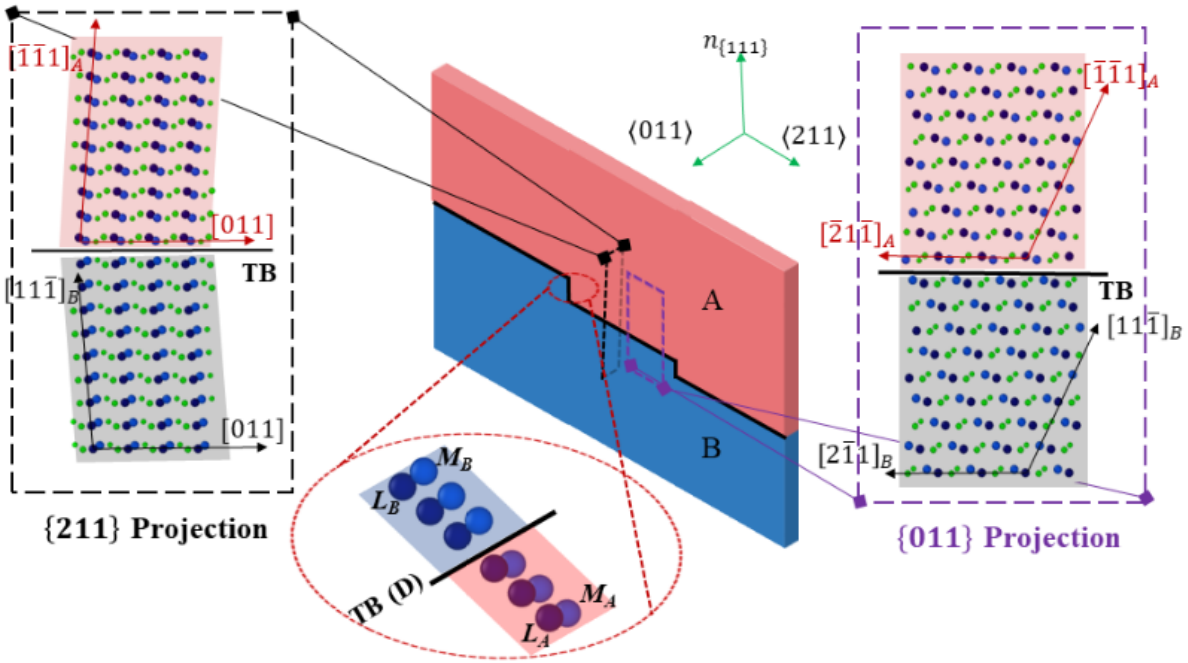

Figure 18: The disconnected twin interface geometry is shown with projections of the atomic structure on the coherent terrace planes. The crystallography surrounding the disconnection is also schematically shown, where TB (D) represents the Twin Boundary Disconnection; L_A, M_A are the lattice and motif Ti sites in variant A respectively, and for variant B we have the analogous designations L_B and M_B

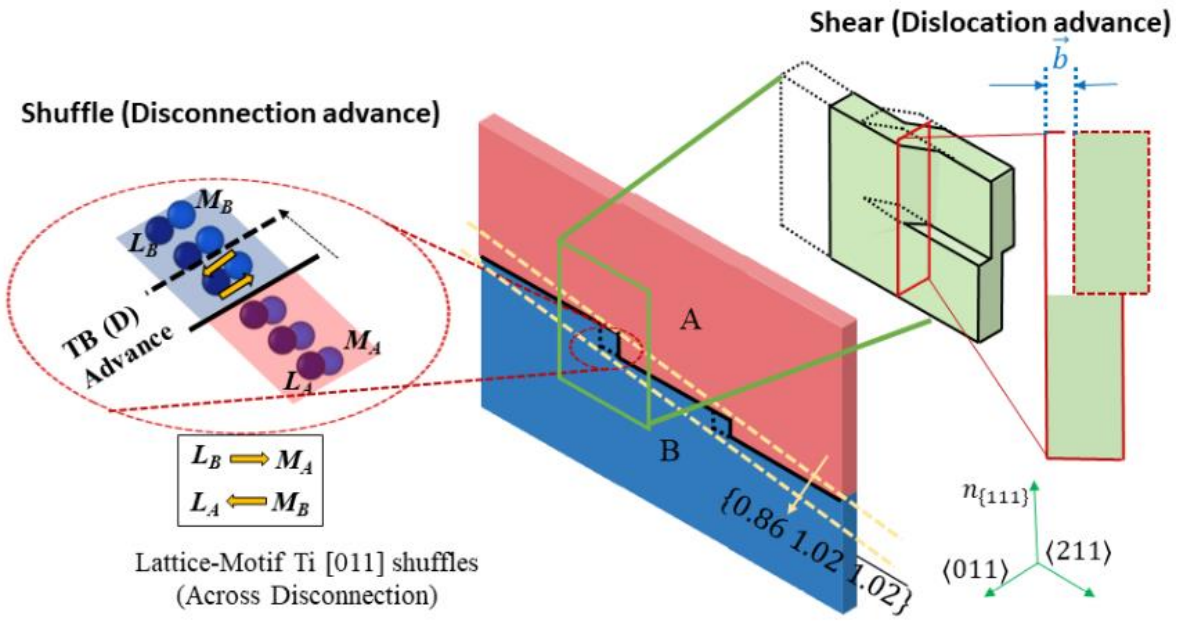

Figure 19: The mechanism of TB migration of the effective twin interface $\{0.86\ 1.02\ \overline{1.02}\}$ is shown; It occurs through the motion of the interface twinning dislocations comprising a dislocation component (Burgers vector $\vec{b}$ carrying the twinning shear) and a disconnection component (involving the lattice-motif shuffles for Ti atoms; although not shown here for clarity, there are also shuffles associated with Ni atoms, as per section 2.4)

2.3.5. Reconciling the HRTEM and the TM model

In section 2.1, it was mentioned that a consensus between the HRTEM model and the TM approach would be reached through atomistics. This is elaborated by noting the following two links:

a. The TM approach [83] cites difficulties in formulating disconnections on an irrational twin plane. The HRTEM-model [64] observes the effective irrationality of the plane to arise from a stepping between rational terrace planes. Having adopted the latter explanation, the key question was: Why does the twin interface prefer such a geometry over a single coherent plane? And interestingly, through the detailed characterization of atomic registry on the rational terrace plane (section 2.2.1), a coherence strain was determined. Such interface coherence strains constitute a crucial aspect of the TM theory [70, 107], and the

same framework immediately explains the irrational indices adhering to the disconnected geometry proposed by the HRTEM-model.

b. Although the concept and role of a disconnection in boundary migration had been formalized within TM theory, the HRTEM model identified its existence (called it "steps") on the TB independent of those findings. This could possibly be the reason why the step/disconnection was treated as a pure geometrical feature, and no significant role was attributed to it for the twin migration mechanism. The HRTEM model was blind to the idea of having dislocations on these disconnections, or blind to the idea of transformation/twinning dislocations. The dislocation component carries the twinning shear (heterogeneous mechanism) while the disconnection geometrically advances the boundary causing one twin variant to grow at the cost of the other (figure 19). These were basic tenets of the TM theory. Linking the two concepts required the GPFE simulation (section 2.2.7) to which the lattice offset simulation is a precursor (section 2.2.5).

2.4. Conclusions

This study attempts to provide a complete structural model of the $\langle 011 \rangle$ Type II twin boundary in $B19'$ NiTi, building on experimental HRTEM propositions [64]. A concerted modelling approach coupling atomistic simulations with TM theory is utilized to provide a physical explanation for the irrational indices of the TB. Adopting the $\{111\}$-terrace model of [64], requirements for atomic registry on the terrace plane are established. It is found that the TB cannot be crystallographic and is a virtual plane separating the variants. Also, an interface coherence strain is required for atomic registry across this boundary. The issue of lattice offset arises and is addressed using an iterative energy minimization scheme within MS, thereby determining the offset parameters that complete the terrace atomic model of [64]. Subsequently, the crystallography of the TB is analyzed to

establish the necessary atomic motions for detwinning. This detwinning mechanism is simulated within a MS framework by way of calculating the twin migration segment of the GPFE curve. The interplay of shear and shuffles in migrating the TB are established. An estimate for the twinning dislocation is obtained along with a step/disconnection height that can separate energetically degenerate $\{111\}$ terraces. These are combined within a TM [70] to causally explain the irrational indices of the effective twinning plane K_1, formerly determined from classical theories [39, 40]. Physical explanations for some of the classical twinning elements (K_1, η_1, s, in particular) were provided. The predicted K_1 in fact agrees better with more recent experimental findings [38] than the phenomenological characterization [39]. The role of the dislocation component in carrying the twinning shear and the shuffling mechanisms undergone during disconnection advancement are also established, thereby providing a complete description of the twin migration mechanism. The merits of the proposed approach in reconciling the HRTEM-based model within the TM theory have been outlined, highlighting the crucial insights from atomistics that bridged the hitherto disjoint propositions. In conclusion, this study attempts to provide both a complete structural model and a mechanism for twin propagation for Type II twins in $B19'$ NiTi. It attempts to fill a void in the physical understanding of this interface [83], the crucial implications of which have been discussed.

CHAPTER 3: TWIN MIGRATION AND FAULT-EMISSION

3.1. Introduction

SMAs form a special class of materials that can handle large strains (several percent) and exhibit exceptional strain-recoverability owing to a diffusionless martensitic transformation [1]. When their microstructures are engineered to have load orientations favoring transformation over plasticity [5], they offer the exciting solution of handling large reversible strains under fatigue loading, possibly evading plasticity-induced fatigue damage dominant in conventional metallic materials [54, 108]. Such reversibility is enhanced when the critical slip stresses of the individual phases (austenite and martensite) are higher than the critical stress for transformation. Considerable research in the field of SMAs is directed at further separating the two stress levels [13, 109]. Nevertheless, these materials are not immune to fatigue damage mechanisms, and are subject to irreversible plastic slip activity, typically observed to accumulate in the austenite phase [6, 7, 9, 12, 110-114]. The manifestations of such mechanisms have two fronts, one is structural fatigue damage as observed in conventional metallic materials while the other is functional fatigue where shape memory performance characteristics such as recoverable strain, stress hysteresis etc. are significantly diminished [4, 11, 52, 53, 113, 115, 116]. In turn, the prevalence of such damage mechanisms negatively impacts applications of SMAs in all domains, spanning biomedical (stents, orthodontics), automotive (valves) and aerospace fields [3].

One of the most puzzling aspects of SMA fatigue is the occurrence of plastic slip accumulation at stress levels far lower than the plastic flow stresses of the individual phases [13]. In fact, even stress-free thermal cycling of SMAs exhibit increasing dislocation density [7, 8]. A continuum micromechanical approach to the problem may state that the higher local stress state at the interface, necessary to accommodate lattice and constitutive mismatch, can drive plastic slip.

However, without a dislocation source, the stress levels must approach those of the ideal shear slip strength of the phases and this is unlikely. This is supported by the high unstable stacking fault energy barrier in the Generalized Stacking Fault Energy (GSFE) curves of the austenitic phase, particularly in those slip systems which have been shown to prevail under fatigue loading [14]. Further, several studies over the past few decades have consistently shown that the fatigue-activated slip system emanates from the austenite-martensite interface. Also, the slip system was found to align with the internal twinning system of martensite. In other words, the direction of Burgers vector of the emitted slip dislocation and the corresponding slip plane match the direction of twinning shear and twinning plane within the martensite phase, respectively (figure 20) [6-8]. These arguments lead us to believe that there is indeed a dislocation mechanism that is active at nominal stress levels (at the transformation stress) and is closely tied to the internal twinning within martensite.

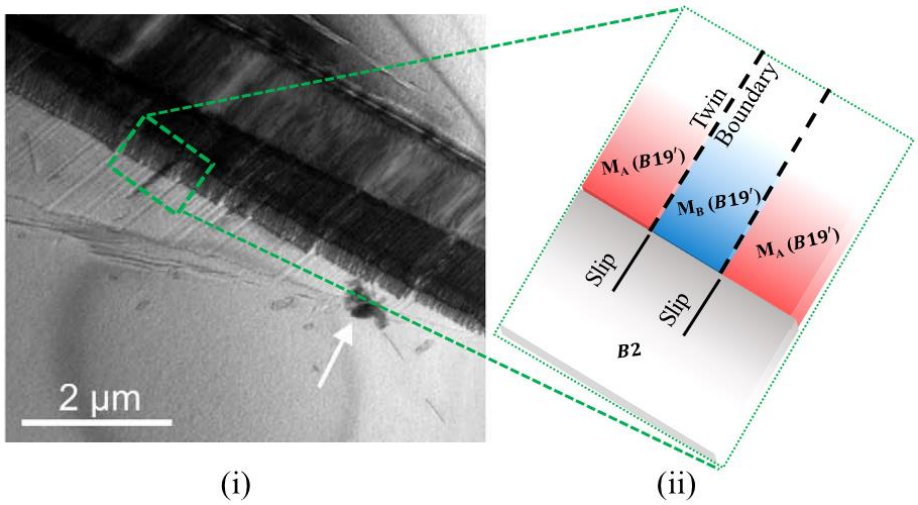

Figure 20: (i) This TEM micrograph was captured *in situ* during the reverse transformation from martensite to austenite. The micrograph shows a receding martensite phase (dark colored needle) which is subdivided into very fine twins, and the austenite phase (lighter color matrix) exhibiting fine slip lines aligned with the internal subdividing twin boundaries of the martensite phase; image was taken from [7], the arrow points out a reference feature in the sample utilized for TEM imaging (ii) An accompanying schematic is shown for clarification (labelled phases are specific to NiTi, for this study); the emitted slip line in the austenite B2 phase aligns with the twinning system in the martensite $B19'$ phase

To the best of the author's knowledge, only one proposition of candidate dislocation reaction exists in literature and it involves a build-up of twinning partials on the martensitic TB [9, 12]. While this mechanism proved a key step toward conceptual understanding of slip-emission during transformations, few pressing issues remain that could not be addressed due to the limitations of available tools at the time. The source of the participating twin partials is unclear. Even if the presence of such partials is presumed and a dislocation reaction follows, the accommodation of the residual dislocation within the participating TB must be addressed. The core atomic movements that underlie the reaction are unknown. Finally, the energetic feasibility of the dislocation reaction requires justification. An elementary energy-balance of the reactant and product dislocations (following Frank's rule) would render it infeasible. What is not accounted for is the energy influx due to a build-up of one or more twinning partials against a barrier to TB motion. In Kajiwara's scheme [9], the barrier is provided at the austenite-martensite phase due to the high resistance to slip in the austenite phase on the slip system aligned with the internal twinning. This explanation is based on the knowledge of accepted slip systems of the austenitic phase and lacks further quantification.

Multiple developments over the past two decades allow us to address aforementioned issues and examine the problem with exceptional detail that not only clarify mechanistic intricacies but also elicit key physical parameters that quantify the viability of the mechanism. Topological Modeling has established the disconnection-dislocation model for interfaces that migrate in a diffusionless manner [71, 76-80]. They have been applied to twin interfaces to explain TB migration [71, 76, 85], consolidating classically understood dislocation-mediated twin-growth mechanisms [23, 24, 63, 75]. These models establish the association between a TB disconnection to the corresponding twinning dislocation or twinning partial. Given the presence of such

disconnections on the TB (as found in the chosen study target), the presence of participating twinning partials is then known. The advent of atomistic simulation tools implementing Molecular Dynamics (MD) [88] and Density Functional Theory (DFT) [89] allow a first-principles rooted analysis of dislocation interactions. The physical fidelity of these simulations is ensured by development of reliable interatomic interaction potentials [93, 94, 117]. Simulations of this nature present a framework for a quantitative concerted exploration of energetics implicitly accounting for dislocation self-energies, interaction energies, lattice friction characterized by Generalized Fault energies (GSFE and GPFEs) [48, 91] while capturing core atomic motion with adequate detail.

In the following study, equiatomic NiTi is chosen as the model shape memory material owing to its commercial success [32, 33], and because many of its potential applications characteristically involve cyclic loading conditions [54]. For instance, functional fatigue of NiTi actuator springs and structural fatigue of NiTi wires, particularly in medical components negatively impact performance and has inspired active research in the field spanning the past two decades [118-122]. As noted before, an effective way of quantitatively understanding the mechanism is by way of atomistic simulation. For this purpose, a MS approach is chosen by running energy minimization routines in LAMMPS under appropriate boundary conditions. The choice was governed by the need to simulate dislocation mechanisms at a scale higher than those involving ab-initio DFT calculations. Also, the distinction of MS over Molecular Dynamics (MD) is key here because the energy minimization allows a framework based solely on the potential energy of the atomic arrangements and is unperturbed by statistical kinetic effects associated with finite temperature dynamics. The chosen interatomic potential [94] was proven to consistently reproduce the right formation energies and elastic constants of both austenite and martensite

phases. The ability to simulate shape memory and superelastic effects was demonstrated [123], and further it can structurally reproduce shuffled atomic positions characteristic of the phase. The importance of such shuffles will find relevance throughout the study. Nevertheless, it must be emphasized that since the potential is not fitted to slip or twin energy signatures which are the GSFE and GPFE respectively, the capacity to reproduce such features is indeed an open question. However, the fact remains that no potential for NiTi has been developed to account for all these phenomena [92-94, 117, 124-127]. In fact, developing potentials for such complex systems is still an active area of research and by no means is it reasonable to expect an empirical potential to be fit to all possible structural parameters. However, the present approach does not demand accuracy to quantitatively reproduce the energy signatures. It is known that different atomic configurations will correspond to highs and lows on the potential energy landscape and the potential is only required to capture these differences in a relative sense. It will be shown that the chosen potential has sufficient physical fidelity for this purpose.

Since the internal twinning in martensite consistently correlates with the fatigue-activated slip system in many SMAs, the TB in $B19'$ is chosen as the system under scrutiny. The $\langle 011 \rangle$ type II system is favored owing to its common occurrence experimentally [33, 39]. The HRTEM imaging of the boundary [38, 64] was a breakthrough in understanding the structure of the TB. A key finding was the direct observation of a disconnected geometry for the TB, explaining the irrational $\sim\left(0.7205\ 1\ \bar{1}\right)$ indices to result from stepping between consecutive $\left(1\ 1\ \bar{1}\right)$rational terrace planes. Consequently, it implies that twinning partials reside on these disconnections [71, 75, 76], and could participate in a slip-emission mechanism, similar to that of [9]. Surprisingly, only one study thus far has established the magnitude of this partial, obtained from the periodicity of the twin-migration region in the Generalized Planar Fault Energy (GPFE) curve [37]. It also

provides sufficient insight into the detwinning mechanism useful for this study. Understanding this mechanism is vital to know the core atomic motions involved during twin partial motion and subsequently understand the consequence when a barrier is presented to it.

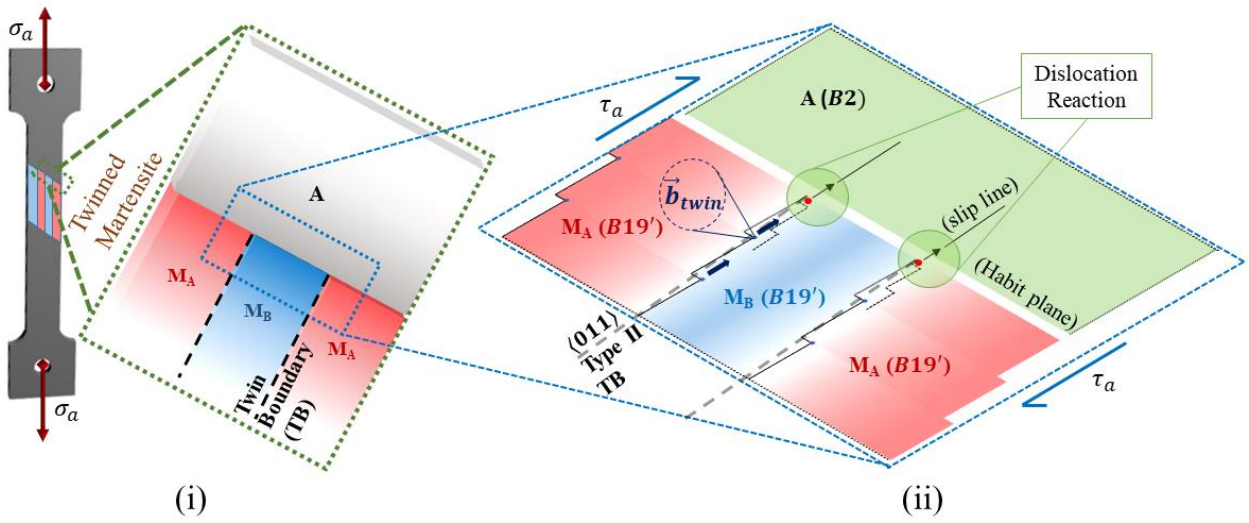

Figure 21: (i) An SMA dog-bone specimen undergoing martensitic transformation (austenite phase, A, to martensite phase) under applied load; the martensite phase forms as a twinned structure with variants M_A and M_B, separated by the twin boundary (compare with figure 20) (ii) This schematic is specific to the system of interest i.e. NiTi (transformation from austenite B2 to B19′ martensite phase), with the internal twin boundary as the $\langle 011 \rangle$ Type II TB; The TB is typically approximated as a straight irrational plane (dashed line) at higher scales, but at the nanoscale it has a disconnected geometry with rational $\{111\}$ terrace planes (solid lines); The schematic depicts the motion of twinning partials on disconnections and a possible dislocation reaction emitting slip into austenite (note the alignment of the slip line with the TB); the reaction occurs in the event the leading twin partial encounters a barrier (depicted as a red dot)

In summary, the dislocation mechanism proposed by Kajiwara [9] is examined quantitatively for the NiTi SMA within a MS framework. For this purpose, the type II twinning system of $B19'$ is studied. Following the atomic models in [37, 38, 64], coherent twin segments are setup with a twinning-partial on a disconnection in between the segments. Under an applied shear strain, twin partial motion and subsequent build-up against a barrier is enforced and a candidate dislocation reaction is simulated and proposed as a possible irreversibility active during fatigue (refer figure 21). The current study is but the starting step in analyzing fatigue-induced

irreversibilities in SMAs. It is intended to subsequently steer toward physics-based fatigue modeling (similar to [128]) in SMAs, by providing characteristic structural parameters instrumental in relevant dislocation mechanisms.

3.2. Methodology

A brief outline of the approach will be presented. Given the crystallography and the atomic models provided in [37, 38, 64], coherent twin "segments" are constructed within a MS framework. In each twin variant, the atomic sites are color-coded differently to aid visual identification of the detwinning mechanism. The rationale for this choice will be evident later in the study. Each twin "segment" corresponds to the TB structure on the $\{111\}$ terraces (excluding the disconnections). To ensure that this structure is in a stable configuration, a MS energy minimization is carried out for each twin segment. Multiple segments with the TB on successive $\{111\}$ planes are assembled to set-up a disconnected twin geometry in the simulation box. In order to locate the twin partial dislocations at the disconnections, an indirect approach is employed where continuum displacement fields of the dislocation are enforced outside a central core, and the core allowed to relax under their constrained positions, at the mercy of the chosen interatomic potential. This method is often used to obtain the right atomic arrangement at the core of the dislocation. The calculation of displacement fields at the interface between two highly anisotropic media (i.e. the martensite variants) is performed by employing the Eshelby-Stroh formalism [129], given the elastic constants of both phases and the magnitude of the twinning partial. A crucial catch in this procedure is in knowing how to apply the displacement fields around the core. It is not applied to all atoms but only to certain atoms, the choice of which is informed through a study of the detwinning mechanism. Once the displacement fields are enforced in accordance with the mechanism, the cores of the partials are in arrangements that ensure a twinned wake as they move.

The entire system is carefully relaxed using MS. Finally, a displacement-controlled shear strain is applied to initiate motion of the partials and generate a build-up against an artificially enforced barrier. The build-up of a single twinning partial against a barrier is simulated, and the consequent dislocation reaction is reported with justification.

3.2.1. Coherent $\{\mathbf{111}\}$ Twin Segments

The unit cell parameters are chosen consistent with the interatomic potential [94]. The atomic sites in the unit cell are depicted in Figure 22 (i) where one of the Ti atoms is at the lattice point $(0,0,0)$, following a commonly adopted crystal description [33, 95]. This Ti atom shall henceforth be called a lattice Ti while the other Ti atom of the unit cell shall be called a motif Ti. Inverted color-coding of the lattice-motif Ti sites are employed for the variants as shown in the figure 22 (i). This distinction will be instrumental in describing the atomic shuffles associated with the detwinning mechanism necessary for TB migration. Notice that the Ni atoms are not distinguished. Their shuffles are completely analogous to the Ti atom shuffles and another distinction adds unrequited complication in understanding the study.

As mentioned earlier, a twin "segment" will be used to refer to the part of the type II TB between consecutive disconnections. Henceforth, the variant on top of the twin interface shall be labelled A (colored red) while that on the bottom shall be labelled B (blue). The interface between the variants is rational and coherent [73]. The atomic model of the variants are constructed following the crystallography elaborated in Chapter 2, and assembled to form the twin segment (figure 22 (ii)). The construction of this twinned configuration is not trivial and requires accounting of interface coherence strains and a lattice offset between the variants (discussed in Chapter 2). The resulting structure is relaxed within MS to ensure that the configuration is stable as governed by the interatomic potential. The simulation box axes are aligned as

$x \parallel [011]$, $y \parallel [\bar{2}1\bar{1}]_A$, $z \parallel n_{\{111\}}$. Periodic conditions can be applied along *x* and *y* because these directions are crystallographic, thereby approximating the bulk of the material parallel to the plane of the coherent terrace. Due to the monoclinic distortion of $B19'$ martensite, the *z* direction is not crystallographic and periodic conditions cannot be enforced. Instead, shrink-wrapped conditions are employed with a $6\,\mathring{A}$ thick layer "frozen" in place on the top and bottom. These atoms are presumed to be sufficiently far from the TB within the bulk of each variant to remain unaffected by the local interface structure. The size of the layer is chosen to be higher than the potential's cut-off ($r_c = 5.2\,\mathring{A}$) [94]. The box size is chosen to be approximately $63.6 \times 82.9 \times 125.8\,\mathring{A}^3$, which is 10 times the periodic spacing in both $x \parallel \langle 011 \rangle$ and $y \parallel \langle 211 \rangle$ directions, and 60 $\{111\}$ planes stacked along the normal to the twin interface.

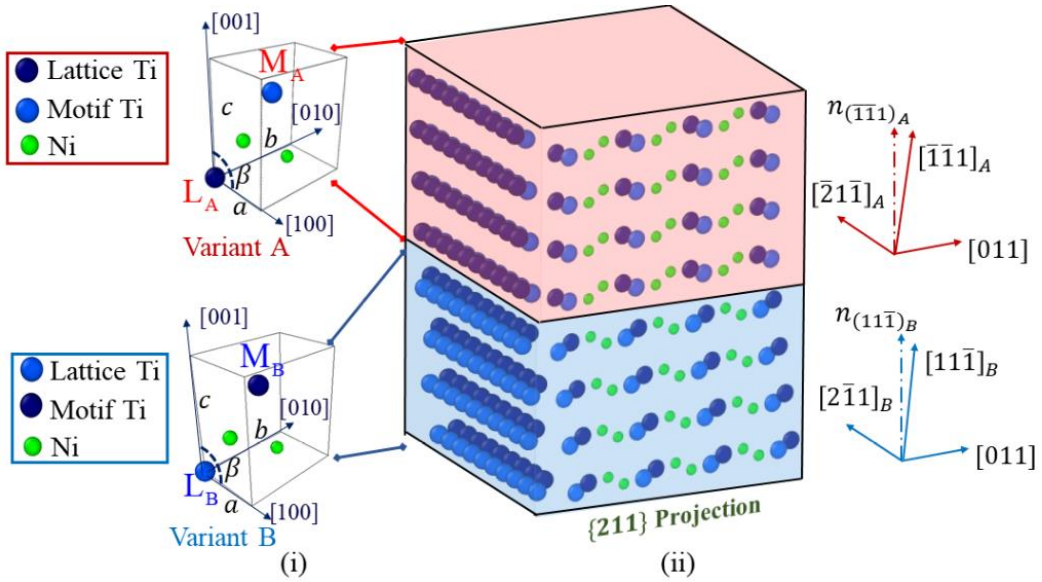

Figure 22: (i) Labelling of atomic sites in the unit cell of NiTi $B19'$ martensite; notice the lattice (L)-motif (M) Ti labelling distinct for each variant (ii) A 3-dimensional view of Coherent $\{111\}$ twin segment relaxed within MS (the frontal $\{211\}$ projection is shown along with a lateral view of the 3D structure only showing the Ti atoms, utility of which is realized ahead in visualizing twin partial motion); the crystallography used for construction of the atomic structure is given adjacently

The structure is relaxed under the conjugate gradient energy minimization scheme in LAMMPS [88], whose fractional energy tolerance for convergence is set at 1.0×10^{-8}. The simulation box size is kept constant throughout. Figure 22(ii) represents the relaxed atomic structure of the twin segment. These twin segments will be instrumental in setting up a TB disconnection, in section 3.2.3.

3.2.2. Locating Twin-partials in an atomistic framework

An accepted approach to positioning a dislocation within a discrete atomic structure (in a Molecular Statics or Dynamics framework) involves enforcing atomic displacements corresponding to the continuum field solution of the dislocation. All atoms beyond a specified core radius from the dislocation line are displaced in accordance to those fields and constrained while the mobile core is allowed to relax, governed by the interatomic potential [130]. The purpose of the enforced displacement fields is to prepare the atomic configuration in a manner from which a constrained minimization by the potential leads to the right core structure. Nevertheless, the first step is to solve for the continuum displacement fields. The linear elastic anisotropic Eshelby-Stroh formalism is adopted for this purpose, where the relevant equations and their results are presented in the following subsection. Subsequently, the application of these displacement fields within an atomistic framework is discussed.

3.2.2.1. Continuum Displacement fields of the Twin partials

In the anisotropic Eshelby-Stroh formalism for an interface dislocation, the displacement fields are described by a set of complex constants, solved for each of the two phases sharing the interface. Constants corresponding to the twinning variant A shall be indicated with a superscript A, while those for variant B shall be indicated by a superscript B. The coordinate system is defined

by the triad of vectors $\vec{t} - \vec{m} - \vec{n}$, where the normal $\vec{n} = [0\ 0\ 1]$ points from phase B to A, $\vec{t} = [1\ 0\ 0]$ corresponds to the dislocation line vector parallel to $[011]$, and $\vec{m} = [0\ 1\ 0]$ points away from the dislocated half-plane $(x_2 < 0)$. In this system, the burger's vector is given by $\vec{b} = \frac{1}{9}\,[011]_M \approx [0.7066\ 0\ 0]$ $\overset{0}{\text{A}}$. The displacement fields u_i $(i = 1,2,3)$ for the two domains are given by:

$$u_i^A(\mathbf{x}) = \frac{1}{2\pi\sqrt{-1}} \sum_{\alpha=1}^{6} A_{i\alpha}^A E_\alpha^A \ln(\mathbf{m}.\mathbf{x} + p_\alpha^A \mathbf{n}.\mathbf{x}) \qquad (\mathbf{n}.\mathbf{x} > 0) \tag{3.1}$$

$$u_i^B(\mathbf{x}) = \frac{1}{2\pi\sqrt{-1}} \sum_{\alpha=1}^{6} A_{i\alpha}^B E_\alpha^B \ln(\mathbf{m}.\mathbf{x} + p_\alpha^B \mathbf{n}.\mathbf{x}) \qquad (\mathbf{n}.\mathbf{x} < 0) \tag{3.2}$$

The constants $(p_\alpha, A_{i\alpha}),\ (\alpha = 1,2,...,6)$ for each domain is obtained by solving the equilibrium condition for the stress-field. For instance, the equilibrium condition in the variant A gives us:

$$\sigma_{ij,j}^A = C_{ijkl}^A u_{k,lj}^A = 0 \tag{3.3}$$

For a non-trivial solution, this leads to a set of algebraic equations,

$$C_{ijkm}^A (\mathrm{m}_i + p_\alpha^A \mathrm{n}_i)(\mathrm{m}_m + p_\alpha^A \mathrm{n}_m) A_{k\alpha}^A = 0 \tag{3.4}$$

And for a non-trivial $(p_\alpha^A, A_{i\alpha}^A)$, the following condition ensues:

$$\det\{C_{ijkm}^A (\mathrm{m}_i + p_\alpha^A \mathrm{n}_i)(\mathrm{m}_m + p_\alpha^A \mathrm{n}_m)\} = 0 \tag{3.5}$$

And for every p_α^A, there exists a vector a values for $A_{k\alpha}^A (k = 1,2,3)$ from equation (3.4). The constants E_α for each phase is obtained by solving conditions that relate tractions and displacements across the slip plane. For the half-plane given by $x_2 < 0$, the displacements and tractions are both continuous, yielding the following equations respectively

$$\sum_{\alpha=1}^{6} A_{i\alpha}^A E_\alpha^A - \sum_{\alpha=1}^{6} A_{i\alpha}^B E_\alpha^B = 0 \qquad \text{(i=1,2,3)} \tag{3.6}$$

$$\sum_{\alpha=1}^{6} L_{i\alpha}^{A} E_{\alpha}^{A} - \sum_{\alpha=1}^{6} L_{i\alpha}^{B} E_{\alpha}^{B} = 0 \qquad \text{(i=1,2,3)} \tag{3.7}$$

For the half-plane $x_2 < 0$, the Burgers vector represents the discontinuity across the slip plane, resulting in the following displacement and traction conditions respectively:

$$\sum_{\alpha=1}^{6} \eta A_{i\alpha}^{A} E_{\alpha}^{A} + \sum_{\alpha=1}^{6} \eta A_{i\alpha}^{B} E_{\alpha}^{B} = 2b_i \qquad \text{(i=1,2,3)} \tag{3.8}$$

$$\sum_{\alpha=1}^{6} \eta L_{i\alpha}^{A} E_{\alpha}^{A} + \sum_{\alpha=1}^{6} \eta L_{i\alpha}^{B} E_{\alpha}^{B} = 0 \qquad \text{(i=1,2,3)} \tag{3.9}$$

In these equations, the expression for $L_{i\alpha}$ in each phase is given by the following example for variant A:

$$L_{i\alpha}^{A} = -n_j C_{ijkm}^{A} (\mathrm{m}_m + p_{\alpha}^{A} \mathrm{n}_m) A_{k\alpha}^{A} \tag{3.10}$$

The elastic constants are picked consistent to those reproducible by the interatomic potential [94]. The constants are given in Table 3. Due to twin symmetry, $p_{\alpha}^{A} = p_{\alpha}^{B} = p_{\alpha}$.

Table 3: Eshelby-Stroh Constants for Twin-partial of $\langle 011 \rangle$ Type II twin

p_1	-0.3273+1.3438*i*	E_1^A	-0.2204+0.0154*i*	E_1^B	0.2204-0.0154*i*
p_2	-0.3091+0.9710*i*	E_2^A	0.3171-0.0462*i*	E_2^B	0.3171-0.0462*i*
p_3	0.2313+0.7117*i*	E_3^A	0.0848+0.0174*i*	E_3^B	-0.0848-0.0174*i*
p_4	-0.3273-1.3438*i*	E_4^A	0.2204+0.0154*i*	E_4^B	-0.2204-0.0154*i*
p_5	-0.3091-0.9710*i*	E_5^A	-0.3171-0.0462*i*	E_5^B	-0.3171-0.0462*i*
p_6	0.2312-0.7117*i*	E_6^A	-0.0848+0.0174*i*	E_6^B	0.0848-0.0174*i*

The twin-partial is of screw nature and the displacement component parallel to the dislocation line (the major component) is shown in figure 23 (ii). To aid visualization, an accompanying schematic representation is shown in figure 23 (i). Now, the continuum displacement solution is available for superposition to individual atoms in the MS simulation.

3.2.2.2. Applying Displacement fields: Non Cauchy-Born adherence

In MS or MD, the primary focus is to setup a physically consistent dislocation core that can move under an applied load, and in the event of dislocation reactions, present atomic configurations that can interact to form product dislocations. Both features find relevance in this study. A crucial assumption implicit in the procedure is the Cauchy-Born (CB) assumption whereby all atoms outside the core are assumed to adhere to the continuum displacement fields. An argument is made in the following subsection as to why it may not lead to the right core structure in $B19'$ owing to the presence of shuffles.

As mentioned earlier, the enforced displacement fields provide a surrounding constraint that guides the MS relaxation. The goal is to relax the sharp displacement gradient of the continuum solution to a smoother physically consistent atomic-scale disregistry at the dislocation core. By nature of the twin-partial, it resides on a TB disconnection [71, 76] and the core-structure transitions the atomic arrangement from that in one variant to the other variant across the disconnection. Within the core, the nature of disregistry (as the structure transitions) has a one-one correspondence to the interface disregistries encountered in atomistic simulation of the GPFE curve (refer chapter 2, section 2.2.7). The role of continuum displacement fields in conditioning the core structure is exactly analogous to the role of rigid displacements in the GPFE calculation used to enforce local disregistry at the twin interface.

For high-symmetry systems such as cubic structures (FCC, BCC etc.), the disregistries are dominantly translational and do not involve shuffle of any significant proportion. For this reason, the GPFE displacements can be applied to all atoms to achieve the detwinning (refer chapter 2, section 2.2.8). This relates with the enforcement of continuum displacement fields on all atoms surrounding the dislocation core, and the Cauchy-Born assumption prevails. This is the case in several atomistic studies involving dislocations, where the assumption is often tacit [131-136]. In the case of $B19'$, detwinning requires disregistries of both a translational and shuffle character. There is a lattice-motif Ti shuffle and also a shuffle of Ni atoms. To achieve the detwinning in the GPFE, the displacements must only be enforced on specific Ti sites while the remaining atoms shuffle about their positions. This is addressed in more detail in chapter 2, section 2.2.8. The major takeaway being that the continuum displacement fields must be applied more selectively around the core, and the Cauchy-Born assumption is not followed.

Surmising the detwinning mechanism in as much is relevant to this section: The lattice-motif Ti shuffles occur along $[011]$ while the Ni shuffles occur perpendicular to this direction (refer chapter 2, section 2.2.6). The displacement field is then applied to select Ti sites in both variants whose detwinning atomic motions align with the direction of the displacement field at that location. In variant A, these correspond to lattice Ti sites while in variant B they correspond to motif Ti sites. This is illustrated in figure 23 (iii).

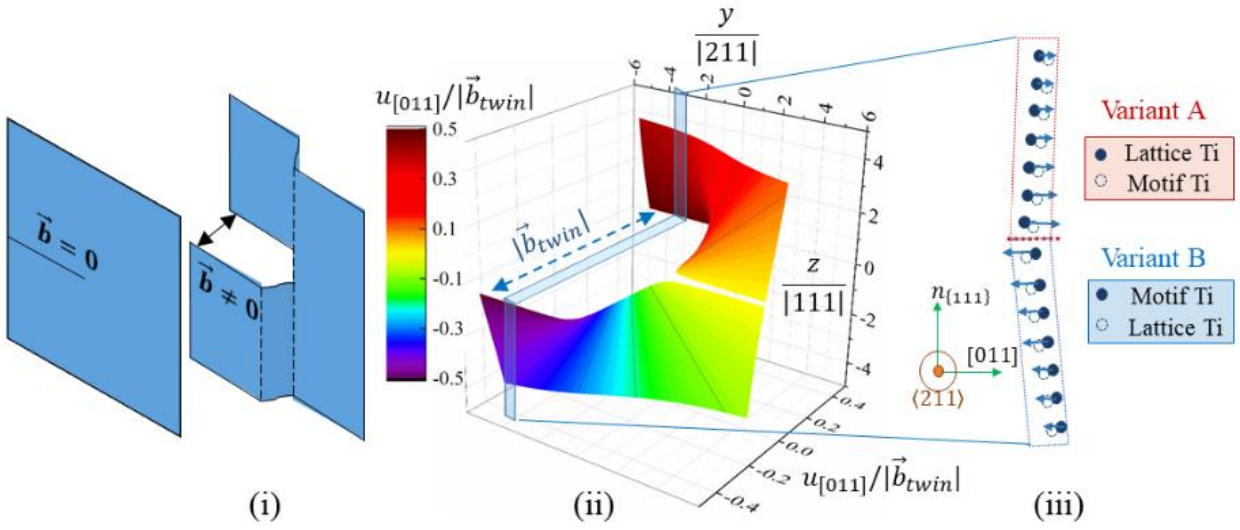

Figure 23: (i) Schematic representation of displacement discontinuity introduced by a screw dislocation, included to aid visualization of displacement field (ii) Major component of the displacement field solved from the Eshelby-Stroh formalism; the Burgers vector is shown, and a 2D displacement profile is sectioned (iii) Superposition of the 2D displacement profile onto a representative column of atoms on the $\{211\}$ plane; the displacement fields are applied selectively to certain Ti sites in both variants, indicated by the coloring schema

The following section addresses the construction of the TB disconnection upon which the twin partials are positioned in the manner described above.

3.2.3. Construction of TB disconnection and Twin-partial core structure

To construct a TB disconnection, coherent twin segments that were independently relaxed (section 3.2.1) are assembled piecewise. The choice of the number of disconnections in the simulation box indirectly decides the number of participating twinning partials for the simulated dislocation reaction. It must be reiterated, that no knowledge of such a dislocation reaction is yet available in literature. There is only a hypothesis that it could relate to twin-partial build-up but the number of reacting partials, and the outcome of such a reaction have not been established conclusively. To that extent, the approach presented here is exploratory, does not force a specific reaction, and only sets conditions conducive for it. A disconnected TB is setup with one disconnection and a twin partial located on that disconnection.

Lateral periodicity is preferred to mimic conditions closer to a bulk material, and to avoid boundary effects (or any unwanted image force resistance to dislocations) during simulation of the reaction. Ideally, it would be preferred to orient the effective twinning plane $\{0.7205\ 1\ \bar{1}\}$ aligned with the *xy* plane of the simulation box and enforce periodicity. However, the effective plane is not a crystallographic one and will cause issues when implemented with periodicity. For this reason, the coherent terrace of the TB i.e. the $\{1\ 1\ \bar{1}\}$ plane is preferred instead. And to include disconnections with twinning partials, a mirrored ledge structure is constructed as shown in figure 24 (i). A large span is chosen for the central ledge to allow one half of the simulation box to mimic the physical TB and the twin-partial interaction.

At each disconnection, the displacement fields are enforced as outlined in section 3.2.2.2 and the atoms are relaxed to produce the right core structure. The relaxation refers to the energy minimization using the conjugate gradient scheme with the same tolerance as in section 3.2.1. Physically, this guides the core of the twinning partial to a state where there is a gradation of shuffled positions. This is illustrated in figures 24 (ii) and 24 (iii), by visualizing the atomic positions at the core of the twin partial, on the slip plane, and the transition in Ti-shuffles is observed along $\langle 211 \rangle$. The right core structure renders the required mobility for the twinning partials under applied load, while ensuring that the all-important detwinning mechanism is followed as it propagates on its plane.

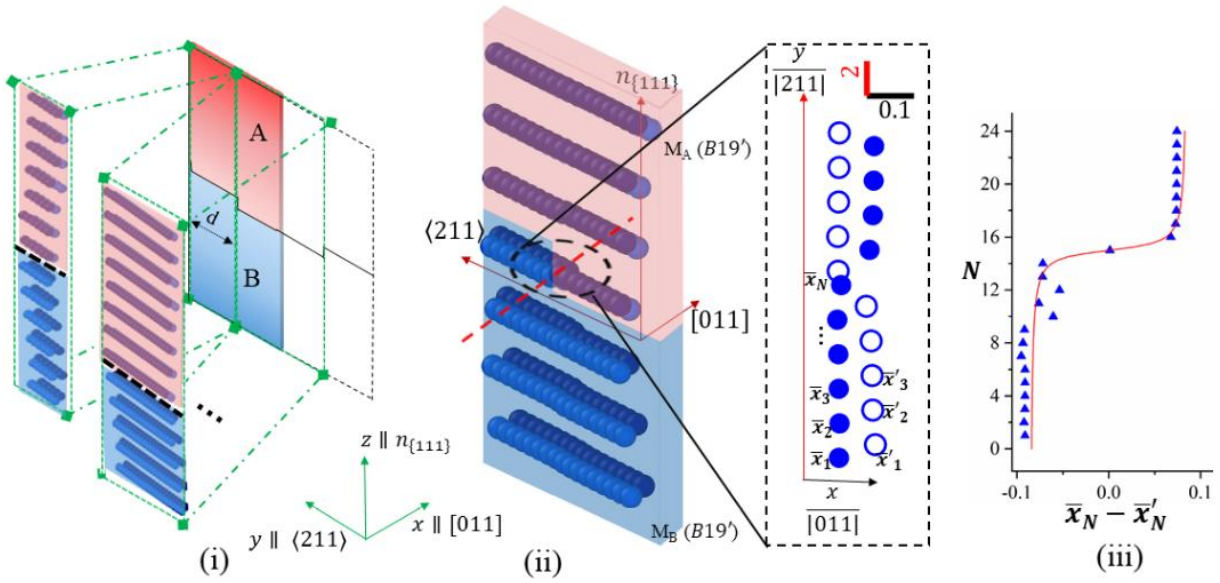

Figure 24: (i) Construction of MS Simulation setup for dislocation reaction, indicating the mirrored ledge construction of twin interface (assembled piecewise from independently relaxed $\{111\}$ twin segments) (ii) Relaxed atomic configuration around a TB disconnection, after introduction of the displacement fields on specific Ti sites (only the Ti atoms are shown for brevity and as mentioned in text, coloring schema of variant B is reversed to emphasize the shuffle across variants) (ii) After identifying corresponding lattice and motif sites, the transition in shuffled states at the core of the twin-partial (represented through a scaled schematic and plot) is visualized; $\bar{x}_N$ and $\bar{x}'_N$ respectively represent normalized $[011]$ coordinates of lattice and motif Ti atoms, and the shuffles are quantified by $(\bar{x}_N - \bar{x}'_N)$ where N is a simple count of the lattice-motif pairs tracked across the disconnection

3.2.4. Final Simulation: Setup of Dislocation Reaction within MS

So far, only the atomic configuration suitable for the final simulation of the dislocation reaction has been setup. Now a displacement-controlled shear loading is enforced to move the twinning-partial (figure 25(ii)). Subsequently, a barrier is presented to the motion of this partial and the outcome of that interaction is observed. The procedure for setting up these conditions will be elaborated.

Following the boundary conditions of section (3.2.1), lateral periodic conditions are enforced and shrink-wrapped conditions applied parallel to the TB. A constrained layer with

thickness larger than the potential's cut-off radius is chosen at the top and bottom of the simulation box. The constrained layers parallel to the TB serve to provide rigid atomic blocks at the boundaries which can be moved to enforce a strain-controlled deformation within the box. Note that in this setup, the twinning partial is a screw partial (Burgers vector parallel to dislocation line). The partial is moved by applying a shear on the simulation box by incrementally displacing the top and bottom frozen layers. The top is moved in the positive *x* direction (along $[011]$) while the bottom layer in the negative *x* direction, thereby enforcing a *xz* shear conducive to motion of the screw partial on the TB, along $\langle 211 \rangle$. At each incremental displacement of the boundary, the simulation box is relaxed under the same parameters of section 3.2.1. In this manner, a strain-controlled shear load is applied within the framework of molecular statics. No kinetic energy is involved, and the configuration is allowed to find the minimum energy positions at every strain increment, ensuring a "quasi-static" condition as best as it can be expected within atomistic simulation frameworks. Note that since there is no dynamics in this system, this applied loading is not coupled with high strain-rates which is often the caveat in such simulations, furnishing more reasonable stress estimates.

Thus, the simulated mechanical stress-strain response focuses on manifestation of intrinsic potential energy barriers and hence captures the athermal response. Although sufficient for the purposes of the present work, it is prudent here to mention relevance to physical experiments where one is necessarily in the regime of finite temperatures (say ambient temperature ~ 300 K) and finite strain-rates (for instance $10^{-3}s^{-1}$). In such conditions, the structure is assisted by additional thermal energy to overcome the energy barrier, governed by statistical thermodynamics. Consequently, the stress level required to activate the sought dislocation mechanism (to occur at a rate that is significant in comparison to the applied strain-rate) would be lower than that predicted by the

present athermal approach. Nonetheless, results of the present work could, in principle, be extended to this scenario by interpreting the determined athermal energy barriers as an activation energy in an Arrhenian expression. This is better elaborated in texts concerning thermally activated deformation, a good exposition for which can be found in [137].

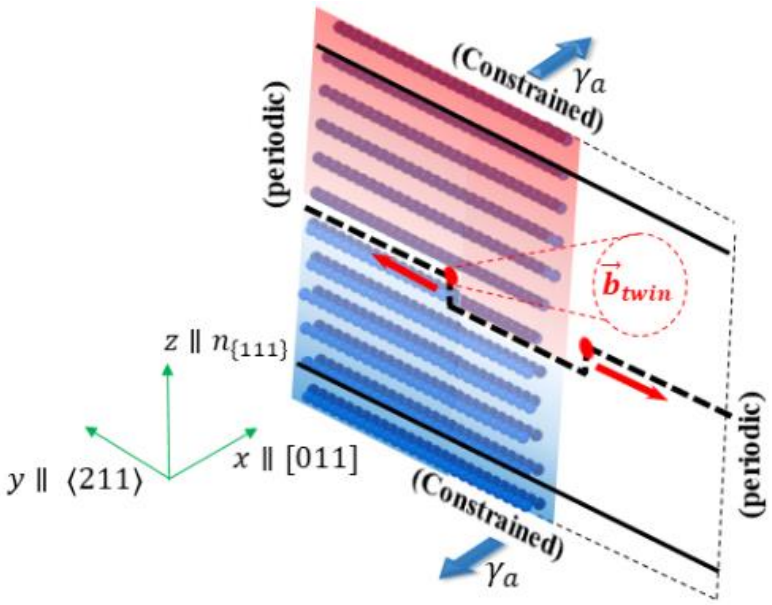

Figure 25: Final Simulation setup: Under constrained/periodic boundary conditions, motion of twin partials on disconnections is simulated under applied shear (a dislocation dipole is constructed, a positive twin partial is positioned on the left-side disconnection and a negative twin-partial on the right-side disconnection)

Under applied shear, the twin-partial moves and migrates the TB. This migration is achieved by motion of the disconnections, progressively converting atoms in variant B configuration to that of variant A (refer figure 25). To generate a build-up a barrier needs to be provided ahead of the leading partial. The question now becomes: how is the barrier/stop enforced? The answer lies in knowing the detwinning mechanism (refer chapter 2, section 2.2.6). Since, the twin partial essentially shuffles the Ti and Ni positions, a stop can be introduced by preventing these shuffles explicitly. An explicit prevention of lattice-motif Ti shuffles at a certain location ahead of the leading partial was implemented. When the leading partial reaches this juncture, it cannot progress

further because shuffle is disallowed. Implementing the barrier is not trivial. For a small group of atoms at the barrier location, forces in the direction of shuffle were selectively ignored during the relaxation. Nevertheless, these atoms were allowed to follow the applied shear motion by imposing displacements equal to the average of displacements experienced by surrounding atoms. Now that a twin-partial motion is setup and a barrier enforced, dislocation reactions are set-up by creating a build-up of one twin-partial against the barrier. Visualization is done using Open Visualization Tool (OVITO) [138] where snapshots at incremental shear strains are recorded. The results will be discussed in the following section.

3.3. Simulation Results on Twin Partial Slipping and Barrier Interaction

When no barrier is imposed to the motion of the twin partial, the partial slips across the coherent terrace, and reaches the lateral boundaries of the simulation box. A few snapshots of a focused subset of atoms are shown in figure 26, labelled with the average shear strain on the simulation box at that instant. At a certain critical shear stress, the shuffle-reliant detwinning mechanism activates and advances the partial, and the partial continues to the boundary. The advancement of the shuffle is visualized more closely, emphasizing the importance of the core structure elaborated in subsection 3.2.3. The benefit of the choice in color coding of atomic sites (section 3.2.1) is now realized as the shuffles are visualized in the exchange in the position of the dark-blue and light-blue spheres, representative of the lattice-motif Ti shuffles.

When a barrier is imposed to the shuffle (in the manner explained in section 3.2.4), the partial halts at that position, and the applied shear builds up. Eventually, a dislocation reaction seems to occur at the TB. The most conspicuous change is that the direction of advancement of the shuffle is reversed, progressing in a direction opposite to that associated with the original twin partial. Thus, along the TB, the original progression of detwinning has reversed, now converting

atoms in variant A arrangement to that of variant B. This indicates that a negative twin partial has nucleated which under the action of the applied shear moves in the opposite direction, achieving such a detwinning effect. In the onward direction, there seems to be a formation of a stacking fault at the TB. In other words, given that the shuffle has been disallowed, a translational disregistry has nucleated at the barrier and has progressed forward. And interestingly, it does not form within either of the variants but rather nucleates at the TB between them. Intuitively, this is an agreement with the twin symmetry of the structure as there is no special preference given to either of the variants. The relevant snapshots of the sequence are shown in figure 26. Analogous to the shuffle-progression, a snapshot showing the core atomic motions are visualized, for the fault nucleation. For a better illustration, short animation videos corresponding to both cases have been provided as supplementary material. At this stage, the hypothesis for fault nucleation is more argumentative and a more thorough analysis will be presented subsequently.

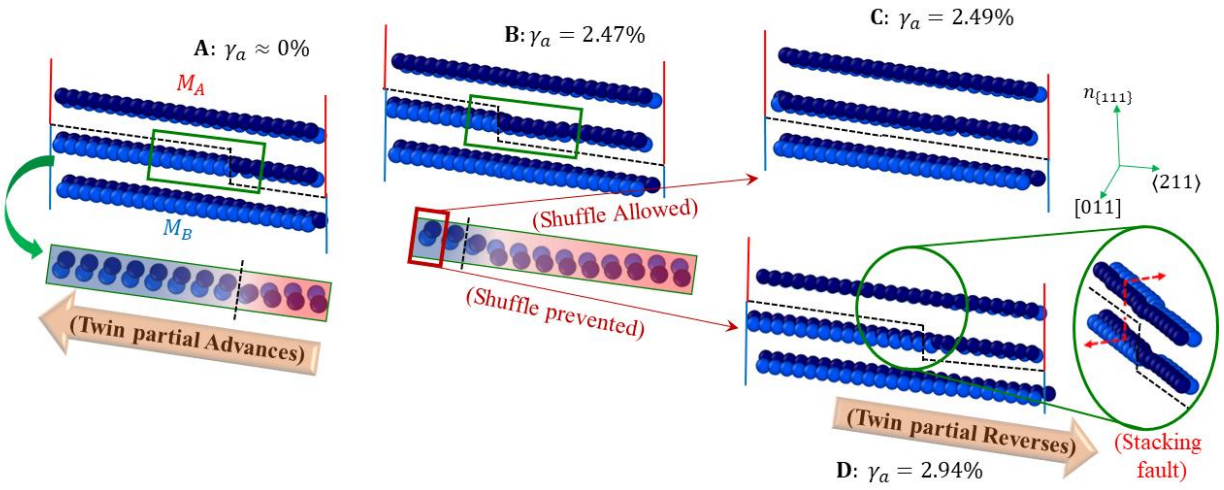

Figure 26: Snapshots of dislocation reaction simulation depicting twin partial advancement and reversal in the presence of a shuffle barrier (bordered red)

The stress-strain curves for both cases are shown in figure 27. The twin-partial motion can be inferred from the stress-plateau in both scenarios. When a barrier is present, there is an additional hardening regime to a slightly higher stress-level at which the fault partial is

hypothesized to nucleate and slip. Notice that the stress-level for fault nucleation is close to that corresponding to the onset of twin-partial motion.

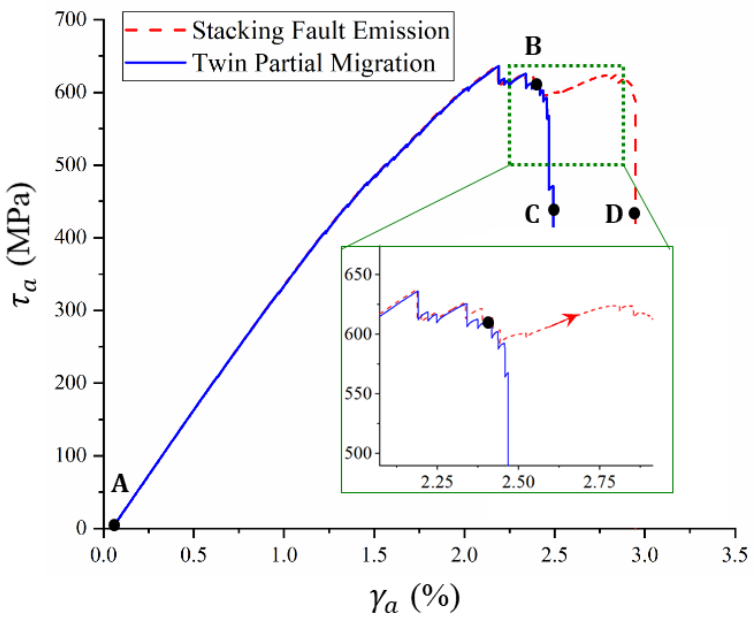

Figure 27: Stress-Strain response in the event of twin partial migration and fault emission; the inset reflects the additional hardening in the presence of a shuffle barrier

A Region of Interest (ROI) is defined in the path of the migrating twin partial, ahead of the shuffle barrier. Thus, the ROI is positioned close to the extremity of the $\langle 211 \rangle$ edge of the simulation box (shown in figure 28(i)). It is defined as a thin cuboidal region, with the longest edge along the *z* axis of the simulation box. It is used to query certain averaged properties of the atoms contained within the region. Hence the ROI only acts as a measuring probe during the simulation. Two parameters, relative displacement and energy density (per unit area), are calculated from it. The relative displacement is taken as the average displacement of variant A contained within the ROI minus that of variant B within the same region. The ROI is chosen to be small along $[011]$ and $\langle 211 \rangle$ to resolve local changes due to motion of the partial. The choice of the parameters is motivated from the state variables that are typically reported in GPFE/GSFE

calculations (planar energy and relative displacement). The dimensions of the ROI are approximately $\sim|011|\times|211|\times z_{\max}$, which is one periodic spacing in the *x* and *y* directions and spanning the entire simulation box normal to the TB. A larger span was chosen along z to capture far-field average displacement discontinuities introduced by sweeping of a dislocation through the ROI. If the *z* dimension is chosen to be smaller, then the average displacements are marred by the twinning shuffles anti-parallel to the applied shear, and a representative trend is not observed. The difference of average displacement between atoms in the top and bottom twin variants within the ROI is recorded along with the total energy which is normalized against $A_{ROI} \sim|011|\times|211|$. The energy at zero shear strain is taken as the reference datum. The results are shown in figure 28 (iii, iv).

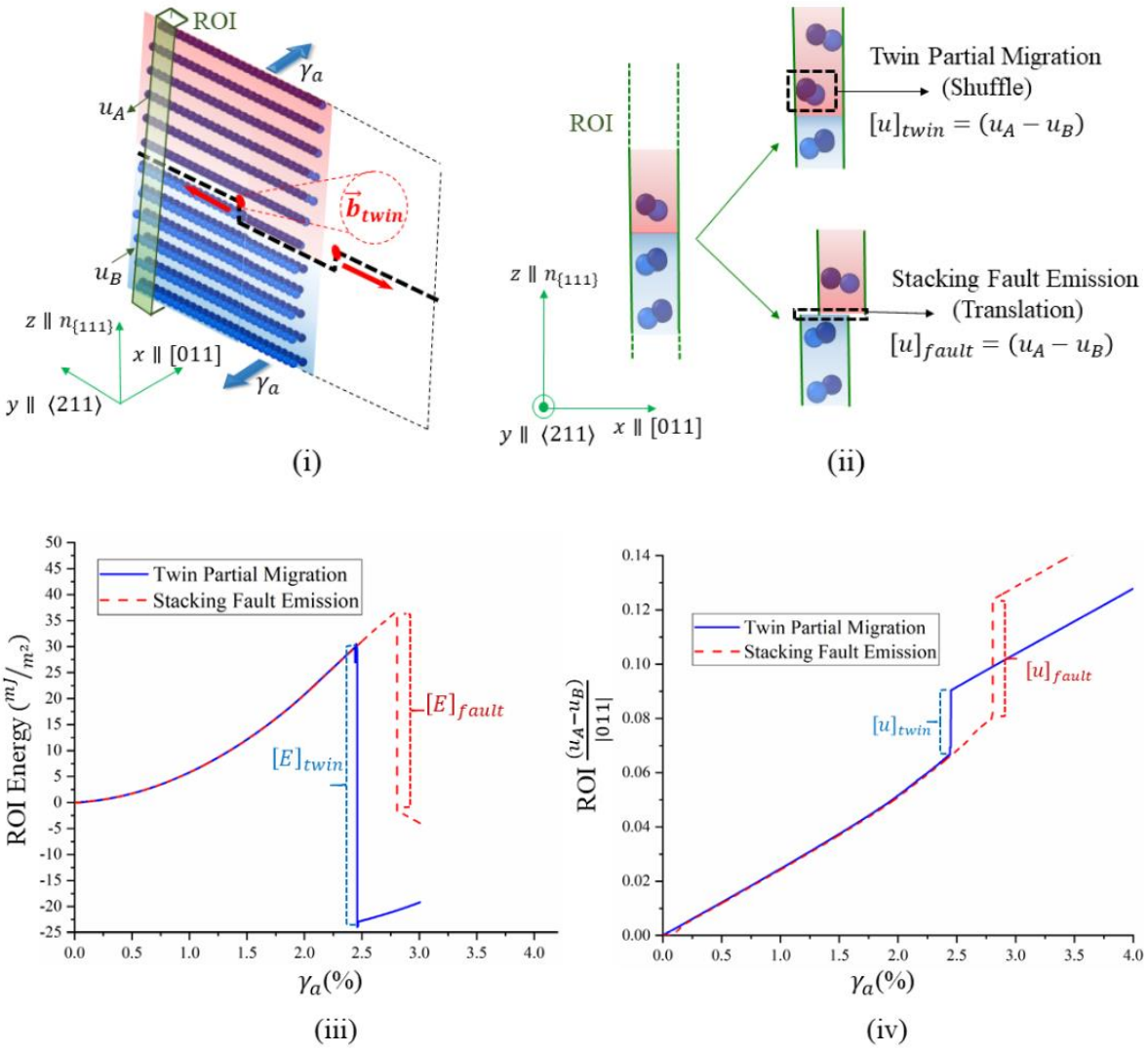

Figure 28: (i) Region of Interest (ROI) to capture relative displacements and energy changes (ii) Snapshots of the central region within the ROI, emphasizing the difference in displacement jumps due to twin partial motion and stacking fault emission (iii) Energy change of ROI, emphasizing jumps $[E]$ (iv) Relative displacement within ROI, emphasizing jumps $[u]$ associated with dislocation motion; note that the jump associated with stacking fault emission is higher than for motion of the twinning partial

There is a sharp discontinuity in displacement (denote as $[u]$) and the energy (denote as $[E]$) in both cases, which is expected when any dislocation sweeps through the ROI. The magnitudes of the displacement jump $[\boldsymbol{u}]$ do not exactly match the dislocation magnitude because of averaging over displacement gradients within the finite span of the ROI. Nonetheless, they

correlate with the dislocation magnitudes and will only be used as a relative measure in this context. It was observed that only the $\langle 011 \rangle$ displacement (aligned with the applied shear) component exhibits appreciable change while the relative displacements in the other directions are minor (lower by atleast one order of magnitude) and shall be ignored. During twin partial motion, the discontinuous jump in displacement (normalized) is approximately $[u]_{twin} \approx 0.025$. Note that there is a shuffle that occurs within the ROI as the partial sweeps through, and the average displacement difference within the ROI is considered here. The energy jump $[E]_{twin} \approx 55 \text{ mJ/m}^2$ also reasonably corresponds with the unstable energy barrier γ_{ut} in the GPFE (refer chapter 2, section 2.2.7). When a barrier is presented and the twin-partial arrests, the first observation is that there is still a displacement jump within the ROI, implying that a dislocation (partial or full) has swept through. The jump is delayed in both the displacement and energy curves, occurring at a higher applied shear strain than in the former case. Note that the magnitude of the displacement jump is nearly twice that of the twinning partial, $[u]_{fault} \approx 0.045$. Still $[u] << |011|$, implying that it cannot be a full dislocation but is a leading partial of a fault within the TB. The energy barrier to be crossed before emission of said fault is higher than in the twinning case by $\approx 10 \text{ mJ/m}^2$, while the energy jump $[E]_{fault} \approx 40 \text{ mJ/m}^2$ is smaller.

Visualizing the changes in the ROI, it is observed that there is a translational disregistry corresponding to the observed displacement discontinuity, and there is no shuffle. Analogous to the previous case, the displacement jump is treated as a measure of the Burgers vector magnitude associated with the fault's leading partial. The emitted partial has a Burgers vector magnitude nearly twice of the twinning partial. This estimate shall be consolidated in the next section. Recall, it was argued before that there is a residual twinning partial of a negative sense emitted in the

reverse direction away from the barrier. These observations agree with the crystallographic conservation laws governing dislocation reactions. In summary, the authors hypothesize the prevalence of the following dislocation reaction at the barrier:

$$\frac{1}{9}[011] \rightarrow \frac{2}{9}[011] - \frac{1}{9}[011] \tag{3.11}$$

This is schematically shown in figure 29. A single twin partial participates in the reaction. The reaction is dissociative in nature and does not occur spontaneously, as will be discussed in the following section. It requires a build-up against a barrier to the detwinning mechanism hindering motion of the participating twin partial.

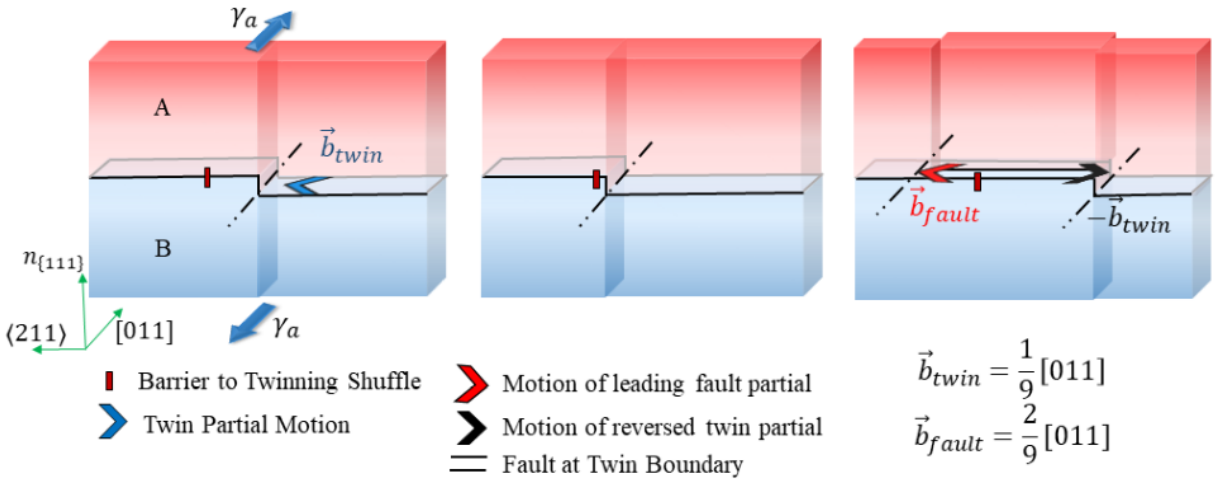

Figure 29: Schematic of the proposed dislocation reaction at the shuffle barrier; From left to right, the twin partial moves under applied shear, stops at the barrier and dissociates into a leading fault partial and a retreating negated twin partial

3.4. Discussion of Simulation Results

3.4.1. Generalized Stacking Fault Energies

Based on the observed atomic motions, a candidate reaction has been proposed. The nature of the emitted partial has been established as having a character of translational disregistry rather than a shuffle. It leads a fault that forms at the TB and has a Burgers vector aligned with the twinning partials, along $[011]$ and no other components. The magnitude was assigned on the

grounds of the displacement jump measured in the ROI and is also consistent with the conservation of Burgers vector, given the participating and residual twinning partials involved in the reaction. To make this more conclusive, a GSFE calculation is carried out at the TB. A rigid relative displacement is introduced between the two variants in the $[011]$ direction, while allowing the atoms to relax (minor atomic motions) in the $\langle 211 \rangle$ and $n_{\{111\}}$ directions. The objective is to determine if there is a local minimum at a relative displacement matching the estimated Burgers vector, explaining the formation of the fault and its corresponding leading partial. The results are shown in figure 30. As expected, an energy minimum corresponding to a stable fault exists at the expected magnitude of the Burgers vector $u/|011| \approx 2/9$. Notice that the magnitude of the corresponding unstable stacking fault energy barrier, γ_{us}^{twin} is only slightly higher than γ_{ut} , the difference being $(\gamma_{us}^{twin} - \gamma_{ut}) \approx 10 \text{ mJ/m}^2$. Also, the energy drop following this peak γ_{us}^{twin} to the fault position is $\approx 45 \text{ mJ/m}^2$ reasonably close to the energy jump $[E]_{fault}$ determined before. Hence, these values are consistent with the difference in energy barriers and displacement jumps crossed within the ROI, shown in figure 28. This correspondence confirms the nature of the fault and the corresponding Burgers vector of the stacking fault partial that is emitted. Note that although there is a preceding energy minimum at $u/|011| \approx 0.13$, it is not a candidate for the emitted fault partial because the residual Burgers vector that would remain after its emission would neither correspond to a negated twin partial, nor any other interface dislocation for the structure. Also, the corresponding energy signatures for this position (unstable fault barrier and the following energy drop) do not match the calculations at the ROI. Hence, the emitted fault partial is $\vec{b}_{fault} = 2/9[011]$.

The residual twin partial that is emitted in the reverse direction also resides on a disconnection. Despite an attractive elastic interaction with the twinning partial on the next successive plane, it wouldn't annihilate with the partial because there is an increasing energy cost associated with the reducing generalized planar fault length between successive twin partials. This energy cost is associated with the impending formation of an unstable 2-layer fault smaller than the stable nucleus for the type II twin in $B19'$ martensite [37]. This is schematically illustrated in figure 31. Eventually, it is proposed that the solitary residual partial along with the rest of the twinning partials on the plane, does not perturb the spacing of disconnections by that much thereby maintaining the effective twinning plane to be nearly the same.

In order to justify that the formation of the fault at the TB, and not within any of the individual variants, a GSFE calculation is repeated within a variant. The results are shown in figure 30. The unstable fault energy barrier $\gamma_{us}^{A}(=\gamma_{us}^{B})$ is significantly higher and no minimum is observed at the expected Burgers vector magnitude. This confirms that the emitted fault resides within the TB, and not within any of the variants.

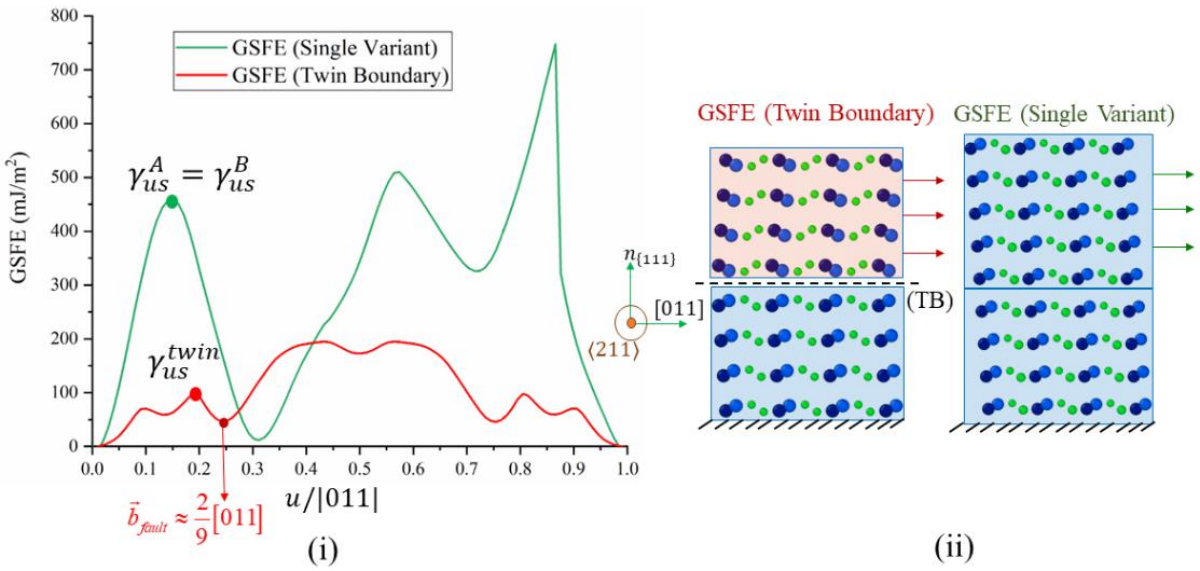

Figure 30: (i) Generalized Stacking Fault Energy (GSFE) curves within a single martensitic variant, and across the TB, reflecting the slip resistance at both positions (the minimum corresponding to the fault partial is indicated) (ii) Schematic showing the procedure to calculate the GSFE curves for both cases

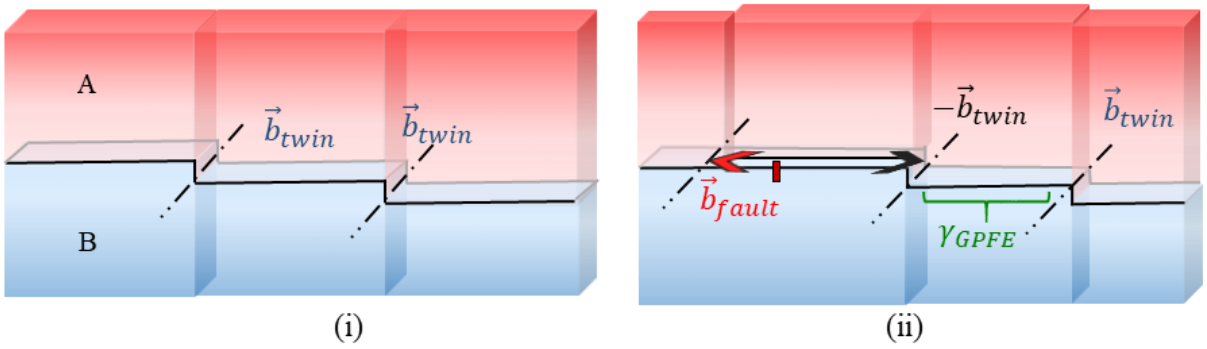

Figure 31: A comparison of the twinning partial arrangement (i) before and (ii) after the dislocation reaction has occurred; the residual twinning partial does not annihilate with the next successive twin partial due to a repulsive component from increasing GPFE value

3.4.2. Energetic feasibility of the proposed reaction

Now, a discussion on the energetics of the dislocation reaction will be addressed. An energy-balance based on Frank's rule makes it obvious that this reaction cannot happen spontaneously. Additional energy-input is required to drive the reaction. In the case of a single-partial, the additional energy is provided by the external load, as observed in the distinct hardening

increment pointed out in figure 27. If there was no barrier, then the stress would have plateaued and done work sufficient to counter the lattice friction for detwinning. However, the fault emission requires a higher stress and corresponding energy influx which is manifested as a hardening in the stress-strain curve. In the case of NiTi, it is observed that the difference $(\gamma_{us}^{twin} - \gamma_{ut}) \approx 10 \text{ mJ/m}^2$ is very small and reflects as a minor hardening in the stress-strain curve before fault emission. This energy parameter quantifies the ease of occurrence of the reaction. Since the reaction is proposed as a source of irreversibility, the energy parameter is proposed as a characteristic physical measure of susceptibility to fatigue across different SMAs.

In this formulation employing a single twin partial, the supplementary energy influx for the reaction is furnished by the external shear. A brief argument outlining the role of elastic interaction between multiple twin-partials on the TB is prudent here. A schematic of the TB geometry is shown in figure 32 (i) indicating the disconnection spacing. The continuum strain energy density per unit area of the TB is estimated against a parametric variation of the disconnection spacing. A representative volume element is chosen as shown in figure 32 (ii). Since there is a twin symmetry, the energy partitioned between each of the variants is identical. Further, the periodic disconnection spacing provides a convenient cell size for the RVE. A large span is chosen normal to the direction of the TB. The strains, and consequently the strain energy density, only vary in the yz plane (figure 25) and hence the energy estimate is normalized per unit length along x, and with the disconnection spacing in y, yielding a planar energy density per unit area of the TB.

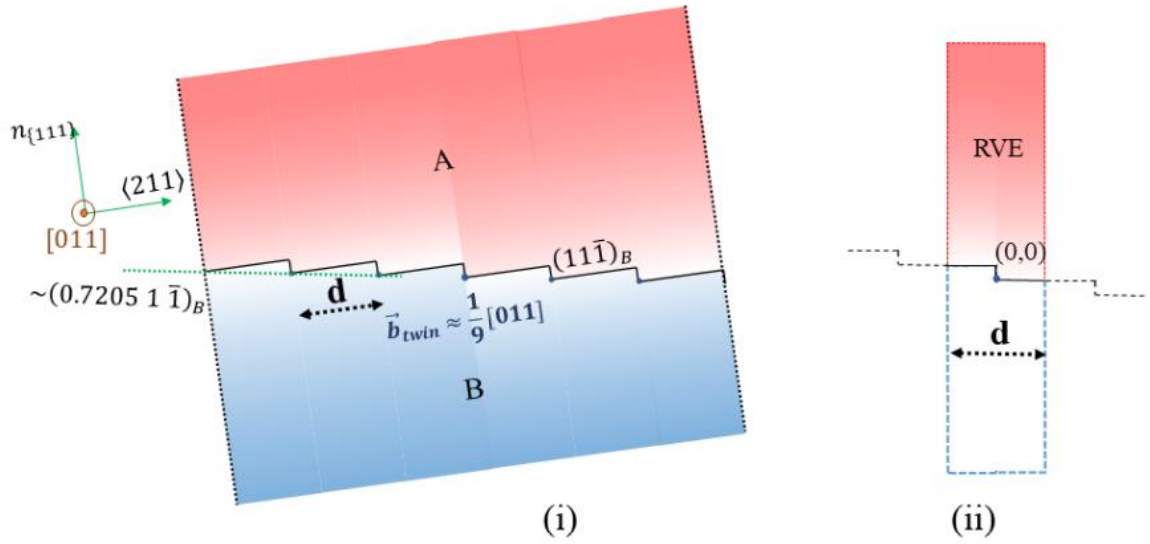

Figure 32: (i) Schematic for the disconnected TB geometry (as suggested in [64]), indicating the $\{111\}$ terraces, the disconnections on which twin-partials reside and the effective plane $\{0.7205\ 1\ \bar{1}\}$ (figure adapted from [139]) (ii) RVE used to calculate the elastic energetics of the disconnected TB

The continuum elastic strain $\boldsymbol{\varepsilon}_{partial}(y,z)$ surrounding an isolated partial are derived from the displacement fields calculated in section 3.2.2.1. Within each RVE, the contribution of strain fields from $N_p = 50$ (needs to be sufficiently large) twin partials on either side are included to approximate the infinitely extending periodically spaced dislocation array on the TB. A crucial catch is that these strain fields are to be superposed over a coherence strain $\boldsymbol{\varepsilon}_{coh}$ (mentioned in section 3.2.1 and elaborated in chapter 2, section 2.2.2) required for atomic registry at the interface. The strain energy density at each point within the RVE is calculated as,

$$\boldsymbol{\varepsilon}(y,z) = \sum_{k=-N_P}^{N_P} \boldsymbol{\varepsilon}_{partial}(y - kd, z + kh_{\{111\}}) + \boldsymbol{\varepsilon}_{coh} \tag{3.12}$$

where $h_{\{111\}}$ is the normal distance between consecutive $\{111\}$ terraces, representing the step height at a disconnection. The planar energy density is calculated as an area integral over the RVE, normalized with the disconnection spacing:

$$E_{twin} = \frac{1}{d} \int_{\text{RVE}} \boldsymbol{\varepsilon}^{\text{T}}(y,z) C_{\text{A}} \boldsymbol{\varepsilon}(y,z) \, \text{dS} \tag{3.13}$$

The integration is done numerically because of the complex analytical forms of the displacement fields of the twin partial (subsection 3.2.2.1). The energy density is plotted against the choice of disconnection spacing, shown in figure 33. There is a competing effect between the dislocation array and the coherence strain. The least energy configuration corresponds to the state when the dislocation array relieves the coherence strain far away from the interface. This minima corresponds to the equilibrium spacing $d = 36.74 \ \overset{0}{\text{A}}$, close to the predictions of [38, 64]. At lower values, the energy is higher due to repulsive interaction between the dislocations. At higher spacing, the energy is higher due to the extended influence of the coherence strain further from the interface. Notice the asymmetry in the gradient of potential energy about the minimum point.

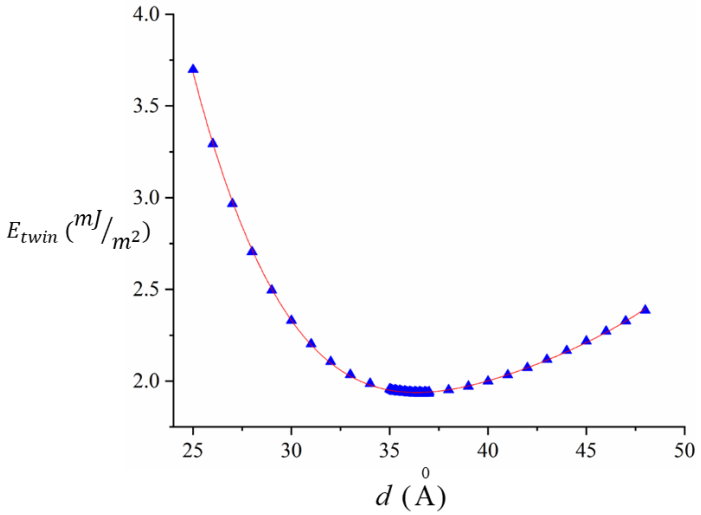

Figure 33: Dependence of $\langle 011 \rangle$ Type II TB energy in NiTi on disconnection spacing

One of the specialties of the Type II system is this behavior of the elastic interaction energy where a further separation of the interface dislocations can also incur a potential energy increase. Thus, any perturbation of the disconnection spacing, either as a build-up (reducing *d*) or a further separation (increasing *d*), can raise the potential energy and provide additional energy influx for the dislocation reaction. And while a theoretical argument for the role of build-up (reducing *d*) was provided in [140], the possible role of the latter behavior (increasing *d*) has not been studied.

The authors would like to mention that the interaction of multiple partials was also attempted within the same MS framework. However, the simulations were unstable, and often found disordered configurational minima. This is attributed to the limited capabilities of the chosen interatomic potential, unable to capture higher-scale micromechanics such as the interactions between partials. Nevertheless, given the repeatability of the observations associated with a single twin partial and supporting results/arguments explaining it, the physical fidelity of the simulated reaction is trusted and proposed as an active mechanism in this system. For an exact discourse on the role of twin-partial build-up, a more formal micromechanical study shall be undertaken as a future endeavor.

3.4.3. The source of irreversibility during transformation: Slip emission

This phenomenon also has fundamental relevance to functional fatigue. The superelastic hysteresis of SMAs is associated with the motion of transformation dislocations within the twinned martensite and the austenite-martensite interface. The lattice frictional barrier that must be overcome by these dislocations during the forward and reverse transformation constitute the energy loss during superelastic cycling. Since the focus is on the TB within martensite, the motion of twinning partials shall be considered. In the absence of any of the aforementioned irreversibilities, the twinning partials move in the forward and reverse directions, migrating the

TB reversibly. The energy dissipation corresponds to the area under the GPFE twin migration curve. In the presence of a barrier and the ensuing dislocation reaction, a higher lattice friction barrier must be overcome for the forward motion of the fault partial. This difference would correlate with the parameter $(\gamma_{us}^{twin} - \gamma_{ut})$, and fundamentally dictate the change in the recoverable hysteresis under superelastic cycling. Further, the emitted slip contributes to the irrecoverable strain that accumulates over multiple cycles.

All these implications arise out of the subtle distinction in structural evolution during twin-partial motion and interaction. It is in understanding this distinction, that the true potential of atomistic simulations has been realized. In the case without a barrier, the twin-partial migrates through a progression shuffles while in face of a barrier, the progression switches to a translation disregistry, forming a fault at the TB. These have been visualized and clarified in figures 26, 28 and 29. This shuffle-translation dichotomy at the TB (refer figure 28 (ii)), the associated Burgers vectors and the energy barriers form the crux of the reaction and its corresponding consequences to mechanical behavior.

The relevance of the proposed reaction in explaining the observed irreversible slip within austenite is explained. The emitted fault partial still resides within the twinned martensite but it is proposed as a precursor to a subsequent dislocation reaction that will emit a perfect dislocation into the austenite phase. In order to build an argument for this, a brief consideration of the morphology of the austenite-martensite (A-M) interface is necessitated. Multiple studies, based on topological modeling, have addressed the presence of transformation dislocations and disconnections on the A-M interface [70, 79, 80]. For the specific case of NiTi, this is still an open problem under study, particularly when it comes to clarifying the meeting point of the twinned martensitic boundary with the A-M habit plane. Drawing from the topological models, a schematic

is presented where the TB meets the A-M interface at a disconnection, shown in figure 34. When there is twin partial migration, it eventually meets the habit plane, and advances the disconnection as shown. Thereby the TB migration and habit-plane motion go hand-in-hand. In the presence of a barrier, and the subsequent occurrence of the proposed reaction, the partial is interrupted and a fault emitted. The residual twin partial of the reaction conserves the twin-boundary morphology in the wake, while the emitted fault disturbs it. As the leading fault partial approaches the disconnection, it is hypothesized that there must be a second reaction that occurs, which leads to an emission of a perfect dislocation in the austenite phase, and a residual partial $-\vec{b}_{fault}$ which restores the fault back to the pristine TB. In contrast to the former case, without any barrier, the disconnection does not advance, but a dislocation is emitted into the austenite phase. Similar to the slip system of the fault partial, the emitted slip dislocation would also agree with the twinning system of martensite, thereby explaining several experimental results on fatigue of SMAs. Nevertheless, this idea, in its current form, is out of scope of the present study and is only proposed as a hypothesis to guide future studies in this direction.

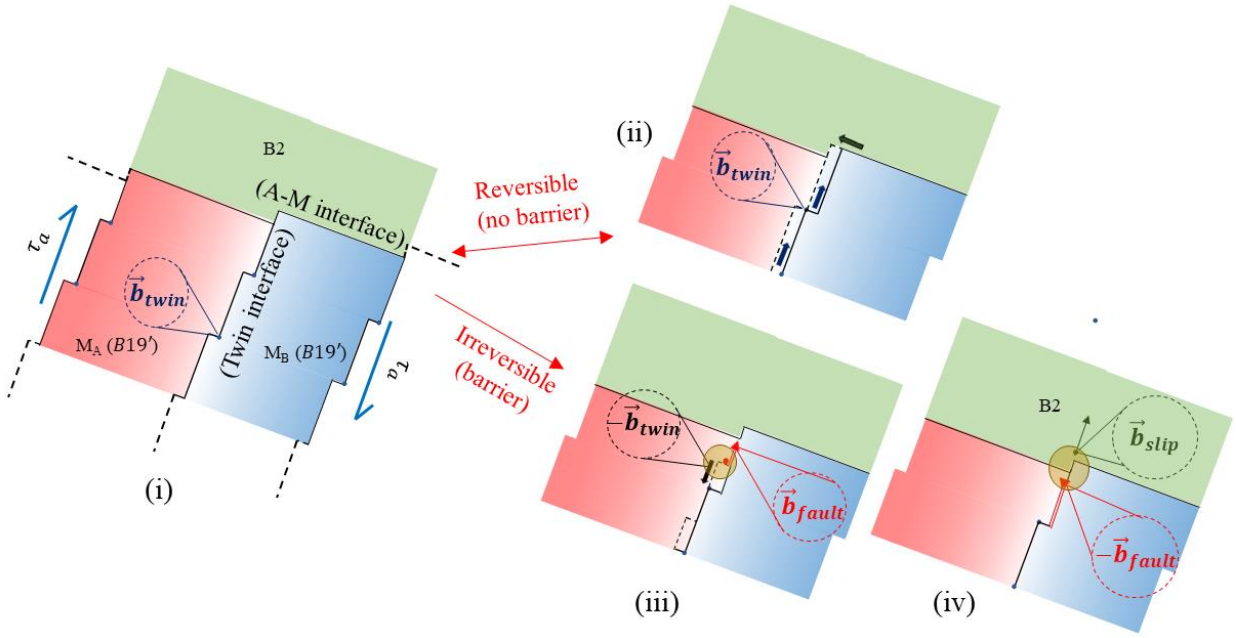

Figure 34: (i) Topology of the martensitic twin interface and the Austenite-Martensite (A-M) interface (ii) Reversible twin partial migration to the A-M interface causing a disconnection advancement (iii) Dissociation of leading partial to form an advancing fault and a receding negated twin partial (analyzed and proposed by this study) (iv) Second dislocation reaction involving the leading fault partial and disconnection hypothesized to emit an austenitic slip dislocation while correcting the stacking fault

In closing, few directions for further research are mentioned. The energetics of the dislocation reaction merits further attention. Apart from clarifying the feasibility of the reaction, it can allow calculation of critical stress levels for the reaction to occur. An estimate of how high this critical stress is, in comparison to the transformation stress levels, can quantify susceptibility to such dislocation irreversibilities. The significance of the energy influx from elastic interaction of multiple twin-partials (section 3.4.2) must be considered. The energy barriers (γ_{us}^{A}, γ_{ut}^{twin}, γ_{us}^{twin}) proposed in this study will be vital atomistic inputs to calculate lattice friction stresses for the dislocations. An ab initio calculation using DFT can provide more reliable estimates for these energy barriers. While the scope of the present study was on one system in NiTi, the approach is more pervasive, providing a framework to analyze such reactions across different SMAs.

3.5. Conclusions

The present study focused on providing a causal explanation of fatigue-activated slip in NiTi SMA. Motivated by the consistent agreement of the slip system with the internal twinning system of martensite, the internal $\langle 011 \rangle$ Type II TB was analyzed. An exploratory study of possible dislocation reactions was undertaken within a framework of atomistic simulations (molecular statics), guided by an early mechanism proposed by Kajiwara [9]. The present study proposes the prevalence of a dislocation reaction during martensitic TB migration. The product dislocation is proposed to be a precursor to austenitic slip emission, so far understood only from an experimental standpoint. The following are the key contributions of this work:

a. The core structure of the twinning partial was constructed by a non-Cauchy-Born enforcement of the continuum displacement fields around the core, within a MS framework. A gradation of shuffles was observed through the core, consistent with the mechanism of detwinning.
b. The disconnected geometry of the TB was constructed within a MS framework, and the partials positioned at the disconnections. Under an applied shear, twin partial motion and subsequent build-up against a barrier was simulated. On the basis of simulation results, a dislocation reaction is proposed where the incoming twin partial dissociates to form a stacking fault on the TB ahead of the barrier. The leading partial of the fault has twice the magnitude of the incoming twin partial, and leaves behind a residual negated twin partial on a disconnection on the TB.
c. The crux of this reaction lies in the dichotomy between twinning shuffles and translational fault disregistry at the twin-boundary. The latter is preferred when there is any barrier

presented to the progression of shuffles. The additional energy influx could be aided by the build-up of twin partials against the barrier.

On the basis of the reaction, a physical parameter that can be used to characterize fatigue susceptibility of SMAs is proposed. The proposed reaction serves as a step toward understanding irreversible fatigue damage mechanisms in SMAs, from first principles. The goal is to lead toward a physics-based fatigue model, furnishing key material parameters that can profoundly affect fatigue behavior and hence real-world performance.

CHAPTER 4: STRAIN-SENSITIVE TWIN INTERFACE EVOLUTION

4.1. Introduction

Crystalline materials majorly constitute the technologically important structural and functional materials of today. The phenomenon of twinning is ubiquitous in this material class encompassing metals [23, 24, 84, 141], ceramics [142], and minerals [99, 143, 144]. The boundaries of twins or Twin Boundaries (TBs) have long been one of the most well-researched crystalline interfaces, serving as a logical starting point to understand other complex interfaces such as grain boundaries, or phase-transformation fronts. Their presence plays an active role in dictating material strength (capable of raising it 4-5 times [145, 146]), fracture-resistance [147], fatigue-resistance (possibly doubling it [148]) and functional performance [139, 149, 150]. Inevitably, this dictates performance in applications spanning multiple domains (e.g. biomedical devices [32], energy-harvesting [151], aeronautics, and space exploration [152]) across multiple scales of operation (from micro-scale actuators to macro-scale strengthening).

The predominant class of twins in structural and functional materials are twins formed by deformation [24, 63, 84], hence named “deformation twins”. These twins form by shear and migrate through diffusionless dislocation-mediated mechanisms [24, 71, 153]. The classical theory of deformation twinning [40] established types of deformation twins based on symmetry relations between the matrix and the twin phases. There are three dominant (also called “classical”) modes, namely:

1. Type I twins: The twin lattice is a reflection of the matrix lattice with the twin boundary K_1 as the mirror plane of symmetry
2. Type II twins: The twin lattice is obtained by a 180-degree rotation of the matrix lattice about the direction of twinning η_1

3. Compound twins: The twin lattice exhibits both symmetry relations above

It is worth mentioning that in cubic structures (FCC, BCC etc.) the only types of twins are compound twins [100]. All three modes will be considered in the present study. Of these classes, the best understood twinning systems are Type I and Compound twins. This is primarily because their TBs are crystallographic planes with rational Miller indices. There is little to no debate surrounding the structure/topology of the TB. On the contrary, there is considerable debate around understanding of Type II TBs and a consensus on its nanostructure is yet to be reached [82, 83, 154, 155]. This is primarily because the TBs have irrational Miller indices and seem to be of a non-crystallographic nature. It is of high importance to gain a complete understanding of Type II TBs as they play a significant role in the mechanical response of several successful functional materials e.g. NiTi [114, 116, 139, 156, 157], NiMnGa [27, 55, 56, 154, 158, 159], CuZnAl [60] etc.

The interface which best exemplifies these challenges in understanding Type II TBs is the $\langle 011 \rangle$ Type II TB in NiTi, an important Shape Memory Alloys (SMA). The classical theory [40] analytically determines the twin plane to be of identity $(0.7205\ 1\ \bar{1})$, a close rational approximant of which is $(34\bar{4})$. Upon experimental discovery [39], the TB closely confirmed this identity, subtending an angle around 10 degrees with the $(11\bar{1})$ plane. It must be noted that the exact indices of the irrational interface (i.e. the exact irrational index value) cannot be fully experimentally determined. Instead, the evidence provides a close confirmation of the theoretically proposed identity of $(0.7205\ 1\ \bar{1}) \approx (34\bar{4})$. It was not until about 20 years later that contrasting evidence was put forth where the indices were proposed to be around $(89\bar{9})$ [38]. The latter observed interface

subtends a much lower angle, about 5 degrees. We note a similar disagreement in experimental results across multiple studies of the time [62, 64, 66, 67], summarized in Figure 35. We clarify that the quoted TEM micrographs in Figure 35 are only representative results from the cited experimental studies [38, 67] where the contrasting identities have been observed and proposed. These quoted micrographs are not the sole basis behind the concluded identities of the interface and the reader is referred to the respective experimental studies [38, 67] (also others [38, 39, 62, 64, 66]) for a more detailed exposition. In parallel with these studies, an advanced theory of interfaces known as Topological Modeling had evolved [70]. To add to the debate, two contrasting topological models currently exist for this interface: (i) a Terrace-Disconnection (T-D) model reproducing indices $(89\bar{9})$ (Figure 35(c)), recently proposed by the authors [155] and (ii) a Tilt-Wall model (T-W) (Figure 35(d)) reproducing the indices $(0.7205\ 1\ \bar{1})$ [83]. At present, after nearly 4 decades, a consensus on the nanostructure is yet to be reached.

The present study first addresses this debate and compares both proposed nanostructures based on energies on two scales: meso-scale continuum strain-energies and sub-nano-scale atomistic potential energies. The anisotropic Eshelby-Stroh formalism [129] is employed for continuum calculations and Molecular Statics is employed within the LAMMPS [88] framework for atomistic simulations. It will be shown that one of the nanostructures is energy-minimal and will be proposed as the preferred Type II TB structure. Subsequently, an "Evolving Interface" theory is developed within a linear-elastic framework emphasizing that it is energetically favorable for the proposed nanostructure to evolve depending on microstructural strain and local twin volume fraction. Consequently, we stake that the experimental observations that establish competing interface identities are in fact observations of the same nanostructure at different

evolved states. The proposed evolving behavior is extended to $(11\bar{1})$ Type I and (001) Compound TBs in NiTi [33], proposing its prevalence in all major deformation twin modes.

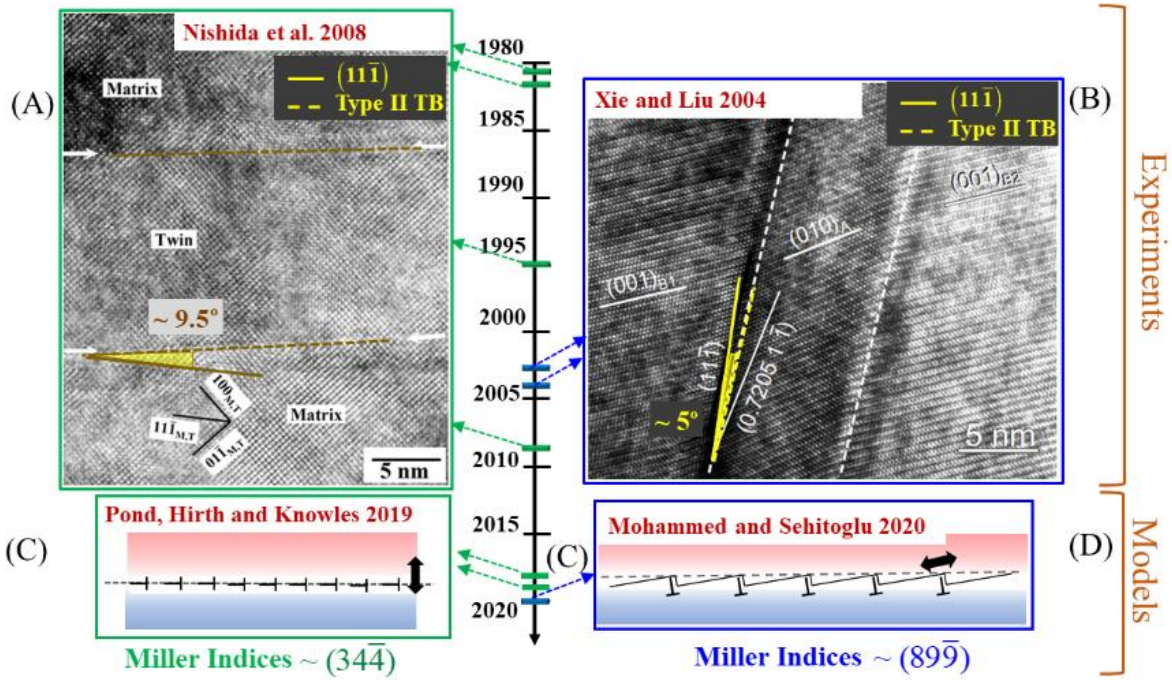

Figure 35: A debate over three indices across four decades: (a) Experimental evidence from [67] proposing indicial identity as $(0.7205\ 1\ \bar{1}) \approx (34\bar{4})$. (b) Contrasting experimental evidence from [38] proposing the interface to be closer to $(89\bar{9})$, exhibiting a trace distinct from $(0.7205\ 1\ \bar{1})$. (c) Tilt-Wall (T-W) interface model corroborating the suggested identity in (a); the dislocations reside on consecutive (011) planes nearly normal to the interface. (d) Terrace-Disconnection (T-D) model corroborating proposed identity in (b); the terraces are $(11\bar{1})$ planes separated by periodically spaced dislocations/disconnections (In (c, d), dashed line represents the effective interface and double-arrow represents the direction of dislocation glide; blue/green arrows indicate the time of other experimental/analytical research [62, 64, 66, 82, 83, 155] corroborating one of the two interface nanostructures).

4.2. Modeling methodology and Results

The modeling methodology is presented concurrently with the results. The first two sub-sections are focused on evaluating the atomistic potential energy and continuum strain energy of both Type II nanostructural models proposed till date (refer Figure 35). The final sub-section

outlines the theory used to predict the evolution/change in nanostructure in response to external strain, for changing twin volume fractions. This theory will be used to explain the experimental observations of the $\langle 011 \rangle$ Type II TB in NiTi. It is further applied to the Type I and Compound TBs (specifically $\{111\}$ Type I and $\{001\}$ Compound TB in NiTi) to show general applicability to deformation TBs.

4.2.1. Evaluation of atomistic potential energies for both Tilt-Wall (T-W) and Terrace-Disconnection (T-D) nanostructures

We first evaluate potential energies on a sub-nano scale where continuum methods do not apply. The atomic structures were constructed and equilibriated using a Molecular Statics (MS) approach in LAMMPS [88], utilizing an interatomic potential developed in the authors' group [94]. The potential is capable of reproducing cohesive energies of multiple phases of NiTi (B2, B19, B19') close to that predicted by ab initio Density Functional Theory (DFT) [94], and is preferred for the study. First, the atomistic evaluation of the T-W is considered. The atomic structure can be constructed by positioning the crystals of the two twin variants to meet on the $(34\bar{4})$ plane, which is a close rational approximant to the irrational $(0.7205\ 1\ \bar{1})$ plane. The tilt misorientation between the two crystals is introduced by way of construction in their respective orientations [160]. The lattice constants and motif positions of atoms inside the unit cell are picked consistent with the interatomic potential [94]. The twin and the matrix lattices are oriented to have specific directions aligned with the global *x-y-z* axes ($\vec{e}_x, \vec{e}_y, \vec{e}_z$ unit vectors) of the simulation box. For the twin, we align the following directions: $\vec{e}_x \| [011]$, $\vec{e}_y \| [\bar{8}3\bar{3}]_{\mathrm{T}}$ and $\vec{e}_z \| n_{(\bar{3}\bar{4}4),\mathrm{T}}$. For the matrix, we align the directions as $\vec{e}_x \| [011]$, $\vec{e}_y \| [8\bar{3}3]_{\mathrm{M}}$ and $\vec{e}_z \| n_{(34\bar{4}),\mathrm{M}}$, ensuring the Type II twin

symmetry. The subscripts T or M indicate that the crystallographic directions are referenced to the unit cell lattice vectors in the twin or the matrix respectively. The $[011]$ direction (which is the twinning direction η_1 for the Type II TB) of the twin and the matrix are aligned. Let C_{LAT} represent a 3x3 matrix whose columns give the *x*-*y*-z components of the lattice vectors of the unit cell. Then for the twin and matrix phases, we have:

$$C_{LAT}^{T} = \begin{pmatrix} -0.1165 & 3.0248 & 3.3354 \\ -1.9885 & 2.0474 & -2.0474 \\ -1.8213 & -2.4284 & 2.4284 \end{pmatrix}; C_{LAT}^{M} = \begin{pmatrix} -0.1165 & 3.0248 & 3.3354 \\ 1.9885 & -2.0474 & 2.0474 \\ 1.8213 & 2.4284 & -2.4284 \end{pmatrix} \quad (4.1)$$

There are additional considerations in the creation of the simulation box, namely the absence of a crystallographic twin plane and the necessity of a lattice offset. The underlying analysis and methods of calculation are elaborated in section 4.2.2 that follows. Given that the *x* and *y* directions are crystallographic, periodic boundary conditions are chosen for the lateral boundaries (across *xz* and *yz* planar boundaries of the simulation box). Note that the *z* direction is not a rational crystallographic direction as it is the normal to the $(34\bar{4})$ plane, i.e. $\vec{e}_z \parallel n_{(34\bar{4}),\mathrm{M}}$, and not the direction $[34\bar{4}]$. Consequently, we do not apply periodic boundary conditions along z and shrink-wrapped conditions are employed across this boundary. On the top and the bottom, a layer of width $6\,\text{Å}$ (higher the potential's cut-off value $r_c = 5.2\,\text{Å}$) is frozen in position with the assumption that the atoms farther away from the twin boundary are representative of the bulk structure in the twin/matrix phases and are relatively unaffected by the relaxation. Having constructed the structure and specified these conditions, the conjugate gradient relaxation scheme in LAMMPS is employed specifying the tolerance for energy convergence as 1.0×10^{-8} (fractional change of energy between successive iterations should be lower than this value for convergence). Representative snapshots

of the unrelaxed and relaxed structures are presented in figure 36(a). The atomistic potential energy of the T-W model is calculated as 4.19 J/m^2 and is quoted later in table 6.

For the T-D model, the energy evaluation is two-step. First is the determination of the relaxed potential energy of the $(11\bar{1})$ terraces. Second is the augmentation of this value with the core energy of a twinning disconnection. The energy of the $(11\bar{1})$ terrace is determined identical to that of the $(34\bar{4})$ plane described above. The orientation of the twin variant is chosen such that $\vec{e}_x \| [011]$, $\vec{e}_y \| [\bar{2}1\bar{1}]_\mathrm{T}$ and $\vec{e}_z \| n_{(\bar{1}\bar{1}1),\mathrm{T}}$. For the matrix, we align the directions as $\vec{e}_x \| [011]$, $\vec{e}_y \| [2\bar{1}1]_\mathrm{M}$ and $\vec{e}_z \| n_{(11\bar{1}),\mathrm{M}}$, ensuring the Type II twin symmetry. Since the *x* and *y* directions are crystallographic, periodic boundary conditions are enforced along them (i.e. across the *xz* and *yz* planar boundaries of the simulation box). The *z* direction is not a rational crystallographic direction as it is normal to the $(11\bar{1})_\mathrm{M}$ plane, i.e. $\vec{e}_z \| n_{(11\bar{1}),\mathrm{M}}$, and not the rational direction $[11\bar{1}]_\mathrm{M}$. We do not apply periodic boundary conditions along *z* and shrink-wrapped conditions are employed instead.

A key aspect in this crystallography is that with the $[011]$ directions of both variants aligned, the vectors $[\bar{2}1\bar{1}]_T$ and $[2\bar{1}1]_M$ do not align. An in-plane shear γ_{xy} coherence strain must be applied to have the directions aligned such that $\vec{e}_y \| [2\bar{1}1]_\mathrm{M} \| [\bar{2}1\bar{1}]_\mathrm{T}$. This is described in detail in [155] and a further discussion is not necessary for the purposes of this study. The unit cell lattice vectors of the coherently strained lattices required for the chosen orientation on the $\{111\}$ terrace is given by the matrices:

$$C_{LAT}^{T}=\begin{pmatrix}-0.1326 & 3.0475 & 3.3127\\ -1.6954 & 2.3858 & -2.3858\\ -2.0968 & -2.0968 & 2.0968\end{pmatrix};C_{LAT}^{M}=\begin{pmatrix}-0.1326 & 3.0475 & 3.3127\\ 1.6954 & -2.3858 & 2.3858\\ 2.0968 & 2.0968 & -2.0968\end{pmatrix} \quad (4.2)$$

Note that a similar consideration was not necessary in the T-W model because the shear-mismatch between $\left[\bar{8}3\bar{3}\right]_T$ and $\left[8\bar{3}3\right]_M$ is found to be negligibly small i.e. $\gamma_{xy}\approx 0$. The same boundary conditions and relaxation routines mentioned before are followed. Representative snapshots of the unrelaxed and relaxed structures are presented in figure 36(b). The atomistic potential energy of the $\left(11\bar{1}\right)$ terrace in the T-D model is calculated as 2.424 J/m^2. A detailed account of constructing the twinning disconnection for the T-D structure can be found in chapter 3 and is briefly presented here (also refer [139]). It is done by assembling two $\left(11\bar{1}\right)$ terraces side by side (along $y\parallel\langle 211\rangle$) with the terraces separated along *z* by one interplanar spacing ($d_{\{111\}}=2.097\,\text{Å}$). Then the anisotropic displacement field of an isolated twinning dislocation (calculated using the Eshelby-Stroh formalism as described in section 4.2.2 and 4.2.3) are superimposed around the core. The structure is relaxed under governance of the interatomic potential to yield the equilibrium core structure of the twinning disconnection. This is represented in figure 36(c), only showing the positions of the Ti-atoms for clarity. The Ti-atoms are color-coded in a specific way (refer [139] for further details) to emphasize the disconnection. A supplementary video file (*VideoSuppl_TwinDisconMotion.mp4*) is also provided to show the simulated motion of the disconnection under external shear. The potential energy of the core is determined from selection of atoms within a cylinder around the center of the disconnection (axis aligned with the dislocation line) bounded by a radius slightly over $R=5|b_{TD}|$. If sampling a

larger radius it must be remembered that contributions from strain-energy of the dislocation will also contribute to the energy. Since the continuum evaluation (refer 4.2.4) is done independent of this atomistic evaluation, the choice of a large radius is not necessary. The core-energy of the twinning disconnection contributes 0.264 J/m^2 to the atomistic energy of the T-D nanostructure. In total, the atomistic potential energy of the T-D nanostructure comes out to be 2.69 J/m^2 as quoted in table 6.

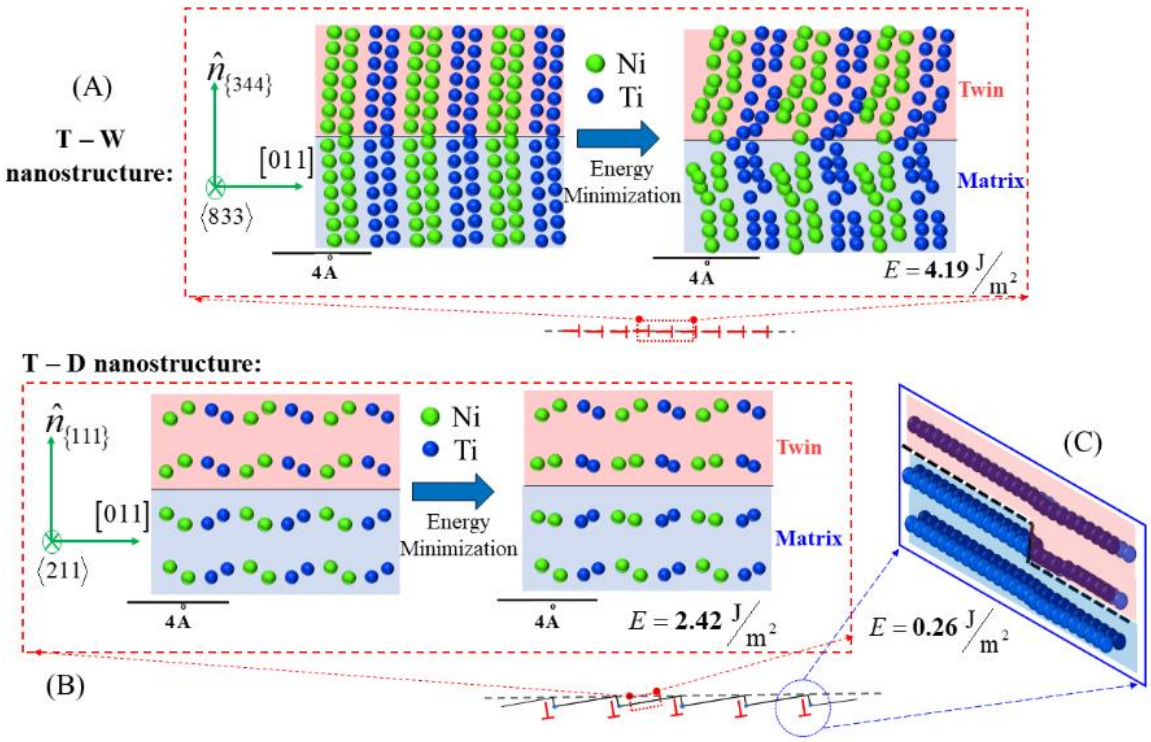

Figure 36: Determining atomistic potential energies of T-W and T-D topologies: (a) Atomic structure of the T-W topology showing the as-constructed (unrelaxed) and energy-minimized (relaxed) structures. (b) Atomic structure of the T-D topology showing the as-constructed (unrelaxed) and energy-minimized (relaxed) $\{111\}$ terrace structure and (c) atomic structure of a disconnection on the T-D nanostructure (only showing Ti atoms which are color-coded to emphasize the location of the disconnection, refer [139] for more details).

4.2.2. Construction of T-W Twin Boundary structure for atomistic simulation

This section outlines the construction of atomic structures for the atomistic simulations described in section 4.2.1. The unit cell lattice constants and motif positions are chosen consistent with the interatomic potential [94]. Figure 37 represents the unit cell, where a Ti atom is chosen on the lattice site and the remaining motif atoms are positioned accordingly. The lattice constants are $a = 2.699\ \text{Å}; b = 4.386\ \text{Å}; c = 4.606\ \text{Å}; \beta = 93.41^{o}$, with the motif positions given in fractional coordinates (along the unit cell crystallographic directions): Ti $(0,0,0)$, Ti $(0.3413, 0.5, 0.6973)$, Ni $(0.6768, 0.5, 0.2067)$ and Ni $(0.6645, 0, 0.4906)$.

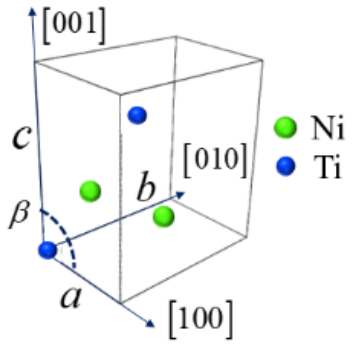

Figure 37: Unit cell of B19' NiTi martensite; The lattice constants and motif positions are chosen consistent with the interatomic potential [94] used for atomistic simulations.

Now we detail the construction of the T-W structure. We start with the simulation box in Figure 38 (a) with global axes *x-y-z* (unit vectors ($\vec{e}_x, \vec{e}_y, \vec{e}_z$) unit vectors) of the simulation box. The dimensions of the simulation box are specified in LAMMPS by a start and end coordinate. We define them as $(0, x_{\max})$, $(0, y_{\max})$, $\left(-z_{\max}/2, z_{\max}/2\right)$. The normal to the twin boundary is chosen to be parallel to the z-axis, i.e. $\vec{e}_z \parallel n_{\{34\bar{4}\}}$. The choice of the z-axis limits is made with the notion of having the twin boundary at position $z = 0$. Hence, the twin variant is constructed in the region defined by the limits: $(0, x_{\max})$, $(0, y_{\max})$, $\left(0, z_{\max}/2\right)$. And the matrix is constructed in the

region defined by the limits: $(0, x_{\max})$, $(0, y_{\max})$, $\left(-z_{\max}/2, 0\right)$. For the twin, we align the following directions: $\vec{e}_x \| [011]$, $\vec{e}_y \| [\bar{8}3\bar{3}]$ and $\vec{e}_z \| n_{(\bar{3}\bar{4}4)}$. For the matrix, we align the directions as $\vec{e}_x \| [011]$, $\vec{e}_y \| [8\bar{3}3]$ and $\vec{e}_z \| n_{(34\bar{4})}$. The dimensions of the simulation box are chosen to be $x_{\max} = 8L_{\langle 011 \rangle} = 50.88$ Å, $y_{\max} = 2L_{\langle 833 \rangle} = 56.38$ Å and $z_{\max} = 2L_{\langle 344 \rangle} = 49.62$ Å, where $L_{\langle uvw \rangle}$ represents the periodic lattice distance along any crystallographic direction in the family $\langle uvw \rangle$. The number of atoms in the simulation is $N \approx 10{,}500$, sufficiently large for the purposes of the study. The orientation of the lattice vectors required to achieve this crystallographic alignment is given by the $C_{LAT}^{T,M}$ matrices in equation (4.1). A more detailed description to calculate these matrices can be found in chapter 2. The final parameter to be defined to complete construction of the twin is the *origin* of the twin and matrix regions in the simulation box. The origin simply specifies the position of a lattice site in the simulation box. It is used to specify the position of the lattice in the global coordinate system attached to the simulation box. The origin is specified in normalized coordinates $\left(\bar{x} = x/|011|, \bar{y} = y/|833|, \bar{z} = z/|344|\right)$, where the normalization is done using the periodic lattice distance along the chosen axes. Hence, given the translational symmetry of the lattice over periodic lattice distances, origin values only in the range $(0 \le \bar{x} < 1, 0 \le \bar{y} < 1, 0 \le \bar{z} < 1)$ define unique positions of the lattice. Given that we want to create a twin and a matrix (i.e. two crystal lattices), we need to specify two origins. If the origins of both lattices are coincident, then there is no *lattice offset* between the two lattices. If the difference of origins is non-zero, then there exists a non-zero lattice offset between the two lattices. The concept of a lattice offset has long been known [24, 71, 101, 102] and its necessity for the Type II TB has

been discussed in detail in chapter 2. It is only briefly described here, as much is necessary to construct the atomic structure of twin-boundaries in this study. The origin of the matrix variant is chosen such that the no atoms lie on the partitioning twin boundary at $z = 0$. This is shown in Figure 38(b). This choice is consciously made because the twin-boundary is not a crystallographic plane accommodating atoms from both variants. The fundamental reason behind this is the incommensurate atomic structures of the two twin variants which cannot be reconciled to form a common atomic plane at the twin boundary. Once again, this has been discussed in detail in [155] and a further discussion is out of scope for the study and avoided here. The origin of the matrix is chosen as $O_M(0, 0, z_\varepsilon = 0.3)$. This choice of z_ε is not unique and another value can be chosen accordingly as long as it is ensured that the twin boundary is not a crystallographic plane with atoms. If the origin of the twin is chosen such that $O_T = O_M$, then there is no lattice offset. However, it is shown in [155] that there is a necessity for a non-zero lattice offset from crystallographic and energetic considerations. Following the procedure detailed in that study, the energy-minimizing lattice-offset for the twin variant can be calculated as $O_T - O_M = (0.688, 0.038, 0.006)$. The constructed twin-variant is shown in Figure 38(c), and the relative position of both origins are shown in Figure 38(d) to highlight the lattice offset. This is the atomic structure used in the simulation of the T-W model in section 4.2.1.

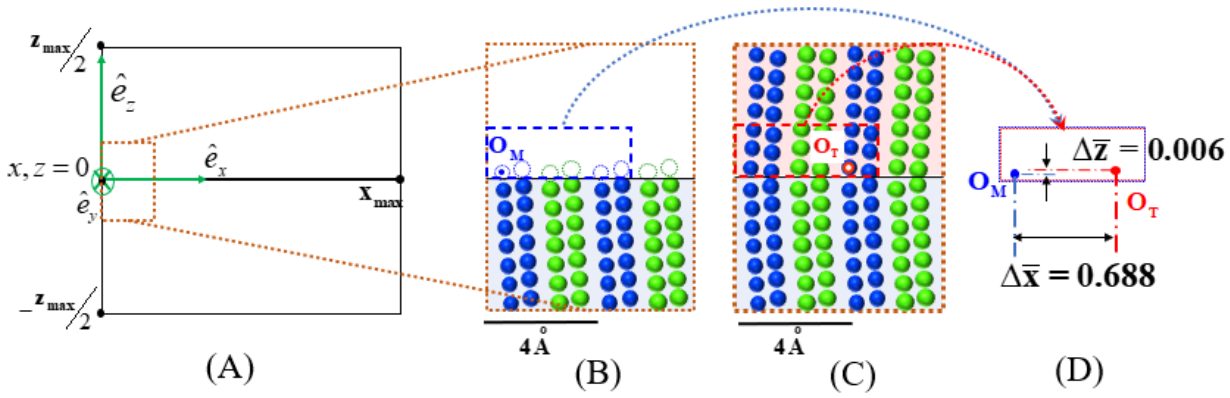

Figure 38: Construction of T-W atomic-structure involving lattice offsets: (a) The simulation box is schematically represented with a boundary partitioning the matrix and twin variants. (b) The matrix is constructed by specifying origin O_M (only positive values of the origin are allowed, as defined in LAMMPS; the origin only specifies the relative position of the lattice inside the simulation box and the matrix atomic structure is only created below the twin boundary as intended). (c) The twin is constructed by specifying origin O_T. (d) Overlapped regions of the matrix and twin highlighting the lattice offset $O_T - O_M$; only the x-z offsets can be shown in this 2D projection and it must be noted that there is a y-offset involved as well.

4.2.3. Calculation of Eshelby-Stroh constants to determine continuum strain-fields

In this section, we briefly outline the equations used to solve for the Eshelby-Stroh constants that are involved in determination of the strain-field and strain-energies of both nanostructures (in section 4.2.1). The constants $(p_\alpha, A_{i\alpha}),\ (\alpha = 1,2,...,6)$ are obtained by solving equilibrium equations in both the phases. In the matrix phase for instance, we must have:

$$\sigma^M_{ij,j} = C^M_{ijkl} u^M_{k,lj} = 0 \tag{4.3}$$

This reduces to a set of algebraic equations given by,

$$C^M_{ijkl}(\mathrm{m}_i + p^M_\alpha \mathrm{n}_i)(\mathrm{m}_l + p^M_\alpha \mathrm{n}_l) A^M_{k\alpha} = 0 \tag{4.4}$$

And to have a non-trivial solution for $(p^M_\alpha, A^M_{i\alpha})$, it follows that:

$$\det\{C^M_{ijkl}(\mathrm{m}_i + p^M_\alpha \mathrm{n}_i)(\mathrm{m}_l + p^M_\alpha \mathrm{n}_l)\} = 0 \tag{4.5}$$

For each p_α^M , we obtain a vector $A_{k\alpha}^M (k=1,2,3)$ from equation **(3.4)**. These complex constants appear as three conjugate pairs (i.e. three conjugate pairs in p_α and three conjugate vector pairs in $A_{k\alpha}$). It will be assumed henceforth that the constants are ordered such that the complex constants with positive imaginary parts have indices $\alpha = 1,2,3$, with their respective conjugates having indices $\alpha = 4,5,6$. The E_α constants for each phase are solved for by enforcing traction and displacement continuity across the slip plane. On the half-plane where $(\hat{n}.\mathbf{x}) = 0$ and $(\hat{m}.\mathbf{x}) > 0$, continuity of displacements and tractions are enforced through the following equations respectively:

$$\sum_{\alpha=1}^{6} A_{i\alpha}^T E_\alpha^T - \sum_{\alpha=1}^{6} A_{i\alpha}^M E_\alpha^M = 0 \qquad \text{(i=1,2,3)} \tag{4.6}$$

$$\sum_{\alpha=1}^{6} L_{i\alpha}^T E_\alpha^T - \sum_{\alpha=1}^{6} L_{i\alpha}^M E_\alpha^M = 0 \qquad \text{(i=1,2,3)} \tag{4.7}$$

For the half-plane where $(\hat{n}.\mathbf{x}) = 0$ and $(\hat{m}.\mathbf{x}) < 0$, a displacement jump associated with the Burgers vector is to be enforced as a discontinuity, while maintaining equality of tractions. This is respectively enforced by:

$$\sum_{\alpha=1}^{6} \eta_\alpha A_{i\alpha}^T E_\alpha^T + \sum_{\alpha=1}^{6} \eta_\alpha A_{i\alpha}^M E_\alpha^M = 2b_i \qquad \text{(i=1,2,3)} \tag{4.8}$$

$$\sum_{\alpha=1}^{6} \eta_\alpha L_{i\alpha}^T E_\alpha^T + \sum_{\alpha=1}^{6} \eta_\alpha L_{i\alpha}^M E_\alpha^M = 0 \qquad \text{(i=1,2,3)} \tag{4.9}$$

where, $\eta_\alpha = 1$ for $\alpha = 1,2,3$ and $\eta_\alpha = -1$ for $\alpha = 4,5,6$, and $L_{i\alpha}$ is given by

$$L_{i\alpha}^M = -n_j C_{ijkl}^M (\mathrm{m}_l + p_\alpha^M \mathrm{n}_l) A_{k\alpha}^M \tag{4.10}$$

The elastic constants are picked consistent to those reproducible by the interatomic potential [94]. For the T-D model, the Burgers vector is $\vec{b}_{TD} = [0.7066\ 0\ 0]\ \overset{0}{\text{A}}$ [155] whereas for the T-W model it is $\vec{b}_{TW} \approx [0\ 0\ 0.86]\ \overset{0}{\text{A}}$ [83] in the respective chosen coordinate frame. The Eshelby-Stroh constants for the T-D and T-W dislocations are given in Tables 4 and 5 respectively (here $i = \sqrt{-1}$). The twin symmetry offers some simple relations between the constants.

Table 4: Eshelby-Stroh Constants for T-D interface dislocation

$p_1^T = p_1^M$	-0.3273+1.3438i	$E_1^T = -E_1^M$	-0.2204+0.0154i
$p_2^T = p_2^M$	-0.3091+0.9710i	$E_2^T = E_2^M$	0.3171-0.0462i
$p_3^T = p_3^M$	0.2313+0.7117i	$E_3^T = -E_3^M$	0.0848+0.0174i
$p_4^T = p_4^M$	-0.3273-1.3438i	$E_4^T = -E_4^M$	0.2204+0.0154i
$p_5^T = p_5^M$	-0.3091-0.9710i	$E_5^T = E_5^M$	-0.3171-0.0462i
$p_6^T = p_6^M$	0.2312-0.7117i	$E_6^T = -E_6^M$	-0.0848+0.0174i

Table 5: Eshelby-Stroh Constants for T-W interface dislocation

$p_1^T = -p_4^M$	0.4988+1.1532i	$E_1^T = E_4^M$	-0.2453+0.3714i
$p_2^T = -p_5^M$	-0.5180+0.8425i	$E_2^T = E_5^M$	0.4509+0.1573i
$p_3^T = -p_6^M$	0.1543+0.8272i	$E_3^T = -E_6^M$	-0.6041+0.1865i
$p_4^T = -p_1^M$	0.4988-1.1532i	$E_4^T = E_1^M$	0.2453+0.3714i
$p_5^T = -p_2^M$	-0.5180-0.8425i	$E_5^T = E_2^M$	-0.4509+0.1573i
$p_6^T = -p_3^M$	0.1543-0.8272i	$E_6^T = -E_3^M$	0.6041+0.1865i

The displacement-field of $\vec{b}_{TD}$ is plotted in Figure 39 (b). The displacement component $u_1(\mathbf{x})$ is plotted as it is the major component of the screw-dislocation $\vec{b}_{TD} = [0.7066\ 0\ 0]$ $\overset{0}{\text{A}}$, in the T-D model. The triad of vectors $\hat{t} - \hat{m} - \hat{n}$ used in the formalism (here and in section 4.2.4) is indicated in the plot. In Figure 39(c), the expression for the far-field displacement-gradient from the dislocation array can be derived as $\left(\frac{\vec{b}}{2d} \otimes (-\hat{m})\right)$ (in the twin region).

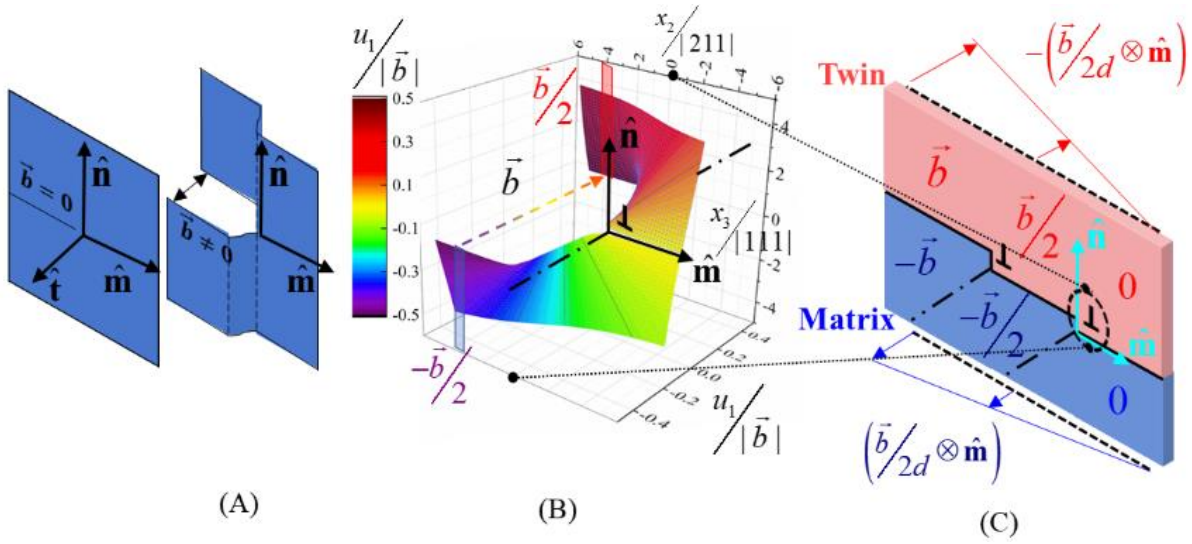

Figure 39: Plot of anisotropic displacement-field of T-D twinning dislocation and far-field displacement-gradient caused by a periodic dislocation array: (a) Schematized screw-dislocation indicating the displacement discontinuity caused by a non-zero Burgers vector; the coordinate system triad $\hat{t} - \hat{m} - \hat{n}$ involved in the Eshelby-Stroh formalism (used in this section 4.2.5, section 4.2.4 and 4.2.6) is indicated; note that $\hat{m}$ points away from the dislocated half-space (figure adapted from [139]). (b) A plot of the $u_1(\mathbf{x})$ displacement component of the $\vec{b}_{TD}$ dislocation calculated from the Eshelby-Stroh formalism outlined in this section 4.2.5; the displacement disregistry sustained by the twin variant is $\vec{b}/2$ (with small spatial variations) and that sustained by the matrix is $-\vec{b}/2$ (figure adapted from [139]). (c) A notional derivation of the far-field displacement-gradient introduced by a periodic array of interface disconnections with Burgers vector $\vec{b}$, spaced at a distance d along $\hat{m}$; Arbitrarily choosing a reference region with zero displacements, the displacement-continuity introduced by each dislocation over its adjacent periodic spacing is augmented; this effectively translates to a far-field shear displacement gradient derived as $-\left(\frac{\vec{b}}{2d} \otimes \hat{m}\right)$ in the twin and $\left(\frac{\vec{b}}{2d} \otimes \hat{m}\right)$ in the matrix

This derivation is based on the simple notion that displacements are increasing by $\vec{b}$ for every *d* spacing, as we traverse along the vector $(-\hat{m})$. The term indicated is the major contributor to the far-field displacement gradient from the dislocation-array. There is a second-term involving the anisotropic Eshelby-Stroh constants (equation (4.14)), is known to be atleast an order lower in comparison to $\left(\frac{\vec{b}}{2d}\otimes(-\hat{m})\right)$ (refer section 4.2.4).

4.2.4. Evaluation of continuum strain energies for both Tilt-Wall (T-W) and Terrace-Disconnection (T-D) nanostructures

Both the T-D and T-W nanostructural models consist of an array of interface dislocations. The strain-field of isolated interface dislocations must first be determined. The matrix and twin phases are constituted by the highly anisotropic monoclinic $B19'$ phase of NiTi. Hence, the Eshelby-Stroh formalism [129] is applied with the theory of anisotropic strain-fields of interface dislocation arrays [161]. The coordinate system is defined by a triad of vectors $\hat{t}-\hat{m}-\hat{n}$, where $\hat{t}\,\|\,[011]_{\mathrm{M}}=[011]_{\mathrm{T}}, \hat{m}\,\|\,[2\bar{1}1]_{\mathrm{M}}=[\bar{2}1\bar{1}]_{\mathrm{T}}, \hat{n}\,\|\,n_{(11\bar{1}),\mathrm{M}}=n_{(\bar{1}\bar{1}1),\mathrm{T}}$ for the T-D model and $\hat{t}\,\|\,[\bar{8}3\bar{3}]_{\mathrm{M}}=[8\bar{3}3]_{\mathrm{T}}, \hat{m}\,\|\,[011]_{\mathrm{M}}=[011]_{\mathrm{T}}, \hat{n}\,\|\,n_{(34\bar{4}),\mathrm{M}}=n_{(\bar{3}\bar{4}4),\mathrm{T}}$ for the T-W model. The choice of this triad is not arbitrary but follows a certain convention in the Eshelby-Stroh formalism [129]. By convention, we choose $\hat{m}$ to be on the slip plane pointing away from the direction of the dislocated half-space (of the interface twinning dislocation). Secondly, $\hat{n}$ is chosen to point from the matrix to the twin, i.e. the slip plane normal pointing toward the dislocated half-space (refer Figure 39 in section 4.2.3). In this system, the displacement-field u_i $(i=1,2,3)$ (and consequently the strain-field) is defined by a set of complex constants given by the expressions:

$$u_i^T(\mathbf{x}) = \frac{1}{2\pi\sqrt{-1}}\sum_{\alpha=1}^{6} A_{i\alpha}^T E_\alpha^T \ln(\hat{m}.\mathbf{x} + p_\alpha^T \hat{n}.\mathbf{x}) \qquad (\hat{n}.\mathbf{x} > 0)$$
$$u_i^M(\mathbf{x}) = \frac{1}{2\pi\sqrt{-1}}\sum_{\alpha=1}^{6} A_{i\alpha}^M E_\alpha^M \ln(\hat{m}.\mathbf{x} + p_\alpha^M \hat{n}.\mathbf{x}) \qquad (\hat{n}.\mathbf{x} < 0) \tag{4.11}$$

where $A_{i\alpha}$, E_α, p_α are the Eshelby-Stroh constants and the superscripts M and T stand for the matrix and twin phases respectively. The equations used to determine the Eshelby-Stroh constants and their corresponding values are detailed in section 4.2.3. Next, the strain-field of a dislocation array needs to be computed. We follow the approach in [161], given for homogeneous anisotropic materials and adapt it to the present case of an interface between distinct anisotropic phases. If dislocations with Burgers vector $\vec{b}$ are positioned periodically on the interface with a spacing *d*, then the spatially varying strain-field can be analytically computed and shown to reflect the same periodicity. The dislocation Burgers vectors and periodic spacings are: $\left(\vec{b}_{TD} = [0.7066\ 0\ 0]\ \overset{0}{\text{A}},\ d_{TD} = 36.8\overset{0}{\text{A}}\right)$ for the T-D model (following [155]) and $\left(\vec{b}_{TW} = [0\ 0\ 0.86]\ \overset{0}{\text{A}}, d_{TW} = 3.07\overset{0}{\text{A}}\right)$ for the T-W model (following [83]). The ensuing calculations are done in the twin phase, keeping in mind that twin-symmetry (and also a assumption of equal volume fraction which is removed later) affords a symmetric partitioning of energy between the two phases, allowing the convenience of only calculating one of them. The spatially varying displacement gradient in the twin phase ($\hat{n}.\mathbf{x} > 0$) is given by:

$$u_{j,l}^T(\mathbf{x}) = \frac{1}{2d\sqrt{-1}}\sum_{\alpha=1}^{6} A_{j\alpha}^T E_\alpha^T \left(m_l + p_\alpha^T n_l\right)\cot\left(\frac{\pi}{d}(\hat{m}.\mathbf{x} + p_\alpha^T \hat{n}.\mathbf{x})\right) \tag{4.12}$$

The far-field strains generated by an anisotropic dislocation array is non-zero and would render the strain-energy divergent. This is a non-trivial aspect and is discussed in [161]. We present, for the first time (to the best of the authors' knowledge), a framework to account for these far-field

gradients in computing the interface strain energy. The non-zero far-field displacement gradient ($\hat{n}.\mathbf{x} \to \pm\infty$) is given by:

$$\begin{aligned} u_{j,l}^{T,far} &= \frac{-1}{2d}\sum_{\alpha=1}^{6}\eta_\alpha A_{j\alpha}^{T}E_\alpha^{T}\left(m_l + p_\alpha^{T}n_l\right) \qquad \left(\hat{n}.\mathbf{x} \to \infty\right) \\ u_{j,l}^{M,far} &= \frac{1}{2d}\sum_{\alpha=1}^{6}\eta_\alpha A_{j\alpha}^{M}E_\alpha^{M}\left(m_l + p_\alpha^{M}n_l\right) \qquad \left(\hat{n}.\mathbf{x} \to -\infty\right) \end{aligned} \tag{4.13}$$

It can be shown that $\sum_{\alpha=1}^{6}\eta_\alpha A_{j\alpha}^{T}E_\alpha^{T} = -\sum_{\alpha=1}^{6}\eta_\alpha A_{j\alpha}^{M}E_\alpha^{M} \approx b_j$, due to twin-symmetry and the displacement-jump condition (4.8). This equality is approximate because there are additional terms due to the anisotropic constants. The approximation is reasonable because the additional terms are at least an order of magnitude lower for all TBs considered in this study. Consequently, the far-field gradient can be approximated to:

$$\begin{aligned} u_{j,l}^{T,far} &= \frac{-1}{2d}\left(b_j m_l + \sum_{\alpha=1}^{6}\eta_\alpha A_{j\alpha}^{T}E_\alpha^{T}p_\alpha^{T}n_l\right) \\ u_{j,l}^{M,far} &= \frac{1}{2d}\left(b_j m_l + \sum_{\alpha=1}^{6}\eta_\alpha A_{j\alpha}^{M}E_\alpha^{M}p_\alpha^{M}n_l\right) \end{aligned} \tag{4.14}$$

Note that the first of the terms is the component which falls out from the tensor $\left(\frac{\vec{b}}{2d}\otimes(-\hat{m})\right)$.

Intuitively, this terms represents a shear displacement gradient introduced in the twin due to interface dislocations of magnitude $\vec{b}$, spaced periodically along $(-\hat{m})$ by spacing *d*. The direction is written as $(-\hat{m})$ because this direction points toward the dislocated half-space. Hence, for the dislocation array, it points towards the direction in which the displacement introduced by each interface dislocation is accumulating (refer Figure 39(c) in section 4.2.3). This interpretation will be used later in section 4.2.6. The contributions from the second term of (4.14) are found to be considerably lower (for all three TBs considered in the study). For the purposes of the theory

developed in section 4.2.6, we ignore this second term and approximate the far-field displacement-gradient (introduced by the interface dislocation array) as $\left(\frac{\vec{b}}{2d}\otimes(-\hat{m})\right)$.

The far-field displacement-gradients (given by (4.13) or (4.14)) can be eliminated in the following way. The initial strained state can be imposed on the system before insertion of the interface dislocation array. Both the twin and the matrix can be subject to a homogeneous deformation arising out of a linear displacement field given by:

$$\begin{aligned} u_j^T(\mathbf{x}) &= \frac{1}{2d}\sum_{\alpha=1}^{6}\eta_\alpha A_{j\alpha}^T E_\alpha^T\left(\hat{m}.\mathbf{x}+p_\alpha^T\hat{n}.\mathbf{x}\right) \qquad (\hat{n}.\mathbf{x}>0) \\ u_j^M(\mathbf{x}) &= \frac{-1}{2d}\sum_{\alpha=1}^{6}\eta_\alpha A_{j\alpha}^M E_\alpha^M\left(\hat{m}.\mathbf{x}+p_\alpha^M\hat{n}.\mathbf{x}\right) \qquad (\hat{n}.\mathbf{x}<0) \end{aligned} \tag{4.15}$$

Note that these displacement fields can be appended with a rigid-body translation with no change to the strains or the strain-energies. Hence, they are unique up to a rigid translation. What is of more physical interest is the displacement gradient which is given by:

$$\begin{aligned} u_{j,l}^T &= \frac{1}{2d}\sum_{\alpha=1}^{6}\eta_\alpha A_{j\alpha}^T E_\alpha^T\left(m_l+p_\alpha^T n_l\right) \qquad (\hat{n}.\mathbf{x}>0) \\ u_{j,l}^M &= \frac{-1}{2d}\sum_{\alpha=1}^{6}\eta_\alpha A_{j\alpha}^M E_\alpha^M\left(m_l+p_\alpha^M n_l\right) \qquad (\hat{n}.\mathbf{x}<0) \end{aligned} \tag{4.16}$$

The continuity of tractions are ensured by the fact that the chosen Eshelby-Stroh constants adhere to the conditions (4.7) and (4.9). The displacement gradients however are not continuous. On the interface, the discontinuity in the in-plane displacement gradients (i.e. only consider the in-plane terms of (4.16), which are nothing but terms with $n_l=0$) is given by:

$$\left[u_{j,l}\right]^{in-plane} = u_{j,l}^{T,in-plane} - u_{j,l}^{M,in-plane} = \frac{1}{2d}\sum_{\alpha=1}^{6}\left(\eta_\alpha A_{j\alpha}^T E_\alpha^T m_l + \eta_\alpha A_{j\alpha}^M E_\alpha^M m_l\right) = \left(\frac{b_j m_l}{d}\right) \tag{4.17}$$

This follows from (4.8). A closer inspection would reveal that this is but a re-statement of the Frank-Bilby equation [70] (briefly outlined in section 4.2.5). The displacement gradients given by (4.16) are coherence displacement gradients required for atomic registry on the interface. We can also compute the total discontinuity in interface displacement-gradients (in-plane and out-of-plane) as:

$$\left[u_{j,l}\right] = u^{T}_{j,l} - u^{M}_{j,l} = \left(\frac{b_j m_l}{d}\right) + \frac{1}{2d}\left(\eta_\alpha A^{T}_{j\alpha} E^{T}_{\alpha} p^{T}_{\alpha} n_l + \eta_\alpha A^{M}_{j\alpha} E^{M}_{\alpha} p^{M}_{\alpha} n_l\right) \tag{4.18}$$

In the T-D model, the in-plane shear gradient $\left[u_{j,l}\right]_{\gamma}$ required for terrace coherence on $\left(11\bar{1}\right)$ is

$$\left[u_{j,l}\right]^{in-plane}_{\gamma} = \begin{pmatrix} 0 & \gamma_{12} & 0 \\ 0 & 0 & 0 \\ 0 & 0 & 0 \end{pmatrix} \tag{4.19}$$

, where $\gamma_{12} = 1.92\%$ [155]. In the case of the T-W model the in-plane coherence gradient $\left[u_{j,l}\right]^{in-plane}_{\alpha}$ is part of the total rotational misorientation $\left[u_{j,l}\right]_{\alpha}$ between the phases,

$$\left[u_{j,l}\right]^{in-plane}_{\alpha} = \begin{pmatrix} 0 & 0 & 0 \\ 0 & 0 & 0 \\ 0 & -2\tan\alpha & 0 \end{pmatrix}; \left[u_{j,l}\right]_{\alpha} = \begin{pmatrix} 0 & 0 & 0 \\ 0 & 0 & 2\tan\alpha \\ 0 & -2\tan\alpha & 0 \end{pmatrix} \tag{4.20}$$

, where $\alpha = 7.98^{o}$ [83] (also, $s = 2\tan\alpha = 0.280$ is the *classical* twinning shear). Hence, in both models, the two variants must be coherently strained for atomic registry (with these coherence strains also satisfying the traction continuity) following which the introduction of the interface dislocation array relieves the coherence strain away from the interface, rendering $u^{far}_{j,l} = 0$ in the matrix and twin phases. An illustration is provided to visualize this process in figure 40.

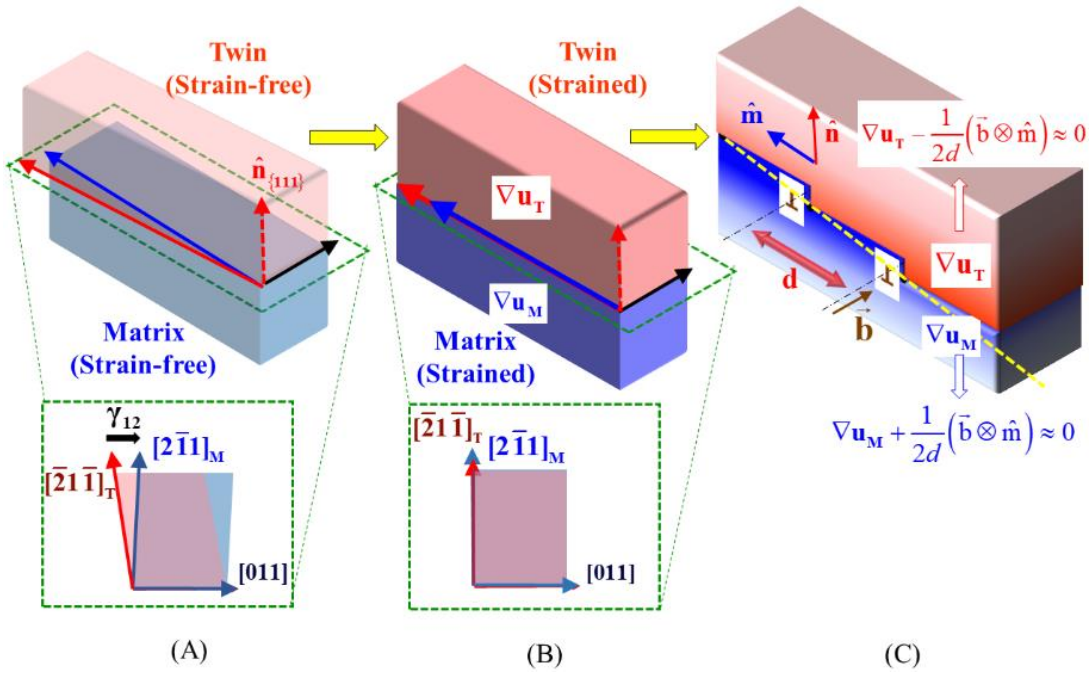

Figure 40: Schematic illustration of the theoretical analysis in section 4.2.4, using the T-D model as the example (We presume zero external strain and equal volume fraction of the twin and the matrix): (a) The crystallography of the $[011]$ Type II twin showing the matrix and twin variants in their strain-free configurations; With the common twinning direction $\eta_1 = [011]$ aligned, there is a shear-mismatch on the $(11\bar{1})_M$ plane. (b) Coherence strains applied to matrix and twin variants for atomic registry on the terrace plane; the applied in-plane gradient for terrace coherence is $\nabla \mathrm{u}_T = -\nabla \mathrm{u}_M = \frac{1}{2}\nabla \mathrm{u}_{coh}$ (refer equation (4.41)). (c) The coherence strains on the terrace are relieved by introduction of a periodic array of interface dislocations spaced by *d*; the far-field displacement gradient introduced by the dislocation array can be well-approximated by $\pm \frac{1}{2d}(\vec{b} \otimes \hat{m})$ as discussed in section 4.2.4 and in 4.2.3

The net-inhomogeneous displacement-gradient $u_{j,l}(\mathbf{x})$ which is used to obtain the strain-field ($\varepsilon_{jl}(\mathbf{x}) = 0.5(u_{j,l} + u_{l,j})$) and consequently strain-energy density ($e(\mathbf{x}) = \frac{1}{2} C_{ijkl}\varepsilon_{ij}\varepsilon_{kl}$) is given by:

$$u^T_{j,l}(\mathbf{x}) = \frac{1}{2d\sqrt{-1}} \sum_{\alpha=1}^{6} A^T_{j\alpha} E^T_\alpha \left(m_l + p^T_\alpha n_l\right)\left(\cot\left(\frac{\pi}{d}(\hat{m}.\mathbf{x} + p^T_\alpha \hat{n}.\mathbf{x})\right) + \eta_\alpha \sqrt{-1}\right) \qquad (4.21)$$

The distributions of continuum strain-energy densities are presented in Figure 41 (a, b). The T-W nanostructure exhibits a highly localized strain-field in stark contrast to the T-D nanostructure

whose strain-fields exhibit a larger domain of influence away from the TB. A converged strain-energy estimate can be obtained by integrating the densities to sufficiently large distances away from the interface. A distance of $z = 10\,\text{nm}$ was sufficient for both T-D and T-W nanostructures. Integrated strain-energies presented in Table 6 favor the T-W nanostructure whose strain-energy is orders of magnitude lower than the T-D strain energy. However, the atomic potential energy of both topologies (evaluated in section 4.2.1) are orders of magnitude higher than their respective macro-scale strain-energy. It is the decisive criterion which ultimately favors a T-D topology over a T-W topology for the nanostructure of the Type II TB.

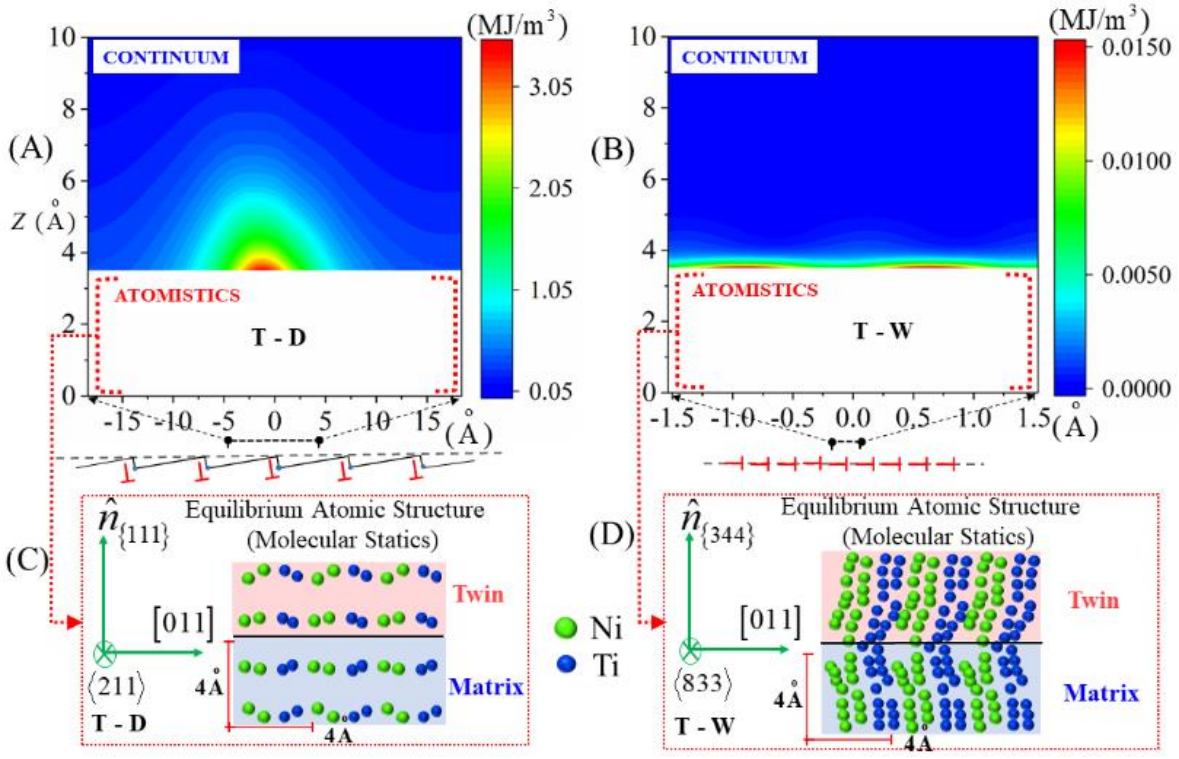

Figure 41: Continuum and atomistic energies of TB nanostructures: (a) Strain-energy density distribution of the T-D model exhibiting larger domain of influence and higher strain energy as compared to the (b) T-W model (The fields are plotted beyond a cut-off distance, away from dislocation cores). (c) Equilibriated atomic structure on $(11\bar{1})$ terraces of the T-D structure exhibiting low distortion in atomic positions. (d) Equilibriated atomic structure on the $(34\bar{4})$ T-W exhibiting high distortions and consequently higher atomistic energy (Note that, in (c, d), not all atoms are on the plane of the figure).

Table 6: Interface energy of the Type II TB

Multi-scale Energetics of Topological Nanostructures	Continuum Strain Energy $\left(\mathrm{J}/\mathrm{m}^2\right)$	Atomistic Potential Energy $\left(\mathrm{J}/\mathrm{m}^2\right)$	Total Energy $\left(\mathrm{J}/\mathrm{m}^2\right)$
Terrace-Disconnection (T-D) Model	5.05×10^{-4}	2.69 (lower)	2.69 (preferred)
Tilt-Wall (T-W) Model	5.82×10^{-7} (lower)	4.19	4.19

4.2.5. The Frank-Bilby equation

The Frank-Bilby equation gives the required defect/dislocation density on an interface required to relieve coherence strains on the interface. Suppose, $F_T = I + \nabla u_T$ is the coherence deformation gradient applied to the twin and $F_M = I + \nabla u_M$ is the coherence deformation gradient applied to the matrix. We take the example of the Type II TB terrace and the respective coherence gradients for atomic registry on the $\left(11\bar{1}\right)_{\mathrm{M}} = \left(\bar{1}\bar{1}1\right)_{\mathrm{T}}$ terrace planes. Note that the displacement gradients $\nabla u_{\mathrm{T,M}}$ are the same as those referred to in equation (4.42). Also, $\left(\nabla u_{\mathrm{T}}\right)_{jl} = u^{\mathrm{T}}_{j,l}$ and $\left(\nabla u_{\mathrm{M}}\right)_{jl} = u^{\mathrm{M}}_{j,l}$ as used in equation (4.17). The Frank-Bilby equation [70] dictates that the dislocation-spacing d along a direction $\hat{m}$ (we pick the same definition as adopted in section 4.2.4 and 4.2.6) required to nullify this coherence strain is given by:

$$-\left(F_{\mathrm{T}}^{-1} - F_{\mathrm{M}}^{-1}\right)\hat{m} = \frac{\vec{b}}{d} \tag{4.22}$$

With the linear-elastic approximation $F_{\mathrm{T,M}}^{-1} \approx I - \nabla u_{\mathrm{T,M}}$, this reduces to:

$$\left(\nabla u_{\mathrm{T}} - \nabla u_{\mathrm{M}}\right).\hat{m} = \frac{\vec{b}}{d} \tag{4.23}$$

This is equivalent to (4.17).

4.2.6. Evolving Interface Theory: Dependence of TB topology on external strain and twin volume fraction

A theoretical framework is developed to determine the energy-minimal T-D nanostructure under external strain, enforced as an external displacement gradient ∇u_{EXT}. This is done for all major classes of deformation TBs i.e. Type II, Type I and Compound, continuing with NiTi as the study target. While the energy-optimality of the T-D topology for the Type II TB has been established, we treat both $\{111\}$ Type I and $\{001\}$ Compound TBs in NiTi as T-D topologies with dislocation spacings $d = \infty$. The crystallographic identity of the terrace plane (with normal $\hat{n}$), the step height of the disconnection, *h*, dislocation spacing, *d*, and the unit vector along this spacing, $\hat{m}$, together parametrize the nanostructure (Figure 42). The Burgers vector of the dislocation is calculated using $\vec{b} = sh\hat{\eta}_1$ [24], where *s* is the twinning shear and $\hat{\eta}_1$ is the direction of shear, both well-defined "twinning elements" known for all TBs [40].

We first define a coordinate system using the triad of vectors $\hat{e}_1 = \vec{b} / |\vec{b}|$, $\hat{e}_3 = \hat{n}$ (TB normal pointing into the twin), and $\hat{e}_2 = \hat{n} \times \hat{t}$. There are two variables which define the T-D nanostructure: (1) the vector $\hat{m}$ on the terrace plane which is perpendicular to the dislocation line and which, if positioned at a disconnection, points from the twin phase into the matrix phase (i.e. points away the dislocated space, following the same convention as in section 4.24, also clarified in Figure 39) (2) the spacing *d* along this vector. Since the vector $\hat{m}$ is a unit vector on the terrace plane, it can be replaced with a scalar ϕ parameter where

$$\hat{m} = \hat{e}_1 \cos\phi + \hat{e}_2 \sin\phi \tag{4.24}$$

and $-\pi \le \phi \le \pi$. Hence, we treat the T-D nanostructure as being parametrized by the pair of scalar variables (d,ϕ). Say, we begin with a specific value-pair fixing the T-D nanostructure. Under external ∇u_{EXT}, the deformation partitions (not necessarily in a symmetric manner) between the matrix and the twin phases. We presume that the twin and the matrix sustain the homogeneous gradients given by ∇u_T and ∇u_M respectively. Also, the components are given as $\left(\nabla u_{T,M}\right)_{ij} = \dfrac{\partial u_i^{T,M}}{\partial x_j}$. These homogeneous gradients in conjunction with the far-field gradient introduced by the interface dislocation array together determine the net strain in the matrix and twin phases, and consequently the strain-energy. Given the T-D nanostructure i.e. (d,ϕ), we have 18 components of the two displacement gradients to solve for.

First, we need to establish the coherence deformation/strain. Coherence strain is the necessary deformation to ensure atomic registry on the terraces. This concept, proposed in the Topological Modeling framework [70] is generalized by us to a coherence displacement gradient (which will include both strains and in-plane rotations). We first partition the individual displacement gradients into an in-plane component and an out-of-plane component. For instance, in the twin-phase, we can write:

$$\left(\nabla u_T^{in-plane}\right) = \begin{pmatrix} \dfrac{\partial u_1^T}{\partial x_1} & \dfrac{\partial u_1^T}{\partial x_2} & 0 \\ \dfrac{\partial u_2^T}{\partial x_1} & \dfrac{\partial u_2^T}{\partial x_2} & 0 \\ \dfrac{\partial u_3^T}{\partial x_1} & \dfrac{\partial u_3^T}{\partial x_2} & 0 \end{pmatrix} \tag{4.25}$$

$$\left(\nabla u_T^{out-plane}\right)=\begin{pmatrix} 0 & 0 & \dfrac{\partial u_1^T}{\partial x_3} \\ 0 & 0 & \dfrac{\partial u_2^T}{\partial x_3} \\ 0 & 0 & \dfrac{\partial u_3^T}{\partial x_3} \end{pmatrix} \tag{4.26}$$

$$\nabla u_T = \nabla u_T^{in-plane} + \nabla u_T^{out-plane} \tag{4.27}$$

The coherence condition can then be written as

$$\nabla u_T^{in-plane} - \nabla u_M^{in-plane} = \nabla u_{coh} \tag{4.28}$$

, where ∇u_{coh} is the coherence gradient unique to the parent crystal structure and the twin boundary type. While $\nabla u_{coh} = \mathrm{O}_{3\times 3}$ (zero) for Type I and Compound twin modes, for the Type II TB in NiTi we have:

$$\nabla u_{coh}^{Type-II} = \begin{pmatrix} 0 & \gamma_{12} & 0 \\ 0 & 0 & 0 \\ 0 & 0 & 0 \end{pmatrix} \tag{4.29}$$

where $\gamma_{12} = 4.90\%$. Next, we have the average strain-condition which is essentially enforcing a boundary condition on the microstructure, for its average deformation. This can be written as

$$(1-f)\left(\nabla u_M + \frac{1}{2d}\left(\vec{b}\otimes\hat{m}\right)\right) + f\left(\nabla u_T - \frac{1}{2d}\left(\vec{b}\otimes\hat{m}\right)\right) = \nabla u_{EXT} \tag{4.30}$$

where *f* is the volume fraction of the twin that can take values from 0 to 1. Note that, in (4.30), we augment the coherence displacement gradient with the far-field displacement gradient introduced by the dislocation array, in the matrix and twin phases. For instance, the far-field gradient in the

twin is approximated as $-\frac{1}{2d}\left(\vec{b}\otimes\hat{m}\right)$, motivated by the derivation in section 4.2.4 (equation (4.14)). Now, if partitioned to the in-plane and out-of-plane components, we have:

$$(1-f)\left(\nabla u_M^{in-plane}+\frac{1}{2d}\left(\vec{b}\otimes\hat{m}\right)\right)+f\left(\nabla u_T^{in-plane}-\frac{1}{2d}\left(\vec{b}\otimes\hat{m}\right)\right)=\nabla u_{EXT}^{in-plane} \tag{4.31}$$

and

$$(1-f)\left(\nabla u_M^{out-plane}\right)+f\left(\nabla u_T^{out-plane}\right)=\nabla u_{EXT}^{out-plane} \tag{4.32}$$

Now, (4.28) and (4.31) together result in:

$$\begin{aligned}\nabla u_T^{in-plane}&=\nabla u_{EXT}^{in-plane}+(1-f)\nabla u_{coh}+(2f-1)\frac{1}{2d}\left(\vec{b}\otimes\hat{m}\right)\\ \nabla u_M^{in-plane}&=\nabla u_T^{in-plane}-\nabla u_{coh}\end{aligned} \tag{4.33}$$

This determines 12 out of the initial 18 components in the displacement-gradients. Now consider the remaining 6 out-of-plane components of the external deformation (i.e. in $\nabla u_M^{out-plane}$ and $\nabla u_T^{out-plane}$). We enforce traction continuity across the terrace and necessitate the condition:

$$\left(\mathbf{C_M}\varepsilon_M\right)\hat{n}=\left(\mathbf{C_T}\varepsilon_T\right)\hat{n} \tag{4.34}$$

where $\varepsilon_M=\left(\nabla u_M\right)_{\mathbf{SYM}}$ and $\varepsilon_T=\left(\nabla u_T\right)_{\mathbf{SYM}}$ are the strains on the terrace and $\mathbf{C_{M,T}}$ represent the elasticity tensor of the matrix and twin respectively. Note that the terrace strains include no contribution from the strain-field of the interface dislocation array. The equations (4.32) and (4.34) determine the final 6 components, ultimately determining the complete ∇u_T and ∇u_M displacement gradients.

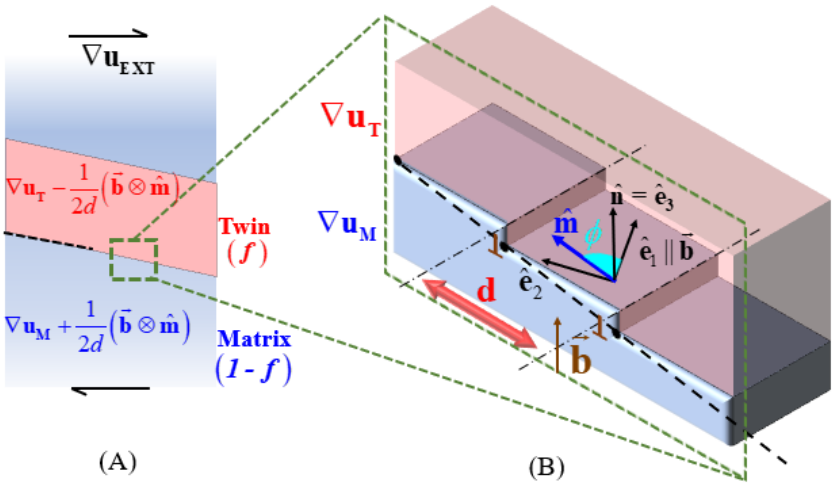

Figure 42: Elements of the Evolving Interface theory: (a) Schematized microstructure representing a twin of volume fraction *f* growing in the matrix; ∇u_{EXT} represents the external microstructural deformation (strain) and the individual tensor expressions in the twin and matrix represent the bulk deformations sustained by each respectively (refer terms in equation (4.30)). (b) Schematized nanostructure of the TB, representing the $(\hat{e}_1 - \hat{e}_2 - \hat{e}_3)$ coordinate frame, the Burgers vector of the dislocations $\vec{b}$, the direction of the spacing $\hat{m}$, normal to the terrace planes $\hat{n}$, and coherence gradients $\nabla u_{T,M}$ sustained by the twin and matrix phases respectively on the terrace.

The theory has thus far established that, given the (d,ϕ) parameters of the nanostructure, a complete determination of the displacement gradients in the matrix and twin phases is possible, under any general external deformation ∇u_{EXT}. Hence, we can write them as functions of these parameters i.e. $\nabla u_T(d,\phi)$ and $\nabla u_M(d,\phi)$. It follows, that the net strain in the bulk of the matrix and twin phases are also functions of the same parameters i.e.:

$$\begin{aligned} e_T &= e_T(d,\phi) = \left(\nabla u_T(d,\phi) - \frac{1}{2d}\left(\vec{b} \otimes \hat{m}(\phi)\right) \right)_{\mathbf{SYM}} \\ e_M &= e_M(d,\phi) = \left(\nabla u_M(d,\phi) + \frac{1}{2d}\left(\vec{b} \otimes \hat{m}(\phi)\right) \right)_{\mathbf{SYM}} \end{aligned} \tag{4.35}$$

Now, we state the converse problem: Given an external imposed deformation ∇u_{EXT}, we want to determine the T-D nanostructure (i.e. the parameters *d* and ϕ) which minimizes the microstructural strain-energy:

$$E(d,\phi) = (1-f)(\frac{1}{2}e_M : \mathbf{C_M} e_M) + f(\frac{1}{2}e_T : \mathbf{C_T} e_T) \tag{4.36}$$

To illustrate the behavior, varying displacement gradients ∇u_{EXT} are applied to the TBs, with the strain magnitude parametrized by γ. For a range of strain values, the nanostructure (as parametrized by (d,ϕ)) minimizing the average microstructural energy is computed. Results are further interpreted as an angle of deviation from the terrace plane, calculated as $\theta = \tan^{-1} h/d$. This metric is presented as it ties with trace analysis methods in microscopy used to determine the Miller indices of the interface (for example, in Figure 35(a, b)). Each value of θ corresponds to a different identity of the interface. The results are presented in Figure 43.

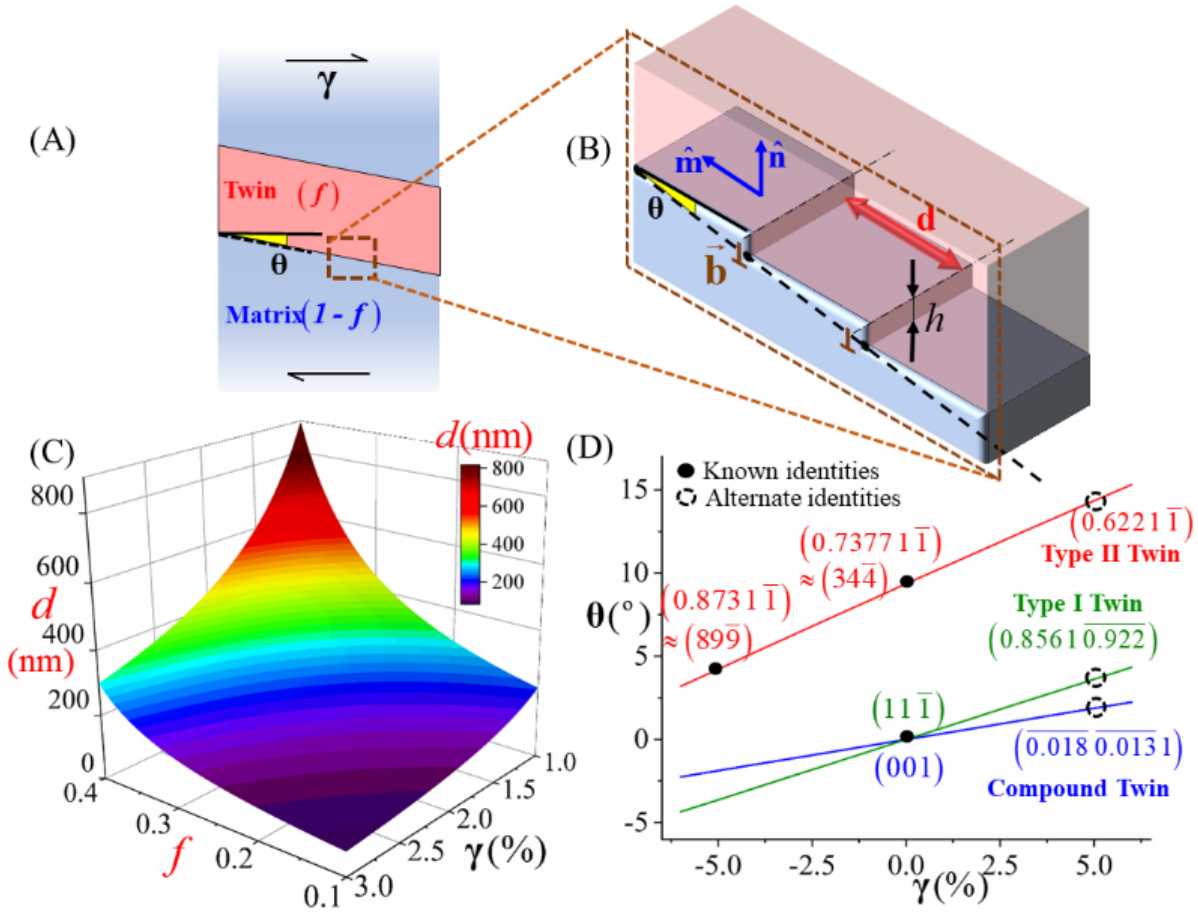

Figure 43: Evolution of T-D nanostructure as a function of strain and twin volume fraction: (a) Schematized microstructure representing a twin of volume fraction *f* growing in the matrix, with the TB's trace making an angle Θ with a reference crystallographic plane (chosen to be the terrace plane). (b) The T-D nanostructure of the TB constituting terrace planes (with normal $\hat{n}$) separated by disconnections (height *h* and Burgers vector $\vec{b}$) spaced at distance *d* along unit vector $\hat{m}$.(c) Sensitivity of the spacing *d* to external strain and microstructural volume fraction exhibiting over an 8-fold change in dislocation spacing and consequently the planar dislocation density on the TB (example chosen here is the (001) compound TB in NiTi under external deformation $\nabla u_{EXT} = \gamma(\hat{\eta}_1 \otimes \hat{\eta}_1)$). (d) Strain sensitivity of TBs permitting an evolution across a continuous spectrum of indicial identities (enforced displacement gradients are chosen as $\nabla u_{EXT}^{\text{Type II}} = \gamma(\hat{n} \otimes \hat{n})$ and $\nabla u_{EXT}^{\text{Type-I, Compound}} = \gamma(\hat{\eta}_1 \otimes \hat{n})$, assuming $f = 0.5$), establishing the known contrasting identities of the Type II TB as experimental evidence of distinct states across this spectrum

4.2.7. Calculation of the Burgers vector based on the Topological Modeling framework

In this section, the calculation of the Burgers vector through the Topological Modeling framework is shown for all TBs in this study, for the sake of completion. The mathematical approach proposed in [69], adopted in several works including [82, 83, 159] has been employed. We begin by specifying the orientation of the matrix and twin variants with respect to a global coordinate frame $x-y-z$ ($\vec{e}_x, \vec{e}_y, \vec{e}_z$ unit vectors) of the simulation box similar to the setup in 4.2.1. The orientation of the matrix variant is specified by a 3x3 matrix C_{LAT}^{M}, where the columns of the matrix gives the coordinates of the 3 lattice vectors (of the martensitic unit cell in the global axes, similar to section 4.2.1). This matrix is determined by aligning specific crystallographic directions along the global axes (discussed in section 4.2.1, also elaborated further in an appendix in [155]). The chosen aligned directions for each TB type are listed in Table 7. Note that experimental lattice constants [97] (and not the lattice constants associated with the interatomic potential [94]) of $\mathrm{B19'}$ NiTi are employed as in section 4.2.6. Once C_{LAT}^{M} is obtained based on the chosen orientation, the orientation of the twin variant is determined by calculating the same matrix C_{LAT}^{T} for the twin. This is done by using equations from the classical theory of deformation twinning [40]. For the $\langle 011 \rangle$ type II TB, the symmetry relation is a 180 degree rotation about $\eta_1 = [011]$. Note that this direction is common between the matrix and twin variants and hence does not need further specification via a T or M subscript. The lattices are related to each other by the equation:

$$C_{LAT}^{T} = \left(2\left(\hat{\eta}_1 \otimes \hat{\eta}_1\right) - I\right) C_{LAT}^{M} \tag{4.37}$$

where $\hat{\eta}_1$ is the unit vector (specified in the global frame) along the twinning direction for the type II TB, which in this case is $[011]$. For the $\{111\}$ type I twin, the symmetry relation is a reflection in $K_1 = (11\bar{1})_M$. The lattices are related to each other by the equation:

$$C_{LAT}^{T} = \left(I - 2(\hat{n} \otimes \hat{n})\right) C_{LAT}^{M} \tag{4.38}$$

where $\hat{n}$ is the unit vector normal to K_1. For the compound twin, we can employ any one of the two symmetry relations above. We choose the type II symmetry relation about its twinning shear direction $\eta_1 = [100]_{\mathrm{M}}$. Table 7 lists the orientations lattices $C_{LAT}^{M,T}$ corresponding to the matrix and twin of all TB types. The Burgers vector is calculated by the equation:

$$\vec{b} = \left(\vec{t}_T - \vec{t}_M\right) \tag{4.39}$$

where it is presumed that all vectors are specified in the same global coordinate frame. For example, if the vector $\vec{t}_M = [uvw]_{\mathrm{M}}$ is specified in the crystallographic basis of the matrix, then to convert the vector to its global frame, we perform the matrix operation $\vec{t}_M = C_{LAT}^{M} \begin{pmatrix} u \\ v \\ w \end{pmatrix}$ to get the coordinates in the global frame (likewise for a vector specified in the twin frame). The vectors $\vec{t}_T$ and $\vec{t}_M$ are translational symmetry vectors in the twin and the matrix respectively. The step height is calculated by the equation:

$$h_D = \hat{n}.\vec{t}_M \tag{4.40}$$

where $\hat{n}$ is a normal vector pointing from the matrix to the twin. It is the normal to the twin plane in the case of the $\{111\}$ type I twin and $\{001\}$ compound twin and normal to the terrace planes in the case of the $\langle 011 \rangle$ type II twin. All results of the calculation are summarized in Table 7 below.

Table 7: Crystallography and Burgers vector calculation of Type I, II and Compound TB in NiTi

TB type	Global axes	C_{LAT}	$\vec{b} = (\vec{t}_T - \vec{t}_M)$	$h_D = \hat{n}.\vec{t}_M$ (Å)	$\vec{b}$ (Å)
$[011]$ Type-II	$\hat{e}_x \parallel [011]$ $\hat{e}_y \parallel [2\bar{1}1]_M$ $\hat{e}_z \parallel \hat{n}_{(11\bar{1}),M}$	$C^M_{LAT} = \begin{bmatrix} -0.3013 & 2.7946 & 3.3972 \\ 1.8755 & -2.1668 & 2.1668 \\ 2.1826 & 2.1826 & -2.1826 \end{bmatrix}$ $C^T_{LAT} = \begin{bmatrix} -0.3013 & 2.7946 & 3.3972 \\ -1.8755 & 2.1668 & -2.1668 \\ -2.1826 & -2.1826 & 2.1826 \end{bmatrix}$ (Involves terrace coherence strains)	$[001]_T - [010]_M$	$2.1826 = h_{(11\bar{1})}$	$\begin{pmatrix} 0.6026 \\ 0 \\ 0 \end{pmatrix} = s_{II} h_{(11\bar{1})} \hat{\eta}_1$ $\|\vec{b}\| = 0.6026$ Å
$(11\bar{1})$ Type-I	$\hat{e}_x \parallel [011]_M$ $\hat{e}_y \parallel [2\bar{1}1]_M$ $\hat{e}_z \parallel \hat{n}_{(11\bar{1}),M}$	$C^M_{LAT} = \begin{bmatrix} -0.2553 & 2.7415 & 3.4502 \\ 1.8755 & -2.1668 & 2.1668 \\ 2.1826 & 2.1826 & -2.1826 \end{bmatrix}$ $C^T_{LAT} = \begin{bmatrix} -0.2553 & 2.7415 & 3.4502 \\ 1.8755 & -2.1668 & 2.1668 \\ -2.1826 & -2.1826 & 2.1826 \end{bmatrix}$ (No coherence strains involved)	$[\bar{1}01]_T - [110]_M$	$4.3652 = 2h_{(11\bar{1})}$	$\begin{pmatrix} 1.2193 \\ 0.5826 \\ 0 \end{pmatrix} = 2s_I h_{(11\bar{1})} \hat{\eta}_1$ $\|\vec{b}\| = 1.3513$ Å
(001) Comp-ound	$\hat{e}_x \parallel [100]$ $\hat{e}_y \parallel [010]_M$ $\hat{e}_z \parallel \hat{n}_{(001),M}$	$C^M_{LAT} = \begin{bmatrix} 2.889 & 0 & -0.5473 \\ 0 & 4.12 & 0 \\ 0 & 0 & 4.5895 \end{bmatrix}$ $C^T_{LAT} = \begin{bmatrix} 2.889 & 0 & -0.5473 \\ 0 & -4.12 & 0 \\ 0 & 0 & -4.5895 \end{bmatrix}$ (No coherence strains involved)	$[00\bar{1}]_T - [001]_M$	$4.5895 = h_{(001)}$	$\begin{pmatrix} 1.0946 \\ 0 \\ 0 \end{pmatrix} = s_C h_{(001)} \hat{\eta}_1$ $\|\vec{b}\| = 1.0946$ Å

In Table 7, the direction $\hat{\eta}_1$ is a unit vector along the twinning direction for the TB (one of the classical twinning elements of the boundaries which can be obtained found in [33]). Note that the Burgers vector satisfy the equation based on the twinning shear justifying this choice in the

approach of section 4.2.6. It is also worth mentioning that the Type II TB has the least step height of the three TB types (Table 7). The step height has been proposed as a guide to quantify mobility of twinning disconnections [82], where a lower step height promotes higher TB mobility. Consequently, the calculation above indicates a higher mobility of Type II twins as compared to Type I and Compound twins. A complete calculation of the twin migration energetics, as done in [37, 155, 162] would establish this behavior more conclusively but is out of scope for the present study and is suggested for future work.

4.3. Discussions

The current study first establishes the topology of the Type II TB with least interface energy. This is done by combining nanoscale continuum strain-energies with sub-nanoscale atomistic potential-energies. Continuum strain-energy considerations are typical of prominent classical defect theories which would invariably prefer the T-W topology. This agrees with historical understanding of the tilt-boundary as a low-energy grain boundary that only introduces a rotational misorientation between grains without strain. The advent of atomistic simulation tools, being more recent in this history, introduces new criteria for evaluation. The atomic potential energy dominates the strain-energy of the nanostructures and ultimately favors the T-D topology for the Type II TB's nanostructure, in stark contrast to classical expectations.

One of the challenges in atomistic modeling of Type II TBs is the irrationality of the interface which results in limited periodicity. For instance, for the $[011]$ Type II TB of NiTi with $K_1 = (0.7205\ 1\ \bar{1})$, the interface is periodic along $[011]$ and not along any other rational crystallographic direction. This presents a challenge for a computationally efficient implementation within an atomistic framework as periodic boundary conditions cannot be applied easily. In our approach, we have circumvented this challenge to model both TB nanostructures.

For the T-W model, we have chosen a close rational approximant of the Type II plane $\left(0.7205\ 1\ \bar{1}\right) \approx \left(34\bar{4}\right) = \left(0.75\ 1\ \bar{1}\right)$ that has been suggested before [39]. Periodic boundary conditions can now be imposed on this plane as elaborated in section 4.2.1. Constructing the variants in the respective crystallographies described in the section effectively introduces a rotational misorientation on this plane, faithfully capturing the features of the nanostructure as proposed in [82, 83]. For the T-D model, we stake that it is not necessary to simulate the exact irrational plane. The structure is constituted of $\left(11\bar{1}\right)$ rational terrace planes with periodically spaced twinning disconnections. The irrationality is the result of periodically spaced twinning disconnections. The twinning disconnections are spaced at distances of tens of angstroms which are far higher than the Burgers vector magnitude of the twinning disconnection [155]. Consequently, the disconnections are sufficiently far that we can ignore any potential energy contribution due to core interaction between the disconnections. They only interact via their continuum strain-fields which is accounted for by the analytical methods described in section 4.2.4. Thus, by treating the rational terrace and the disconnection disjointly, and by accounting for the strain-energy of the periodic dislocation array, the calculation of energies for the T-D model of the Type II TB can be performed faithfully without having to construct the exact irrational plane in an atomistic framework.

Intuitively, the reason behind the high potential energy of the T-W model is the close spacing of dislocation cores (on consecutive $\left(011\right)$ slip planes) arranging on a $\left(34\bar{4}\right) \approx \left(0.7205\ 1\ \bar{1}\right)$ plane with very low atomic planar density. Consequently, the potential energy of the interface is considerably high, relaxing to the highly distorted atomic structure of figure 36(a). If a better rational approximation to the irrational plane was made for the nanostructure, for instance by

choosing the rational approximants $\left(72\ 100\ \overline{100}\right)=\left(18\ 25\ \overline{25}\right)$ or $\left(7205\ 10^4\ \overline{10^4}\right)=\left(1441\ 2000\ \overline{2000}\right)$ etc., the resulting potential energies would be higher because the atomic planar densities of these approximants are lower. Thus, in the limit of the irrational plane, it is plausible that the atomistic potential energy will still be higher than what we have computed on the $\left(34\bar{4}\right)$ plane. This would only further support the conclusion of this study that the T-W model has a higher interface potential energy without the need to simulate the exact irrational plane $\left(0.7205\ 1\ \bar{1}\right)$. The choice of the TB to prefer a T-D topology is rooted in the preference of nearest $\{111\}$ planes for their high planar density. It is the same reason behind preference of this family of planes in slip/twinning of FCC materials. However, there is a coherence strain necessitated on the $\{111\}$ terrace which the interface relieves by accommodating a periodic array of dislocations. Hence, instead of a coherent TB residing on $\left(11\bar{1}\right)$, the TB prefers to be semi-coherent and optimally balances the strain-energies and atomistic potential energies. Since, the twinning disconnections reside on a rational crystallographic plane, their nucleation and migration can be considered much in the same way as is proposed for the Type I TB [82, 83].

While such a T-D topology was previously considered by the authors for the $\langle 011\rangle$ Type II TB [155], an interface identity closer to $\left(89\bar{9}\right)$ was found, matching only one set of experimental observations [38]. The key parameter which dictates the indicial identity is the periodic spacing between two consecutive dislocations. In the model of [155], the topology is described by $\left(d=36.86\ \text{Å},\phi=\pi/2\right)$ explaining the indicial identity of $\left(89\bar{9}\right)$ for the interface (dashed line in figure 35(c)). This prediction, done within the framework of the atomistic approach, employs

material lattice constants reproducible by the underlying interatomic potential [94]. These constants deviate from experimental measures by 2.70%, on average. In Molecular Statics/Dynamics, this discrepancy would generally be considered minor as it is a formidable task for modern interatomic potentials to exactly reproduce measured lattice constants. This is particularly the case with phase-transforming materials such as NiTi, where the potential must account for physical parameters (cohesive energies, elastic moduli etc.) associated with multiple phases, inevitably leading to admittance of minor discrepancies in the lattice constants or unit cell motif positions (prevalent in other potentials developed for NiTi [92-94, 117, 125, 127, 163, 164] as well). However, such deviations can critically influence the coherence strains and the dislocation spacing in the T-D model. We find that with the use of experimental lattice constants [97] in the model, the dislocation spacing is significantly lower at $\left(d = 13.2\ \mathring{\text{A}}, \phi = \pi/2\right)$. This yields an effective interface identified by the indices $\left(0.7377\ 1\ \bar{1}\right) \approx \left(34\bar{4}\right)$. Hence, the T-D topological model agrees closely with the experimental observations of [39, 62, 66, 67], albeit there is a slight deviation from prediction of the classical theory (i.e. $\left(0.7205\ 1\ \bar{1}\right)$). It must be mentioned that this deviation is quite minor. Similar minor deviations between classical/phenomenological theory and modern topological theory has been shown and explained for other interfaces [78]. Given this change in topology, it is worth re-evaluating the strain-energy of the T-D nanostructure. With $\left(d = 13.2\ \mathring{\text{A}}, \phi = \pi/2\right)$, the strain-energy can be recomputed using methods of section 2.2 as $1.1\times10^{-4}\ \text{J}/\text{m}^2$ lower than the value quoted in table 6. This magnitude is still orders lower than the atomistic potential energies and further supports the conclusion that the T-D nanostructure is energetically more favorable than the T-W nanostructure. However, while

the proposed theory explains the $(34\bar{4})$ identity, the alternate observation of the Type II TB with indices $(89\bar{9})$ [38, 64] is yet to be explained.

The T-D nanostructure can portray multiple different indicial identities contingent on the spacing between consecutive dislocations (refer figures 43(a, b)). Further, the nanostructure can seamlessly transition between these identities by glide of dislocations on the terraces. For instance, if dislocation-glide increases spacing from $d = 13.2$ Å to $d = 34.21$ Å, identity changes to $(89\bar{9})$. We propose, for the first time, that the experimental observations (Figure 35(a, b)) do not disagree but have fortuitously caught the interface in different equilibrium states gleaning an inherent ability of the interface to evolve across them. The interface is proposed to evolve in response to external strain which in the experimental studies previously referenced [38, 39, 62, 64, 66, 67] could come from local residual strain in the sample. Note that that such strains are only external to the interface topology but local to the microstructure. Such strains are inevitably introduced during the sample's mechanical/thermal loading history or TEM sample preparation. Microstructural heterogeneities such as the presence of multiple martensitic twin variants (for instance, this can be seen in the bright-field micrographs of analyzed samples in [39, 64, 67]), precipitates or grain boundaries can significantly elevate local strains (to the order of few percent) [165, 166]. This is particularly plausible in shape memory alloys such as NiTi, where external macroscopic strains under pseudoelastic transformation easily exceed 5% [113, 167, 168]. At such strain levels or upon unload from such strains it can be expected that local elastic strains of the same order can be locked in the microstructure. In fact, local microstructural strains of such order have been measured around precipitates in NiTi [169, 170] using the Geometric Phase Analysis (GPA) method [171, 172]. In addition to such heterogeneities, there can also be a compounded effect due to

unsymmetric twin volume fraction (i.e. twin volume fraction is not equal to the matrix volume fraction or $f \neq 0.5$), the exact value of which can significantly affect the dislocation-spacing and consequently the interface identity. Wide variation of *f*, from 2.09 to 5.57 has been previously reported for the $[011]$ Type II Twin [34]. Consequently, an "Evolving Interface" (EI) theory is forwarded to establish these sensitivities to strain and volume fraction showing how it follows from energy minimization. A general framework is developed showing this capability in the three major classes of TBs [40]: Type I TBs, Type II TBs and Compound TBs, continuing with NiTi as the study target.

In order to develop a general framework applicable to all TBs, we idealize the twinning disconnection's Burgers vector as $\vec{b} = sh\hat{\eta}_1$ (with step height equal to one interplanar spacing, *h*). However, it is well-recognized that a disconnection can span multiple interplanar spacings and, in general, we have $\vec{b} = qsh\hat{\eta}_1$ [24], where q is a positive integer. The exact step height is determined by the energy degeneracy between consecutive terraces separated by the disconnection [155] and is not a topological quantity [69]. However, for the present study, it turns out that if the Burgers vector scales up by a factor of $q > 1$, then the spacing between the disconnections commensurately increases i.e. $d \to qd$, conserving the $\vec{b}/d$ ratio. And with the step height scaling up as qh, the slope of the interface $\theta = \tan^{-1} h/d$ will also remain the same, keeping the same identity for the interface. Hence, the predictions of the theory are not affected by the multiplicity (*q*) of the elementary twinning dislocation ($\vec{b} = sh\hat{\eta}_1$). Only the exact dislocation spacing (and consequently the interface dislocation-density) would be affected (Figure 42(c)). We include a calculation of the

Burgers vector based on the Topological Modeling framework in section 4.2.7 for the sake of completion. It can be verified that all calculated Burgers vector satisfy the condition $\vec{b} = qsh\hat{\eta}_1$.

The adoption of T-D topologies by Type I and Compound twins in their migration/growth is already recognized [82, 154]. However, in equilibrium, their respective TB topologies are accepted as being completely coherent, residing on rational crystallographic planes with no disconnections. The proposed theory suggests that the equilibrium state can transition between coherent and semi-coherent topologies depending on the local strain-state around the interface. Consequently, they can adopt T-D topologies with finite dislocation-spacing $d < \infty$ and give the impression of an irrational-indexed interface. In fact, under small strains, the dislocation-spacing can change quite significantly and alter the dislocation-density ($\rho \sim 1/d$) on the interface (about 8-fold in Figure 43(c)). Further, their observed traces on micrographs can be at angles that are significantly off from the expected crystallographic plane (refer Figure 43(d)). The question remains as to why the topologies evolve under strain. The Topological Model predicts fixed interface topologies with the premise that the dislocation-array cannot have any long-range strain fields. This is based on strain-energy considerations that the interface's strain-energy will become divergent. Consequently, the predicted topologies are presumed not to interact with external strain and hence retain fixed topologies. However, we claim that it is energetically favorable for the interface to interact with external strain to further reduce energy. The energy to be minimized is not only the interface strain-energy but the average microstructural energy per unit volume. The latter energy includes the strain-energy of the interface dislocation array coupled with external strain applied on the microstructure.

We use the example of the Type II twin to show that it is energetically favorable for the interface nanostructure to cause non-zero long-range strain-fields in the presence of an external strain. We

apply the external deformation $\nabla u_{EXT}^{\text{Type II}} = \gamma\left(\hat{n}\otimes\hat{n}\right)$. When $\gamma = 0$, i.e. in the absence of external strain, it can be shown that

$$\nabla u_T^{in-plane} = -\nabla u_M^{in-plane} = {}^{\nabla u_{coh}}\!/_{2} \tag{4.41}$$

In other words, the coherence strain is equally partitioned between the twin and the matrix. This is one of the assumptions in our previous work [155]. The strain-fields from the interface dislocations exactly nullify this coherence gradient in the matrix and twin phases yielding no long-range strains i.e.

$$\begin{aligned} e_T &= \left(\nabla u_{\mathrm{T}}^{in-plane} - \frac{1}{2d}\left(\vec{b}\otimes\hat{m}\right)\right)_{\mathbf{SYM}} = 0 \\ e_M &= \left(\nabla u_{\mathrm{M}}^{in-plane} + \frac{1}{2d}\left(\vec{b}\otimes\hat{m}\right)\right)_{\mathbf{SYM}} = 0 \end{aligned} \tag{4.42}$$

For this condition, we get the energy-minimal nanostructure with $\left(d = 13.25\,\text{Å}, \phi = {}^{\pi}\!/_{2}\right)$. This nanostructure does not generate any long-range fields and hence does not interact with external microstructural strain. However, we find that in the presence of external strain on the nanostructure, the coherence strain is not necessarily equally partitioned. Such an unequal partitioning has been recognized across phase interfaces involving significant elastic mismatch [98]. However, it is unexpected for cases where we have twin symmetry, where both phases are of the same crystal structure and nearly equal elastic constitution (there is a slight difference in the elastic constants due to the different orientation of the twin with respect to the matrix). The proposed theory accounts for such unequal partitioning in the presence of external strain and varying volume fractions, an effect which has not been considered till date, to the best of the authors' knowledge. In the presence of external strain, the nanostructure evolves to a different state

$\left(d = 29.6\,\text{Å}, \phi = \pi/2\right)$ where the long-range fields do not satisfy (4.42). This implies that long-range fields are generated by the nanostructure despite which the configuration obtained is energy-minimal. This effect is illustrated in figure 44.

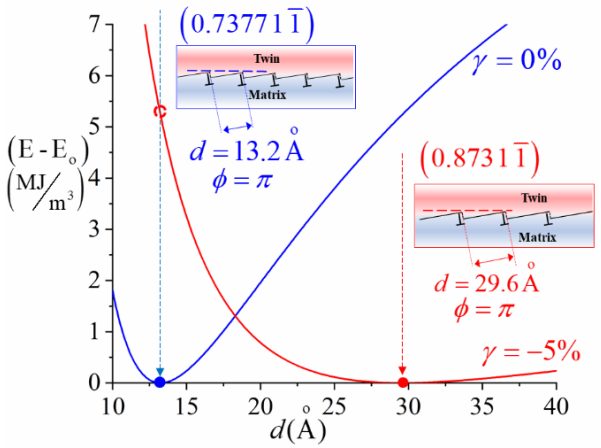

Figure 44: Variation of microstructural strain-energy (the minima of each plot is taken to be the reference value E_o, to facilitate comparison of both plots with the same scale) against dislocation spacing; The blue dotted arrow indicates the spacing, and the consequent nanostructure, which is energy-minimal at no applied strain ($\gamma = 0\%$) and produces no net long-range strain-fields; In the presence of external strain however, it is energetically favorable for the configuration to reduce energy further by evolving to the state indicated by the red-dotted arrow, allowing the nanostructure to have long-range strain fields

Contrary to existing theories, we establish that it is energetically favorable for interface nanostructures to generate long-range strain fields. These fields couple with external microstructural strain to reduce energy (Figure 44), ultimately responsible for the evolution of the T-D nanostructure to a different identity. This evolving capability is, to the best of the authors' knowledge, the only plausible explanation for the observations of the Type II TB in NiTi. Experimental evidences which were thus far considered contrasting (Figure 35(a, b)) fit consistently as distinct states in a continuous spectrum of identities (Figure 43(d)), fortuitously transposing as experimental evidence of the proposed evolving behavior. And given that this theory is built on fundamental equations in material mechanics and is devoid of any empiricism,

it ensues that other TBs considered in the study also exhibit the same evolving capability. This theory is proposed as an extension to the Topological Modeling approach, allowing prediction of equilibrium T-D topologies under the influence of strain and varying volume fractions.

It is interesting to note that the Type II TB exhibits the highest sensitivity, followed by Type I TBs and then Compound TBs. This sensitivity is likely correlated to the high-known mobility of Type II TBs as compared to Type I TBs [154, 173]. The change of TB dislocation-density in dependence of elastic external strain is significant in the field of Shape Memory Alloys (SMAs), as it is likely a key factor in the mechanism of slip emission [9, 12, 139]. Note that this behavior of the twin interface is disjoint from twin growth or twin propagation accommodating external strain. Whether or not the twin grows under external strain, the current study proposes that if the strain is held at a non-zero value, either externally or residually locked in the local microstructure (even after external unloading), the broad faces of the twin would not remain constant but reorient due to a change in the interface disconnection density. If we have an externally applied stress, there can be local relaxation due to twin growth/shrinkage (twin boundary motion). This would change the prevailing elastic strain on the twin boundary as the twin grows/shrinks, but the magnitude remains finitely non-zero under the applied stress. Hence, the boundary orientation also evolves according to the local strain evolution. Nevertheless, the T-D model parameters respond to this strain state based on the same approach. We further propose that this behavior will be exhibited by any crystalline interface that migrates via diffusionless dislocation-mediated mechanisms (e.g. habit planes), consequently adopting T-D topological nanostructures in the presence of external strain. We establish that the interfaces can evolve to varying identities, exhibiting traces on micrographs at varying slopes (i.e. Figure 43(a, d)). A recent example of such change was observed in Ni-Mn-Ga, where the trace of internal twin boundaries in the martensite phase showed significant

deviation from its expected crystallographic plane [174]. This observation was made in the vicinity of the habit plane where the lattice-mismatch between the austenite-martensite phases gave rise to significant strains (calculated to be of the order of few percent). These strains may also be augmented due to the well-known elastic softening prior to the martensitic transformation [175-178], further influencing the local twin interface topology as proposed in this study. Furthermore, this study elevates the role of such interfaces in experimental characterization, allowing a measure of local interface slope to quantify local microstructural strain (strain-mapping).

4.4. Conclusions

This study proposes to reconcile the debated nanostructure of the Type II TB in NiTi using energy-considerations on both atomistic and continuum scales. Among the T-W and T-D topologies that have thus far been proposed, it is shown that the T-D topology is energy-minimal primarily because the atomic potential energy of this topology is lower. Subsequently, an "Evolving Interface" theory is developed to establish the strain-sensitivity of the T-D topology. The framework is developed for all major deformation twin modes in general (Type I, Type II and Compound) and applied to examples of each twinning mode in NiTi. It is shown that under the coupled influence of microstructural strain and local twin volume fraction, the T-D topology can evolve to a different identity. This is achieved by dislocation-glide on the terrace planes, consequently changing the dislocation-density on the TB and the slope of its trace (say, on a micrograph). It is proposed that such an evolution has been indirectly evidenced by observation of contrasting identities of the Type II TB in NiTi. The theory is proposed as an extension to the Topological Modeling framework allowing the determination of equilibrium topologies under the influence of strain. The implications of such an evolving behavior in experimental characterization of interfaces and in functional materials have been discussed.

4.5. Revisiting K-K slip-mechanism in context of strain-sensitive interface evolution

The capacity for twin-interfaces to evolve under strain have a direct implication on the slip-emission mechanism of functional fatigue. A hypothesis is offered in this section. For instance, consider a superelastic cycle under external stress as schematically represented in figure 45 (a). Consider two analogous points during the forward and reverse transformation, F and R, where the total-transformation strain ε_{TR} is the same, correlated with the same underlying martensitic volume fraction (refer figures 15 (b, c)). During the forward transformation at F, the magnitude of elastic-strain is higher and therefore enforces a higher twin-disconnection density (refer figure 15(d)). During the reverse-transformation at R, the magnitude of elastic-strain is reduced and therefore enforces a lower twin-disconnection density (refer figure 15(e)). Thus, between the two analogous points F and R, the only difference is a deficit in the twin-disconnection density on the internal martensitic twin boundary. Then from the law of conservation of Burgers vectors, it is plausible to expect that this deficit is emitted as austenitic slip at the transformation front, during the reverse transformation, as represented in figure 15(c). And the underlying atomistic mechanism of the emission is expected to follow the simulations proposed in chapter 3. This mechanism revamps and provides a modern interpretation of the K-K mechanism (chapter 1, figure 4) following new understanding of the internal martensitic twin boundary and their behavior under strain, as proposed in prior chapters of this thesis. And such an understanding will be instrumental in narrowing future research focus on aspects such as the sensitivity of twin-boundary topology to external strain and the mobility of the twin-disconnection on the twin-boundary as tailorable parameters, in search of fatigue-resistant shape memory alloys.

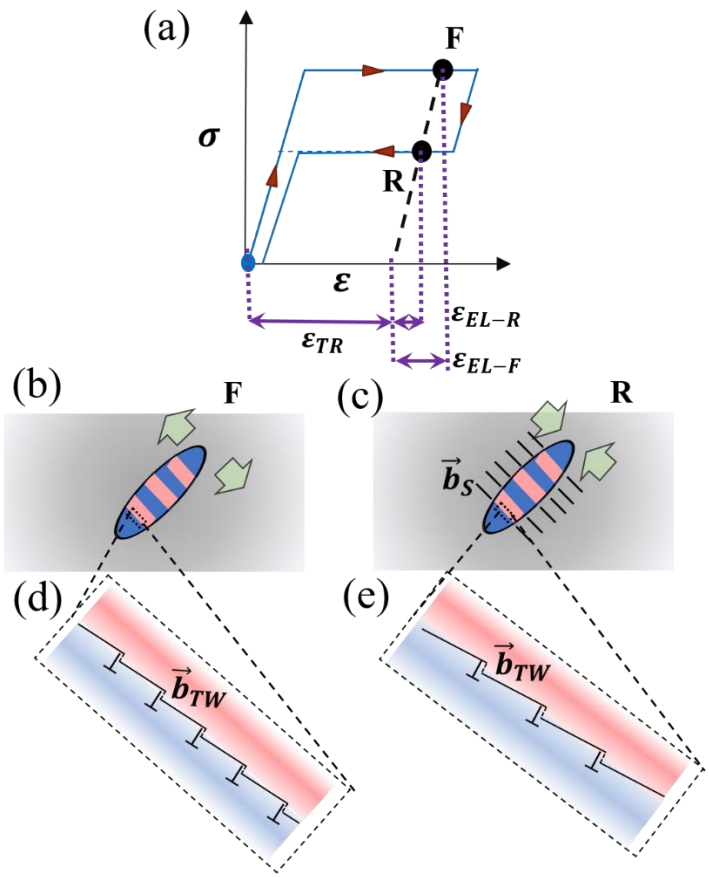

Figure 45: Implications of strain-sensitive twin interface evolution on slip-emission. (a) Schematic illustration of a superelastic response of a Shape Memory Alloy, also showing the partitioning of the prevailing strain-state at any point based on the transformation-strain ε_{TR} and elastic-strain ε_{EL} (b) Nucleated martensitic inclusion within the austenitic phase growing outward, and the internal twinned morphology of the martensite (c) Receding martensitic inclusion and the internal twinned morphology along with emitted slip-lines, with Burgers vector $\vec{b}_S$ (d) martensitic twin interface under higher elastic-strain at F, given by ε_{EL-F}, consequently exhibiting higher twin-disconnection density, with Burgers vector $\vec{b}_{TW}$ (e) martensitic twin interface under lower elastic-strain at R, given by ε_{EL-R}, consequently exhibiting lower twin-disconnection density; the deficit in twin-disconnection density is used to explain the emitted slip based on the law of conservation of Burgers vectors in the system

CHAPTER 5: STRUCTURAL CHARACTERISTICS OF TYPE II TWIN INTERFACES

5.1. Introduction

The understanding of Type II Twin Boundaries (TBs) developed thus far in NiTi, has paved the way for understanding general behaviors of TBs in general, encompassing both Type I and Compound TBs. Admittedly, if not for all the research attention drawn by the irrational structure of the TB, none of the results and consequent resolutions proposed in the previous chapters could have been achieved. Furthermore, the Shape Memory Alloy (SMA) of NiTi, provided a strong foundation for these developments simply because of the strong research interest drawn by the material. And at this stage, it is worthwhile to examine Type II TBs in other SMAs in general, and that is the focus of this chapter.

Type II TBs in the SMAs of TiPd, TiPt, and AuCd are considered in this study, all of which exhibit a B2 austenitic phase and transform to a B19-orthorhombic martensite phase. The Type II TBs are observed in the B19 phase, a generalized unit cell description of which is provided in figure 46. The atomic-site at the lattice point of the unit cell is termed a lattice-site and the remaining atomic-positions within the cell are defined as the motif points. The focus of this study is to examine the applicability of the Terrace-Disconnection (T-D) topology to explain the irrationality of the Type II TBs in these SMAs. And by doing so, the goal is to reveal salient characteristics of the irrational TB that have broader relevance beyond a given specific SMA. Furthermore, such an understanding is further necessary since Type II TBs are commonplace in the thermomechanical responses of several functional materials [55, 58, 179-186]. Table 8 lists all the lattice parameters, atomic positions and crystallographies of the twin interfaces considered in this chapter.

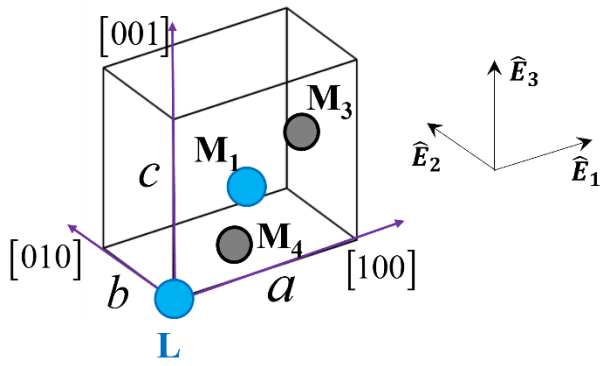

Figure 46: Orthorhombic unit cell of martensitic crystal structures of SMAs considered in this study, comprising unequal lattice parameters a, b, and c, and atomic-sites at lattice (L) and Motif (M) positions; All SMAs in this study have two elemental species, one of them is indicated in blue and the other in gray; an orthonormal coordinate system $\hat{E}_1 - \hat{E}_2 - \hat{E}_3$ aligned with the crystallographic lattice vectors is also shown

Table 8: Crystallography of Type II TBs in SMAs considered in this study

Material	**Austenitic crystal structure**	**Martensitic crystal structure**	**Lattice-Motif atomic positions**	**Crystallography of Type II Twin Boundary**
TiPd	B2 cubic $a_0 = 3.18$ Å [187]	$B19$ Orthorhombic $a = 4.89$ Å, $b = 2.81$ Å, $c = 4.56$ Å [188]	Ti (0,0,0), (0.402, 0,0.5) Pd (0.89, 0.5, 0.5), (0.512, 0.5, 0) [189]	$K_1 = (\bar{1}\ 0.678\ \overline{0.356})$ $\eta_1 = [121], s = 0.361$ [184]
TiPt	B2 cubic $a_0 = 3.192$ Å [187]	$B19$ Orthorhombic $a = 4.84$ Å, $b = 2.76$ Å, $c = 4.59$ Å [188]	Ti (0,0,0), (0.394, 0.0,0.5) Pt (0.885, 0.5,0.5), (0.509,0.5,0) [189]	$K_1 = (\bar{1}\ 0.751\ \overline{0.502})$ $\eta_1 = [121], s = 0.386$ [186]
AuCd	B2 cubic $a_0 = 3.323$ Å [61]	$B19$ Orthorhombic $a = 4.86$ Å, $b = 3.15$ Å, $c = 4.766$ Å [190]	Cd (0,0,0), (0.41,0,0.5) Au (0.9053,0.5,0.5), (0.5047,0.5,0) [190]	$K_1 = (\bar{1}\ 0.774\ \overline{0.547})$ $\eta_1 = [121], s = 0.156$ [61]

The results from Chapters 2 and 4 make it clear that the Terrace-Disconnection topology would be preferred by the twin interfaces owing to the dominance of atomistic potential energies

and its propensity to dictate preference of rational crystallographic terraces. However, there is no basis for the choice of rational terrace preferred by the twin interfaces. This issue is very much unlike NiTi where significant prior research work [35, 36, 38, 39, 62, 64, 66, 67] identified the {111} plane as the rational terrace. Thus, an evaluation of newer Type II systems such as those listed in table 8 offer the opportunity to examine the basis behind the choice of the rational terrace. And given this terrace, the atomistic structure needs to be constructed. Here again, there is no benefit of a reliable interatomic potential as was available in the case of NiTi [92-94]. But this challenge provides the opportunity to determine lattice-offsets more accurately using more accurate Density Functional Theory (DFT) simulations as employed in this study. Furthermore, the analysis of the new Type II systems reveals an important distinction between the classical twinning shear and the shear carried by the twinning disconnections on rational terraces, revealed for the first time in this study to the best of the authors' knowledge.

5.2. Methodology and Results

This section describes the methodology for defining the Terrace-Disconnection topology and the determination of the atomic-structure on the terraces. First, a formal basis behind the choice of rational terraces is provided. The presence of coherence-strains on the terraces is illustrated and the physical origin behind these strains is revealed, grounding the origin in the deformation gradient relating the twin to the matrix. Subsequently, a distinction between the classical twinning shear and a newly-defined "terrace-shear" is forwarded, noting the stronger physical relevance of the latter metric over the former classical definition. Next, the DFT simulations to determine lattice-offset are described, beginning with determination of the lattice-parameters and lattice-motif positions suited to the chosen pseudopotentials. The shear-shuffle twinning mechanisms at the determined offset are illustrated. Finally, the Burgers vector for the twinning disconnection is

crystallographically determined, establishing its relevance to the previously defined "terrace-shear" and finally their periodic spacing in the T-D topology to explain the irrational indices of the Type II TB.

5.2.1. Rational terrace for the Type II TB

The rational-terrace with the lowest Miller-indices is determined for each of the irrational TBs listed in table 8. For this purpose, the real-space and reciprocal-space lattices of the martensitic crystal structure must be defined. The real-space lattice can be defined by a matrix C_{LAT} in which the columns represent the coordinates of the crystallographic basis $[100]-[010]-[001]$ in reference to an orthonormal coordinate system $\hat{E}_1-\hat{E}_2-\hat{E}_3$ (shown in figure 46), given by the equation:

$$C_{LAT}=\begin{pmatrix} a & 0 & 0 \\ 0 & b & 0 \\ 0 & 0 & c \end{pmatrix} \tag{5.1}$$

where a, b and c are the lattice constants of the orthorhombic B19 phase. The coordinates of any crystallographic lattice vector $[uvw]$ is then given by $C_{LAT}\begin{pmatrix} u \\ v \\ w \end{pmatrix}$. The reciprocal space lattice is then defined by the matrix P_{LAT}:

$$P_{LAT}=C_{LAT}^{-T} \tag{5.2}$$

where the columns of P_{LAT} represent the coordinates of the unit-cell lattice vectors of the reciprocal lattice. The coordinates of the normal of any crystallographic plane is given by $\hat{n}=d_{(hkl)}P_{LAT}\begin{pmatrix} h \\ k \\ l \end{pmatrix}$, where $d_{(hkl)}$ is the interplanar spacing given by the inverse-norm of $P_{LAT}\begin{pmatrix} h \\ k \\ l \end{pmatrix}$. With the reciprocal lattice defined, all crystallographic planes (hkl) are plotted in this space and the irrational TB K_1 is also plotted. By viewing the reciprocal space along the direction of twinning $\eta_1=[121]$, the crystallographic plane nearest to K_1 is determined as the rational terrace K_T,

illustrated in figure 47. More precisely, the rational terrace is one which has the nearest normal to that of the irrational interface K_1. Note that the direction of twinning has orthonormal coordinates given by $C_{LAT}\eta_1$ and the reciprocal lattice is viewed along this vector. The rational terrace for all the orthorhombic systems in table 8 is found to be $K_T = (\bar{1}1\bar{1})$. The case of NiTi is also illustrated for reference where the rational terrace $K_T = (11\bar{1})$ is well-known for the irrational type II TB, as also discussed in the previous chapters.

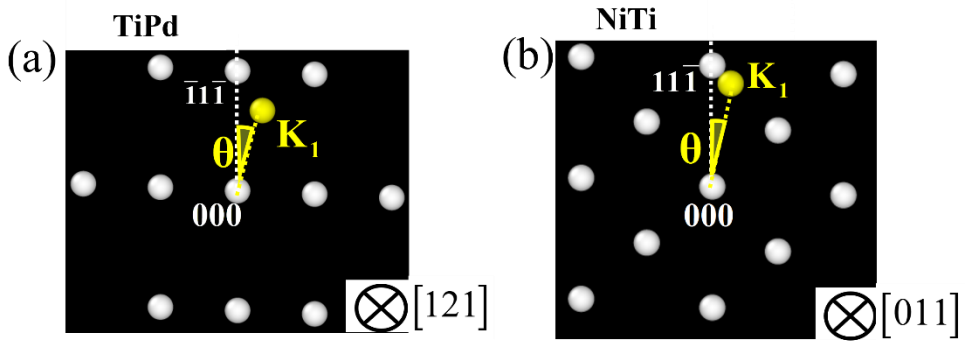

Figure 47: Identification of nearest "least-index" rational terrace of Type II TB from the reciprocal space of the underlying lattice, shown for (a) TiPd, where $K_1 = (\bar{1}\ 0.678\ \overline{0.356})$, $\theta = 17.22^o$ and the rational terrace is $K_T = (\bar{1}1\bar{1})$, and for the better known case of (b) NiTi, where $K_1 = (0.7205\ 1\ \bar{1})$, $\theta = 10.07^o$ and the rational terrace is $K_T = (11\bar{1})$

5.2.2. Coherence strains on the rational terrace K_T

Having established the rational-terrace, the crystallography on the terrace must be examined to construct the equilibrium atomic-structure on this plane. The crystallography is defined with reference to a new orthonormal coordinate system $\hat{e}_1 - \hat{e}_2 - \hat{e}_3$ (refer figure 48). The lattice of the matrix variant is defined as follows. The direction of twinning $\eta_1 = [121]$ is aligned with $\hat{e}_1$, the normal to the rational terrace $K_T = (\bar{1}1\bar{1})$, given by $\hat{n}_T$, is aligned parallel to $\hat{e}_3$. The C_{LAT}^M matrix, introduced in section 5.2.1, can be redefined consistent with this orientation for the matrix variant, and for the case of TiPd, is given by:

$$C_{LAT}^{M} = \begin{pmatrix} 2.7377 & 1.8080 & 2.3807 \\ 3.4350 & -0.0967 & -3.2417 \\ -2.1489 & 2.1489 & -2.1489 \end{pmatrix} \tag{5.3}$$

The crystallographic of the twin variants are chosen consistent with the Type II orientation relationship. Consequently, for the twin variant, C_{LAT}^{T} is given by:

$$C_{LAT}^{T} = (2(\hat{\eta}_1 \otimes \hat{\eta}_1) - I)C_{LAT}^{M} \tag{5.4}$$

where $\hat{\eta}_1 = {C_{LAT}^{M}\eta_1}/{|C_{LAT}^{M}\eta_1|}$ is the unit vector along the direction of twinning $\eta_1 = [121]$. Having defined these orientations, the crystallographic registry between the twin variants, on the rational terrace must be addressed. There exists a shear-mismatch on the rational-terrace K_T as illustrated in figure 48. With the twinning direction η_1 aligned in both variants, the vectors $\vec{\mathrm{v}}_M = [10\bar{1}]_M$ and $\vec{\mathrm{v}}_\mathrm{T} = [\bar{1}01]_T$ are misaligned. An in-plane shear-strain, γ_T must be applied to both the twin and matrix variants for atomic-registry on the terrace (figure 48). The magnitude of the shear-strains for all SMAs considered is listed in table 9, and note that the magnitudes are significant, of the order of few percent. The coherently-strained lattices are defined by the matrices in (5.5).

$$C_{LAT}^{M,C} = \begin{pmatrix} 1 & -\gamma_T & 0 \\ 0 & 1 & 0 \\ 0 & 0 & 1 \end{pmatrix} C_{LAT}^{M} \tag{5.5}$$

$$C_{LAT}^{T,C} = \begin{pmatrix} 1 & \gamma_T & 0 \\ 0 & 1 & 0 \\ 0 & 0 & 1 \end{pmatrix} C_{LAT}^{T}$$

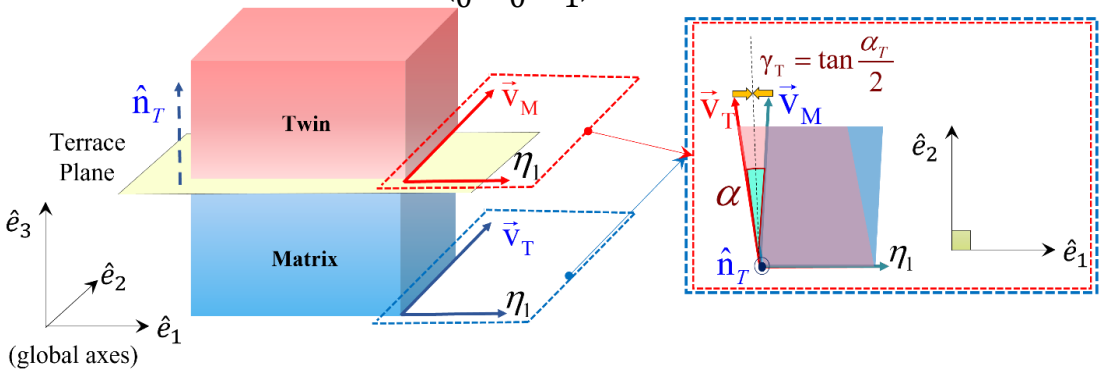

Figure 48: Crystallography of the rational terrace plane with normal $\hat{n}_T$, indicating the common twinning direction η_1, shear-mismatch between lattice vectors $\vec{v}_A$ and $\vec{v}_B$ and coherence strain γ_T required for atomic-registry on the rational terrace; the orthonormal global axes $\hat{e}_1 - \hat{e}_2 - \hat{e}_3$ are also indicated

5.2.3. Concept of "Terrace-shear" and distinction from classical twinning shear

Thus far, the necessity of a coherence-strain was determined from crystallographic considerations on the rational terrace plane. In this section, a physical origin from a continuum mechanics standpoint is offered, noted for the first time in literature, to the best of the authors' knowledge. From classical twinning theory [40] and conventional understanding of twinning, it is well established that the twin variant is related to the matrix by an Invariant Plane Strain (IPS) and the invariant plane is the plane of twinning. And the IPS is given by the deformation gradient of the form:

$$F_{tw} = \left(I + s(\hat{\eta}_1 \otimes \hat{n}_K)\right) \tag{5.6}$$

where s is the classical twinning shear (listed in table 8), the unit vector along the direction of twinning $\hat{\eta}_1$ and the unit normal $\hat{n}_K$ of the irrational twinning plane (refer figure 49(a)). In the coordinate system $\hat{\eta}_1 - \vec{v}_K - \hat{n}_K$ defined on the irrational twinning plane, the deformation gradient is given by:

$$[F_{tw}]_K = \begin{pmatrix} 1 & 0 & s \\ 0 & 1 & 0 \\ 0 & 0 & 1 \end{pmatrix} \tag{5.7}$$

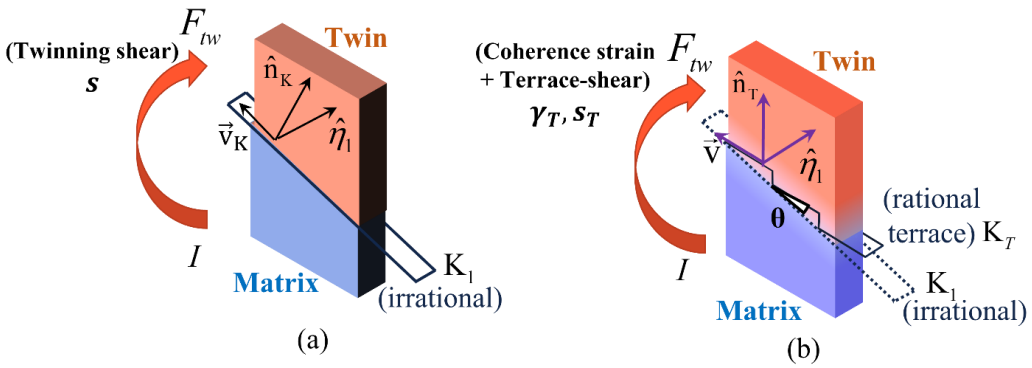

Figure 49: Deformation gradient relating the twin to the matrix described in two frames of reference (a) the conventional coordinate system based on normal to the irrational plane of twinning $\hat{n}_K$, direction of twinning shear η_1 and a third orthonormal vector $\vec{v}_K$; the deformation-gradient only reveals the classical twinning shear s in this system. (b) In the terrace coordinate system described by the terrace-normal $\hat{n}_T$, twinning-shear direction η_1 and third orthonormal vector $\vec{v}$, the deformation-gradient reveals both the coherence-strain γ_T and the terrace-shear s_T; the angle between the rational terrace and irrational plane, θ, is also illustrated

Consider the same deformation gradient resolved along a coordinate system attached to the rational terrace plane, $\hat{\eta}_1 - \vec{v} - \hat{n}_T$ as illustrated in figure 49(b). In this coordinate system, the deformation gradient is obtained from a rotational transformation, given by the following equations:

$$[F_{tw}]_T = [Q]^T [F_{tw}]_K [Q]$$

$$[Q] = \begin{pmatrix} 1 & 0 & 0 \\ 0 & \cos\theta & \sin\theta \\ 0 & -\sin\theta & \cos\theta \end{pmatrix} \tag{5.8}$$

$$[F_{tw}]_T = \begin{pmatrix} 1 & -\gamma_T & s_T \\ 0 & 1 & 0 \\ 0 & 0 & 1 \end{pmatrix}$$

where θ is the angle between the irrational plane K_1 and the rational terrace K_T (refer figure 49 and figure 47, illustrating the angle in the reciprocal space). Note that the components of the deformation gradient F_{tw} resolved in the terrace coordinate system directly yields the coherence strain γ_T. Additionally, a new metric s_T is revealed which is defined as the "terrace-shear". The terrace-shear s_T is the shear required to twin on the rational terrace. It transforms the coherently-strained matrix to the coherently-strained twin variant, and recall that these coherence-strains are necessary for atomic-registry on the terrace. Figure 50 (a) illustrates the role of terrace-shear s_T in twinning the atomic-structure on the terrace-plane for TiPd. A comparison is provided with the well-studied {111} twinning mode in Face-Centered-Cubic materials (Copper, Cu, chosen as example) shown in figure 50(b), where such a distinction between terrace-shear and twinning-shear is not required. The significance of this distinction will be discussed in section 6.3. Table 9 lists all the terrace-shears for the SMA systems considered, note that they are all not equal to the classical twinning shears listed in table 8 previously. The following section outlines the procedure to determine the atomic-structure on the rational terrace planes.

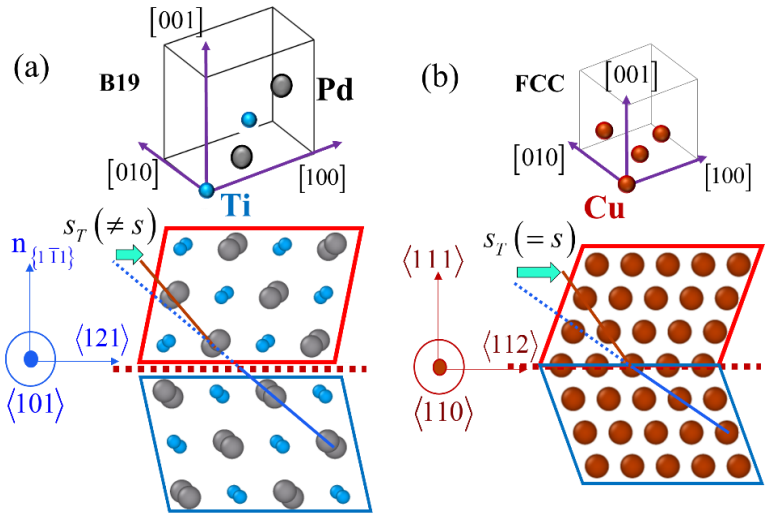

Figure 50: Physical significance of the distinction between twinning-shear s and terrace-shear s_T: (a) the terrace-shear s_T describes the shear on coherently-strained rational-terrace of the Type II twin in orthorhombic TiPd, and this shear is distinct from the classical twinning shear s. (b) Such a distinction is absent and thus cannot be inferred from twinning behavior of highly-symmetry crystal structures such as {111} twinning in FCC materials e.g. Cu, as shown

Table 9: Coherence-strains required on rational terraces of Type II TBs

Material	**Type II Twin Boundary (K_1)**	**Twinning shear, s**	**Rational-Terrace K_T** (with normal $\hat{n}_T$)	**Coherence-strain, γ_T** (%)	**Terrace-Shear, s_T**
TiPd	$(\bar{1}\ 0.678\ \overline{0.356})$	0.361	$(\bar{1}1\bar{1})$	5.35	0.345
TiPt	$(\bar{1}\ 0.751\ \overline{0.502})$	0.386	$(\bar{1}1\bar{1})$	4.09	0.376
AuCd	$(\bar{1}\ 0.774\ \overline{0.547})$	0.156	$(\bar{1}1\bar{1})$	1.42	0.153

5.2.4. Determining the atomic-structure on the terrace: Lattice offsets

The atomic-structures are determined using atomistic simulations performed within a Density Functional Theory (DFT) framework using the Vienna Ab-initio Simulation Package (VASP) [89]. For the simulations, the pseudopotentials with Projector-Augmented-Wave (PAW) basis wavefunctions and Perdew-Burke-Ernzerhof parametrization of Generalized-Gradient-

Approximation (PBE-GGA) exchange-correlation functional were employed. First, the converged DFT parameters are determined, namely the plane-wave energy cut off E_{CUT} and the number of k-points. Self-Consistent-Field (SCF) simulations are run on a B2 unit cell, with the lattice constant a_0 chosen to be that obtained from experiment (listed in table 8). The energy tolerance for convergence of the SCF calculations was chosen to be 1 meV. The simulations are performed at increasing magnitudes of the energy cut-off E_{CUT} and the number of *k*-points until the total energy of the system converges within 5 meV/atom. The values of parameters at which this convergence is achieved are used for subsequent simulations of the twin boundary atomic structure. The converged magnitudes of the plane-wave energy cut-off and the number of k-points are found to be $E_{CUT} = 550$ eV and $k_{CUT} = 12$ respectively (illustrated in figure 51). Note that, although results in figure 51 are illustrated from simulations on TiPd, individual simulations for each SMA system were performed and converged parameters were obtained. It was found that the set of values ($E_{CUT} = 550$ eV, $k_{CUT} = 12$) sufficed for all the systems considered in this study.

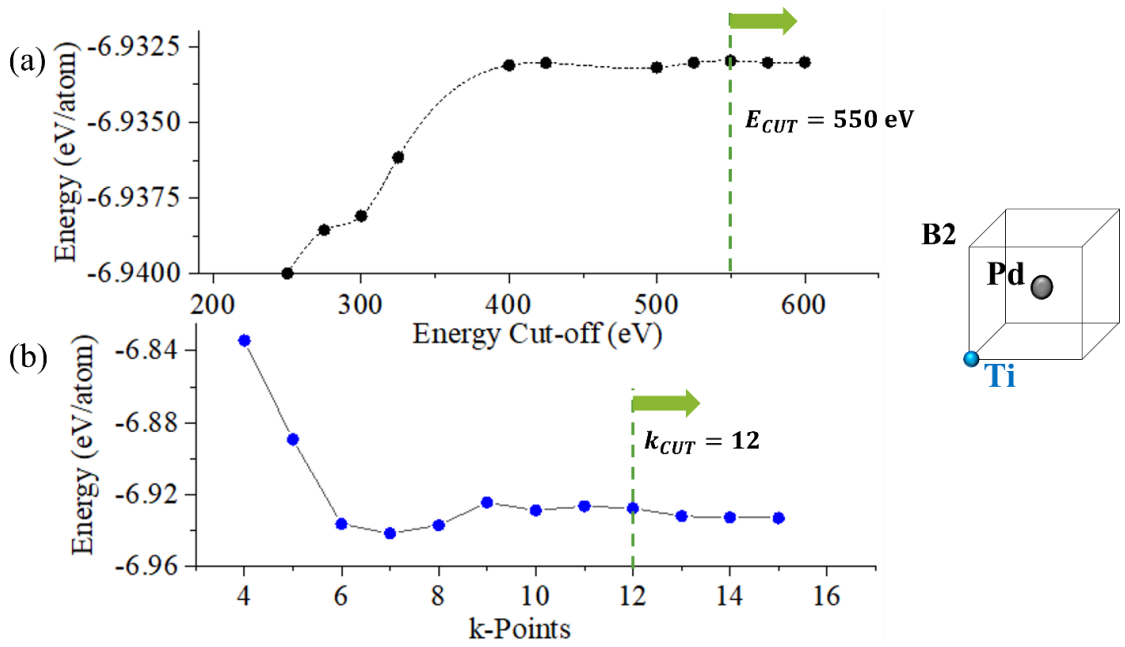

Figure 51: DFT parameters for simulations of lattice-offset and twin boundary energy: (a) Energy cut-off E_{CUT} and (b) number of k-points; the B2 simulation cell used for the simulations is illustrated, with the example of TiPd

Next, the B19 orthorhombic lattice constants consistent with the chosen pseudopotentials must be determined. The procedure is described for TiPd in this section, and the same was applied for both TiPt and AuCd as well. First, the volume of the unit cell is determined, by performing fixed-volume SCF calculations results of which are given in figure 52 (a). Then the individual ratios b/a and c/a are varied across a grid to determine the most energetically favorable pair, the results of which are illustrated in figure 52 (b). With the energy-minimizing lattice constants, a, b, c, an ionic-relaxation is performed (with a force tolerance of 5 meV/Å) to determine the equilibrium atomic-positions within the B19 unit cell. Results of the DFT lattice constants and lattice-motif positions for the unit cell are listed in table 10.

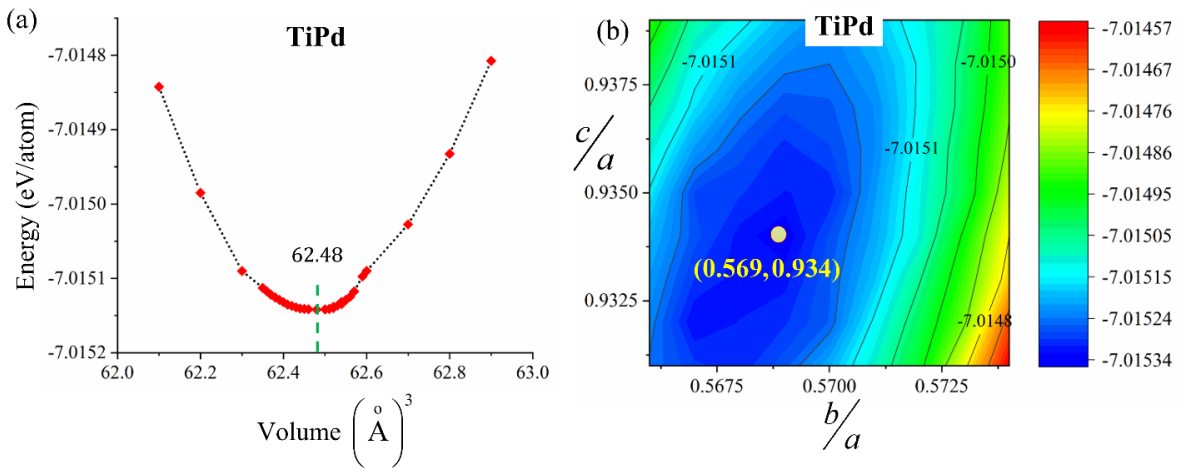

Figure 52: Determination of (a) B19 unit-cell volume and (b) B19 lattice-parameter ratios of orthorhombic cell of TiPd

Having determined the lattice constants suitable for the simulations, the twin boundary structure can now be determined. Note that both the atomic-structures of both the matrix and twin variants will be subject to the coherence-strains defined in section 5.2.2 and defined by $C_{LAT}^{M,C}$, $C_{LAT}^{T,C}$ respectively, defined by equation (5.5). First, a periodic simulation cell suitable for the TB structure must be defined. And since DFT calculations are expensive and scale quickly with the number of atoms, care must be taken to involve the least number of atoms in the structure. And owing to the non-cubic structure of the martensite, the simulation cell is found to be triclinic, illustrated in figure 53 (a). The bounding box vectors $\vec{L}_1 - \vec{L}_2 - \vec{L}_3$ are defined with reference to the same orthonormal coordinate system $\hat{e}_1 - \hat{e}_2 - \hat{e}_3$. And the vector components for these vectors are obtained through the matrix $C_{LAT}^{M,C}$ defined in equation (5.5). For instance, the vector $\vec{L}_2 = [110]_M$ has the coordinates $C_{LAT}^{M,C}\begin{pmatrix}1\\1\\0\end{pmatrix}$, and the other vectors $\vec{L}_1 = [121]$, $\vec{L}_3 = 4[\bar{1}1\bar{1}]_M$ are determined similarly. There is no subscript on $[121]$ as it is identical in both the matrix and the twin variant. The vector $\vec{L}_2$ is aligned with $[011]_T$ in the coherently-strained twin crystal structure. A total of 12 $K_T = (\bar{1}1\bar{1})$ planes are simulated with $N = 6$ planes corresponding to the twin

variant, remaining 6 to the matrix variant, and with each plane containing 4 atoms (shown in figure 53 (b)). And to incorporate 6 twin planes, the vector $\vec{L}_3$ must be incremented by $Ns_T d_{(\bar{1}1\bar{1})}$, where $d_{(\bar{1}1\bar{1})}$ is the interplanar spacing, accounting for the presence of the twinning shear in the system (figure 53 (b)). This is necessary as without this shear, the periodicity across the top and bottom boundaries of the simulation cell would be broken precluding an accurate simulation of the twinned structure.

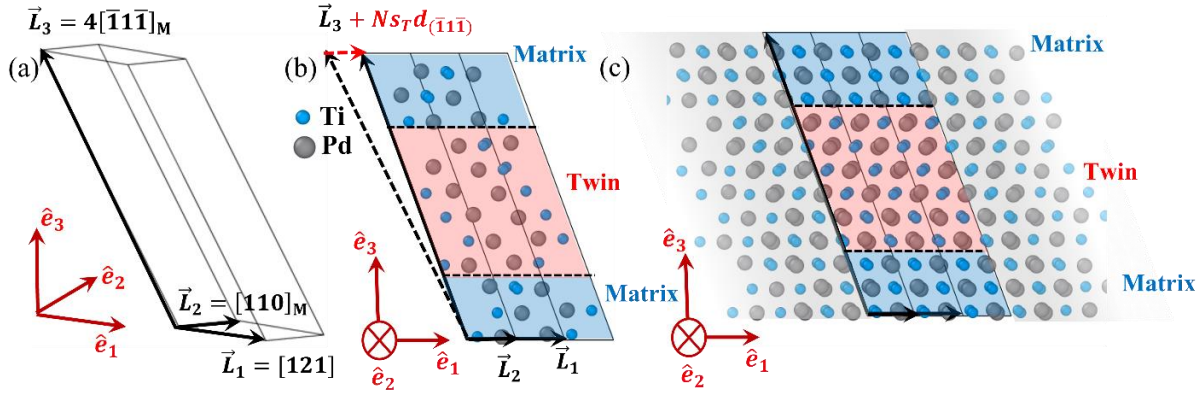

Figure 53: Construction of simulation cell in DFT for analysis of twinned structure: (a) Triclinic simulation cell with lattice vectors $\vec{L}_1 - \vec{L}_2 - \vec{L}_3$ defined in an orthonormal basis $\hat{e}_1 - \hat{e}_2 - \hat{e}_3$; this cell is suitable to construct a single pure variant of the matrix crystal structure (b) Twinned structure constructed within simulation cell, where the vector $\vec{L}_3$ is corrected with the applied terrace-shear, s_T based on the number of twin-planes (with interplanar spacing $d_{(\bar{1}1\bar{1})}$) included in the simulation cell, N; there are 4 atoms per $\{111\}$ plane within this cell (c) Twinned structure illustrated with multiple periodic images across the periodic boundaries, illustrated only for visualization and not used in simulation

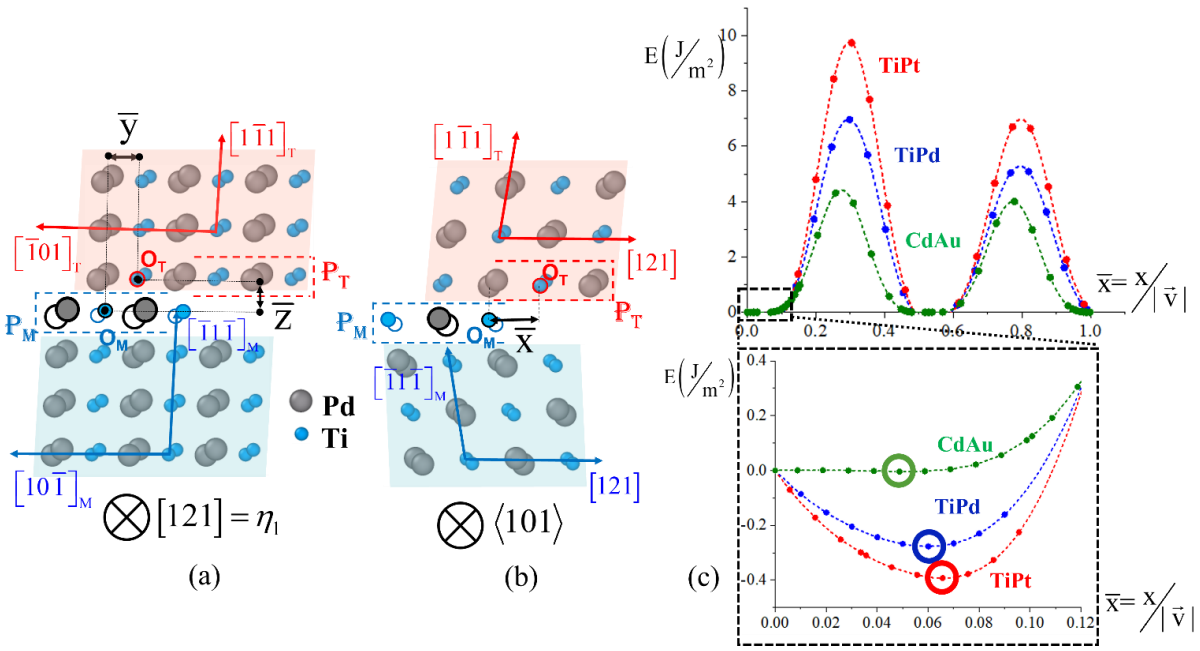

Figure 54: Determination of lattice-offset for construction of twin boundary structure: Defining the normalized lattice-offsets (a) $(\bar{y}, \bar{z})$ and (b) $\bar{x}$; the energy-minimizing offset is determined from DFT simulations, results of which are shown in (c)

Having defined the simulation cell, the TB structure can now be determined. The crystallography of the K_T terrace is not atomically flat as noted previously in figure 50. Furthermore, the atomic-positions in the matrix and twin are not commensurate with each other precluding the construction of the TB as a common plane between the variants (refer figure 53 (c)). The atomic-structure must be unambiguously defined by determining the relative position of the twin variant with respect to the matrix. This relative position is otherwise termed as the lattice-offset, defined and determined for the TBs considered as follows. Two reference origin points O_T and O_M are chosen on the lattice-sites of two crystallographic planes P_T and P_M, shown in figure 54 (a). Recall that the lattice and motif sites were defined in section 5.1. The plane P_T lies on the twin variant and P_M is a virtual crystallographic plane that were to exist if the matrix variant was presumed to extend by one more plane into the twin. The triad vector (x, y, z) describing the

relative position of O_T with respect to O_M defines the lattice-offset vector to be determined. Given the periodicity of the lattice, the vector can be defined in a normalized form given by:

$$\bar{x} = \frac{x}{|[121]|}; \bar{y} = \frac{y}{|[10\bar{1}]|}; \bar{z} = \frac{z}{d_{(\bar{1}1\bar{1})}} \tag{5.9}$$

where $d_{(\bar{1}1\bar{1})}$ is the interplanar spacing of the $(\bar{1}1\bar{1})$ planes. The components $(\bar{y}, \bar{z})$ can be determined based on two considerations:

a. The volume must be conserved during twinning, therefore requiring the interplanar spacing to be preserved as one moves from the matrix to the twin. This determines $\bar{z}$.
b. The crystal structure of the matrix and the twin would look identical when seen along the direction of twinning $\eta_1 = [121]$. This determines $\bar{y}$.

The magnitude of $\bar{x}$ however requires atomistic simulation and is not known apriori. At incremental magnitudes of $\bar{x}$ between 0 and 1, an SCF simulation is performed to determine the potential energy of the atomic-structure at that offset. The magnitude of $\bar{x}$ that yields the lowest energy is determined. The results are plotted in figure 54 (c). The relative changes in the TB potential energy are plotted with respect to the energy at zero-offset i.e. at $\bar{x} = 0$. Non-trivial lattice-offsets were found and are reported in table 10, determined to within ± 0.01. These findings of non-trivial lattice-offsets are consistent with priorly discussed results in NiTi in chapter 2, also reported in ref. [155]. And without the simulation of the energetics, there is no basis on which a reliable choice for $\bar{x}$-offset can be made apriori. The second set of minima near 0.5 is a crystallographic equivalent position thereby being energetically degenerate. Determination of the lattice-offset unambiguously defines the relative position of the twin variant with respect to the matrix and completes definition of the TB structure on the rational terrace.

Table 10: Energy-minimal lattice-parameters and lattice-offset triads determined from DFT to determine the equilibrium twin boundary structure on rational terraces

Material	**Martensitic crystal structure (From DFT)**	**Lattice-Motif atomic positions (from DFT)**	**Lattice-Offset triad** $(\bar{x}, \bar{y}, \bar{z})$
TiPd	$a = 4.899$ Å, $b = 2.787$ Å, $c = 4.576$ Å	Ti (0,0,0), (0.403,0,0.5) Pd (0.89,0.5,0.5), (0.513,0.5,0)	(0.06,0.450,0.097)
TiPt	$a = 4.874$ Å, $b = 2.764$ Å, $c = 4.626$ Å	Ti (0,0,0), (0.395,0,0.5) Pt (0.885,0.5,0.5), (0.509,0.5,0)	(0.066,0.446,0.105)
AuCd	$a = 5.009$ Å, $b = 3.176$ Å, $c = 4.899$ Å	Cd (0,0,0), (0.409,0,0.5) Au (0.504,0.5,0), (0.905,0.5,0.5)	(0.05,0.454,0.091)

5.2.5. Shear-shuffle partitioning of the twinning mechanism

Now that the lattice-offsets are determined, the final atomic-structure on the rational terrace is known. This can be used to determine the mechanism of twinning the matrix variant to the twin, involving shuffle-movements of atoms in addition to the twinning shear. The shuffle motions are determined by overlapping the sheared matrix variant (figure 55 (a, b)) with the atomic-structure of the TB at the determined offset (figure 55 (c)). The shuffle movements indicate both horizontal and vertical shuffle motions for the Ti and Pd atoms, extending over two crystallographic planes. The net average shuffle over both the planes is zero, consistent with classical twinning theory [40]. Thus, knowledge of the atomic-structure at the right offset determines the correct shear-shuffle partitioning in the mechanism of twinning.

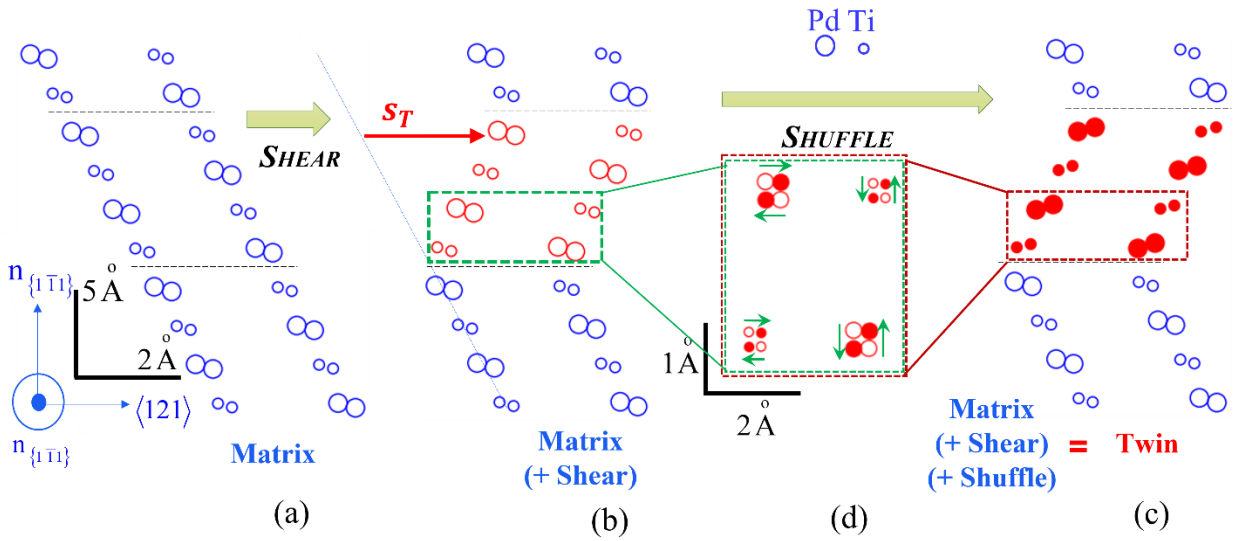

Figure 55: Shear-Shuffle mechanism of twinning at the energy-minimal lattice-offset, illustrated for TiPd: (a) Atomic-structure of the matrix variant (b) Sheared matrix variant without shuffle (c) Atomic-structure of the twin at the determined lattice-offset (d) Overlapped atomic-positions of the sheared-variant and twinned structure yielding the shuffle-mechanisms involved in twinning

5.2.6. Twinning disconnection Burgers vector

So far the crystallography and atomic-structure of the rational terrace plane has been addressed. Defining the Terrace-Disconnection (T-D) topology requires the Burgers vector and step height of the twinning disconnection. The Burgers vector is determined following the methods developed in refs. [40, 69, 82, 83, 159], found to be the smallest-norm difference-vector between two translational symmetry vectors in the matrix and twin variant. The translational symmetry vectors are found to be $[1\bar{1}0]_T$ and $[\bar{1}10]_M$, thereby yielding the Burgers vector as:

$$\vec{b}_{tw} = [1\bar{1}0]_T - [\bar{1}10]_M = 2s_T d_{(\bar{1}1\bar{1})} \tag{5.10}$$

Thus the step height of the disconnection is $h_D = 2d_{(\bar{1}1\bar{1})}$. Note that Burgers vector corresponds to the terrace-shear defined in section 5.2.3, and not the twinning shear. The Burgers vector is illustrated in figure 56 plotted over what is known as the "Dichromatic complex" [69, 191] of the matrix and twin variants, determined at the calculated lattice-offset. The Burgers vectors are all aligned with the direction of twinning shear η_1 and their magnitudes are listed in table 11.

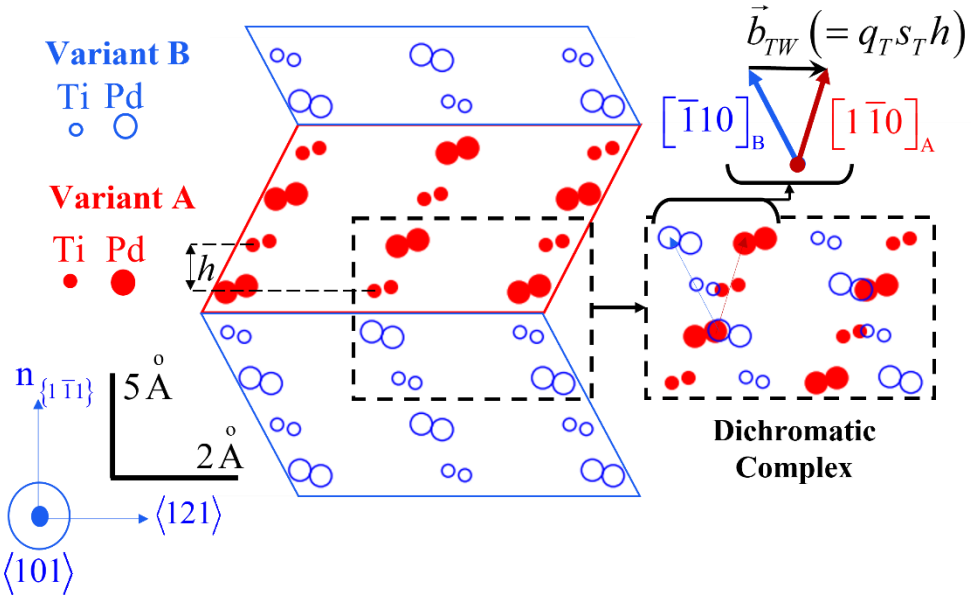

Figure 56: Dichromatic complex of the Twin Boundary illustrating the Burgers vector of the twinning disconnection $\vec{b}_{TW}$ on the constructed dichromatic complex [69, 191]

5.2.7. Terrace-Disconnection topology of the Type II TBs

Finally, the irrationality of the Type II TBs are explained using the T-D model by deriving the spacing between the twinning disconnections and the Miller-index identity of the effective stepped topology. The twinning disconnections will be periodically spaced on the rational terrace such that their strain-field exactly cancels out the coherence-strains on the rational terrace. For the shear-mismatch strain on the rational terraces, an array of screw-dislocations with dislocation lines parallel to η_1 will cancel out the coherence strain exactly. The spacing of these dislocations to nullify the strain is determined from the Frank-Bilby equation, given by:

$$\vec{B} = \frac{\vec{b}_{tw}}{d} = -\boldsymbol{E}_c.\vec{\mathrm{v}} = -\left(\boldsymbol{D}_{\boldsymbol{T}}^{-\mathbf{1}} - \boldsymbol{D}_{\boldsymbol{M}}^{-\mathbf{1}}\right)\vec{\mathrm{v}} \tag{5.11}$$

where $\vec{\mathrm{v}}$ is the vector perpendicular to the direction of the dislocation line, in this case perpendicular to η_1 (refer figure 57). The tensor $\boldsymbol{E_c}$ represents the three-dimensional coherence-strain-mismatch tensor between the matrix and the twin variant. The tensors $\boldsymbol{D}_{\boldsymbol{T,M}}^{-\mathbf{1}}$ represent the

deformation gradients that map the coherently-strained state of the twin and matrix, respectively, to their unstrained states, given by the equations:

$$\boldsymbol{D}_{\boldsymbol{T}}^{-\mathbf{1}} = \begin{pmatrix} 1 & -\gamma_T & 0 \\ 0 & 1 & 0 \\ 0 & 0 & 1 \end{pmatrix}; \; \boldsymbol{D}_{\boldsymbol{M}}^{-\mathbf{1}} = \begin{pmatrix} 1 & \gamma_T & 0 \\ 0 & 1 & 0 \\ 0 & 0 & 1 \end{pmatrix} \tag{5.12}$$

The disconnection spacing is consequently determined as:

$$d = {}^{2\gamma_T}\Big/_{|\vec{b}_{tw}|} \tag{5.13}$$

Consequently, the angle of inclination of the stepped topology is given by $\theta = \tan^{-1}\frac{h_D}{d}$. Both d and θ are listed in table 11 for all SMAs considered in this study. The Miller-indices of the effective plane defined by the topology can be obtained from the reciprocal space lattice P_{LAT}^{M} given by the equation (5.14). The indices are normalized such that one of the index is unity and listed in table 11.

$$\begin{pmatrix} h \\ k \\ l \end{pmatrix} = (P_{LAT}^{M})^{-1} \begin{pmatrix} 0 \\ -\sin\theta \\ \cos\theta \end{pmatrix} \tag{5.14}$$

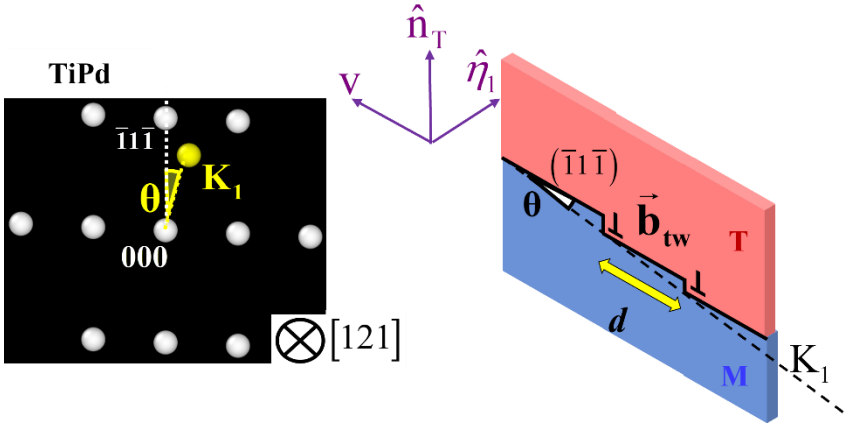

Figure 57: Terrace-Disconnection topology of Type II Twin Boundary, with periodic array of twinning disconnections $\vec{b}_{tw}$ with spacing d; the angle of deviation θ between the irrational plane and the rational-terrace initially seen in the reciprocal lattice is reproduced in the T-D topology

Table 11: Effective irrational-plane predicted by Terrace-Disconnection topology, through the Frank-Bilby equation

Material	**Burgers vector of twinning disconnection $\lvert\vec{b}_{TW}\rvert$ (Å)**	**Spacing between disconnections, d (Å)**	**Angle of deviation, θ (^{o})**	**Type II Twin Boundary (K_1)**
TiPd	1.482	13.85	17.24	$(\bar{1}\ 0.678\ \overline{0.355})$
TiPt	1.608	12.2	12.2	$(\bar{1}\ 0.748\ \overline{0.496})$
AuCd	0.715	24.986	10.48	$(\bar{1}\ 0.786\ \overline{0.573})$

5.3. Discussions

The purpose of this study is to apply the Terrace-Disconnection topological structural model to explain the irrationality of Type II TBs in other SMAs. And by doing so, it is expected that further generalized characteristics of this TB could be deciphered. In the well-studied NiTi system, research on the Type II TB has greatly benefited from the availability of extensive experimental results, postulates regarding the possible rational terrace and the availability of interatomic potentials for atomistic simulations [35, 36, 38, 39, 62, 64, 66, 67, 92-94]. In moving beyond this system and examining other Type II TBs, the conspicuous absence of similar groundwork posed multiple challenges associated with definition of the rational terrace plane, the physical origins of the coherence strains, choice of a suitable atomistic framework etc. This study proposes to resolve these aforementioned challenges and gleans certain generalized characteristics of Type II TBs that would be of both academic relevance in the field of twinning and of technological relevance in SMA materials.

The first challenge in studying the Type II TBs is the definition of the rational terrace. On first look, it is not trivial to determine the nearest rational terrace for all the irrational TBs listed in

table 8. For instance, in TiPd, the rational terrace for irrational plane $\left(\bar{1}\ 0.678\ \overline{0.356}\right)$ could be postulated as either $K_T = (\bar{1}1\bar{1})$ or $K_T = (\bar{1}10)$. An objective approach was proposed in section 5.2.1 where the nearest-terrace could be determined by visualizing the discrete reciprocal space lattice, immediately noting the preference of $(\bar{1}1\bar{1})$ over $(\bar{1}10)$. Note that this approach, in effect, only finds the rational-terrace with a normal closest to the irrational plane. Although simple, there is an important challenge that this approach overcomes. When it comes to the choice of rational terraces, one could always choose a better rational-approximation, say $K_T = (\bar{5}3\bar{1})$ or $K_T = (\bar{7}5\bar{3})$. And in the reciprocal space, the normals to these terraces would indeed be closer to the normal to K_1. However, their high Miller-indices imply the atomic-densities on these planes would be low and a low planar density would lead to higher atomistic potential energy of the TB. In fact, this was recently illustrated explicitly in NiTi [192], where the potential energy of a low-index rational plane was shown to have much lower potential energy than a higher-index rational plane, using Molecular Statics simulations. Therefore, it is energetically preferable for the rational terrace to have the *least possible* Miller indices. And by visualizing the reciprocal space lattice points, the least-index planes closest to K_1 can be unambiguously determined by focusing only on the lattice-points closest to the central 000 zone (refer figure 47 (a)).

Once the rational terrace is determined, the required coherence-strains on the terrace can be determined by examining the crystallography on the terrace as illustrated in section 5.2.2. The necessity of atomic-registry on the terrace dictates the alignment of crystallographic vectors $\vec{\mathrm{v}}_M = [10\bar{1}]_M$ and $\vec{\mathrm{v}}_\mathrm{T} = [\bar{1}01]_T$, revealing the requirement of coherence-strain γ_T. Though from a continuum mechanics, it is a necessary question to ask where this strain originates from. And for the first time, a partitioning between the terrace coherence-strain and terrace-shear is shown in section 5.2.3, resulting from a simple rotational transformation of the twinning deformation

gradient. This partitioning is necessary to understand since, on the terrace, the shear that transforms the matrix to the twin is indeed the terrace-shear and not the twinning-shear (illustrated in figure 50). This effect is also illustrated in the calculated Burgers vector of the twinning disconnection in section 5.2.6. The Burgers vector was determined crystallographically, from a difference of lattice-symmetry vectors, and the calculated magnitude turns out to be a multiple of s_T and not s. Therefore, as the Burgers vector sweeps through the terrace, it carries the shear of ${}^{b_{tw}}/_{h_D} = s_T$ i.e. the terrace-shear and not the twinning shear. Such an understanding could not have been achieved from more common Compound twins in FCC materials or even rational Type I twins in SMAs where none of the aforementioned issues are observed. It was the problem of irrationality of the Type II TBs and consequent necessity of the T-D topology that has led to this understanding.

Furthermore, in the absence of a reliable interatomic potential, a formal procedure to determine the atomic-structure on the rational terraces of Type II TBs is offered within a DFT framework, in section 5.2.4. The lattice-offsets are critical to establish the correct TB structure, TB energy and to reveal the shear-shuffle mechanism as done in section 5.2.5. For non-single-lattice structures, as considered in this study and as prevalent in multiple other martensitic phases of SMAs, these offsets overcome the ambiguity in determining the TB given the incommensurate and non-flat atomic-structures of the twinning plane (i.e. $(\bar{1}1\bar{1})$ in this case). And these offsets, particularly $\bar{x}$, cannot be determined without a simulation of the energetics of the TB. And although $\bar{x}$ is determined to be zero, it is obtained only as a result of such a simulation and cannot be presumed as such apriori. The importance of such offsets has been noted in crystal structures beyond SMAs as well, such as in HCP materials [193]. It is only at the correct offset that the shuffle-mechanism necessary for twinning is revealed (section 5.2.5 and figure 55). And although out of scope for the current work, it must be mentioned that the energetics of twin-migration can

only be determined after the shuffle-mechanism is known. The orthorhombic SMAs in this study exhibit a 2-plane shuffle mechanism, the net vectorial average of which is zero, consistent with classical twinning theory [40].

Finally, section 5.2.7 establishes how the T-D topology sufficiently explains the irrationality of all Type II TBs considered in this study. The twinning-disconnections are spaced such that they nullify the coherence-strain at the terrace, γ_T, in the far-field away from the TB. And recall from previous discussion that the twinning-disconnections only carry the terrace-shear s_T. Both these points reveal an elegance behind the adoption of the T-D topology by the TB. This is illustrated in figure 58 below. In figure 58 (a), the classical notion is illustrated. By this notion, for minimum strain-energy from a continuum-mechanics standpoint, the twin plane must inhabit an invariant plane shared between the twin and matrix so that there are no strain-energies in the system and both the crystal-structures are in their un-strained native configurations. This requirement leads to determination of the invariant plane K_1 as having an irrational Miller-index identity, and the twinning shear s necessary to transform the matrix to the twin. However, here lies the catch. The irrational plane, while a perfectly plausible continuum entity, is not an energetically favorable atomic-plane for the TB. As has been shown before in chapter 4, if the TB were to reside on such a plane it would have to pay the cost of a high atomistic potential energy. This is not preferred by the material and instead an alternative route is taken. The interface adopts a T-D topology where there are rational terraces that are strained into coherence, with coherence-strains γ_T. By inhabiting a low-index rational terrace, the atomistic potential energy is minimized, at the cost of the continuum strain-energy of having coherence-strains. However, these strains-are relieved by a periodic arrangement of twinning-disconnections on the topology. And note that when the twin-migrates, the twinning disconnections only carry a part of the classical twinning

shear s, and it is only the terrace-shear s_T. And by relieving the strain-energy in the bulk, the cost additional of continuum strain-energy is minimized to a magnitude near insignificant compared to the gained reduction of atomistic potential energy in preferring a rational terrace. Thus, the picture of twinning changes from a continuum-compatible (K_1, s) description to a continuum- and atomistic- compatible (K_T, s_T, γ_T) picture as shown in figure 58 (b). In summary, the T-D topology is, in a manner of speaking, the material's solution to exhibiting an effective irrational plane by involving atomistically-favorable rational terraces and continuum-favorable periodic disconnections relieving far-field strains.

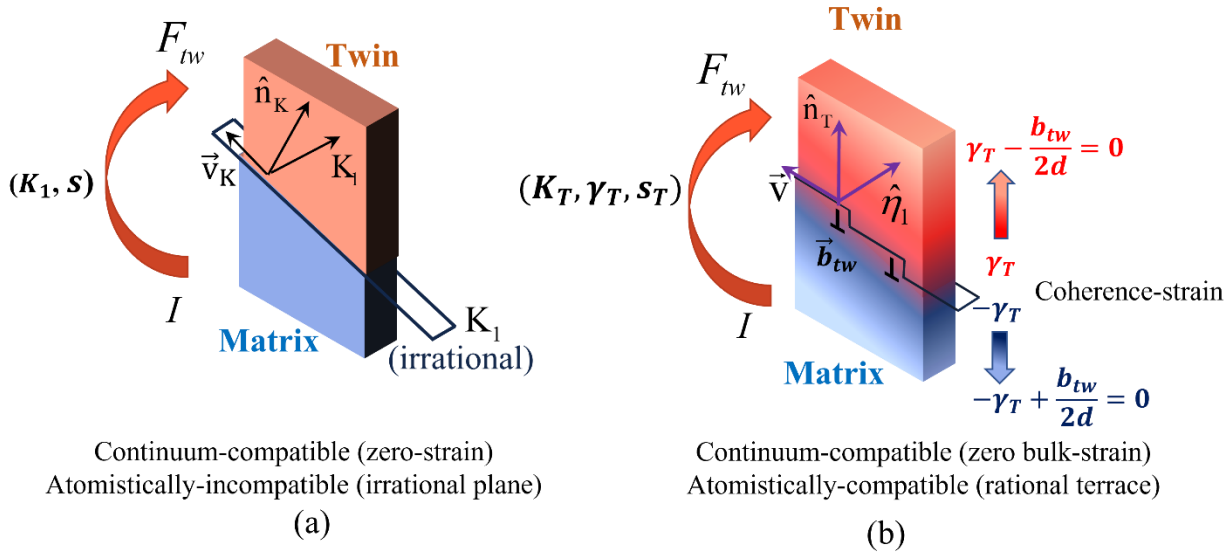

Figure 58: Physical significance of the Terrace-Disconnection (T-D) topology for Type II TB: (a) In the classical twinning description, the twinning shear s is applied on the irrational twinning plane K_1; this structure would yield zero continuum strain-energy but implies a higher atomistic potential energy on the irrational plane. (b) The T-D topology achieves an effective compromise where there are coherence-strains γ_T sustained on a rational terrace K_T, subsequently nullified by a periodic arrangement of twinning disconnections $\vec{b}_{tw}$, ultimately attributing a stepped nature that explains the irrational indices

5.4. Conclusions

This chapter focuses on Type II twins in multiple SMAs exhibiting orthorhombic martensitic crystal structures. The irrational identities of all TBs are explained using the T-D topology revealing novel general characteristics exhibited by this type of TB. It is shown that the choice of rational terrace comes from the reciprocal space of the crystal lattice and that the terrace should be a low-index plane to have the highest planar atomic-density. The origin of the coherence strain on the terrace is shown from both a crystallographic standpoint and from a continuum kinematics standpoint. The continuum perspective reveals the partitioning of the classical twinning shear s on the irrational plane K_T to coherence-strain and terrace-shear (γ_T, s_T) components on the T-D topology. The atomic-structure on the rational-terraces are determined from DFT calculations establishing formal procedures to construct TB structures within the simulation framework. The energy-minimizing lattice-offsets are determined to construct the TB structure on the terrace. The knowledge of the TB structure led to determination of the shear-shuffle mechanism of twinning illustrating a 2-plane shuffle mechanism. The Burgers vector of the twinning disconnection was determined from both a crystallographic approach, involving translational symmetry vectors, and it is shown for the first time that the Burgers vector carries the terrace-shear s_T and not the twinning shear s, on the rational terrace. The spacing of the twinning disconnections on the terrace is calculated from the Frank-Bilby equation, closely reproducing the irrational Miller-index identity of the Type II TB. A novel perspective on the energetic preference of the T-D topology by the Type II TB is forwarded, discussing how the topology balances both the continuum-energy and atomistic-energy considerations. Such an understanding could not have been achieved from rational TBs such as Compound twins in FCC materials or Type I twins in SMAs and is a necessary advancement in understanding the energetics of twin interfaces.

CHAPTER 6: AUSTENITE-MARTENSITE ORIENTATION RELATIONSHIPS

6.1. Introduction

The study thus far has focused on the internal twin interface within the transformed martensite and its role in slip-emission. To fully explain the formation of dislocation-slip in the austenitic (henceforth symbolized by A) phase, the emission mechanism must address the relative orientation of the slip-planes in the austenitic phase in relation to the internal twin interface of the martensite (henceforth symbolized by M). In other words, the relative lattice orientation between the parent austenite and the transformation martensite must be addressed. This Orientation Relationship (OR) between A and M phases are generally described by two parallelism conditions: (i) the first parallelism is between two crystallographic planes, one in the A-lattice $(hkl)_A$ and another in the M-lattice $(h'k'l')_M$, (ii) the second parallelism is between two crystallographic directions, one in the A-lattice $[uvw]_A$ and another in the M-lattice $[u'v'w']_M$ (refer figure 59). Such ORs have long been established experimentally for several SMAs [39, 97, 194-197] and are typically attributed to be a unique property of the material. The OR can equivalently be stated as an invariancy of the two elements in the parent phase involved in the parallelism condition – a crystallographic plane $(hkl)_{\mathrm{A}}$ and a crystallographic direction $[uvw]_A$ – during the transformation. Therefore, the OR can be specified by the invariant plane $(hkl)_{\mathrm{A}}$ and direction $[uvw]_A$ in the parent phase, or more generally by the families $\{hkl\}_A$ and $\langle uvw\rangle_A$.

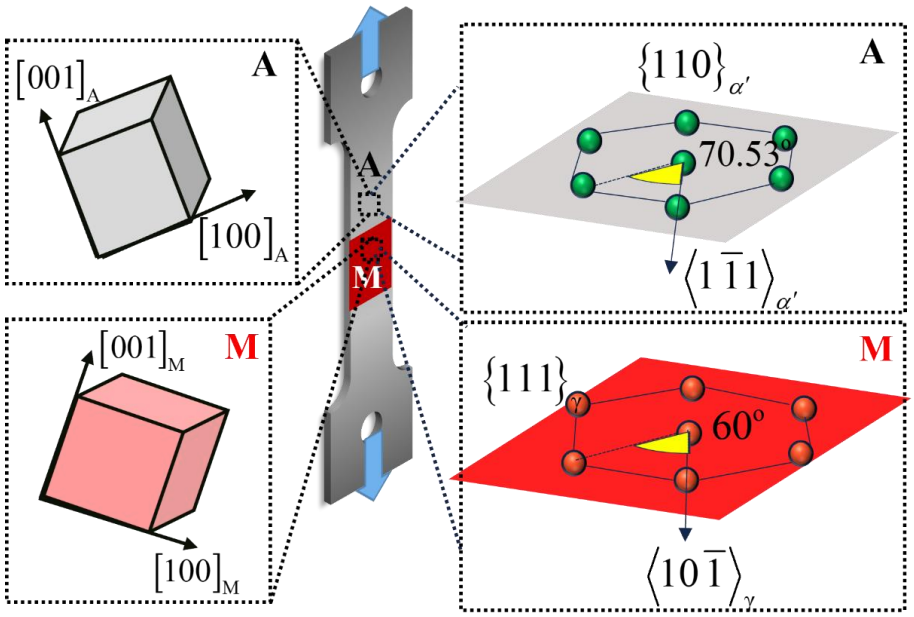

Figure 59: Superelastic phase-transformation behavior of parent Austenite (A) to Martensite (M); the focus of the study is on the lattice-orientation relationship between the two crystal structures, generally established as a parallelism between a crystallographic direction and a crystallographic plane; for the case of Body-Centered-Cubic (BCC α') austenite and Face-Centered-Cubic (FCC γ) martensite, the directions and planes are illustrated

Although ORs for multiple SMAs have been proposed and well-characterized experimentally, there are few knowledge-gaps that remain in these relationships, listed as follows:

a. Relation of OR to internal morphology of the M-phase: The ORs are generally specified for the SMA system in a seemingly independent manner from the internal structure of the martensite, whether twinned or stacking faulted. Particularly if the M-phase is internally twinned, how does the OR connect with the orientation of each of the twin variants.

b. Lattice-correspondence and OR: In converting the A-crystal structure to the M-crystal structure, there are known lattice-correspondences that are proposed. These correspondences describe which crystallographic vector-basis of the parent transform into the unit cell crystallographic basis of the martensite. It is not clear how the lattice-correspondences are linked to the OR. If the correspondences describe a relationship

between crystallographic directions in the A-phase and M-phase (as described previously), it is necessary to understand how they differ from the observed ORs.

c. Exactness of the OR: It is important to know if the parallelism conditions used to define the OR are exact in nature or if there is a tolerance of a few degrees in them. The existence of such tolerance and their magnitude is essential to understand the gradient of crystal structures at the transformation front and how the twin-interface in the M-phase impinges into the A-phase.

d. Prediction framework for the OR: While ORs are largely established experimentally, a clear predictive framework that can determine the OR ab initio from the crystallography of the transformation is missing.

This chapter focuses on addressing all aforementioned issues and to develop a predictive framework for the OR. The framework is developed from the energy-minimization of theory of martensite, typically used to predict the crystallography of habit planes. The study target is chosen to the SMA – FeMnNiAl, specifically the composition $Fe_{43.5}Mn_{34}Al_{15}Ni_{7.5}$. This SMA alloy has been of recent interest in the field as a promising inexpensive alternative to NiTi, offering a temperature-invariant transformation stress and large transformation strains exceeding 10% [198-201]. Furthermore, there is the added advantage of working with cubic crystal structures in the A and M phases. With a cubic structure, the reciprocal space lattice is in perfect alignment with the real-space lattice allowing the convenience of discussing alignment of crystallographic planes and directions in an interchangeable manner. In other words, the parallelism of two crystallographic planes $(hkl)_A$ and $(mnp)_M$ is exactly equivalent to stating parallelism of the normal crystallographic directions $[hkl]_A$ and $[mnp]_M$. In FeMnNiAl, the austenitic phase is Body-

Centered-Cubic and the martensitic phase is Face-Centered-Cubic. These structures provide an ideal starting case to examine the OR between the A and M phases.

6.2. Methodology and Results

This section begins with the experimental observations of ORs between the BCC (α') austenite (lattice constant $a_A = 2.903$ Å) and FCC (γ) martensite (lattice constant $a_M = 3.672$ Å) in FeMnNiAl. Results from Selected Area Electron Diffraction (SAED) obtained from Transmission Electron Microscopy (TEM) and from Electron Backscatter Diffraction (EBSD) are presented. Then the predictive framework for the OR is developed starting from the lattice correspondence between the phases. The energy minimization theory of martensite is outlined and applied to the problem. The resulting ORs from the theory are compared with the experimentally observed ORs.

6.2.1. Experimental observations

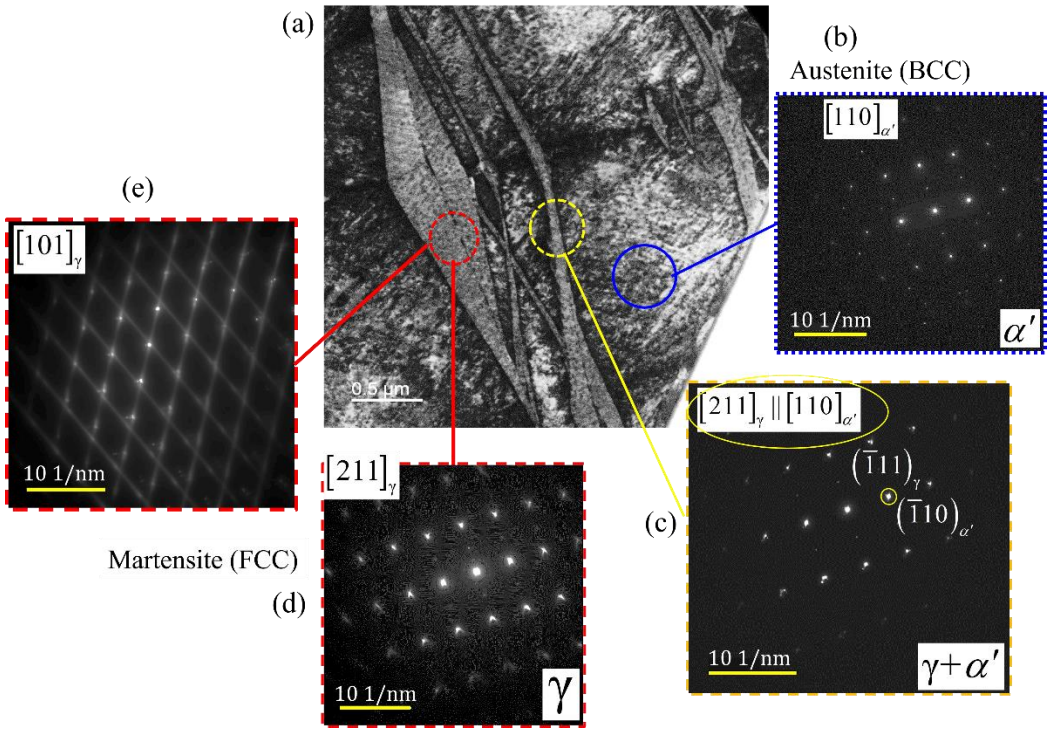

Figure 60: TEM observation of orientation-relationship between austenite and martensite in FeMnNiAl: (a) Bright-field TEM image illustrating the transformed martensite, forming in a "diamond-shape" self-accommodating morphology; other parallel bands of transformed martensite can also be seen (b) Selected-Area Electron Diffraction (SAED) pattern taken from the austenite phase (BCC α'), the zone-axis is $[110]_{\alpha'}$ (c) SAED pattern from both the austenite (BCC α') and martensite (FCC γ) phases (D) SAED from the martensite phase (FCC γ), where the zone-axis is parallel to $[211]_{\gamma}$; the SAED from (c) consequently illustrates a parallelism between the zone-axes $[211]_{\gamma}||[110]_{\alpha'}$ and the planes $(\bar{1}11)_{\gamma}||(\bar{1}10)_{\alpha'}$ (from near coincidence of the corresponding diffraction spots), confirming the Nishiyama-Wasserman orientation relationship (e) SAED pattern from the martensite taken at a different zone-axis $[101]_{\gamma}$, illustrating a "streaking" nature and thus the prevalence of stacking-faults in the underlying martensite

Compression-tested samples of FeMnNiAl exhibiting stress-induced transformation under room-temperature load were used to characterize the OR. TEM samples were milled out of transformed region using Focused Ion Beam (FIB) milling and thinned to electron-transparency. The results of the TEM imaging and SAED are presented in figure 60. The Selected-Area (SA) aperture has a diameter of 0.2 μm. The martensite is observed to form in a diamond-shaped self-

accommodation morphology as shown in figure consistent with prior reports in this system [202]. The diamond-morphology consists of 4 distinct Habit-Plane Variants (HPVs) with 4 planar transformation fronts that form together and alongside to comprise the diamond-shape. Other independent HPVs forming parallel to the sides of the diamond-martensite are also observed. SAED patterns are collected from multiple regions as indicated in figures 60 (b-e). With the austenite aligned to the $[110]_{\alpha'}$ zone (figure 60 (b)), the martensite is also on an aligned zone-axis of $[211]_{\gamma}$ thereby yielding the SAED pattern shown in figure 60 (d). By placing the SAED aperture on a region that includes both A and M phases, the combined diffraction patterns from both phases are obtained, and used to infer the OR. It is found that the planes $(\bar{1}11)_{\gamma}||(\bar{1}10)_{\alpha'}$ are nearly parallel as their diffraction spots are at close proximity to each other, and the zone-axis crystallographic directions $[211]_{\gamma}||[110]_{\alpha'}$ are aligned. Therefore for this OR, we have $(hkl)_A = (\bar{1}10)_{\alpha'}$ and $[uvw]_A = [110]_{\alpha'}$. More generally, the OR is expressed based on the family of corresponding planes and directions i.e. $\{hkl\}_A = \{\bar{1}10\}_{\alpha'}$ and $\langle uvw\rangle_A = \langle 110\rangle_{\alpha}$. This OR is known as the Nishiyama-Wasserman OR.

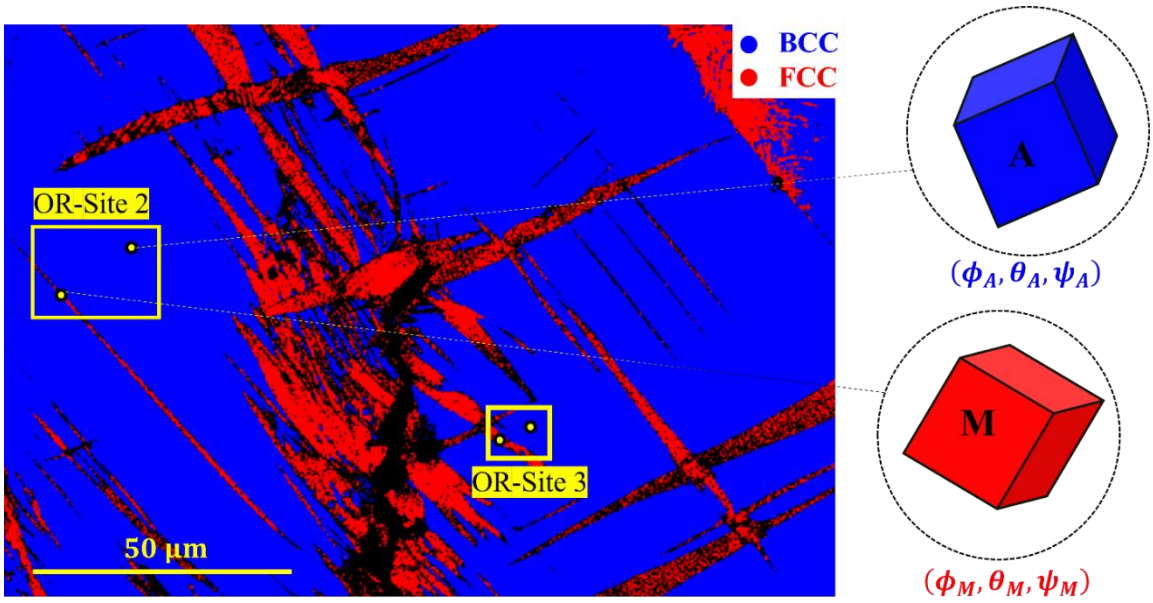

Figure 61: Electron Back-Scatter Diffraction (EBSD) map of deformed FeMnNiAl sample around a crack; the local Euler-angles (ϕ, θ, ψ) of the austenite (A, in blue) and martensite (M, in red) lattices are obtained pairwise sites (sites 2 and sites 3) and mutually compared to deduce the relative orientation relationship

The ORs were further examined using EBSD. Figure 61 presents an EBSD map on the surface of a deformed FeMnNiAl sample. The EBSD scan provides the Euler-angles at each spatial location as indicated – a triad $(\phi_A, \theta_A, \psi_A)$ for austenite and $(\phi_M, \theta_M, \psi_M)$ for martensite, with respect to a common global frame of reference $x_1 - y_1 - z_1$. These measured Euler angles are used to determine the OR between the phases. The orientation of each phase is given by the rotation matrices Q_A, Q_M, respectively the columns of which represent the coordinates of the crystallographic vectors of each respective phase in the global frame. The Euler angles are obtained in the extrinsic "zxz" convention and the respective rotation matrices for both phases are given by:

$$Q_{A,M} = \begin{pmatrix} \cos\phi_{A,M} & \sin\phi_{A,M} & 0 \\ -\sin\phi_{A,M} & \cos\phi_{A,M} & 0 \\ 0 & 0 & 1 \end{pmatrix} \begin{pmatrix} 1 & 0 & 0 \\ 0 & \cos\theta_{A,M} & \sin\theta_{A,M} \\ 0 & -\sin\theta_{A,M} & \cos\theta_{A,M} \end{pmatrix} \begin{pmatrix} \cos\psi_{A.M} & \sin\psi_{A,M} & 0 \\ -\sin\psi_{A,M} & \cos\psi_{A,M} & 0 \\ 0 & 0 & 1 \end{pmatrix} \quad (6.1)$$

The OR is visualized in a stereographic projection as illustrated in figure 62. All unit crystallographic directions are projected onto a selected crystallographic plane ($(0\bar{1}1)$ in the case shown in figure 62(a)), and visualized as a 2D plot of points (figure 62(b)). The closest points from

the A phase and M phase correspond to the most closely aligned/parallel directions between the phases and are used to determine the OR. The crystallographic orientation of the FCC (M) phase is taken as reference, and the BCC (A) orientation is plotted relative to it. A unit vector along the crystallographic direction $C_A = a_A[uvw]_A$ in the austenite phase has the components (x_A, y_A) in the stereographic projection where:

$$\begin{pmatrix} x_A \\ y_A \\ z_A \end{pmatrix} = \frac{1}{\|C_A\|} \begin{pmatrix} 0 & 1/\sqrt{2} & 1/\sqrt{2} \\ -1 & 0 & 0 \\ 0 & -1/\sqrt{2} & 1/\sqrt{2} \end{pmatrix} Q_M^T Q_A \begin{pmatrix} u \\ v \\ w \end{pmatrix} \tag{6.2}$$

A unit vector along the crystallographic direction $C_M = a_M[rst]_M$ in the martensite phase has the components (x_M, y_M) in the stereographic projection where:

$$\begin{pmatrix} x_M \\ y_M \\ z_M \end{pmatrix} = \frac{1}{\|C_M\|} \begin{pmatrix} 0 & 1/\sqrt{2} & 1/\sqrt{2} \\ -1 & 0 & 0 \\ 0 & -1/\sqrt{2} & 1/\sqrt{2} \end{pmatrix} \begin{pmatrix} r \\ s \\ t \end{pmatrix} \tag{6.3}$$

Results of the relative orientations from EBSD site-pairs 2 and 3 from figure 61 are plotted in figure 63 (a, b) respectively. It is found that the Pitsch OR is followed at site 2 where $\{hkl\}_A = \{112\}_{\alpha'}$ and $\langle uvw\rangle_A = \langle 1\bar{1}0\rangle_{\alpha'}$. Whereas at site 3, the Kurdjumov-Sachs OR for which $\{hkl\}_A = \{110\}_{\alpha'}$ and $\langle uvw\rangle_A = \langle 1\bar{1}1\rangle_{\alpha}$. All three observed ORs are listed in table 12.

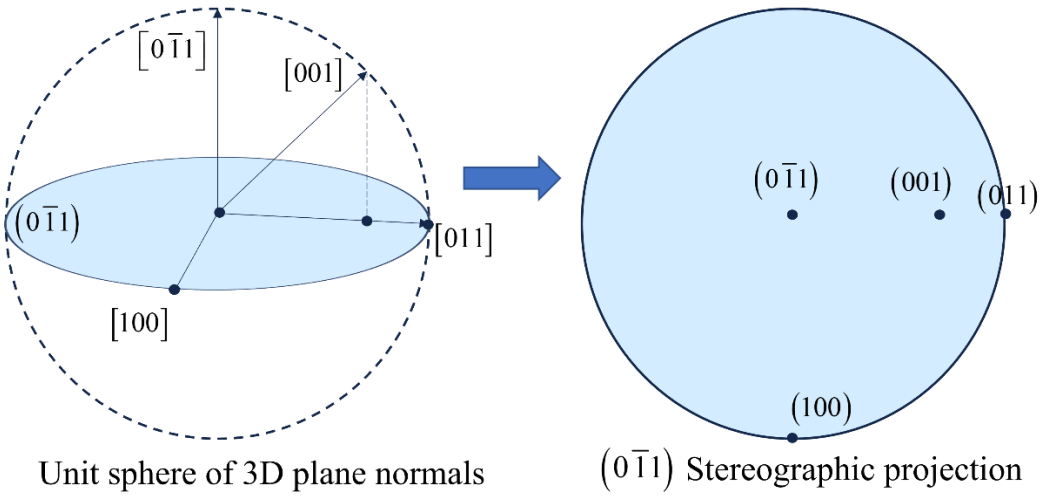

Figure 62: Concept of a stereographic projection illustrating how the 3-dimensional plane normal are projected to obtain a 2-dimensional visualization, useful to compare the orientations of austenite and matensite lattices in this study

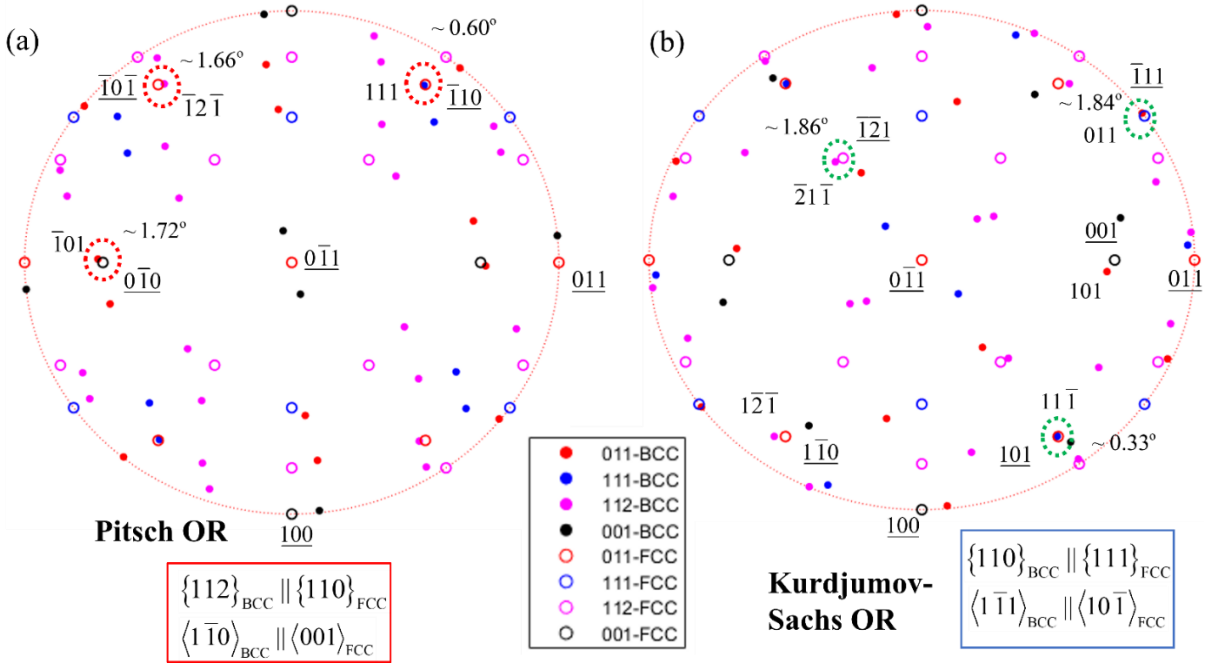

Figure 63: Overlapped stereographic projection of BCC austenite (filled circles) and FCC martensite (open circles) from EBSD results; (a) the relative orientations obtained from OR Site 2 (refer figure 3) are plotted and based on the nearest coincident directions, the Pitsch OR is observed (b) the relative orientations obtained from OR Site 3 (refer figure 3) are plotted and based on the nearest coincident directions, the Krudjumov-Sachs OR is observed

Table 12: Observed Orientation Relationships in FeMnNiAl

Label	**Invariant plane in austenite (A)** $\{hkl\}_A$	**Invariant direction in austenite (A)** $\langle uvw\rangle_A$	**Parallelism condition between phases**
Nishiyama-Wasserman	$\{1\bar{1}0\}_{\alpha'}$	$\langle 110\rangle_{\alpha'}$	$\{110\}_{\alpha'}\|\|\{\bar{1}11\}_{\gamma}$ $\langle 110\rangle_{\alpha'}\|\|\langle 211\rangle_{\gamma}$
Pitsch	$\{112\}_{\alpha'}$	$\langle 1\bar{1}0\rangle_{\alpha'}$	$\{112\}_{\alpha'}\|\|\{110\}_{\gamma}$ $\langle 1\bar{1}0\rangle_{\alpha'}\|\|\langle 001\rangle_{\gamma}$
Kurdjumov-Sachs	$\{110\}_{\alpha'}$	$\langle 1\bar{1}1\rangle_{\alpha'}$	$\{110\}_{\alpha'}\|\|\{111\}_{\gamma}$ $\langle 1\bar{1}1\rangle_{\alpha'}\|\|\langle 10\bar{1}\rangle_{\gamma}$

6.2.2. Theoretical predictions: Twinned martensite

To predict the OR, the crystallography of the transformed martensite must be predicted in relation to the parent austenitic phase. The Bain lattice-correspondence provides the relation of the martensitic crystal structure with the austenite parent. This correspondence is such that the parent A phase requires the least stretch, alternatively called the "Bain strain", to transform to the M-phase crystal structure. For the BCC parent and FCC transformed martensite, the lattice correspondence and required Bain strains are shown in figure 64. The lattice correspondences are represented by the equations:

$$\begin{aligned} \langle 1\bar{1}0\rangle_{\mathrm{A}} &\leftrightarrow \langle 100\rangle_{\mathrm{M}} \\ \langle 110\rangle_{\mathrm{A}} &\leftrightarrow \langle 010\rangle_{\mathrm{M}} \\ \langle 001\rangle_{\mathrm{A}} &\leftrightarrow \langle 001\rangle_{\mathrm{M}} \end{aligned} \tag{6.4}$$

Note that although a crystallographic family of directions is used to represent the correspondence in (6.4), an orthogonal triad must be chosen for the directions in the austenite phase that become the crystallographic basis of the martensite crystal structure. There are 3 unique correspondences given by the following rotation matrices Q^{LAT} in equation (6.5) below. The rows of the matrix

represent the lattice vectors of the austenite frame that transform to the crystallographic basis in the martensite frame, $[100]_M - [010]_M - [001]_M$ respectively.

$$Q_1^{LAT} = \begin{pmatrix} 1 & 0 & 0 \\ 0 & 1 & -1 \\ 0 & 1 & 1 \end{pmatrix}; \; Q_2^{LAT} = \begin{pmatrix} 0 & 1 & 0 \\ -1 & 0 & -1 \\ 1 & 0 & 1 \end{pmatrix}; \; Q_3^{LAT} = \begin{pmatrix} 0 & 0 & 1 \\ 1 & -1 & 0 \\ 1 & 1 & 0 \end{pmatrix} \tag{6.5}$$

The corresponding unitary rotation matrices are given by Q^{ROT} as follows:

$$Q_1^{ROT} = \begin{pmatrix} 1 & 0 & 0 \\ 0 & {}^{1}/_{\sqrt{2}} & -{}^{1}/_{\sqrt{2}} \\ 0 & {}^{1}/_{\sqrt{2}} & {}^{1}/_{\sqrt{2}} \end{pmatrix}; \; Q_2^{ROT} = \begin{pmatrix} 0 & 1 & 0 \\ -{}^{1}/_{\sqrt{2}} & 0 & -{}^{1}/_{\sqrt{2}} \\ {}^{1}/_{\sqrt{2}} & 0 & {}^{1}/_{\sqrt{2}} \end{pmatrix}; \; Q_3^{ROT} = \begin{pmatrix} 0 & 0 & 1 \\ {}^{1}/_{\sqrt{2}} & -{}^{1}/_{\sqrt{2}} & 0 \\ {}^{1}/_{\sqrt{2}} & {}^{1}/_{\sqrt{2}} & 0 \end{pmatrix} \tag{6.6}$$

The corresponding stretch tensors for the above correspondences, expressed in the crystallographic basis of the A phase are given by the equation:

$$\boldsymbol{U_1} = \begin{pmatrix} \eta_2 & 0 & 0 \\ 0 & \eta_1 & 0 \\ 0 & 0 & \eta_1 \end{pmatrix}; \; \boldsymbol{U_2} = \begin{pmatrix} \eta_1 & 0 & 0 \\ 0 & \eta_2 & 0 \\ 0 & 0 & \eta_1 \end{pmatrix}; \; \boldsymbol{U_3} = \begin{pmatrix} \eta_1 & 0 & 0 \\ 0 & \eta_1 & 0 \\ 0 & 0 & \eta_3 \end{pmatrix} \tag{6.7}$$

where $\eta_1 = a_M/(a_A\sqrt{2})$ and $\eta_2 = a_M/a_A$.

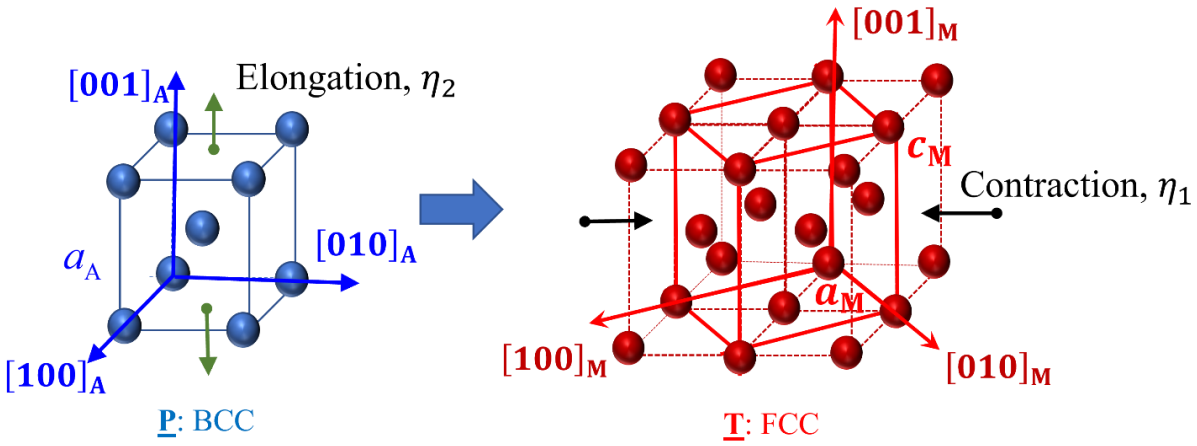

Figure 64: Bain correspondence and Bain strains η_1, η_2 corresponding to the right stretch-tensor **U,** required to transform the parent austenitic phase (BCC) to martensite (FCC)

Given the lattice-correspondences, the energy-minimization theory of martensite can be used to determine the relative orientation between the M and A phases. A brief summary of the theory is provided here and the reader is referred to refs. [16, 203] for further details. Based on the theory,

the M phase forms within the A phase such that it follows an Invariant Plane Strain (IPS) deformation, so that the strain-energy is minimized. And to achieve such a deformation, the M phase is generally internally twinned. In such a case, there are two variants of martensite $\boldsymbol{U_i}$ and $\boldsymbol{U_j}$ with $i \neq j$ that form and the orientation of both variants must be considered individually. The fundamental equations of the theory are as follows:

$$\boldsymbol{R_{ij}U_j} - \boldsymbol{U_i} = \vec{a} \otimes \hat{n} \tag{6.8}$$

$$\boldsymbol{R_h}\left[f\boldsymbol{R_{ij}U_j} + (1-f)\boldsymbol{U_i}\right] = \boldsymbol{I} + \vec{b} \otimes \hat{m} \tag{6.9}$$

where $\boldsymbol{U_i}$ and $\boldsymbol{U_j}$ are the two variants considered, f is the volume-fraction of $\boldsymbol{U_j}$, $\boldsymbol{R_h}$, $\boldsymbol{R_{ij}}$ are rotation tensors, $\boldsymbol{I}$ is the identity tensor, $\vec{a}$ is the twinning shear, $\hat{n}$ is the twinning plane between the variants, $\vec{b}$ is the effective transformation shear of the IPS deformation and $\hat{m}$ is the habit plane of the transformation. Using equation (6.8) in (6.9) we have the simpler form:

$$\boldsymbol{R_h}[\boldsymbol{U_i} + f(\vec{a} \otimes \hat{n})] = \boldsymbol{I} + \vec{b} \otimes \hat{m} \tag{6.10}$$

The theory is well-developed such that, given a choice of two variants $\boldsymbol{U_i}$ and $\boldsymbol{U_j}$, every other term in the equation (6.9) can be determined, resulting in all solutions of Habit Plane Variants (HPVs) of the transformation. Only those HPVs are considered that yield the twinning normal to be parallel to $\langle 111 \rangle$ in the M phase and the twinning shear direction parallel to the corresponding $\langle 112 \rangle$ twinning direction on the plane. In other words, it must be checked that:

$$\hat{n}_{FCC} = \boldsymbol{Q_i^{ROT}U_i^{-1}}\hat{n} \Big/ \left\|\boldsymbol{U_i^{-1}}\hat{n}\right\| \in \{111\}$$

$$\vec{a}_{FCC} = \boldsymbol{Q_i^{ROT}}\vec{a} \Big/ \left\|\boldsymbol{U_i^{-1}}\hat{n}\right\| \in \sqrt{3}/\boldsymbol{6}\,\{112\} \tag{6.11}$$

which would yield $\|a_{FCC}\| = 0.707$, the twinning shear in FCC. It is found that 24 independent HPV solutions exist, all within the family of habit planes $\{0.1678, 0.6455, 0.7451\}$, consistent with prior predictions in ref. [202]. Considering one of the HPV solutions in this family, say with

$i = 2$ and $j = 3$, the deformation gradients $\boldsymbol{F_{M2} = R_h U_2}$ and $\boldsymbol{F_{M3} = R_h R_{ij} U_j}$ are calculated. These deformation gradients represent the mapping between the crystal structure of the austenite to form each individual twin variant. To determine which OR is followed by each variant, the condition of invariance is checked for the crystallographic planes and directions corresponding to each OR (listed in table 12). For instance, to check if the variant with deformation gradient $\boldsymbol{F_{M2}}$ follows the Ptisch OR, the invariance of a plane normal $\hat{n} \in \{112\}_{\alpha'}$ and unit vector $\hat{v} \in \langle 1\bar{1}0 \rangle_{\alpha'}$ must be checked. The plane normal $\hat{n}$ and the unit vector $\hat{v}$ transform under the deformation gradient as per the following equation:

$$\hat{n}_2 = \frac{\boldsymbol{F_{M2}^{-T}}.\hat{n}}{\|\boldsymbol{F_{M2}^{-T}}.\hat{n}\|}; \hat{v}_2 = \frac{\boldsymbol{F_{M2}}\hat{v}}{\|\boldsymbol{F_{M2}}\hat{v}\|} \tag{6.12}$$

An error-function Δe_{PCH} is computed as follows,

$$\Delta e_{PCH} = \sqrt{(\cos^{-1}|\hat{n}_2.\hat{n}|)^2 + (\cos^{-1}|\hat{v}_2.\hat{v}|)^2} \tag{6.13}$$

Similar error-functions are computed to check for the Kurdjumov-Sachs OR, Δe_{KS}, and Nishiyama-Wasserman OR, Δe_{NW}, by selecting the respective plane $\hat{n}$ and direction $\hat{v}$ accordingly from table 12. The least magnitude of the error within the set $\{\Delta e_{PCH}, \Delta e_{NW}, \Delta e_{KS}\}$ decides the OR. It is found that in all the HPV solutions of internally twinned martensites, one of the twin variants follows the Pitsch OR, while the other follows the Kurdjumov-Sachs OR. These predictions explain the ORs observed from EBSD in figure 63. To further confirm the OR, the stereographic projection of both the BCC and FCC phases are plotted. An example of a HPV solution with variants ($\boldsymbol{i = 2, j = 3}$) is used to illustrate the model predicted results. The variant $\boldsymbol{U_2}$, with the deformation gradient $\boldsymbol{F_{M2}}$ follows the Pitsch OR, while variant $\boldsymbol{U_3}$ with the deformation gradient $\boldsymbol{F_{M3}}$ follows the Kurdjumov-Sachs OR.

The stereographic projections are plotted with reference to the parent BCC phase, and a $(001)_{\alpha'}$ projection is chosen. In this standard projection, the unit directions in the BCC crystal structure can be plotted trivially. For the FCC crystal structure, a unit vector along the crystallographic direction $C_M = a_M[uvw]_M$ within variant $\boldsymbol{U_2}$ has the components (x_M, y_M) in the stereographic projection given by:

$$\vec{v}_S = a_A \boldsymbol{F_{M2}} \left(Q_2^{LAT}\right)^T \begin{pmatrix} u \\ v \\ w \end{pmatrix} \tag{6.14}$$

$$\begin{pmatrix} x_M \\ y_M \\ z_M \end{pmatrix} = {\vec{v}_S}/{\|\vec{v}_S\|} \tag{6.15}$$

The stereographic projections for the variants $\boldsymbol{U_2}$ and $\boldsymbol{U_3}$ for the twinned martensite HPV are plotted in figures 65 and 66 respectively, illustrating the Pitsch OR and Kurdjumov-Sachs OR.

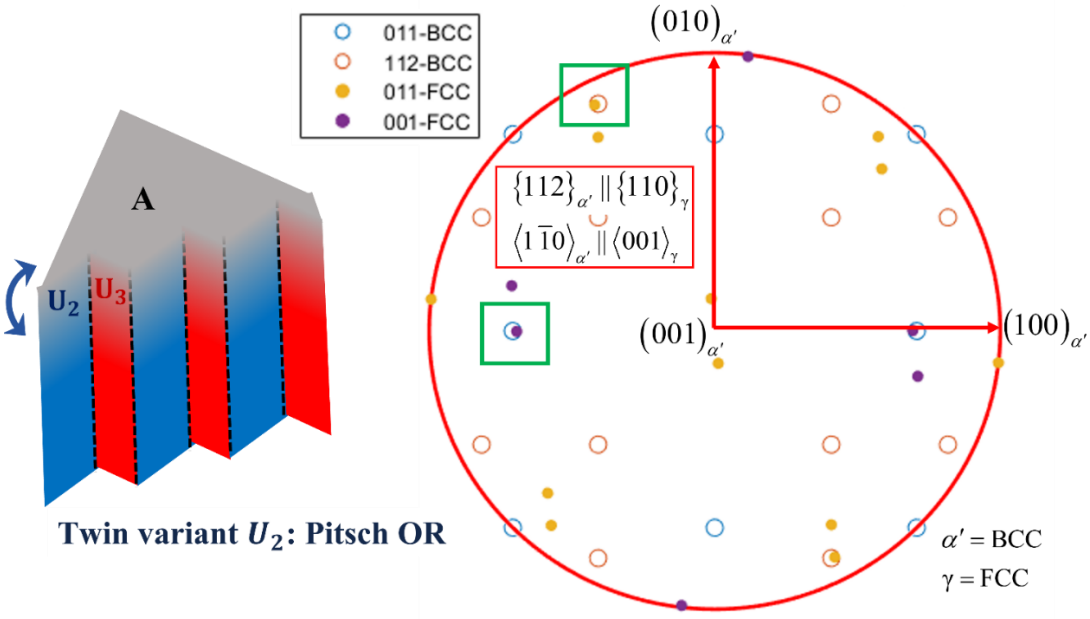

Figure 65: Predictions of relative orientations between twin-variant (with stretch) U_2 and the parent austenite, explaining the Pitsch OR

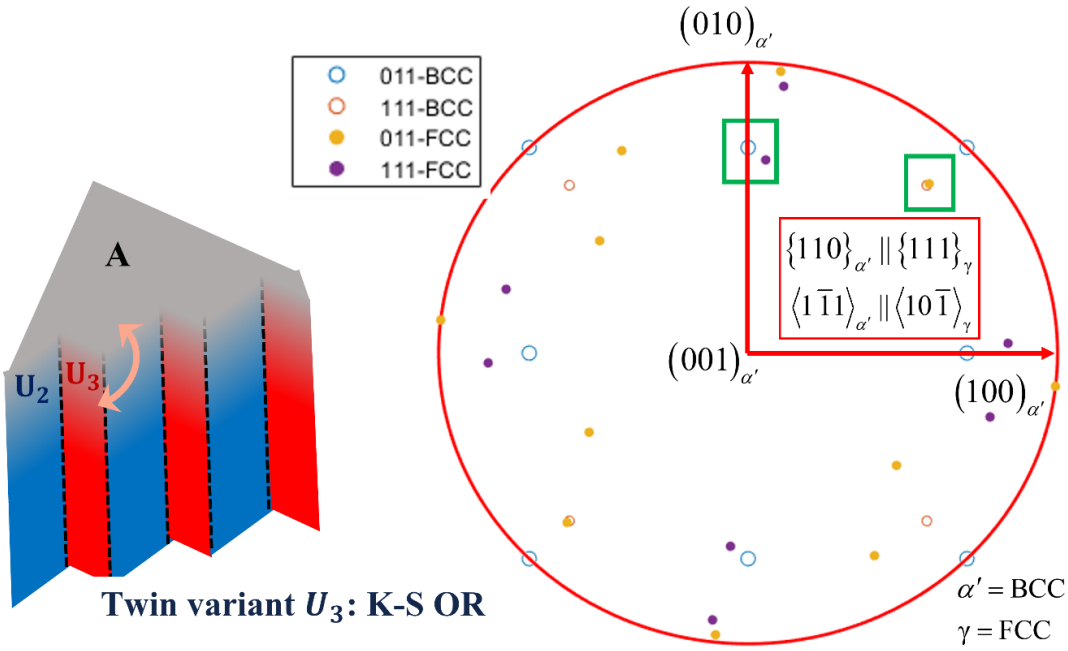

Figure 66: Predictions of relative orientations between the second twin-variant (with stretch) U_3 and the parent austenite, explaining the Kurdjumov-Sachs OR

6.2.3. Theoretical predictions: Stacking-faulted martensite

In addition to twinning, formation of stacking-faults is an alternative Lattice-Invariant-Deformation (LID) mode for the transformed. And given the observations of stacking faults from the SAED results in figure 60(e), a predictive model for the OR of such a morphology is developed. A novel theory is proposed for the case of stacking-faulted martensite, proposed for the first time to the best of the authors' knowledge. Consider the martensite forming as a single variant $\boldsymbol{U_i}$ with periodically spaced stacking-faults on planes $\hat{n}$ and direction of faulting is parallel to the Shockley-partial Burgers vector on the plane $\vec{a}$. Let the faults be periodically spaced by magnitude d. The-stacking-faulted martensite is represented schematically in figure 67(a). Then, for the martensite to follow an IPS deformation, the following condition must be satisfied:

$$\boldsymbol{F_{Mi}} = \boldsymbol{R_h}\left[\boldsymbol{U_i} + \left(\frac{1}{d}\right)(\vec{a} \otimes \hat{n})\right] = \boldsymbol{I} + \vec{b} \otimes \hat{m} \tag{6.16}$$

where $\boldsymbol{R_h}$ is a rotation tensor, $\boldsymbol{I}$ is the identity tensor, $\vec{b}$ is the effective transformation shear of the IPS deformation and $\hat{m}$ is the habit plane of the transformation.

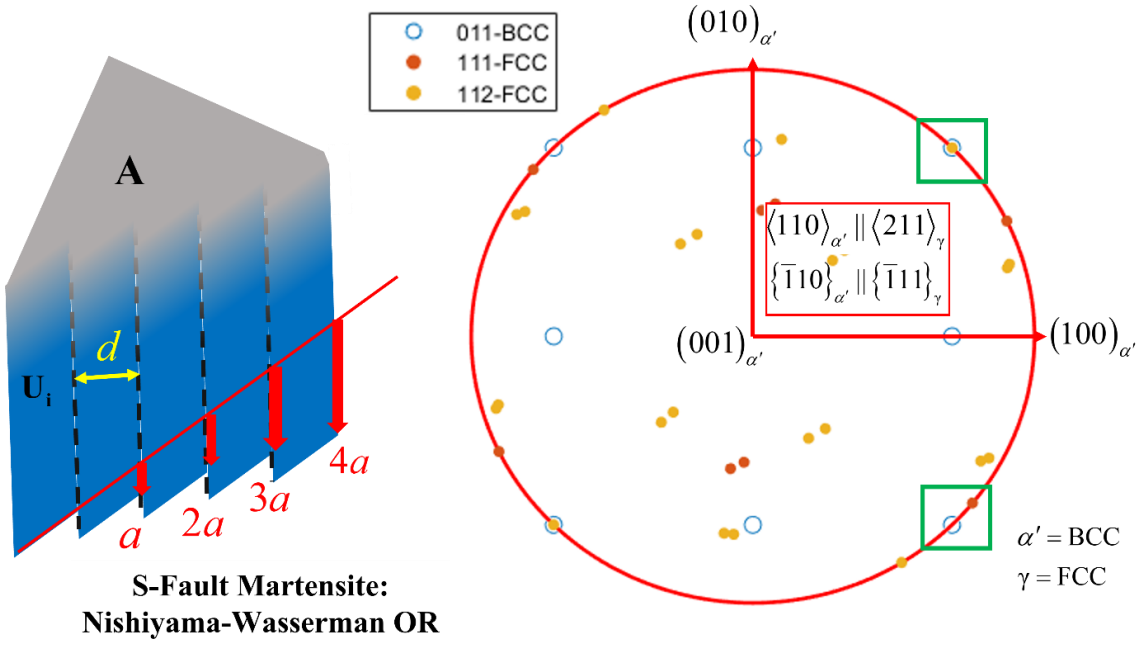

Figure 67: Predictions of relative orientations between the stacking-faulted martensitic variant (with stretch) U_i and the parent austenite, explaining the Nishiyama-Wasserman OR

For a given variant $\boldsymbol{U_i}$, the slip-plane is given by $\hat{n}_{FCC} \in {}^{1}/_{\sqrt{3}}\{111\}$ and $\vec{a}_{FCC} \in {}^{s}/_{\sqrt{6}}\langle 112\rangle$, where $s = {}^{1}/_{\sqrt{2}}$, comprising a total of 12 slip systems. The normal vector $\hat{n}$ and fault-shear $\vec{a}$ are given by:

$$\hat{n} = \frac{\boldsymbol{U_i}\left(Q_i^{ROT}\right)^T \hat{n}_{FCC}}{\left\|\boldsymbol{U_i}\left(Q_i^{ROT}\right)^T \hat{n}_{FCC}\right\|}; \vec{a} = \frac{\left(Q_i^{ROT}\right)^T \vec{a}_{FCC}}{\left\|\boldsymbol{U_i}^{-1}\hat{n}_{FCC}\right\|} \tag{6.17}$$

Note that equation (6.16) is identical to (6.10) if we redefine $d = {}^{1}/_{f}$. Therefore, equation (6.16) can be solved following the same method as solving (6.10), for a given variant $\boldsymbol{U_i}$, and Shockley-partial slip system defined by $\vec{a}$ and $\hat{n}$. It is found that 24 independent HPV solutions exist, which are also the same family of habit planes $\{0.1678, 0.6455, 0.7451\}$. Therefore the same HPVs can form with either an internally-twinned morphology (with 2 twin variants $\boldsymbol{U_i}$ and $\boldsymbol{U_j}$) or stacking-

faulted morphology (with a single variant $\boldsymbol{U_i}$**).** Considering one of the HPV solutions in this family of stacking-faulted solutions, say with $i = 1$, the deformation gradient $\boldsymbol{F_{M1}}$ is calculated from (6.16). Following the same procedures for computing the error-functions and plotting the stereographic projections as described in section 6.2.2, it is found that the stacking-faulted variant obeys the Nishiyama-Wasserman OR (shown in figure 67(b)). Thus, all observations of ORs have been explained from a theoretical standpoint.

6.3. Discussions

A fundamental knowledge-gap in understanding of martensitic transformations lies in the interpretation of the Orientation Relationship (OR) between the parent Austenite (A) and product Martensite (M) phase. Thorough knowledge of these ORs are a prerequisite to construct and understand behavior of the A-M transformation front, ultimately to uncover the unknown mechanisms of slip-emission at these interfaces. These relationships have been proposed for several SMAs and it can often be tacit presumption that these relationships are "exact" and are unique for a specific SMA system. In this chapter, experimental results on FeMnNiAl show that multiple ORs are possible, independently observing a combination of the Nishiyama-Wasserman OR, the Pitsch OR and the Kurdjumov-Sachs OR. And in all the results, it is obvious that the ORs are not obeyed exactly but only within a certain tolerance of mismatch, of the order of few degrees. This can be observed in the lacking coincidence of the TEM diffraction spots in figure 60 (c) or points on the stereographic projections in figure 63. Although it must be mentioned that the alignment is still close given by the highly proximity of the aforementioned spots/points. Given these results, the focus is to address the origin of these multiple ORs based on the morphology of the underlying martensitic structure.

The modeling approach applies the energy-minimization theory of martensite to predict the ORs. This is a continuum theory that is generally used to predict the irrational Miller indices of the habit planes of the transformation. In this study, the same theory is combined with the crystallography of the transformation, involving the Bain lattice correspondences to predict the OR. The OR is clearly shown to depend on the internal morphology of martensite whether twinned or stacking-faulted. If the martensite is twinned, then the individual twin variants explain the Pitsch and Kurdjumov-Sachs ORs. And if the martensite is stacking-faulted, the Nishiyama-Wasserman OR is explained. Additionally, it is proposed that the effective rotation $\boldsymbol{R_h}$ in both morphologies has a role to play (equations (6.10) and (6.16)), and this rotation comes about to ensure the martensite follows an Invariant Plane-Strain (IPS) deformation. Therefore, there is an additional misorientation introduced in the variants in an effort by the martensite to minimize its strain-energy via formation on an invariant irrational plane (i.e. the habit plane). Further, the prediction of the theory checks the OR by computing finite-valued error-functions as discussed in 6.2.2. In that sense, the question is not which exact OR is followed but rather which OR is followed to the "nearest extent" (therefore least error Δe) by the martensite. And by this interpretation it is plausible to expect the material to exhibit more than one OR as it only describes the nearest rotational orientation relation between the planes and directions of both A and M phases.

This study also develops a novel theory for stacking-faulted martensite, for the first time in literature to the best of the authors' knowledge. The stacking-faulted structure appends an additional shear $^1/_d\,(\vec{a} \otimes \hat{n})$ to the single variant $\boldsymbol{U_i}$. Once this understanding is reached it becomes clear that the HPV solution for this morphology can be obtained analogously to the twinned case, as mentioned in section 6.2.3. The predictions are consistent with the experimental results where existence of stacking-faults in the martensite is evidenced in figure 60(e). It is

interesting to note that given the one-one correspondence between the OR and the underlying substructure of the martensite, the observed OR can be used as a marker to identify the underlying martensitic morphology as either twinned or stacking-faulted.

6.4. Conclusions

There are two key knowledge-gaps in the understanding and interpretation of these ORs. The first is regarding the exactness of these relationships. The second is the fact that it is unique for a given material, where in fact it depends on the internal morphology of martensite. In this study, experimental research for the first time showed 3 distinct ORs for transforming FeMnNiAl (BCC to FCC transformation) Shape Memory Alloy. They are the Kurdjumov-Sachs, Nishiyama-Wasserman and Pitsch ORs. Observations of such a non-unique OR poses a basic question of whether the OR is a material property or if it can evolve depending on other microstructural factors. A theoretical treatment to precisely predict these ORs is undertaken in this study. It is shown that the OR depends on the internal microstructural morphology of the martensitic phase. Depending on whether the morphology corresponds to a twinned structure or stacking-faulted structure, the OR can vary. When the martensite is internally twinned, it exhibits two twin variants with a distinct twin plane. One of the variants reproduce the Pitsch OR and the other variant results in the Kurdjumov-Sachs OR. When the martensite involves stacking-faults, the corresponding single variant sustaining the faults is shown to reproduce the Nishiyama-Wasserman OR. A novel theoretical framework underlying the predictions for stacking-faulted martensite was developed for this purpose. It is shown that these ORs are not exact and there exists a non-trivial tolerance in the parallelism relations that have been proposed thus far, upto a order of few degrees. It is crucial to know of the existence of such a tolerance as it dictates how the A and M lattices are oriented

relative to each other and how the transformation front between them can behave during the transformation.

CHAPTER 7: FUTURE WORK: TOWARDS THERMOMECHANICS OF SLIP

7.1. Summary

This research clarifies the following aspects in martensitic phase transformations exhibited by Shape Memory Alloys:

a. The structure of Type II twin boundaries is resolved from both atomistic and topological standpoints, explaining its irrational nature.

b. Motivated from the Kajiwara-Kikuchi mechanism, an atomistic simulation of slip-emission is forwarded showing how the shuffle-disregistered core-structure of a twinning disconnection can form a translational-disregistered core-structure corresponding to emitted slip.

c. A physical justification of the Terrace-Disconnection topology is offered by establishing both the atomistic potential energies and continuum strain-energies, illustrating the dominance of the former component and consequent preference of low-index rational terraces for interfaces. A new "Evolving Interface" theory is forwarded, establishing a framework to predict the equilibrium topologies of twin interfaces (of general type) under strain, generalizing the theory of Topological Modeling.

d. A formal framework to model Type II TBs in other SMAs is forwarded, beginning from identification of the rational terrace, the role of terrace-shear, its connection to the twinning-disconnection's Burgers vector and finally the irrational T-D topology.

e. Orientation Relationships (ORs) between the parent austenite and transformed martensite are analyzed in FeMnNiAl, explaining the observation of non-unique ORs and establishing its dependence on martensite's internal morphology. A theoretical framework for stacking-faulted martensite is forwarded, for the first time, to the best of the author's knowledge.

From a broader perspective in the context of the theory of twinning and phase-transformations, the following contributions are offered:

a. This study offers formal methodologies to construct the atomic-structure of twin interfaces in non-single-lattice structures (such as $B19'$, $B19$), allowing their atomistic potential energies to be calculated accurately. Methods to define and determine "lattice-offsets" and shear-shuffle partitioning in twinning mechanisms are developed, offering a framework to study more complicated twin structures beyond conventional cubic systems (such as BCC and FCC). Recently, the $\{10\bar{1}2\}$ twin in HCP materials was studied and its energetics determined from ab initio Density Functional Theory (DFT) simulations, based on this developed understanding [193].
b. The direct quantitative comparison of energetics from both atomistics and anisotropic continuum theory was crucial to establish the correct interface topology for the Type II TB that explains experimental observations. Thus in studying interfaces, the role of strain-fields must be considered along with atomic-potential energies of the underlying crystal structure. It is in fact the dominance of the atomic potential energies that dictates the preference of low-index rational terraces exhibiting high planar atomic-densities.
c. The theory for strain-sensitive evolution for TBs, illustrates how a T-D topology with periodically spaced disconnections and consequent irrational identity is more the norm rather than a perfectly rational atomically-flat interface. Further it brackets the Type II twin along with Type I and Compound counterparts unifying their treatment. This theory formally rationalizes the tendency of twin interfaces to be observed in orientations deviating from their classical Miller-index identity, since in real microstructures they

would invariably be subject to a non-trivial microstructural strain (see [174] for a recent example).

d. The prediction of OR in this study challenges the notion that the lattice-orientation relationships between the parent and transformed phases are a material characteristic. While the "Lattice Correspondence" can be a unique characteristic of the two phases, the measurable "Orientation Relationship" in which the phases are observed can vary, depending on the internal martensite morphology (twinned/stacking-faulted), for instance.

7.2. Implications and future extensions

The findings of this study can guide research in the following directions in the future:

a. **Structure of the transformation front**: Having established the structure of the internal twin interface and the Orientation Relationship (OR) it would be a worthwhile pursuit to construct the structure of the habit-plane. Results of this study imply that there is a slight misorientation between the crystallographic planes of the martensite and austenite to the extent that it is unlikely a common rational-terrace exists between them. In such a scenario, a semi-coherent Terrace-Disconnection topology for the habit plane is hard to fathom and it seems more likely that the habit plane is a fully-coherent interface gradually transitioning between the crystal structures of the two phases. The nature of this interface dictates its energy and the frictional force required for its motion (i.e. frictional driving force to be overcome for the transformation), the latter being a key metric to determine functional characteristics of SMAs, such as hysteresis.

b. **Equilibrium Twin Boundary density:** While the energy-minimization theory of martensite can predict the volume-fraction of twin variants within the martensite, the physical twin-widths cannot be reliably predicted yet. The twin-interface density would be

dictated by a balance of the continuum strain-energy at the habit-plane and the total atomistic twin boundary energy within the martensite. And given the mechanism of slip-emission from these twin-interfaces, it is vital to have a predictable framework for the density of twin interfaces within the martensite as they can dictate the propensity of transformation-induced slip and functional fatigue.

c. **Functional Fatigue**: The ultimate goal of research in this study is to build towards a predictive model for functional fatigue at a macroscopic level. For instance, the understanding of strain-sensitivity of twin-interfaces was used to develop a slip-emission hypothesis in Chapter 4 and atomistic-energies involved in the mechanism were proposed in Chapter 3. And yet, a governing thermodynamic framework that can incorporate these metrics to thermomechanically explain the occurrence of slip during transformation is elusive. Such an understanding requires a framework that addresses the general "driving force" of the transformation involving the thermodynamic stability of the phases, the continuum interaction energies with external load, and frictional barriers to be overcome from the motion of the transformation front to the emission of slip-dislocations. An initial theoretical framework is developed in section 7.3 below and a Gibbs-free-energy based argument is forwarded to explain the occurrence of transformation-induced slip. It is vital for the field to develop such a framework as it offers the key material parameters to be measured and modified for superior fatigue resistance.

7.3. A framework for the thermomechanics of transformation-induced slip

The thermomechanical framework employed in refs. [17, 18, 204] is adopted. Only key elements of the model are described here, and the reader is referred to the aforementioned works for a more detailed exposition. In this framework, we consider the Gibbs' free energy $G(\sigma_{ij}, T, f)$, as a

function of the three-dimensional applied stress state σ_{ij}^0, the temperature T and the volume fraction of martensite f. For convenience, consider the nucleation and growth of only one martensitic variant in the austenite matrix. The Gibbs' free energy for the transformation can be expressed as:

$$G(\sigma_{ij}, T, f) = E_{chem}(T, f) + E_{elastic}(\varepsilon_{ij}^{tr}, f) - W_{inter}(\sigma_{ij}^0, \varepsilon_{ij}^*) \quad (7.1)$$

, where E_{chem} is the chemical energy difference between the martensite and austenite phase, $E_{elastic}$ constitutes the self-energy of a transformed martensitic inclusion with transformation-strain/"eigen"-strain ε_{ij}^{tr} inside an austenite matrix, W_{inter} constitutes the work interaction energy between the transformed volume and applied load. The chemical energy arises from a difference in bonding energy between the martensite and austenite phases and can be conveniently expressed as $E_{chem} = B(T - T_0)f$ where B is proportional to the Clausius-Clapeyron slope of the SMA and T_0 is the equilibrium temperature of the austenite and martensite phases, both of which are intrinsic material parameters for the SMA. The elastic energy term $E_{elastic}$ can be derived as $E_{elastic} = -1/2\, f\varepsilon_{ij}^{tr}\left(C_{ijkl}(S_{klmn}\varepsilon_{mn}^{tr} - \varepsilon_{kl}^{tr})\right)$, where C is the elastic constant tensor and S is the Eshelby-tensor for the nucleated martensitic inclusion.

The work interaction energy W_{inter} is given by $W_{inter} = \sigma_{ij}^0 \varepsilon_{ij}^{tr} f$. Consider the stress-state to be uniaxial, given by $\sigma_{ij}^0 = \sigma_0(\hat{v} \otimes \hat{v})$ where $\hat{v}$ is the direction of applied load. Under this load, the nucleated martensitic variant will be the one which maximizes W_{inter}. For a Habit Plane Variant (HPV) with a habit-plane normal $\hat{m}$, direction of shear $\hat{t}$ and transformation strain magnitude ε_{tr}, the transformation strain is given by $\varepsilon_{ij}^{tr} = \varepsilon_{tr}(\hat{t} \otimes \hat{m})$. And the nucleated variant will be such that the Schmid factor $SF_m = (\hat{t}.\hat{v}).(\hat{m}.\hat{v})$ is maximized. For simplicity, assume that one such HPV nucleates during the transformation. Note that this HPV would be internally twinned

and sustains disconnection activity on the internal twin interfaces as discussed in this study. The nucleated martensite inside the austenitic matrix is modeled as a penny-shaped inclusion with a given aspect ratio a_2/a_1. The Eshelby tensor S_{klmn} corresponding to this geometry can be obtained from [205]. The expression for the elastic-energy can be simplified as $E_{elastic} = -\frac{1}{2} f \sigma_{tr} \varepsilon_{tr}$, where $\sigma_{tr} = \varepsilon_{tr} C_{ijkl} (S_{klab} t_a m_b - t_k m_l) t_i m_j$. Note that the elastic-energy $E_{elastic}$ has no dependence on the applied load and is the strain-energy associated only with the transformation strain. With these simplifications, the one-dimensional form of the Gibbs' free energy can be written as:

$$G = B(T - T_0) f - \frac{1}{2} f \sigma_{tr} \varepsilon_{tr} - \sigma_0 \varepsilon_{tr} f \tag{7.2}$$

Now consider the superelastic stress-strain curve given in figure 68. Starting from the austenite phase at O ($f = 0$), as increasing strain is applied to the material. The response remains linear-elastic, until a critical point is reached where the following critical condition is achieved at A:

$$F(f = 0) = -\frac{dG}{df}\Big|_{f=0} = F_c \tag{7.3}$$

Where F is the applied driving force obtained from the gradient of reduction of the Gibb's free energy and F_c is the critical driving force for the transformation to be overcome. This driving force corresponds to barriers associated with the lattice friction of the transformation front and is hence an intrinsic material parameter. At this point, the reduction of Gibbs' free energy for unit increase in the volume-fraction of martensite crosses the lattice friction for the transformation. Therefore, martensitic transformation initiates and the corresponding level of stress is the critical transformation stress $\sigma_0 = \sigma^A$. At this point, the critical transformation stress is derived by solving for the stress in the following equation:

$$\sigma^A = \left(F_c + B(T - T_0) - {}^1\!/_2\,\sigma_{tr}\varepsilon_{tr}\right)\Big/_{\varepsilon_{tr}} \tag{7.4}$$

The strain at this point is given by $\varepsilon_A = {}^{\sigma^A}\!/_E$, where E is the uniaxial Young's modulus along $\hat{v}$, the direction of applied load. The physical interpretation is as follows. The required stress for transformation is one that can cross the barriers provided from the lattice friction, the thermodynamic energy barrier and the self-energy of the inclusion in order to form martensite. During the transformation, the consistency condition must be satisfied, given by:

$$\Delta F = \frac{\partial F}{\partial \sigma}\Delta\sigma + \frac{\partial F}{\partial T}\Delta T + \frac{\partial F}{\partial f}\Delta f = \Delta F_c \tag{7.5}$$

It is presumed that there is no hardening associated with the transformation, therefore $\Delta F_c = 0$ on AB (figure 68). Also, no temperature change is assumed during the transformation for simplicity. In real transformations however, it is worthwhile to mention that there can be significant temperature changes (named the "elasto-caloric" effect), and they can be included in the framework as well. The consistency condition can be used to determine the stress-strain curve incrementally from A to B. Point B is dictated the maximum applied external strain. The strain from A to B increments as:

$$\Delta\varepsilon_0 = \frac{\Delta\sigma}{E} + \varepsilon_{tr}\Delta f \tag{7.6}$$

And therefore the strain at any point on AB is given by:

$$\varepsilon_0 = \varepsilon_{tr} f + {}^{\sigma_0}\!/_E \tag{7.7}$$

And when the maximum strain reaches $\varepsilon_0 = \varepsilon_{max}$, the SMA is unloaded. The maximum transformed volume fraction at B is thus given by (7.7) as $f_{max} = \left(\varepsilon_{max} - {}^{\sigma^B}\!/_E\right){}^1\!/_{\varepsilon_{tr}}$. Upon unload, the material unloads elastically until the critical point for reverse transformation is reached (point C in figure 68), characterized by:

$$-F(f = f_{max}) = \left.\frac{dG}{df}\right|_{f=f_{max}} = F_c \tag{7.8}$$

In other words, the reduction in the Gibbs' free energy for a unit reduction in the volume fraction of martensite must equal the critical driving force to reverse the transformation F_c. This critical driving force corresponds to the same lattice-friction for motion of the transformation front albeit in the reverse direction, thus the same F_c as in the forward transformation is employed. The critical reverse-transformation stress at C can be determined as:

$$\sigma^C = \left(B(T - T_0) - F_c - {}^1\!/_2\,\sigma_{tr}\varepsilon_{tr}\right)\Big/_{\varepsilon_{tr}} \tag{7.9}$$

The consistency condition during the reverse-transformation also comes out to be $\Delta\sigma = 0$ as in the forward case, and path CD is parallel to AB. At point D, $f = 0$ is achieved implying the material has fully transformed back to austenite, and the SMA unloads elastically back to O. Thus the path OABCD defines a perfectly reversible transformation pathway without slip-emission. With this foundation, the obvious question is to ask if transformation-induced slip has a thermodynamic basis. If the SMA has a symmetric forward and reverse path without involvement of slip-dislocations why does it not prefer such a path instead of emitting slip?

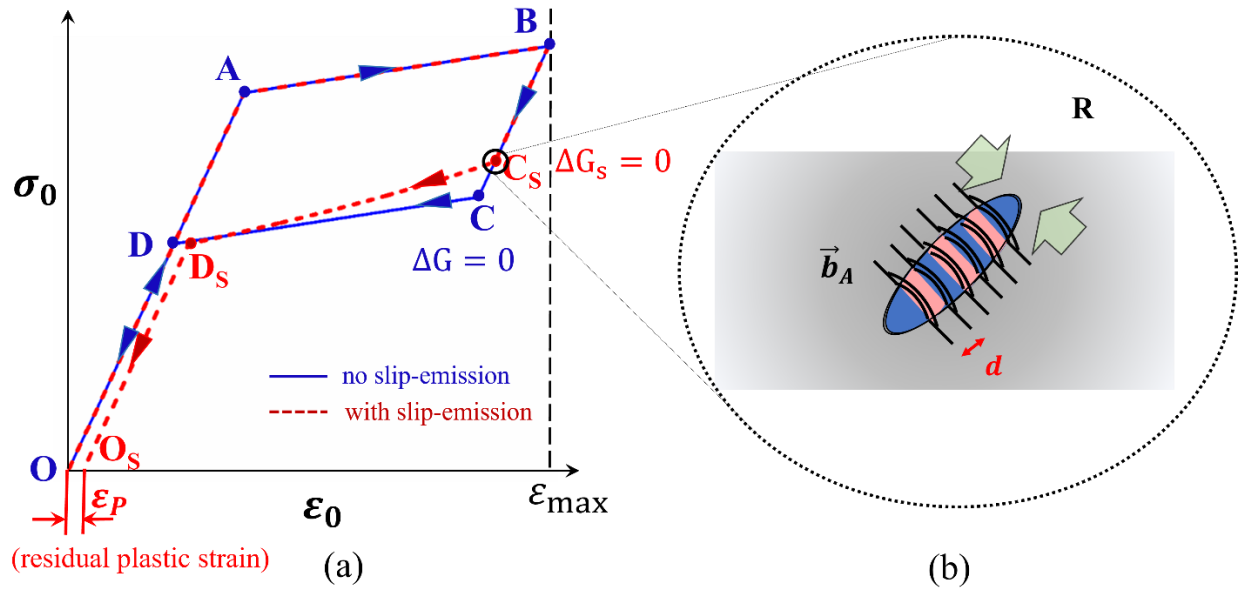

Figure 68: Rationalizing the occurrence of transformation-induced slip from a thermodynamic perspective: (a) Schematic of a superelastic stress-strain curve illustrating scenarios of transformation without slip ($OABCDO$ path in solid blue lines) and transformation with slip ($OABC_SD_SO_S$ path in dashed red lines); it is argued that transformation-induced is only observed because the corresponding Gibbs' free energy condition $\Delta G_S = 0$ is achieved prior to if slip was disallowed (b) Schematic of dislocation-loops forming around a reverse-transforming martensitic inclusion with internal twins; the dislocations have Burgers vector $\vec{b}_A$ and are spaced by distance d corresponding to the internal twin density

An analytical framework involving slip-dislocations is proposed, justifying the preference of transformation-induced slip based on the Gibbs' free energy formulation developed above. Before developing this formulation, an important aspect is to establish the source of residual strain. It is proposed that the residual strain arises from the emission of slip-dislocations at twin interfaces, and their arrangement as parallel dislocation loops around the martensitic inclusion. This is illustrated schematically in figure 68 (b). This process must be considered incrementally. During the reverse-transformation, if the volume-fraction of martensite reduces by $-df$, the increment in emitted residual strain is given by:

$$d\varepsilon^P = {}^{dN}/_{d}\left(\vec{b}_A \otimes \hat{n}_T\right) \tag{7.10}$$

where dN dislocations are emitted from each twin interface, d is the spacing between twin boundaries, $\vec{b}_A$ is the Burgers vector of the slip dislocation and $\hat{n}_T$ is the normal to the slip-plane aligned with the internal twin interface of martensite. The increment in residual strain per unit volume of austenite is then given by:

$$\frac{d\varepsilon^S}{df} = f\frac{d\varepsilon^P}{df} \tag{7.11}$$

where f is the volume-fraction of martensite. The reason the volume-fraction gets involved is because the dislocation-loops enclose a volume around the martensite inclusion and this enclosed volume within the loops determines the volume-averaged residual-strain ε^S. The strain-tensor ε^P defines the strain excluding the volume-fraction. Note that the strain arises from these dislocation loops forming around the inclusion, and not particularly from their plastic-slip around the martensite. This understanding is necessary to quantify the driving force associated with the formation of this residual strain and how it interacts with the transformation strain of the martensite in dictating the thermomechanics. For simplicity, it is assumed that ε_{ij}^P, as a tensor, is parallel to the transformation strain ε_{ij}^{tr}. And let the one-dimensional counterparts of tensors ε_{ij}^S and ε_{ij}^P be represented by ε_S and ε_P respectively. Now, reconsider the unloading from B with the inclusion of the aforementioned residual strain. The effective transformation strain ε^* of the system evolves due to the presence of the emitted dislocation-loops, given by:

$$\frac{d\varepsilon^*}{df} = \frac{d\varepsilon_P}{df} \tag{7.12}$$

The Gibbs' free energy becomes:

$$G_S = B(T - T_0)f - {}^1\!/_2\, f\sigma^*\varepsilon^* - \sigma_0\varepsilon^* f \tag{7.13}$$

where the subscript S on the Gibbs' free energy is used to represent the scenario with emitted slip, ε^* is the modified transformation strain and $\sigma^* = \varepsilon^* C_{ijkl}(S_{klab}t_a m_b - t_k m_l)t_i m_j$ is the modified

Eshelby-inclusion stress sustained within the martensite. Consider the physical implications of (7.13). If the modified transformation-strain ε^* is increased by the slip, the self-energy $-{}^1\!/_2\,\sigma^*\varepsilon^* f$ increases and the work-interaction energy $-\sigma_0\varepsilon^* f$ reduces the Gibbs' free energy. If the critical condition corresponding to G_S is considered, it is given by:

$$-F_S(f = f_{max}) = \frac{dG_S}{df}\Big|_{f_{max}} = F_c + E_S\left(\frac{d\varepsilon_S}{df}\right) \tag{7.14}$$

where E_S is the additional driving-force barrier to be overcome for a given emission of slip-strain ${}^{d\varepsilon_S}\!/_{df}$. And note that from equations (7.12) and (7.11),

$${}^{d\varepsilon_S}\!/_{df} = f\varepsilon^{*\prime} \tag{7.15}$$

The critical stress for reverse-transformation in this case can be determined as:

$$\sigma^{C_S} = \Big(B(T - T_0) - F_c - E_S(f_{max}\varepsilon^{*\prime}) - {}^1\!/_2\,\sigma^*(\varepsilon^* + 2\varepsilon^{*\prime} f_{max})\Big)\Big/_{(\varepsilon^* + \varepsilon^{*\prime} f_{max})} \tag{7.16}$$

A physical interpretation of (7.16) is as follows. At the reverse-transformation stress, the thermodynamic driving force is sufficient to overcome the lattice-friction for the transformation F_c, additional driving force for emitted slip E_S and the change of elastic self-energy and the work-interaction energy. Also note that since this is the first cycle of loading and therefore the first unload, the relations $\varepsilon^* = \varepsilon_{tr}$ and $\sigma^* = \sigma_{tr}$ in (7.16). This equality may not hold over subsequent cycles. Consider the difference $(\sigma^{C_S} - \sigma^C)$ from equations (7.16) and (7.9). The difference yields:

$$\sigma^{C_S} - \sigma^C = \Big(-E_S(f_{max}\varepsilon^{*\prime}) - {}^1\!/_2\,\sigma_{tr}(\varepsilon^{*\prime} f_{max}) - \sigma^C(\varepsilon^{*\prime} f_{max})\Big)\Big/_{(\varepsilon_{tr} + \varepsilon^{*\prime} f_{max})} \tag{7.17}$$

Here is the crux of the process. If $\sigma^{C_S} - \sigma_C \geq 0$, then the Gibbs' free energy condition for reverse-transformation-with-slip (equation (7.14)) is achieved at C_S before the critical condition for reverse-transformation-without-slip (equation (7.8)) at C. This immediately provides a

thermodynamic explanation for why transformation-induced-slip would be preferred in the reverse-transformation. Then the question is how plausible it is to have the condition $\sigma^{C_S} - \sigma_C \geq 0$ to be satisfied. At point C, the gradient of change of the transformation strain weighted with the volume fraction $\varepsilon^{*\prime} f_{max}$ would be sufficiently smaller than the total transformation strain ε_{tr} so that $(\varepsilon_{tr} + \varepsilon^* f_{max}) \geq 0$ in the denominator. In other words, it is unphysical and therefore unlikely that the gradient in the transformation strain $\varepsilon^{*\prime}$ to negate the entire the transformation strain ε_{tr}. Now consider the case where the transformation-strain increases during the reverse-transformation, with the increase caused by the emission of residual strain. In other words, $\varepsilon' \leq 0$, or alternatively, $\varepsilon' = -|\varepsilon'|$. Substituting this expression for $\varepsilon^{*\prime}$ in equation (7.17), one has:

$$\sigma^{C_S} - \sigma^{C} = \left(\left(\sigma_C + {}^{1}/_{2}\, \sigma_{tr} \right) |\varepsilon^{*\prime}| f_{max} - E_S (f_{max} \varepsilon^{*\prime}) \right) \Big/ (\varepsilon^* - |\varepsilon^{*\prime}| f_{max}) \tag{7.18}$$

The physical interpretation of (7.18) is as follows. If the transformation stress σ_C is sufficient to overcome the self-inclusion stress $\left(-{}^{1}/_{2}\, \sigma_{tr}\right)$ and the driving-force for slip-emission E_S, then $\sigma^{C_S} \geq \sigma^{C}$, and reverse-transformation-with-slip is thermodynamically preferred. At this point, it is worthwhile to question the physical origin of the driving-force E_S. Recall that this is associated with the physical origin of the residual strain. And as mentioned previously, the residual strain arises from the emission and arrangement of dislocation-loops such that the residual strain increments according to equation (7.10). It is not associated with plastic-slip of these dislocations, a rationale for which is presented in the next paragraph. Therefore, the driving force E_S necessary corresponds to the core-energy over the total length of dislocation lines emitted around the inclusion. In addition, recall from chapter 6 that there is a reduction in twin disconnection density on the internal interfaces and therefore this change in core-energy is also encompassed in E_S. In summary, E_S measures the net delta of misfit energy (refer ref. [206] for a description of core-

misfit energy) that must be supplied to form slip-dislocations in the austenite at the cost of receding twin-disconnection cores on the interfaces. In this regard, the E_S will depend on the fault-energies on the slip plane, γ_{us}, the twin migration energy barrier γ_{ut} and the sensitivity of twin-disconnection density ρ to microstructural strain covering the propositions from chapters 2, 3 and 4. Also notice that the interpretation of E_S as the net delta of energy in forming slip-dislocations from twinning disconnections is in a way a modern interpretation of the Kajiwara-Kikuchi mechanism proposed 40 years back (introduced in chapter 1).

For arguments' sake, presume that the residual strain ε_S arises from slip of the emitted dislocations on the slip-plane of austenite. Then, the driving-force E_S necessary is nothing other than the austenitic slip-stress σ_S i.e. $E_S = \sigma_S$, which is much higher than the core-energy cost described previously. And it is well-known in SMAs that the austenitic slip-stress σ_S is significantly higher than the forward transformation stress σ_A. And since the reverse-transformation stress σ_C is lower than σ^A, it immediately implies $\sigma_S \gg \sigma^C$. Then, from equation (7.18), one obtains $\sigma^{C_S} - \sigma^C < 0$ and point C would come before C_S during unloading in figure 67 (a). In other words transformation-induced slip is not favored in the reverse-transformation. and a fully-reversible reverse-transformation would be favored instead. So, if plastic-slip of dislocations was the mechanism of residual strain accumulation, then it would never be thermodynamically favored and therefore not occur. This is in contradiction with real experimental observations where residual strain is indeed observed. Therefore, the origin of residual-strain is from the emission and formation of dislocation-cores around the inclusion, accumulating residual strain in the form as proposed in equation (7.10).

Going back to equation (7.18), the rate of evolution of the transformation strain $\varepsilon^{*\prime}$ must be determined as it will eventually dictate the reverse-transformation stress σ^{C_S}. As argued

previously, as the transformation strain is allowed to evolve from $\varepsilon^{*\prime} = 0$ to a negative $\varepsilon^{*\prime} < 0$ raises the reverse-transformation stress σ^{C_S} increases i.e. $\sigma^{C_S} > \sigma^{C}$. It is proposed that the magnitude of $\varepsilon^{*\prime}$ that maximizes σ^{C_S} will be the rate of evolution of the transformation strain observed physically. In other words, the objective is to determine which is the earliest point during the unloading path starting at A, at which the Gibbs' free energy condition for reverse-transformation (equation (7.14)) can be achieved. That would be the physical point of unloading that is realized experimentally. Thus, the derivative condition $\partial\sigma^{C_S}/_{\partial\varepsilon^{*\prime}} = 0$ is applied, for σ^{C_S} given by equation (7.16), yielding

$$D\left(\varepsilon^{*}, \varepsilon^{*\prime}, f_{max}\right) = \left(-\varepsilon^{*} + \left|\varepsilon^{*\prime}\right| f_{max}\right) E_S'\left(f_{max}\varepsilon^{*\prime}\right) + \left(E_S\left(f_{max}\varepsilon^{*\prime}\right) - \sigma^{C}\varepsilon^{*} - \sigma^{*}\varepsilon^{*}\right) = 0 \quad (7.19)$$

Thus, given the function E_S, equation (7.19) can be solved for $\varepsilon^{*\prime}$ and the point of reverse-transformation C_S can be determined.

Next, the consistency condition for the reverse-transformation is derived. This condition determines the increments of stress $\Delta\sigma$, the transformation-strain $\Delta\varepsilon^{*}$, the rate of change of transformation-strain $\Delta\varepsilon^{*\prime}$, and the change in the volume fraction Δf. These 4 increments are determined by solving the following four equations:

$$\frac{\partial F_S}{\partial \sigma}\Delta\sigma + \frac{\partial F_S}{\partial f}\Delta f + \frac{\partial F_S}{\partial \varepsilon^{*}}\Delta\varepsilon^{*} + \frac{\partial F_S}{\partial \varepsilon^{*\prime}}\Delta\varepsilon^{*\prime} + \frac{\partial E_S}{\partial f}\Delta f + \frac{\partial E_S}{\partial \varepsilon^{*\prime}}\Delta\varepsilon^{*\prime} = 0 \quad (7.20)$$

$$\Delta\varepsilon_0 = \frac{\Delta\sigma}{E} + \varepsilon^{*}\Delta f + f\Delta\varepsilon^{*} \quad (7.21)$$

$$\frac{\partial D}{\partial f}\Delta f + \frac{\partial D}{\partial \varepsilon^{*}}\Delta\varepsilon^{*} + \frac{\partial D}{\partial \varepsilon^{*\prime}}\Delta\varepsilon^{*\prime} = 0 \quad (7.22)$$

$$\Delta\varepsilon^{*} = \varepsilon^{*\prime}\Delta f \quad (7.23)$$

Equation (7.20) ensures consistency of the Gibbs' free energy condition (7.14) with the increments. Equation (7.21) enforces the increment of the enforced global strain-increment $\Delta\varepsilon_0$. Equation (7.22) ensures consistency of the derivative condition (7.19) and equation (7.23) captures

the evolution of the eigen-strain. Throughout the reverse-transformation, it must be ensured that $\varepsilon^{*\prime} < 0$ is maintained. In other words, the transformation-strain is consistently increasing $\Delta\varepsilon^* > 0$. If at some point in the reverse-transformation, $\Delta\varepsilon^* \leq 0$ is obtained, then the critical condition for reverse-transformation-without-slip will precede the condition for reverse-transformation-with-slip. From that point onward, the transformation proceeds without emission of residual strain, and consequently without evolution of the transformation-strain. This transformation-strain carries over in the second cycle of loading. This discussion is currently out of scope for the present study and is suggested as an avenue for further research. Nevertheless, the goal was to explain from a thermodynamics standpoint why slip-emission is preferred in the reverse-transformation and an analytical argument for the same has been developed in this chapter.

REFERENCES

[1] K. Otsuka, C.M. Wayman, Shape memory materials, Cambridge university press1999.

[2] P. Müllner, V.A. Chernenko, G. Kostorz, A microscopic approach to the magnetic-field-induced deformation of martensite (magnetoplasticity), Journal of Magnetism and Magnetic Materials 267(3) (2003) 325-334.

[3] J.M. Young, K.J. Van Vliet, Predicting in vivo failure of pseudoelastic NiTi devices under low cycle, high amplitude fatigue, Journal of Biomedical Materials Research Part B: Applied Biomaterials 72B(1) (2005) 17-26.

[4] W. Abuzaid, H. Sehitoglu, Superelasticity and functional fatigue of single crystalline FeNiCoAlTi iron-based shape memory alloy, Materials & Design 160 (2018) 642-651.

[5] H. Sehitoglu, I. Karaman, R. Anderson, X. Zhang, K. Gall, H.J. Maier, Y. Chumlyakov, Compressive response of NiTi single crystals, Acta Materialia 48(13) (2000) 3311-3326.

[6] D.M. Norfleet, P.M. Sarosi, S. Manchiraju, M.F.X. Wagner, M.D. Uchic, P.M. Anderson, M.J. Mills, Transformation-induced plasticity during pseudoelastic deformation in Ni–Ti microcrystals, Acta Materialia 57(12) (2009) 3549-3561.

[7] T. Simon, A. Kröger, C. Somsen, A. Dlouhy, G. Eggeler, On the multiplication of dislocations during martensitic transformations in NiTi shape memory alloys, Acta Materialia 58(5) (2010) 1850-1860.

[8] J. Zhang, C. Somsen, T. Simon, X. Ding, S. Hou, S. Ren, X. Ren, G. Eggeler, K. Otsuka, J. Sun, Leaf-like dislocation substructures and the decrease of martensitic start temperatures: A new explanation for functional fatigue during thermally induced martensitic transformations in coarse-grained Ni-rich Ti–Ni shape memory alloys, Acta Materialia 60(5) (2012) 1999-2006.

[9] S. Kajiwara, T. Kikuchi, Dislocation structures produced by reverse martensitic transformation in a Cu-Zn alloy, Acta Metallurgica 30(2) (1982) 589-598.

[10] S. Kajiwara, Characteristic features of shape memory effect and related transformation behavior in Fe-based alloys, Materials Science and Engineering: A 273-275 (1999) 67-88.

[11] R.F. Hamilton, H. Sehitoglu, Y. Chumlyakov, H.J. Maier, Stress dependence of the hysteresis in single crystal NiTi alloys, Acta Materialia 52(11) (2004) 3383-3402.

[12] S. Kajiwara, W.S. Owen, Substructure of austenite formed by a partial reverse martensitic transformation in an Fe-Pt alloy, Metallurgical Transactions 4(8) (1973) 1988-1990.

[13] P. Chowdhury, H. Sehitoglu, A revisit to atomistic rationale for slip in shape memory alloys, Progress in Materials Science 85 (2017) 1-42.

[14] T. Ezaz, J. Wang, H. Sehitoglu, H.J. Maier, Plastic deformation of NiTi shape memory alloys, Acta Materialia 61(1) (2013) 67-78.

[15] B.A. Bilby, A.G. Crocker, A.H. Cottrell, The theory of the crystallography of deformation twinning, Proceedings of the Royal Society of London. Series A. Mathematical and Physical Sciences 288(1413) (1965) 240-255.

[16] X. Zhang, H. Sehitoglu, Crystallography of the B2 → R → B19′ phase transformations in NiTi, Materials Science and Engineering: A 374(1) (2004) 292-302.

[17] M. Huang, L.C. Brinson, A Multivariant model for single crystal shape memory alloy behavior, Journal of the Mechanics and Physics of Solids 46(8) (1998) 1379-1409.

[18] K. Gall, H. Sehitoglu, The role of texture in tension–compression asymmetry in polycrystalline NiTi, International Journal of Plasticity 15(1) (1999) 69-92.

[19] M. Bönisch, Y. Wu, H. Sehitoglu, Twinning-induced strain hardening in dual-phase FeCoCrNiAl0.5 at room and cryogenic temperature, Scientific Reports 8(1) (2018) 10663.

[20] S. Alkan, P. Chowdhury, H. Sehitoglu, R.G. Rateick, H.J. Maier, Role of nanotwins on fatigue crack growth resistance – Experiments and theory, International Journal of Fatigue 84 (2016) 28-39.

[21] L. Rémy, The interaction between slip and twinning systems and the influence of twinning on the mechanical behavior of fcc metals and alloys, Metallurgical Transactions A 12(3) (1981) 387-408.

[22] C.N. Reid, A review of mechanical twinning in body-centred cubic metals and its relation to brittle fracture, Journal of the Less Common Metals 9(2) (1965) 105-122.

[23] S. Mahajan, D.F. Williams, Deformation Twinning in Metals and Alloys, International Metallurgical Reviews 18(2) (1973) 43-61.

[24] J.W. Christian, S. Mahajan, Deformation twinning, Progress in Materials Science 39(1) (1995) 1-157.

[25] T. Ezaz, H. Sehitoglu, W. Abuzaid, H.J. Maier, Higher order twin modes in martensitic NiTi—The ($20\bar{1}$) case, Materials Science and Engineering: A 558 (2012) 422-430.

[26] J.X. Zhang, M. Sato, A. Ishida, Deformation mechanism of martensite in Ti-rich Ti–Ni shape memory alloy thin films, Acta Materialia 54(4) (2006) 1185-1198.

[27] N. Zárubová, Y. Ge, O. Heczko, S.P. Hannula, In situ TEM study of deformation twinning in Ni–Mn–Ga non-modulated martensite, Acta Materialia 61(14) (2013) 5290-5299.

[28] S. Miyazaki, K. Otsuka, C.M. Wayman, The shape memory mechanism associated with the martensitic transformation in Ti・Ni alloys—II. Variant coalescence and shape recovery, Acta Metallurgica 37(7) (1989) 1885-1890.

[29] S. Miyazaki, K. Otsuka, C.M. Wayman, The shape memory mechanism associated with the martensitic transformation in Ti・Ni alloys—I. Self-accommodation, Acta Metallurgica 37(7) (1989) 1873-1884.

[30] Y. Liu, Z. Xie, J.V. Humbeeck, L. Delaey, Y. Liu, On the deformation of the twinned domain in Niti shape memory alloys, Philosophical Magazine A 80(8) (2000) 1935-1953.

[31] Y. Liu, Z.L. Xie, J. Van Humbeeck, L. Delaey, Effect of texture orientation on the martensite deformation of NiTi shape memory alloy sheet, Acta Materialia 47(2) (1999) 645-660.

[32] T. Duerig, A. Pelton, D. Stöckel, An overview of nitinol medical applications, Materials Science and Engineering: A 273-275 (1999) 149-160.

[33] K. Otsuka, X. Ren, Physical metallurgy of Ti–Ni-based shape memory alloys, Progress in Materials Science 50(5) (2005) 511-678.

[34] T. Onda, Y. Bando, T. Ohba, K. Otsuka, Electron Microscopy Study of Twins in Martensite in a Ti-50.0 at%Ni Alloy, Materials Transactions, JIM 33(4) (1992) 354-359.

[35] M. Nishida, H. Ohgi, I. Itai, A. Chiba, K. Yamauchi, Electron microscopy studies of twin morphologies in B19′ martensite in the Ti-Ni shape memory alloy, Acta Metallurgica et Materialia 43(3) (1995) 1219-1227.

[36] Y. Liu, Z.L. Xie, The Rational Nature of Type II Twin in NiTi Shape Memory Alloy, Journal of Intelligent Material Systems and Structures 17(12) (2006) 1083-1090.

[37] T. Ezaz, H. Sehitoglu, Type II detwinning in NiTi, Applied Physics Letters 98(14) (2011) 141906.

[38] Z.L. Xie, Y. Liu, HRTEM study of ⟨011⟩ type II twin in NiTi shape memory alloy, Philosophical Magazine 84(32) (2004) 3497-3507.

[39] K.M. Knowles, D.A. Smith, The crystallography of the martensitic transformation in equiatomic nickel-titanium, Acta Metallurgica 29(1) (1981) 101-110.

[40] B.A. Bilby, A.G. Crocker, The theory of the crystallography of deformation twinning, Proceedings of the Royal Society of London. Series A. Mathematical and Physical Sciences 288(1413) (1965) 240-255.

[41] H. Tobe, H.Y. Kim, T. Inamura, H. Hosoda, S. Miyazaki, Origin of {332} twinning in metastable β-Ti alloys, Acta Materialia 64 (2014) 345-355.

[42] C. Cayron, Shifting the Shear Paradigm in the Crystallographic Models of Displacive Transformations in Metals and Alloys, Crystals 8(4) (2018).

[43] X. Ji, I. Gutierrez-Urrutia, S. Emura, T. Liu, T. Hara, X. Min, D. Ping, K. Tsuchiya, Twinning behavior of orthorhombic-α" martensite in a Ti-7.5Mo alloy, Science and Technology of Advanced Materials 20(1) (2019) 401-411.

[44] D.S. Lieberman, M.S. Wechsler, T.A. Read, Cubic to Orthorhombic Diffusionless Phase Change— Experimental and Theoretical Studies of AuCd, Journal of Applied Physics 26(4) (1955) 473-484.

[45] C.M. Wayman, The phenomenological theory of martensite crystallography: Interrelationships, Metallurgical and Materials Transactions A 25(9) (1994) 1787-1795.

[46] R.D. James, K.F. Hane, Martensitic transformations and shape-memory materials, Acta Materialia 48(1) (2000) 197-222.

[47] E. Patoor, D.C. Lagoudas, P.B. Entchev, L.C. Brinson, X. Gao, Shape memory alloys, Part I: General properties and modeling of single crystals, Mechanics of Materials 38(5) (2006) 391-429.

[48] P. Chowdhury, H. Sehitoglu, Atomistic Energetics and Critical Twinning Stress Prediction in Face and Body Centered Cubic Metals: Recent Progress, Journal of Engineering Materials and Technology 140(2) (2018) 020801-020801-19.

[49] A. Ojha, H. Sehitoglu, Critical Stresses for Twinning, Slip, and Transformation in Ti-Based Shape Memory Alloys, Shape Memory and Superelasticity 2(2) (2016) 180-195.

[50] J. Wang, H. Sehitoglu, Twinning stress in shape memory alloys: Theory and experiments, Acta Materialia 61(18) (2013) 6790-6801.

[51] Y.H. Zhao, Y.T. Zhu, X.Z. Liao, Z. Horita, T.G. Langdon, Tailoring stacking fault energy for high ductility and high strength in ultrafine grained Cu and its alloy, Applied Physics Letters 89(12) (2006) 121906.

[52] C. Maletta, E. Sgambitterra, F. Furgiuele, R. Casati, A. Tuissi, Fatigue properties of a pseudoelastic NiTi alloy: Strain ratcheting and hysteresis under cyclic tensile loading, International Journal of Fatigue 66 (2014) 78-85.

[53] W. Abuzaid, H. Sehitoglu, Functional fatigue of Ni50.3Ti25Hf24.7 – Heterogeneities and evolution of local transformation strains, Materials Science and Engineering: A 696 (2017) 482-492.

[54] G. Eggeler, E. Hornbogen, A. Yawny, A. Heckmann, M. Wagner, Structural and functional fatigue of NiTi shape memory alloys, Materials Science and Engineering: A 378(1) (2004) 24-33.

[55] N. Zou, Z. Li, Y. Zhang, B. Yang, X. Zhao, C. Esling, L. Zuo, Plastic deformation of Ni–Mn–Ga 7M modulated martensite by twinning & detwinning and intermartensitic transformation, International Journal of Plasticity 100 (2018) 1-13.

[56] O. Heczko, Understanding Motion of Twin Boundary—A Key to Magnetic Shape Memory Effect, IEEE Transactions on Magnetics 50(11) (2014) 1-7.

[57] T. Hara, T. Ohba, S. Miyazaki, K. Otsuka, Electron Microscopy Study of Type II Twins in γ₁′ Cu-Al-Ni Martensite, Materials Transactions, JIM 33(12) (1992) 1105-1113.

[58] D.Z. Liu, D. Dunne, Atomic force microscope study of the interface of twinned martensite in copper–aluminium–nickel, Scripta Materialia 48(12) (2003) 1611-1616.

[59] K. Okamoto, S. Ichinose, K. Morii, K. Otsuka, K. Shimizu, Crystallography of β1 → γ′1 stress-induced martensitic transformation in a Cu-Al-Ni alloy, Acta Metallurgica 34(10) (1986) 2065-2073.

[60] K. Adachi, J. Perkins, C.M. Wayman, Type II twins in self-accommodating martensite plate variants in a Cu-Zn-Al shape memory alloy, Acta Metallurgica 34(12) (1986) 2471-2485.

[61] K. Morii, T. Ohba, K. Otsuka, H. Sakamoto, K. Shimizu, Crystallography of β2 → γ2′ martensitic transformation in Au-47.5 at.% Cd and Au-47.5 at.% Cd-Cu alloys, Acta Metallurgica et Materialia 39(11) (1991) 2719-2725.

[62] K.M. Knowles, A high-resolution electron microscope study of nickel-titanium martensite, Philosophical Magazine A 45(3) (1982) 357-370.

[63] J.W. Christian, CHAPTER 20 - Deformation Twinning, in: J.W. Christian (Ed.), The Theory of Transformations in Metals and Alloys, Pergamon, Oxford, 2002, pp. 859-960.

[64] Y. Liu, Z.L. Xie, Twinning and detwinning of 〈0 1 1〉 type II twin in shape memory alloy, Acta Materialia 51(18) (2003) 5529-5543.

[65] H. Yan, C. Zhang, Y. Zhang, X. Wang, C. Esling, X. Zhao, L. Zuo, Crystallographic insights into Ni-Co-Mn-In metamagnetic shape memory alloys, Journal of Applied Crystallography 49(5) (2016) 1585-1592.

[66] M. Nishida, K. Yamauchi, I. Itai, H. Ohgi, A. Chiba, High resolution electron microscopy studies of twin boundary structures in B19′ martensite in the Ti-Ni shape memory alloy, Acta Metallurgica et Materialia 43(3) (1995) 1229-1234.

[67] M. Nishida, T. Hara, M. Matsuda, S. Ii, Crystallography and morphology of various interfaces in Ti–Ni, Ti–Pd and Ni–Mn–Ga shape memory alloys, Materials Science and Engineering: A 481-482 (2008) 18-27.

[68] M. Matsuda, Y. Yasumoto, K. Hashimoto, T. Hara, M. Nishida, Transmission Electron Microscopy of Twins in 10M Martensite in Ni–Mn–Ga Ferromagnetic Shape Memory Alloy, MATERIALS TRANSACTIONS advpub (2012) 1203191599-1203191599.

[69] J.P. Hirth, R.C. Pond, Steps, dislocations and disconnections as interface defects relating to structure and phase transformations, Acta Materialia 44(12) (1996) 4749-4763.

[70] R.C. Pond, X. Ma, Y.W. Chai, J.P. Hirth, Chapter 74 Topological Modelling of Martensitic Transformations, in: F.R.N. Nabarro, J.P. Hirth (Eds.), Dislocations in Solids, Elsevier2007, pp. 225-261.

[71] J.P. Hirth, J. Wang, C.N. Tomé, Disconnections and other defects associated with twin interfaces, Progress in Materials Science 83 (2016) 417-471.

[72] R.C. Pond, J.P. Hirth, Defects at Surfaces and Interfaces, in: H. Ehrenreich, D. Turnbull (Eds.), Solid State Physics, Academic Press1994, pp. 287-365.

[73] G.B. Olson, M. Cohen, Interphase-boundary dislocations and the concept of coherency, Acta Metallurgica 27(12) (1979) 1907-1918.

[74] F.C. Frank, J.H. van der Merwe, F. Mott Nevill, One-dimensional dislocations. I. Static theory, Proceedings of the Royal Society of London. Series A. Mathematical and Physical Sciences 198(1053) (1949) 205-216.

[75] J.W. Christian, Crystallographic theories, interface structures, and transformation mechanisms, Metallurgical and Materials Transactions A 25(9) (1994) 1821-1839.

[76] R.C. Pond, X. Ma, J.P. Hirth, T.E. Mitchell, Disconnections in simple and complex structures, Philosophical Magazine 87(33) (2007) 5289-5307.

[77] J.M. Howe, R.C. Pond, J.P. Hirth, The role of disconnections in phase transformations, Progress in Materials Science 54(6) (2009) 792-838.

[78] R.C. Pond, S. Celotto, J.P. Hirth, A comparison of the phenomenological theory of martensitic transformations with a model based on interfacial defects, Acta Materialia 51(18) (2003) 5385-5398.

[79] X. Ma, R.C. Pond, Parent–martensite interface structure in ferrous systems, Journal of Nuclear Materials 361(2) (2007) 313-321.

[80] X. Ma, R.C. Pond, Martensitic interfaces and transformation crystallography in Pu–Ga alloys, Journal of Materials Science 46(12) (2011) 4236-4242.

[81] J.S. Bowles, J.K. Mackenzie, The crystallography of martensite transformations I, Acta Metallurgica 2(1) (1954) 129-137.

[82] R.C. Pond, J.P. Hirth, Topological model of type II deformation twinning, Acta Materialia 151 (2018) 229-242.

[83] R.C. Pond, J.P. Hirth, K.M. Knowles, Topological model of type II deformation twinning in NiTi martensite, Philosophical Magazine 99(13) (2019) 1619-1632.

[84] I.J. Beyerlein, X. Zhang, A. Misra, Growth Twins and Deformation Twins in Metals, Annual Review of Materials Research 44(1) (2014) 329-363.

[85] R.C. Pond, J.P. Hirth, A. Serra, D.J. Bacon, Atomic displacements accompanying deformation twinning: shears and shuffles, Materials Research Letters 4(4) (2016) 185-190.

[86] S. Dilibal, Investigation of Nucleation and Growth of Detwinning Mechanism in Martensitic Single Crystal NiTi Using Digital Image Correlation, Metallography, Microstructure, and Analysis 2(4) (2013) 242-248.

[87] J. Wang, H. Sehitoglu, Martensite modulus dilemma in monoclinic NiTi-theory and experiments, International Journal of Plasticity 61 (2014) 17-31.

[88] S. Plimpton, Fast Parallel Algorithms for Short-Range Molecular Dynamics, Journal of Computational Physics 117(1) (1995) 1-19.

[89] J. Hafner, Ab-initio simulations of materials using VASP: Density-functional theory and beyond, Journal of Computational Chemistry 29(13) (2008) 2044-2078.

[90] B. Li, K.M. Knowles, Molecular dynamics simulation of twinning in devitrite, Na2Ca3Si6O16, Philosophical Magazine 93(13) (2013) 1582-1603.

[91] S. Ogata, J. Li, S. Yip, Energy landscape of deformation twinning in bcc and fcc metals, Physical Review B 71(22) (2005) 224102.

[92] W.-S. Ko, B. Grabowski, J. Neugebauer, Development and application of a Ni-Ti interatomic potential with high predictive accuracy of the martensitic phase transition, Physical Review B 92(13) (2015) 134107.

[93] Y. Zhong, K. Gall, T. Zhu, Atomistic study of nanotwins in NiTi shape memory alloys, Journal of Applied Physics 110(3) (2011) 033532.

[94] G. Ren, H. Sehitoglu, Interatomic potential for the NiTi alloy and its application, Computational Materials Science 123 (2016) 19-25.

[95] Y. Kudoh, M. Tokonami, S. Miyazaki, K. Otsuka, Crystal structure of the martensite in Ti-49.2 at.%Ni alloy analyzed by the single crystal X-ray diffraction method, Acta Metallurgica 33(11) (1985) 2049-2056.

[96] N. Hatcher, O.Y. Kontsevoi, A.J. Freeman, Role of elastic and shear stabilities in the martensitic transformation path of NiTi, Physical Review B 80(14) (2009) 144203.

[97] K. Otsuka, T. Sawamura, K. Shimizu, Crystal structure and internal defects of equiatomic TiNi martensite, physica status solidi (a) 5(2) (1971) 457-470.

[98] A.J. Vattré, M.J. Demkowicz, Partitioning of elastic distortions at a semicoherent heterophase interface between anisotropic crystals, Acta Materialia 82 (2015) 234-243.

[99] B. Li, K.M. Knowles, Molecular dynamics simulation of albite twinning and pericline twinning in low albite, Modelling and Simulation in Materials Science and Engineering 21(5) (2013) 055012.

[100] A. Kelly, K.M. Knowles, Chapter 11 - Twinning, Crystallography and Crystal Defects, John Wiley & Sons Ltd., ,Chichester, UK, 2012, pp. 335-361.

[101] P.D. Bristowe, A.G. Crocker, A computer simulation study of the structures of twin boundaries in body-centred cubic crystals, The Philosophical Magazine: A Journal of Theoretical Experimental and Applied Physics 31(3) (1975) 503-517.

[102] R. Schweinfest, F. Ernst, T. Wagner, M. Rühle, High-precision assessment of interface lattice offset by quantitative HRTEM, J Microsc 194(1) (1999) 142-151.

[103] M.D. Sangid, H. Sehitoglu, H.J. Maier, T. Niendorf, Grain boundary characterization and energetics of superalloys, Materials Science and Engineering: A 527(26) (2010) 7115-7125.

[104] V. Vítek, Multilayer stacking faults and twins on {211} planes in B.C.C. metals, Scripta Metallurgica 4(9) (1970) 725-732.

[105] S. Kibey, J.B. Liu, D.D. Johnson, H. Sehitoglu, Generalized planar fault energies and twinning in Cu–Al alloys, Applied Physics Letters 89(19) (2006) 191911.

[106] A. Ojha, H. Sehitoglu, L. Patriarca, H.J. Maier, Twin nucleation in Fe-based bcc alloys—modeling and experiments, Modelling and Simulation in Materials Science and Engineering 22(7) (2014) 075010.

[107] R.C. Pond, D.L. Medlin, A. Serra, A study of the accommodation of coherency strain by interfacial defects at a grain boundary in gold, Philosophical Magazine 86(29-31) (2006) 4667-4684.

[108] K.N. Melton, O. Mercier, Fatigue of NITI thermoelastic martensites, Acta Metallurgica 27(1) (1979) 137-144.

[109] P. Chowdhury, H. Sehitoglu, Deformation physics of shape memory alloys – Fundamentals at atomistic frontier, Progress in Materials Science 88 (2017) 49-88.

[110] M. Sade, R. Rapacioli, M. Ahlers, Fatigue in Cu・Zn・Al single crystals, Acta Metallurgica 33(3) (1985) 487-497.

[111] X. Jiang, M. Hida, Y. Takemoto, A. Sakakibara, H. Yasuda, H. Mori, In situ observation of stress-induced martensitic transformation and plastic deformation in TiNi alloy, Materials Science and Engineering: A 238(2) (1997) 303-308.

[112] C. Damiani, M. Sade, F.C. Lovey, Fatigue in Cu-Zn-Al single crystals during pseudoelastic cycling: In situ observations by SEM and optical microscopy, J. Phys. IV France 112 (2003) 623-626.

[113] R. Delville, B. Malard, J. Pilch, P. Sittner, D. Schryvers, Transmission electron microscopy investigation of dislocation slip during superelastic cycling of Ni–Ti wires, International Journal of Plasticity 27(2) (2011) 282-297.

[114] A.R. Pelton, G.H. Huang, P. Moine, R. Sinclair, Effects of thermal cycling on microstructure and properties in Nitinol, Materials Science and Engineering: A 532 (2012) 130-138.

[115] M.F.X. Wagner, N. Nayan, U. Ramamurty, Healing of fatigue damage in NiTi shape memory alloys, Journal of Physics D: Applied Physics 41(18) (2008) 185408.

[116] C. Maletta, E. Sgambitterra, F. Furgiuele, R. Casati, A. Tuissi, Fatigue of pseudoelastic NiTi within the stress-induced transformation regime: a modified Coffin–Manson approach, Smart Materials and Structures 21(11) (2012) 112001.

[117] W.S. Lai, B.X. Liu, Lattice stability of some Ni-Ti alloy phases versus their chemical composition and disordering, Journal of Physics: Condensed Matter 12(5) (2000) L53-L60.

[118] H. Tobushi, T. Hachisuka, S. Yamada, P.-H. Lin, Rotating-bending fatigue of a TiNi shape-memory alloy wire, Mechanics of Materials 26(1) (1997) 35-42.

[119] H. Tobushi, T. Hachisuka, T. Hashimoto, S. Yamada, Cyclic Deformation and Fatigue of a TiNi Shape-Memory Alloy Wire Subjected to Rotating Bending, Journal of Engineering Materials and Technology 120(1) (1998) 64-70.

[120] S. Miyazaki, K. Mizukoshi, T. Ueki, T. Sakuma, Y. Liu, Fatigue life of Ti–50 at.% Ni and Ti–40Ni–10Cu (at.%) shape memory alloy wires, Materials Science and Engineering: A 273-275 (1999) 658-663.

[121] D.C. Lagoudas, D.A. Miller, L. Rong, P.K. Kumar, Thermomechanical fatigue of shape memory alloys, Smart Materials and Structures 18(8) (2009) 085021.

[122] S.W. Robertson, A.R. Pelton, R.O. Ritchie, Mechanical fatigue and fracture of Nitinol, International Materials Reviews 57(1) (2012) 1-37.

[123] P. Chowdhury, G. Ren, H. Sehitoglu, NiTi superelasticity via atomistic simulations, Philosophical Magazine Letters 95(12) (2015) 574-586.

[124] D. Farkas, D. Roqueta, A. Vilette, K. Ternes, Atomistic simulations in ternary Ni - Ti - Al alloys, Modelling and Simulation in Materials Science and Engineering 4(4) (1996) 359-369.

[125] H. Ishida, Y. Hiwatari, MD simulation of martensitic transformations in TiNi alloys with MEAM, Molecular Simulation 33(4-5) (2007) 459-461.

[126] D. Mutter, P. Nielaba, Simulation of structural phase transitions in NiTi, Physical Review B 82(22) (2010) 224201.

[127] M. Muralles, S.-D. Park, S.Y. Kim, B. Lee, Phase transformations, detwinning and superelasticity of shape-memory NiTi from MEAM with practical capability, Computational Materials Science 130 (2017) 138-143.

[128] M.D. Sangid, H.J. Maier, H. Sehitoglu, A physically based fatigue model for prediction of crack initiation from persistent slip bands in polycrystals, Acta Materialia 59(1) (2011) 328-341.

[129] D.M. Barnett, J. Lothe, An image force theorem for dislocations in anisotropic bicrystals, Journal of Physics F: Metal Physics 4(10) (1974) 1618-1635.

[130] V. Bulatov, W. Cai, Computer simulations of dislocations, Oxford University Press2006.

[131] J. Chang, W. Cai, V.V. Bulatov, S. Yip, Dislocation motion in BCC metals by molecular dynamics, Materials Science and Engineering: A 309-310 (2001) 160-163.

[132] J. Chang, W. Cai, V.V. Bulatov, S. Yip, Molecular dynamics simulations of motion of edge and screw dislocations in a metal, Computational Materials Science 23(1) (2002) 111-115.

[133] J.A. Moriarty, V. Vitek, V.V. Bulatov, S. Yip, Atomistic simulations of dislocations and defects, Journal of Computer-Aided Materials Design 9(2) (2002) 99-132.

[134] X. Liu, S.I. Golubov, C.H. Woo, H. Huang, Glide of edge dislocations in tungsten and molybdenum, Materials Science and Engineering: A 365(1) (2004) 96-100.

[135] G. Lasko, D. Saraev, S. Schmauder, P. Kizler, Atomic-scale simulations of the interaction between a moving dislocation and a bcc/fcc phase boundary, Computational Materials Science 32(3) (2005) 418-425.

[136] S. Groh, E.B. Marin, M.F. Horstemeyer, D.J. Bammann, Dislocation motion in magnesium: a study by molecular statics and molecular dynamics, Modelling and Simulation in Materials Science and Engineering 17(7) (2009) 075009.

[137] A.S. Argon, Kinematics and Kinetics in Crystal Plasticity, Strengthening Mechanisms in Crystal Plasticity, , Oxford University Press, Oxford, 2007.

[138] A. Stukowski, Visualization and analysis of atomistic simulation data with OVITO–the Open Visualization Tool, Modelling and Simulation in Materials Science and Engineering 18(1) (2009) 015012.

[139] A.S.K. Mohammed, H. Sehitoglu, Martensitic twin boundary migration as a source of irreversible slip in shape memory alloys, Acta Materialia 186 (2020) 50-67.

[140] A.W. Sleeswyk, Emissary dislocations: Theory and experiments on the propagation of deformation twins in α-iron, Acta Metallurgica 10(8) (1962) 705-725.

[141] J. Wang, N. Li, O. Anderoglu, X. Zhang, A. Misra, J.Y. Huang, J.P. Hirth, Detwinning mechanisms for growth twins in face-centered cubic metals, Acta Materialia 58(6) (2010) 2262-2270.

[142] G. Arlt, Twinning in ferroelectric and ferroelastic ceramics: stress relief, Journal of Materials Science 25(6) (1990) 2655-2666.

[143] D.J. Barber, H.R. Wenk, Deformation twinning in calcite, dolomite, and other rhombohedral carbonates, Physics and Chemistry of Minerals 5(2) (1979) 141-165.

[144] D. Xie, G. Hirth, J.P. Hirth, J. Wang, Defects in deformation twins in plagioclase, Physics and Chemistry of Minerals 46(10) (2019) 959-975.

[145] K. Lu, Stabilizing nanostructures in metals using grain and twin boundary architectures, Nature Reviews Materials 1(5) (2016) 16019.

[146] O.K. Celebi, A.S.K. Mohammed, J.A. Krogstad, H. Sehitoglu, Evolving dislocation cores at Twin Boundaries: Theory of CRSS Elevation, International Journal of Plasticity 148 (2022) 103141.

[147] B. Gludovatz, A. Hohenwarter, D. Catoor, E.H. Chang, E.P. George, R.O. Ritchie, A fracture-resistant high-entropy alloy for cryogenic applications, Science 345(6201) (2014) 1153.

[148] P. Chowdhury, H. Sehitoglu, R. Rateick, Recent advances in modeling fatigue cracks at microscale in the presence of high density coherent twin interfaces, Current Opinion in Solid State and Materials Science 20(3) (2016) 140-150.

[149] Y. Song, X. Chen, V. Dabade, T.W. Shield, R.D. James, Enhanced reversibility and unusual microstructure of a phase-transforming material, Nature 502(7469) (2013) 85-88.

[150] R. Sidharth, W. Abuzaid, M. Vollmer, T. Niendorf, H. Sehitoglu, Fatigue Crack Initiation in the Iron-Based Shape Memory Alloy FeMnAlNiTi, Shape Memory and Superelasticity (2020).

[151] M. Gueltig, H. Ossmer, M. Ohtsuka, H. Miki, K. Tsuchiya, T. Takagi, M. Kohl, High Frequency Thermal Energy Harvesting Using Magnetic Shape Memory Films, Advanced Energy Materials 4(17) (2014) 1400751.

[152] P. II, S. Benzing, J. Asnani, M. Vivake, Superelastic tire, in: U.S.P.T.O (Ed.) United States of America as Represented by the Administrator of National Aeronautics and Space Administration, United States, 2016.

[153] H.A. Khater, A. Serra, R.C. Pond, Atomic shearing and shuffling accompanying the motion of twinning disconnections in Zirconium, Philosophical Magazine 93(10-12) (2013) 1279-1298.

[154] P. Müllner, Twinning stress of type I and type II deformation twins, Acta Materialia 176 (2019) 211-219.

[155] A.S.K. Mohammed, H. Sehitoglu, Modeling the interface structure of type II twin boundary in B19′ NiTi from an atomistic and topological standpoint, Acta Materialia 183 (2020) 93-109.

[156] Y. Gao, L. Casalena, M.L. Bowers, R.D. Noebe, M.J. Mills, Y. Wang, An origin of functional fatigue of shape memory alloys, Acta Materialia 126 (2017) 389-400.

[157] Y.F. Zheng, L.C. Zhao, H.Q. Ye, HREM studies of twin boundary structure in deformed martensite in the cold-rolled TiNi shape memory alloy, Materials Science and Engineering: A 297(1) (2001) 185-196.

[158] P. Müllner, A.H. King, Deformation of hierarchically twinned martensite, Acta Materialia 58(16) (2010) 5242-5261.

[159] B. Karki, P. Müllner, R. Pond, Topological model of type II deformation twinning in 10M Ni-Mn-Ga, Acta Materialia (2020).

[160] A.P. Sutton, V. Vitek, J.W. Christian, On the structure of tilt grain boundaries in cubic metals I. Symmetrical tilt boundaries, Philosophical Transactions of the Royal Society of London. Series A, Mathematical and Physical Sciences 309(1506) (1983) 1-36.

[161] J.P. Hirth, D.M. Barnett, J. Lothe, Stress fields of dislocation arrays at interfaces in bicrystals, Philosophical Magazine A 40(1) (1979) 39-47.

[162] T. Ezaz, H. Sehitoglu, H.J. Maier, Energetics of twinning in martensitic NiTi, Acta Materialia 59(15) (2011) 5893-5904.

[163] K. Saitoh, K. Kubota, T. Sato, Atomic-level structural change in Ni-Ti alloys under martensite and amorphous transformations, Technische Mechanik 30(1-3) (2010) 269-279.

[164] Y. Zhong, K. Gall, T. Zhu, Atomistic characterization of pseudoelasticity and shape memory in NiTi nanopillars, Acta Materialia 60(18) (2012) 6301-6311.

[165] V.B. Ozdol, C. Gammer, X.G. Jin, P. Ercius, C. Ophus, J. Ciston, A.M. Minor, Strain mapping at nanometer resolution using advanced nano-beam electron diffraction, Applied Physics Letters 106(25) (2015) 253107.

[166] W.Z. Abuzaid, H. Sehitoglu, J. Lambros, Localisation of plastic strain at the microstructurlal level in Hastelloy X subjected to monotonic, fatigue, and creep loading: the role of grain boundaries and slip transmission, Materials at High Temperatures 33(4-5) (2016) 384-400.

[167] A.P. Stebner, H.M. Paranjape, B. Clausen, L.C. Brinson, A.R. Pelton, In Situ Neutron Diffraction Studies of Large Monotonic Deformations of Superelastic Nitinol, Shape Memory and Superelasticity 1(2) (2015) 252-267.

[168] A.N. Bucsek, D. Dale, J.Y.P. Ko, Y. Chumlyakov, A.P. Stebner, Measuring stress-induced martensite microstructures using far-field high-energy diffraction microscopy, Acta Crystallographica Section A 74(5) (2018) 425-446.

[169] W. Tirry, D. Schryvers, Quantitative determination of strain fields around Ni4Ti3 precipitates in NiTi, Acta Materialia 53(4) (2005) 1041-1049.

[170] W. Tirry, D. Schryvers, Linking a completely three-dimensional nanostrain to a structural transformation eigenstrain, Nature Materials 8(9) (2009) 752-757.

[171] M.J. Hÿtch, J.-L. Putaux, J.-M. Pénisson, Measurement of the displacement field of dislocations to 0.03 Å by electron microscopy, Nature 423(6937) (2003) 270-273.

[172] F. Brenne, A.S.K. Mohammed, H. Sehitoglu, High resolution atomic scale characterization of dislocations in high entropy alloys: Critical assessment of template matching and geometric phase analysis, Ultramicroscopy 219 (2020) 113134.

[173] L. Straka, A. Soroka, H. Seiner, H. Hänninen, A. Sozinov, Temperature dependence of twinning stress of Type I and Type II twins in 10M modulated Ni–Mn–Ga martensite, Scripta Materialia 67(1) (2012) 25-28.

[174] E. Bronstein, E. Faran, D. Shilo, Analysis of austenite-martensite phase boundary and twinned microstructure in shape memory alloys: The role of twinning disconnections, Acta Materialia 164 (2019) 520-529.

[175] X. Ren, K. Otsuka, The Role of Softening in Elastic Constant c44 in Martensitic Transformation, Scripta Materialia 38(11) (1998) 1669-1675.

[176] X. Ren, N. Miura, J. Zhang, K. Otsuka, K. Tanaka, M. Koiwa, T. Suzuki, Y.I. Chumlyakov, M. Asai, A comparative study of elastic constants of Ti–Ni-based alloys prior to martensitic transformation, Materials Science and Engineering: A 312(1) (2001) 196-206.

[177] X. Ding, T. Suzuki, X. Ren, J. Sun, K. Otsuka, Precursors to stress-induced martensitic transformations and associated superelasticity: Molecular dynamics simulations and an analytical theory, Physical Review B 74(10) (2006) 104111.

[178] X. Ding, J. Zhang, Y. Wang, Y. Zhou, T. Suzuki, J. Sun, K. Otsuka, X. Ren, Experimental study of elastic constant softening prior to stress-induced martensitic transformation, Physical Review B 77(17) (2008) 174103.

[179] K. Knowles, A high-resolution electron microscope study of nickel-titanium martensite, Philosophical Magazine A 45(3) (1982) 357-370.

[180] K. Adachi, J. Perkins, C.M. Wayman, Type II twins in self-accommodating martensite plate variants in a Cu・Zn・Al shape memory alloy, Acta Metallurgica 34(12) (1986) 2471-2485.

[181] K. Okamoto, S. Ichinose, K. Morii, K. Otsuka, K. Shimizu, Crystallography of β1 → γ′1 stress-induced martensitic transformation in a Cu・Al・Ni alloy, Acta Metallurgica 34(10) (1986) 2065-2073.

[182] K. Morii, T. Ohba, K. Otsuka, H. Sakamoto, K. Shimizu, Crystallography of β2 → γ2′ martensitic transformation in Au-47.5 at.% Cd and Au-47.5 at.% Cd・Cu alloys, Acta Metallurgica et Materialia 39(11) (1991) 2719-2725.

[183] T. Hara, T. Ohba, S. Miyazaki, K. Otsuka, Electron Microscopy Study of Type II Twins in γ₁′ Cu–Al–Ni Martensite, Materials Transactions, JIM 33(12) (1992) 1105-1113.

[184] M. Nishida, T. Hara, Y. Morizono, A. Ikeya, H. Kijima, A. Chiba, Transmission electron microscopy of twins in martensite in Ti・Pd shape memory alloy, Acta Materialia 45(11) (1997) 4847-4853.

[185] Z.L. Xie, Y. Liu, HRTEM study of⟨ 011⟩ type II twin in NiTi shape memory alloy, Philosophical Magazine 84(32) (2004) 3497-3507.

[186] M. Nishida, M. Matsuda, Y. Yasumoto, S. Yano, Y. Yamabe-Mitarai, T. Hara, Crystallography and morphology of twins in equiatomic TiPt martensite, Materials Science and Technology 24(8) (2008) 884-889.

[187] H.C. Donkersloot, J.H.N. Van Vucht, Martensitic transformations in gold-titanium, palladium-titanium and platinum-titanium alloys near the equiatomic composition, Journal of the Less Common Metals 20(2) (1970) 83-91.

[188] A.E. Dwight, R.A. Conner, Jnr, J.W. Downey, Equiatomic compounds of the transition and lanthanide elements with Rh, Ir, Ni and Pt, Acta Crystallographica 18(5) (1965) 835-839.

[189] Y.Y. Ye, C.T. Chan, K.M. Ho, Structural and electronic properties of the martensitic alloys TiNi, TiPd, and TiPt, Physical Review B 56(7) (1997) 3678-3689.

[190] T. Ohba, Y. Emura, S. Miyazaki, K. Otsuka, Crystal Structure of γ₂′ Martensite in Au-47.5 at%Cd Alloy, Materials Transactions, JIM 31(1) (1990) 12-17.

[191] R.C. Pond, D.S. Vlachavas, J.W. Christian, Bicrystallography, Proceedings of the Royal Society of London. A. Mathematical and Physical Sciences 386(1790) (1983) 95-143.

[192] A.S.K. Mohammed, H. Sehitoglu, Strain-sensitive topological evolution of twin interfaces, Acta Materialia 208 (2021) 116716.

[193] G. Gengor, A.S.K. Mohammed, H. Sehitoglu, {101¯2} Twin interface structure and energetics in HCP materials, Acta Materialia 219 (2021) 117256.

[194] K. Madangopal, The self accommodating martensitic microstructure of NiTi shape memory alloys, Acta Materialia 45(12) (1997) 5347-5365.

[195] E. Güler, T. Kirindi, H. Aktas, Comparison of thermally induced and deformation induced martensite in Fe–29% Ni–2% Mn alloy, Journal of Alloys and Compounds 440(1) (2007) 168-172.

[196] U. Sarı, E. Güler, T. Kırındı, M. Dikici, Characterization of martensite in Fe–25%Ni–15%Co–5%Mo alloy, Journal of Physics and Chemistry of Solids 70(8) (2009) 1226-1229.

[197] U. Sarı, T. Kırındı, Effects of deformation on microstructure and mechanical properties of a Cu–Al–Ni shape memory alloy, Materials Characterization 59(7) (2008) 920-929.

[198] R. Sidharth, Y. Wu, F. Brenne, W. Abuzaid, H. Sehitoglu, Relationship Between Functional Fatigue and Structural Fatigue of Iron-Based Shape Memory Alloy FeMnNiAl, Shape Memory and Superelasticity 6(2) (2020) 256-272.

[199] T. Omori, K. Ando, M. Okano, X. Xu, Y. Tanaka, I. Ohnuma, R. Kainuma, K. Ishida, Superelastic Effect in Polycrystalline Ferrous Alloys, Science 333(6038) (2011) 68-71.

[200] J. Xia, Y. Noguchi, X. Xu, T. Odaira, Y. Kimura, M. Nagasako, T. Omori, R. Kainuma, Iron-based superelastic alloys with near-constant critical stress temperature dependence, Science 369(6505) (2020) 855-858.

[201] W. Abuzaid, Y. Wu, R. Sidharth, F. Brenne, S. Alkan, M. Vollmer, P. Krooß, T. Niendorf, H. Sehitoglu, FeMnNiAl Iron-Based Shape Memory Alloy: Promises and Challenges, Shape Memory and Superelasticity 5(3) (2019) 263-277.

[202] A. Leineweber, A. Walnsch, P. Fischer, H. Schumann, Crystallography of Fe–Mn–Al–Ni Shape Memory Alloys, Shape Memory and Superelasticity 7(3) (2021) 383-393.

[203] J.M. Ball, R.D. James, Fine phase mixtures as minimizers of energy, Archive for Rational Mechanics and Analysis 100(1) (1987) 13-52.

[204] R. Sidharth, A.S.K. Mohammed, W. Abuzaid, H. Sehitoglu, Unraveling Frequency Effects in Shape Memory Alloys: NiTi and FeMnAlNi, Shape Memory and Superelasticity 7(2) (2021) 235-249.

[205] T. Mura, Isotropic inclusions, in: T. Mura (Ed.), Micromechanics of defects in solids, Springer Netherlands, Dordrecht, 1987, pp. 74-128.

[206] A.S.K. Mohammed, O.K. Celebi, H. Sehitoglu, Critical stress prediction upon accurate dislocation core description, Acta Materialia 233 (2022) 117989.